Direct measurement of the top-quark width with the ATLAS experiment

Javier Alberto Murillo Quijada

Thesis submitted for the degree of

Doctor of Philosophy

Supervisor:

Dr. John A. Wilson

Particle Physics Group,

School of Physics and Astronomy,

The University of Birmingham.

July, 2015.

Abstract

In this thesis a measurement of the total decay width of the top quark, Γ_{top} is presented using selected semi-leptonic $t\bar{t}$ event candidates, recorded from proton-proton collisions at a centre-of-mass energy of $\sqrt{s} = 8$ TeV with the ATLAS experiment at CERN in Geneva, Switzerland. The total recorded integrated luminosity that was used for this measurement equals to $\int$Ldt = 20.3 fb^{-1}. The analysis includes the two event channels: e + jets and μ + jets. The reconstruction of the $t\bar{t}$ system is achieved by using a per-event χ^2 minimisation technique. Official Monte Carlo samples have been used to simulate the $t\bar{t}$ signal and background contributions in order to perform simulated experiments to obtain the statistical and systematic uncertainties.

The results obtained from the measurement of the Γ_{top} parameter are: $\Gamma_{top} = 1.65$ GeV for the μ + jets channel and $\Gamma_{top} = 0.81$ GeV for the e + jets channel. The upper limits obtained from the measured values and the analysis total uncertainties are: $\Gamma_{top} < 4.60$ GeV at 68 % C.L. and $\Gamma_{top} < 7.16$ GeV at 95 % C.L. for the μ + jets channel, and $\Gamma_{top} < 4.40$ GeV at 68 % C.L. and $\Gamma_{top} < 7.51$ GeV at 95 % C.L. for the e + jets channel. These results are consistent with the expected SM value $\Gamma_{top} \sim 1.33$ GeV.

DECLARATION OF AUTHOR'S CONTRIBUTIONS

The successful operation of the Large Hadron Collider and the ATLAS experiment is the product of the hard work of thousands of people involved in their design, construction and careful usage. The studies and results presented in this thesis could not have been possible without the support of this collaboration. During the course of my PhD I have contributed with technical work to the ATLAS collaboration as a developer of the experiment event display, Atlantis. I have given tutorial presentations in several ocassions at CERN to introduce new collaboration members to the usage of this program. Also I have done performance studies of internal simulation samples produced with different storage formats and from different generators aiming to model the observed data successfully.

The measurements presented in this thesis are the result of my own work, except where explicity stated. I was not involved in the design and construction of the LHC and the ATLAS detector. Their introduction included in chapters 3 and 4 provide fundamental information about the comprehensive methodologies that are followed to record data events for physics research. The different analyses presented in chapter 6 are not my own work, but are described to set the context in which the presented analysis is performed. The analysis work presented in chapters 7 and 8 is entirely my own work. Additionally, the technical work described in chapter 5 is result of my own work.

To my parents Ana y Rodrigo

ACKNOWLEDGEMENTS

Being part of the particle physics group at the University of Birmingham has been for me a wonderful and productive experience. I had the chance to meet with great people during these 4 years. Moving to the United Kingdom meant to me leaving behind family and friends in Mexico to start a new adventure in the other side of the world, where I encountered an interesting culture, a challenging weather and needed to adjust to a time zone shifted forward by 8 hours from my hometown. I learned a lot about particle physics research during these years.

I would like to thank Paul Newman and Pete Watkins for giving to me the chance to go through this learning experience. I remember when I applied to the PhD programme in particle physics while still being a student at the University of New Mexico in Albuquerque. I have to especially thank Paul, for sending to me encouraging e-mail replies since the beginning of my application, and for following carefully the process I had to go through in order to get my english certificate and my visa to live in the UK. I am in debt as well with my professors at the University of New Mexico David Dunlap and Michael Gold for kindly preparing recommendation letters referred to me, making possible the completion of my application to the PhD programme successfully. I also would like to thank Andy Schofield and Ray Jones for their welcome reception to the physics department at the University of Birmingham.

I am grateful with Consejo Nacional de Ciencia y Tecnologia, CONACYT, for providing to me a scholarship to study my PhD at Birmingham for 4 years. I thank Marcelino Barboza Flores and Laura Lorenia Yeomans Reyna for supporting my application for a scholarship with CONACYT. I would like to thank the Physics and Astronomy department of the University of Birmingham for giving to me the chance to have some teaching duties and earn some extra money.

I had the chance to work close to great people, for whom I will always have respect. First of all I would like to thank my supervisor John Wilson, for providing encouraging advice and support throughout my PhD, for the intensive and long discussions we had in his office, especially during the writing of this thesis, for always being respectful and for showing interest in my well-being. I'm grateful with Chris Hawkes who always provided support to me at various stages of my PhD. Also I would like to thank Simon Head for providing insight and advice in the different stages of my analysis. I thank Miriam Watson, Juergen Thomas, Thomas MacLaughlan, Pete Watkins and Alan Watson for their advice and support during my analysis especially while preparing slides for presentations. I'm grateful as well with Juraj Bracinik, Cristina Lazzeroni, Orlando Villalobos-Baillie, Kostas Nikolopoulos, Gron Tudor Jones, Mark Slater and Paul Thompson for providing kind support since my arrival in the department.

I have especial thanks to Andrew Chisholm and Richard Mudd for providing a practical and intuitive view of a physics analysis. For providing insight on the use of valuable analysis tools and for the long and productive discussions we had in the office and in the pub about my analysis during these 4 years.

I enjoyed the company of the other PhD students in the particle physics group: Andrew Daniells, Tim Martin, Benedict Allbrooke, Tony Price, James Broughton, Jimmy McCarthy, Francis Newson, Rhys Owen, Alasdair Winter, Matt Baca, Mark Levy, Andrew Foster, Tim Williams, Jody Palmer, Arvinder Palaha, Neil Collins, Hardeep Bansil and Graham Lee.

I will always be greatful with my parents who always provided unconditional support to me, especially in the moments of illness and emotional crisis. I dedicate this achievement to them, who made me aware during my childhood of the meaning of hard work and the great value of pursuing your dreams constantly.

Study hard what interests you the most in the most undisciplined, irreverent and original manner possible.

- Richard Feynman

Contents

List of Figures

List of Tables

Definition of Acronyms

ADC Analogue-to-Digital Converter

CS Central Solenoid

ECAL Electromagnetic Calorimeter

GUI Graphical User Interface

HCAL Hadronic Calorimeter

HFCAL Hadronic Forward Calorimeter

IBL Insertable B-Layer

IP Interaction Point

ISR Initial State Radiation

FSR Final State Radiation

JEDI Job Execution and Definition Interface

JES Jet Energy Scale

KDE Kernel Density Estimation

LHC Large Hadron Collider

MC Monte Carlo

MPI Multiple Parton Interactions

NLO Next-to-Leading Order

PLC Programmable Logical Controlers

PS Proton Synchrotron

PSB Proton Synchrotron Booster

QCD Quantum Chromodynamics

QED Quantum Electrodynamics

QM Quantum Mechanics

QRL Cryogenic Distribution Line

RF Radio-Frequency

RoI Region of Interest

SCT Semiconductor Tracker

TRT Transition Radiation Tracker

ZDC Zero Degree Calorimeter

Chapter 1

Introduction

The analysis presented in this thesis (chapters 7 and 8) represents the first attempt from the ATLAS experiment (introduced in chapter 4) to reproduce a measurement of the top quark width Γ_{top} with data collected from proton-proton head-on collisions at centre-of-mass energy of $\sqrt{s} = 8$ TeV produced at the Large Hadron Collider. A previous measurement following a similar approach was performed by the CDF collaboration at Fermilab as is briefly described in chapter 6.

As the analysis presented here was performed during Run-I of the LHC, a large amount of the time has been devoted to the understanding of the detector responses, sources of systematic uncertainties and other calibration studies that will be better tuned and understood during Run-II. On the other hand the CDF measurement was completed at the end of the Tevatron campaign, so their result is obtained as a result of more than 10 years of experience within its experiments, so their result can be expected to be comparable to or even more precise than the ATLAS first measument. The statistical uncertainties are reduced substantially due to the increase in the luminosity for the different processes at the LHC, however the systematic uncertanties still dominate. A similar situation is present in other top quark properties measurements, such as the top quark mass measurement, which will be repeated during run-II, where they are expected to obtain more precise results.

For this analysis, it was agreed to follow a similar approach as the one used for the ATLAS spin correlation, W-boson polarisation and colour flow measurements, where a binned likelihood fit is performed with data using several templates carrying different values for the underlying parameter of interest, in this case the top width, Γ_{top}.

The author of this thesis, supported by the ATLAS collaboration, produced a 1-dimensional analysis produced entirely from scratch, and was responsible for forming a bigger group within the collaboration intended to get a final result on the top width for publication, including the measurement of the Jet Energy Resolution (JER). The JER turned out to be the biggest systematic uncertainty for the 1-dimensional analysis. This group is currently supported mostly by The University of Birmingham, University of Goettingen and the Technical University of Dortmund in Germany.

Chapter 2

Standard Model and Beyond

Particle physics is a theoretical and experimental effort to understand at the most fundamental level what everything around us is made of and under what mechanisms all these components interact together. In this chapter a general description of experimental particle physics is provided, going from remarkable historical discoveries to basic information that charaterizes the field currently.

Section 2.1 includes historical highlights, especially from the 20^{th} century that give an insight into why our knowledge in this subject has developed in such a specific way. Section 2.2 introduces the current Standard Model (SM), the theoretical structure that summarizes our current understanding of particle physics and has passed crucial experimental tests. Section 2.3 focuses on the recently discovered Higgs Boson, the particle in the model responsible for the mass of fundamental particles. Basic details of Quantum Chromodynamics (QCD), are briefly described in section 2.4. QCD is the part of the SM which describes the strong forces, mediated by gluons between quarks, the basic constituents of hadrons. The quarks and gluons have a fundamental role in high energy particle collisions. Sections 2.5 and 2.6 describe briefly hadron-hadron collisions under the factorisation model approach. These sections discuss the predicted cross-section for $t\bar{t}$ pair production and explain why the top quark plays a fundamental role in particle physics. Finally, possible extensions to the SM are outlined in section 2.7.

2.1 Historical Development of Particle Physics

Experimental discoveries of great importance that took place during the 19th and 20th centuries changed our understanding of fundamental physics drastically [1]. The discoveries of the electron by J. J. Thomson in 1897 and the atomic nucleus by Ernest Rutherford in 1911, led to the discoveries of the nuclear particles; the proton in 1919 by Rutherford and the neutron by James Chadwick in 1932. The first accurate atomic model by Niels Bohr in 1914 ushered in the new field of Quantum Theory.

In 1861 James Clerk Maxwell summarized the understanding of the electromagnetic interaction, describing the radiation from charged objects as *wave-like phenomena*. A group of scientists led by Max Planck, Albert Einstein, Robert Millikan and Arthur Compton at the beginning of the 20th century expanded Maxwell's description by showing that the electromagnetic radiation at a very fundamental level in certain experiments behaves as if made up of discrete energy packets - the introduction of the quantum nature of electromagnetic interaction. These packets can be described as fundamental particles called photons. This new concept of describing waves as particles gave birth to the idea that matter may have the same dual behaviour as well. This duality introduced interference and other effects, usually associated with waves, to matter, and generated a new approach to analyse physical systems called Quantum Mechanics (QM), developed initially by Erwin Schroedinger and Max Born in the 1920's. Duality implies that any particle with momentum p can be described as a wave of wavelength, λ. The particle wavelength and momentum are related by the De Broglie relationship in Equation (2.1):

$$\lambda = \frac{h}{p} \tag{2.1}$$

where h is Planck's constant. As can be seen from the equation, higher energy leads to smaller wavelengths and hence to a higher resolving power. Scattering at high energy and with large momentum transfer corresponds to probing very close

to the target. Therefore smaller distances can be examined as the collision energies are increased. In the 1920's Paul Dirac developed a theory that combined QM, electromagnetism and special relativity (the theory of space and time formulated by Einstein in 1905), which led to the *Dirac Equation*. This was further developed by Richard Feynman, Julian Schwinger, Freeman Dyson and Sin-Itiro Tomonaga amongst others by quantising the fields and leading to Quantum Electrodynamics (QED), a quantum field theory of electromagnetism in which all the components (matter particles and photons) are described as quantised fields. From the solutions of the relativistic Equation (2.2), the particle mass m_o may be positive or negative as shown in Equation (2.3), where E is the energy and p the momentum of the particle. The states with negative mass are interpreted as antiparticles, Dirac's theory led to the idea of *antimatter* which is a group of fundamental particles with the same mass and spin but opposite electric charge as the ordinary matter particles. This prediction was verified in 1932 with the discovery of the positron by Carl Anderson [2], who called it first "positive electron".

$$E^2 = (pc)^2 + (m_o c^2)^2 \tag{2.2}$$

$$m_o c^2 = \pm \sqrt{E^2 - (pc)^2} \tag{2.3}$$

In 1925 Wolfgang Pauli postulated the QM *exclusion principle* that states that two identical fermions (i.e. the particles with spin $\frac{1}{2}$) cannot occupy the same quantum state. Pauli also postulated the existence of the neutrinos in 1930. Their existence was confirmed during the time period from 1931 to 1956, in the study of *nuclear beta decay*, a theory developed by Enrico Fermi [3]. The neutrinos have tiny mass and no electric charge. Together with the electron and proton, they are produced from the neutrons in nuclear beta decay, as illustrated in the diagram in Figure 2.1. Neutrinos interact through a short range interaction known as the *weak force* and can penetrate huge amounts of dense matter without being detected. They were observed indirectly in decays of pions to muons using photographic emulsions [98].

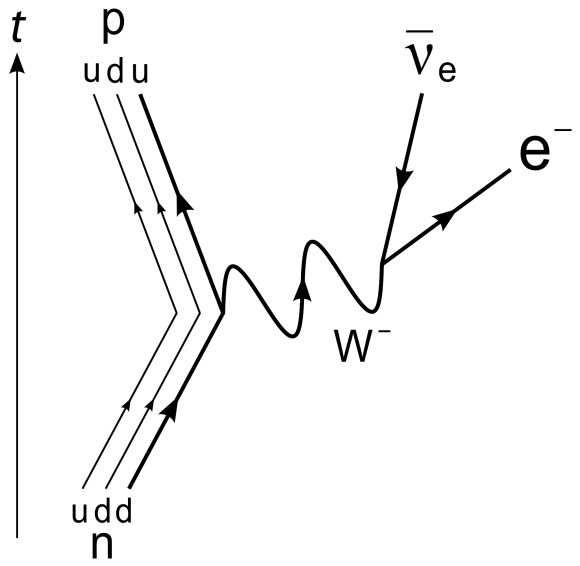

Figure 2.1: Diagram illustrating the β decay interaction between quark components of a proton and a neutron in the atom nuclei that gives rise to the weak decay to an electron and a neutrino. From [1].

The neutrino was detected directly for the first time by Cowan and Reines in 1956 at the Savannah River nuclear reactor, located in South Carolina [7].

Table 2.1: Four Fundamental Forces, [37]

Force	**Mediator**	**Strength**	**Range**
Strong	Gluon (g)	1	$< 10^{-15}$ m
Electromagnetic	Photon (γ)	$\frac{1}{137}$	Infinite
Weak	$W^{\pm}$, Z^0	10^{-6}	$< 10^{-17}$ m
Gravity	Graviton (G)	$6{\times}10^{-39}$	Infinite

After the four fundamental forces listed in Table 2.1 were identified, physical theories describing their behaviour were created, which, when written in the language of Quantum Mechanics, describe the interactions as the exchange of force mediator particles. Each force has its own mediator known as a gauge boson. These are listed

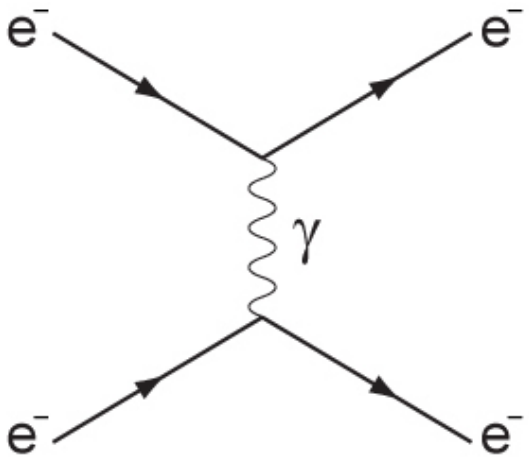

Figure 2.2: Feynman diagram illustrating the exchange of the electromagnetic force mediator, the photon, between two electrons. From [137].

in column two in the same table. Figure 2.2 illustrates the interaction between two electrons by the exchange of a photon, the electromagnetic force mediator. The relative strength of the four interactions is shown in column three of Table 2.1, taking as reference the strength of the strong force which is strongest one with range within $< 10^{-15}$ m, followed by the Electromagnetic interation with infinite range and Weak interaction with range $< 10^{-17}$ m, weaker by three and six orders of magnitude than the strong force respectively. Gravity is the weakest interation being at least 39 orders of magnitude weaker than the strong force and has infinite range. Its particle mediator, the Graviton, has not been found yet at current particle colliders. The $W^{\pm}$ and Z^{o} particles are the mediators of the weak force and the gluons the mediators of the strong force.

A new set of particles known as *strange particles* were detected by the study of V^{o} decays with cloud chamber photographs by Butler and Rochester in 1947. Strange particles were found to be produced through the strong interaction but decayed through a weak process and their properties were measured. In order to explain the different processes for production and decays of strange particles, a new quantum number, *strangeness* was proposed. Strangeness is conserved in the strong interaction but not in the weak interaction. Two examples of these strange particles are the

mesons and hadrons which are composed by combinations of quarks listed in Table 2.2 bound by the strong interation. Mesons are composed by a quark and an anti-quark coupled together, while baryons are a combination of three quarks. Mesons and baryons are part of the group of particles known as hadrons which stand for strongly interecting particles made up by any combination of quarks. Mesons and baryons were found to obey a 'strangeness' number conservation rule for processes that involve the strong interaction.

In the 1950s and 1960s, with the construction and operation of accelerators at even greater energies and the development of larger and more precise particle detectors, many new particles, each with their own distintive properties, were discovered. In 1961 Murray Gell-Mann found that these particles could be arranged by properties related to charge and strangeness numbers so they form symmetric patterns known as "eightfold way". With these patterns Gell-Mann was able to predict sucessfully the existence of other particles like the triply strange *omega-minus* (Ω^-) particle. In 1964 Gell-Mann and Zweig postulated the *Quark Model* which states that hadrons are made up of smaller fundamental constituents called 'quarks' which possess a new property called "colour" which is some sort of charge associated with the strong force. Colour charge can have the values Red (R), Blue (B) and Green (G) for quarks or their corresponding opposite values $\bar{R}$, $\bar{B}$ and $\bar{G}$, for antiquarks. Quarks were found to avoid always being in an isolated state, forming instead composite states with other quarks. This is known as *confinement*. The quarks are found to always form colourless bound states, which are states of three quarks each one with a different colour charge: (R, B, G) or states of two quarks with opposite colour charge: (R, $\bar{R}$), (B, $\bar{B}$) and (G, $\bar{G}$).

Deep inelastic experiments at SLAC in the 1960s and at CERN in the 1970s revealed that indeed the protons are composed of three charged points or partons which had all the properties predicted for quarks such as spin and fractional electric charges listed in Table 2.4. Also half of the momentum of the proton is associated with an electrically neutral component which was found to be gluons, the strong force me-

diators. In 1973 David Gross, David Politzer and Frank Wilczek discovered a new property of the strong force called *asymptotic freedom* which is the observed screening of the colour charge when quarks get very close to each other within baryons. At a small separation or at large momentum transfer the forces between the quarks becomes negligible; they are essentially free.

From the quark model and its properties, several combinations of heavy quarks can be built into colourless final states. This was illustrated by the impressive discovery of the J/ψ particle, made by a c-quark and its anti-quark counterpart $\bar{c}$ in 1974 at SLAC and Brookhaven, which is described by the quark model as a system of two quarks with opposite colour charge. In 1975 the τ lepton was discovered, supporting the idea of the existence of a third generation of fundamental particles. This idea was reinforced further with the discovery of the upsilon Υ particle by Leon Lederman and his collaboration at Fermilab. This particle is made of a $b\bar{b}$ quark pair, the b-quark was predicted to be part of the third generation of quarks together with the top quark.

Sheldon Glasgow, Steven Weinberg and Abdus Salam postulated a Electro-Weak theory in the 1970s, which is a theory of unification that includes electromagnetism and weak interations. It predicts the existence and values for the masses of $W^{\pm}$ and Z bosons, mediators of weak force. These particles were observed directly for the first time at CERN in 1983 by the UA1 experiment led by Carlo Rubbia. These measurements were consistent with the electroweak theory predictions. In 1989 e^+e^- experiments carried out in the LEP collider at CERN, the Z-boson width was measured and was found to be consistent with the existence of only three generation of neutrinos.

In 1995 the top quark, the most massive fundamental particle was discovered at Fermilab. As the top quark decays instantaneously it does not form bound states with other quarks. The special properties of the top quark are discussed in chapter 6. In 2014 a particle responsible for giving mass to the rest of the particles known as the

Higgs boson particle, H, was discovered at CERN. This was a strong confirmation of the SM (sections 2.2 and 2.3). Still several extensions to the current SM will be tested during the following years and exciting new discoveries could be close ahead.

2.2 The Standard Model of Particle Physics

The Standard Model is a description of the strong, electromagnetic and weak interations of the basic building blocks of matter that together represent our up-to-date understanding of particle physics, excluding gravity. Formally it is a locally gauge invariant quantum field theory. Experimental measurements have been to date in good agreement with predictions of the Standard Model. The SM has so far been very successful. It follows the assumption that all matter is made up of a group of 12 different spin-$\frac{1}{2}$ Dirac fermions, divided into 6 leptons and 6 quarks as listed in Tables 2.3 and 2.4 where they are classified by generation. These particles interact through the forces shown in Table 2.1. It is difficult to incorporate gravity into the SM as gravitational interactions are almost negligible when dealing with fundamental particles in an environment with low matter density as in particle colliders. Nonetheless there are some models that predict that gravitons could be produced at the LHC. However such signals have not been observed yet. Different categories of particles are listed in Table 2.2, where they have been classified according to their spin number which can have half-integer value like Leptons and Baryons or integer value like Mesons and the force mediators shown in Table 2.1.

All the charged fermions interact through the electromagnetic force and can be arranged in 3 generations, each generation containing 2 leptons and 2 quarks. Leptons are shown in Table 2.3. The lepton numbers L_e, L_μ and L_τ are conserved quantities in every process involving leptons. The electric charges and mass values are shown in columns 6 and 7.

Table 2.2: Four Fundamental Forces, [37]. All particles with mass different than zero interact through the gravitational force, however its effect is negligible in the scope of particle physics.

Spin	**Category**	**Examples**	**Interactions**
Half-Integer	Leptons	e, μ, τ, ν_e, ν_μ, ν_τ	Electromagnetic and Weak
	Baryons	Protons, Neutrons	Strong, Weak, Electromagnetic
Integer	Meson	Pions: π^+, π^-, π^o	Strong, Weak and Electromagnetic
	Force Mediator	g, γ, Z^o, $W^\pm$	Gluons have strong colour charge and the $W^\pm$ have electric charge

Table 2.3: The Standard Model Leptons. The corresponding SM anti-leptons have charge and lepton numbers opposite to those of the leptons shown in this Table. ν_e mass limit is based on results from $^3H\beta$ decay studies, the ν_μ mass is determined from studies of π^+ decays and the ν_τ mass is from LEP experiments (1991-1995) [37].

Generation	**Flavour**	L_e	L_μ	L_τ	q [e]	**Mass [MeV]**	**Lifetime [s]**
First	e^-	+1	0	0	-1	0.510	Stable
	ν_e	+1	0	0	0	< 0.000002	$> 10^{19}$
Second	μ^-	0	+ 1	0	-1	105.658	2.2×10^{-6}
	ν_μ	0	+ 1	0	0	< 0.19	$> 10^{19}$
Third	τ^-	0	0	+ 1	-1	1776.820	$\sim 10^{-13}$
	ν_τ	0	0	+ 1	0	< 0.18	$> 10^{19}$

The μ and the τ have the same electric charge value as the electron. The masses of the charged leptons increase with generation number; the τ is very massive and correspondingly short lived and the μ lepton is also unstable but still able to penetrate detectors before it decays. The electron on the other hand is believed to be a stable particle. Neutrinos have been found to have non-zero masses and can oscillate between the different generations or flavours, but their mass values are really tiny

compared with the other three leptons [37]. Also all leptons interact through the weak force. As their electric charge is zero the neutrinos interact only weakly and hence interact rarely with matter, which is what makes neutrinos really penetrating.

Table 2.4: Standard Model Quarks. Correspoding SM anti-quarks have opposite electric charge, baryon number and flavour than the matter quarks shown in this table [37].

Generation	**Flavour**	$\mathbf{q}_{EM}$ [e]	**B**	$\mathbf{I}_3$	$\boldsymbol{S}$	$\boldsymbol{C}$	$\boldsymbol{B}$	$\boldsymbol{T}$	**Mass [GeV]**
First	u (up)	$+\frac{2}{3}$	$+\frac{1}{3}$	$+\frac{1}{2}$	0	0	0	0	$0.0023^{+0.0007}_{-0.0005}$
	d (down)	$-\frac{1}{3}$	$+\frac{1}{3}$	$-\frac{1}{2}$	0	0	0	0	$0.0048^{+0.0005}_{-0.0003}$
Second	c (charm)	$+\frac{2}{3}$	$+\frac{1}{3}$	0	0	+1	0	0	1.275 ± 0.025
	s (strange)	$-\frac{1}{3}$	$+\frac{1}{3}$	0	+1	0	0	0	0.095 ± 0.005
Third	t (top)	$+\frac{2}{3}$	$+\frac{1}{3}$	0	0	0	0	+1	$173.07 \pm 0.52 \pm 0.72$
	b (bottom)	$-\frac{1}{3}$	$+\frac{1}{3}$	0	0	0	+1	0	4.18 ± 0.03

The 6 quarks are listed in Table 2.4. Each generation has an up-type and down-type quark, the former with an electric charge of $+\frac{2}{3}$ and the latter a value of $-\frac{1}{3}$ (in units of the electron charge). The quarks cover a large range of masses from 2.3 MeV for the u-quark to $\sim$ 173 GeV for the top quark. Quarks of certain flavour can decay into a quark of different flavour but lower mass via the weak interation. In general, decays will follow the sequential pattern $t \to b \to c \to s \to u/d$ [64]. Analogous to the conservation of lepton number law is the conservation of Baryon Number B. As listed in the table all the quarks have a value, B $= \frac{1}{3}$ and anti-quarks a value B $= -\frac{1}{3}$. This implies that composite particles made of quarks mesons ($q\bar{q}$) and baryons (qqq) have B values equal to 0 and 1 respectively. The isospin number I_3 is a quantum number. Isospin is treated as an intrinsic angular momentum and is quantised like ordinary spin. For the up and down quarks, the third component of isospin, $\mathrm{I}_3 = +\frac{1}{2}$ and $-\frac{1}{2}$ respectively and the rest of the quarks have a value equal to zero. The quantum numbers Strangeness (S), Charm (C), Bottomness (B) and Topness (T) are conserved in strong interactions but not in weak interactions. These numbers determine how many s, c, b, and t quarks, respectively, are present

in hadrons.

Additionally, as mentioned before, the quarks have an associated strong charge named colour charge. This charge by convention can have three different values R, B and G or negative values $\bar{R}$, $\bar{B}$ and $\bar{G}$. Every composite particle made of quarks has a colourless state. For example the proton is made of two up quarks and one down quark $p(uud)$, with different colour charge (RBG) for each one, which produces a colourless state. The neutron is made of two down quarks and an up quark, $n(udd)$ also with different colour charge for each one. Examples of mesons are $\pi^+(u\bar{d})$, $\pi^-(d\bar{u})$ and π^o either $(u\bar{u})$ or $(d\bar{d})$ where the two components have opposite colour charge as $(R\bar{R})$, $(B\bar{B})$ or $(G\bar{G})$. All the states that can be accounted for by the quark model are studied in *hadron spectroscopy*.

Just as atoms possess different energy levels whose transitions emit photons with frequency proportional to the difference in energy level, hadrons experience a similar process. In this case, the different energy levels corresponding to the same quark combination, are regarded as different particles. Energy states corresponding to quark $c\bar{c}$ combination are known as J/ψ resonances (charmonium states) while states corresponding to $b\bar{b}$ combination are known as Υ resonances (bottomonium states). The structure of baryons can be probed by using beams of high energy leptons. For example electrons in certain collisions produce a *hard-interaction* between the electron and a single quark, which produces a track corresponding to the electron and a jet of particles originating from the interacting quark. A jet is a shower of particles produced from the hadronisation process that quarks experience after their production. During this process they form bound states with other quarks. Jets are defined in chapter 7. Such events confirmed the presence of quarks and gluons in hadrons. At the HERA detector, high energy colliding beams of electrons (and positrons) and protons allowed the momentum distributions of quarks and gluons within the proton to be measured with precision [8].

Table 2.5: Standard Model Bosons [37].

Name	**Mass [GeV]**	**Decay Width [GeV]**	**Spin**	**Charge**
Photon (γ)	0	-	1	0
$W^{\pm}$	80.385 ± 0.015	2.085 ± 0.042	1	±1
Z^0	91.1876 ± 0.0021	2.4952 ± 0.0023	1	0
gluon (g)	0	-	1	0
Higgs (H)	125.9 ± 0.4	4.15×10^{-1} (theoretical [39])	0	0

Finally in table 2.5 the boson force mediators are listed. According to the SM gluons and photons have a mass of zero. $W^{\pm}$ and Z^0, the weak force mediators, have comparable mass values and widths whose difference is related to *spontaneous symmetry breaking* [15]. The Higgs is also a boson and has been found to have a mass value around 125 GeV [40]. The SM bosons all have spin 1 apart from the Higgs which has spin 0. From all the bosons the W^+ and W^- are the only ones with electric charge, having values +1 and -1 respectively. The gluons are the strong force mediators and have strong colour charge which means that gluons can interact between themselves through the strong force.

A simplified version of the SM has been provided. It can be expressed more rigorously as a group theory which provides a proper classification of all the particles and makes it possible to visualize several symmetries from where it is posible to derive all the forces and foresee possible extensions [3]. The SM has over 20 free parameters.

2.3 The Higgs Boson

The interaction of the Higgs field with the rest of the particles is responsible for giving particles mass through the *Higgs mechanism*. The theoretical details of the Higgs mechanism were published in three different papers during 1964 by three independent groups, [41], [42], [43]. The SM includes the description of the kinetic energy of the Higgs field, the Higgs potential and its gauge interactions. The Higgs boson is the second most massive fundamental particle observed to-date after the

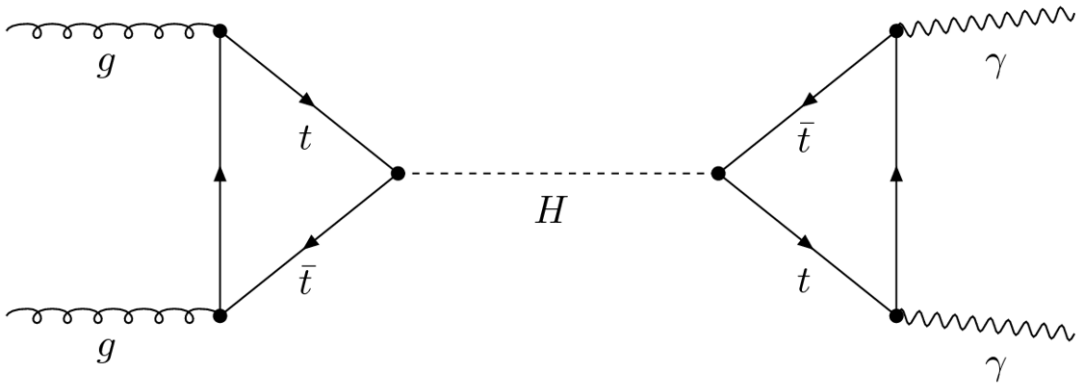

Figure 2.3: Diagram illustrating the production of a Higgs particle through a gluon-gluon fusion interation, finally decaying to a pair of photons. Events with this topology contributed substantially to the Higgs detection at the LHC. From [18].

top quark. So it decays through many processes involving different topologies that are constantly being searched for in current particle colliders. In Figure 2.3 a diagram is shown illustrating the production of a Higgs boson through a gluon-gluon fusion interation producing two photons, $H \to \gamma\gamma$.

As the number of events observed by the different experiments during the run-I of the LHC is very limited, discovering the Higgs was a very challenging process. With the increase in 2015 of the collision energy at the LHC the analyses will be able to measure the Higgs mass m_H and the Higgs width Γ_H with more precision as the branching fraction values for the different channels will increase as shown in figure 2.7. For collisions at a centre-of-mass energy of 8 TeV the branching fractions for different Higgs decays as a function of the Higgs mass values are predicted by the SM. These fractions are shown in Figure 2.4 above for the mass range 90-200 GeV. This plot shows that for most of this range, the decay H→WW is the channel with the highest rate, though the background component for this channel reduces the sensitivity and makes the signal strength not high enough for the discovery. In fact the processes $H \to \gamma\gamma$ (Figure 2.3) and $H \to ZZ$ are the ones that offered higher signal strengths as the discrimination against backgrounds is higher for these channels. On the 4th of July 2012 the ATLAS and CMS collaborations announced that

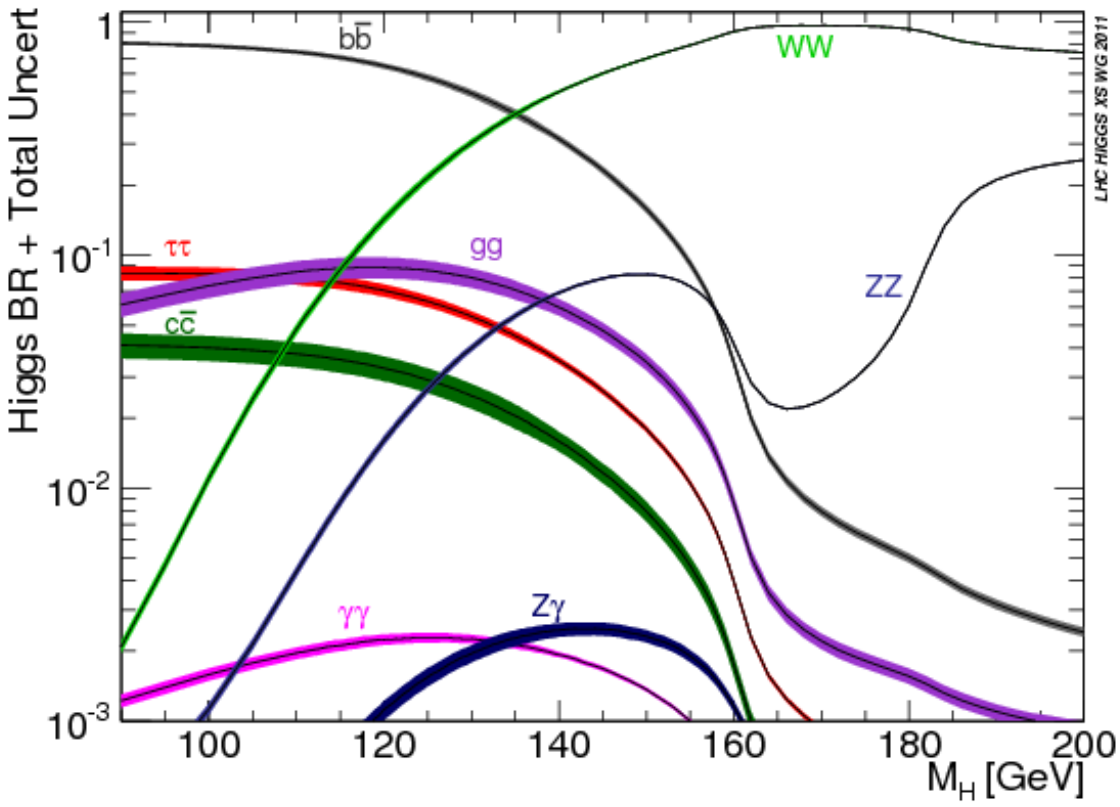

Figure 2.4: Branching fractions corresponding to different Higgs decays as a funtion of its mass m_H. The observed data at the LHC provided a measurement of a mass value around $\sim$ 125 GeV. From [45]

a particle consistent with the SM Higgs boson had been found [91]. Data analysis continued throughout LHC Run-I to increase the strength of the signals in other channels like $H \to b\bar{b}$ and $H \to \tau\tau$. With these the decay of the Higgs to fermions was confirmed [92]. Summaries of up-to-date results on Higgs mass measurement from the LHC have been published [40].

2.4 Quantum Chromodynamics

In this section key elements of Quantum Chromodynamics (QCD), the theory of the strong interaction contained in the SM, are briefly mentioned. Strong interactions are responsible for keeping quarks and gluons within hadrons and also for the

production of a huge variety of processes initiated when two hadrons are collided head-on with each other at high energy colliders such as the LHC. Amongst such processes are those for the production of a $t\bar{t}$ pair a top quark and an anti-top quark. A discussion of QCD is appropriate.

2.4.1 Confinement and Asymptotic Freedom

QCD is a *gauge theory* as is QED and the Electro-Weak unification theory. QCD was the result of gathering together several theoretical ideas and experimental results. The main difference between QCD and QED is that the quantum elements of QCD, the quarks and gluons, the equivalent of the electrons and photons in QED are always bound within hadrons. This property is known as *confinement*. The colour property for the strong interacting particles is necessary to explain spin-$\frac{3}{2}$ hadron systems that are made of three identical quarks, like Δ^{++} (uuu), Δ^{-} (ddd) and Ω^{-} (sss). *Pauli's exclusion principle* is not violated as the quarks each have a different colour index, and so they can share the same spin state. Hadrons do not change their colourless state, however individual quarks are able to decay to their generation partner through weak interactions. These colourless systems in the mathematical framework are known as colour singlet states, where quarks transform according to the group of colour transformations SU(3) known as *three colour model*. This model has passed several tests such as predicting the decay rates for the process $\pi^{o} \rightarrow \gamma\gamma$ correctly [6].

A hadron is usually restricted to dimensions within ~ 1 fm. From the *uncertainty principle* it is possible to conclude that the energy of quarks within the hadrons is pretty much independent of their masses if the mass value is really tiny as it is the case for light quarks like u, d or s. QCD predicts that quarks while they are bounded by the strong force within the hadrons, at distances shorter than hadron dimensions behave as free particles. This property is known as *Asymptotic Freedom*. This property of the strong interactions can be explained in terms of the production of virtual gluons in the vaccum surrounding the colour source. These virtual

gluons screen the colour charge and this is the explanation for the reduction of the strength of the field at short distances. QCD is able to approximate the value of *strong coupling constant*, α_S, which tends to zero at small distances, giving a result in agreement with asymptotic freedom.

Deep inelastic scattering refers to processes used to probe within hadrons such as protons and neutrons usually using beams of electrons, muons or neutrinos. In experiments where the probing energy scales are really high and the strong interacting particles get really close to each other α_S is very small, It is then possible to use perturbative techniques to calculate physical observables that can then be measured experimentally.

2.4.2 Lagrangian Density and Strong Coupling Constant

QCD is a non abelian gauge theory (i.e. its elements do not commute). The Lagrangian density of QCD, (which has the property of being invariant under local transformations) is [6]:

$$\mathcal{L}_{QCD} = \mathcal{L}_{fermion} + \mathcal{L}_{boson} + \mathcal{L}_{gauge} + \mathcal{L}_{ghost} \tag{2.4}$$

The first two terms describe the interactions of spin-1 gluons (which have colour charge and are massless) and quarks with the associated colour field. The third term allows the use of perturbation theory to extract calculations from QCD. A gauge is set by fixing a λ value included in this term to a particular value, 1 for example corresponds to the *Feynman gauge*. The last term $\mathcal{L}_{ghost}$, is introduced because the fixing of the gauge in the third term breaks the local gauge invariance, which is recovered by introducing additional fields known as Faddeev-Popo ghost fields to cancel unphysical degrees of freedom.

The strong coupling constant $\alpha_S(Q)$, as a function of the energy scale, determines

the strength of the strong potential of the Lagrangian with respect to the kinetic component. For a given energy scale, QCD tells how the value of the strong coupling constant varies with scale but does not specify the absolute value of the constant, which needs to be calculated from experiment. An estimation of the strong coupling constant $\alpha_S(Q)$ can be obtained by using perturbation theory techniques over QCD and applying renormalization to remove divergences obtained from the approximated series in order to obtain finite predictions for the observables. For large energy scales $>$ 1 GeV where perturbation theory techniques are applicable the strong coupling constant at leading order (LO) can be expressed as:

$$\alpha_S(Q) = \frac{2\pi}{b_0 \ln(Q/\Lambda)} . \tag{2.5}$$

where Λ is a QCD constant. The value of Λ has been found to have a value $\sim$ 200 MeV. It determines the energy scale where the coupling constant diverges or, in other words, at which order of magnitude $\alpha_S(Q)$ becomes too large and the perturbation theory model breaks down. b_0 is a coefficient of the QCD beta function, $\beta(\alpha_S)$ and $b_0 = 11$ - $N_f/3$ for QCD with three colour charges, where N_f stands for the number of flavours [6]. The estimation can be improved by increasing the order of the calculation. From equation (2.5) we see directly that, by increasing the value of the scale Q, the strong coupling decreases, in effect, asymptotic freedom.

2.5 Hadron-Hadron Collisions and Top Pair Production

Details of the operation of a hadron collider are provided in chapter 3 where crucial processes and components of the Large Hadron Collider, (LHC) are briefly described. At the LHC, protons are accelerated to 3.5 TeV. Two beams of protons are circulated in opposite directions around a large circumference (27 km at the LHC) where the individual particles reach a velocity very close to the speed of light. The two beams

are then focused against each other so the protons experience *head-on collisions*. The most interesting collisions comprise *hard hadron-hadron scattering*. These collisions occur in the LHC at centre-of-mass energies with upper value $\sqrt{s} \geq 7$ TeV.

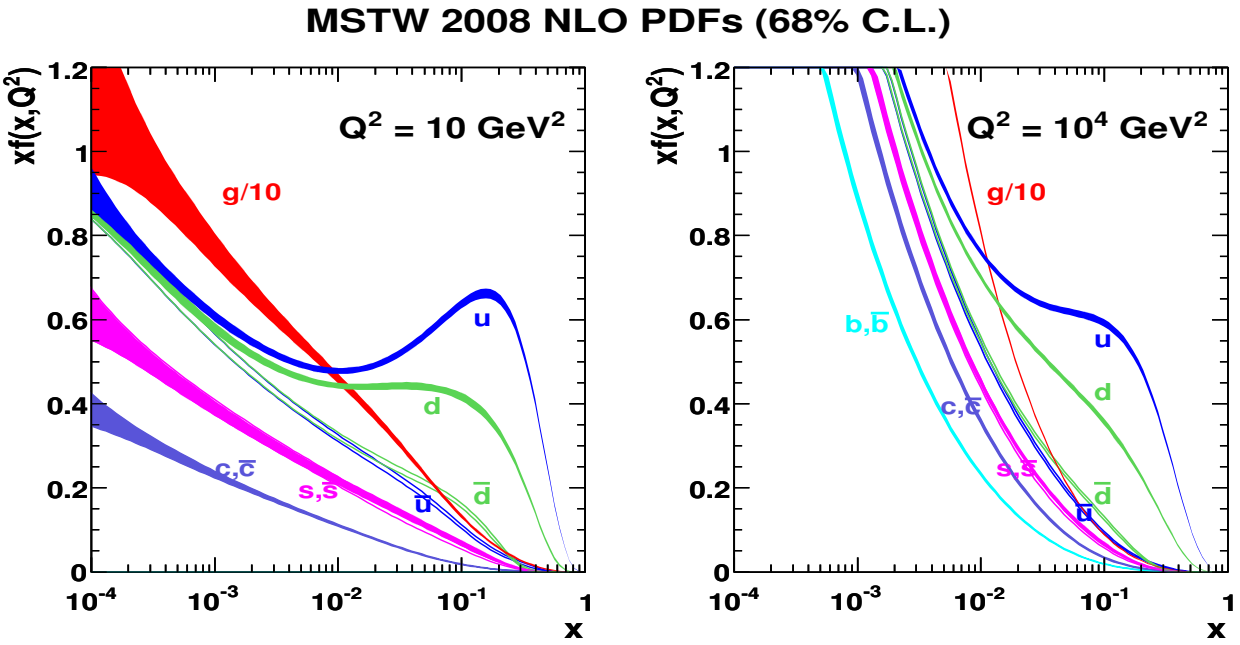

Figure 2.5: Parton momentum densities for the proton. Note that the gluon contribution is supressed by a factor of 10. From [13].

The energy of each of the accelerated hadrons is distributed between its components, partons. $f_i^{(a)}(x_a, Q^2)$ is the *Parton Distribution Function* (PDF), and gives the probability density that a parton of species "i" (including gluons) in a hadron "a" will be found with a fraction of momentum x_a when a hard interaction takes place. Q^2 is the four momentum transfer squared, a characteristic scale related with the resolving power of the hard scattering. These density functions can not be calculated directly from the theory, but can be obtained from QCD global fits to the deep inelastic scattering data. If a parton takes a fraction x of the total hadron momentim P_a its momentum would be xP_a and then the quantity $xf_i^{(a)}(x, Q^2)$ is regarded as *parton momentum density* for each of the hadron components. Figure 2.5 shows a set of two parton momentum density functions for a proton calculated at Next-to-Leading-Order degree of precision with perturbative QCD, using two dif-

ferent scales. At values of x close to 1, all the densities fall down to zero with the exception of the density functions associated with the *valence quarks*, u and d quarks for the protons. The valence quarks determine the quantum numbers of the hadrons.

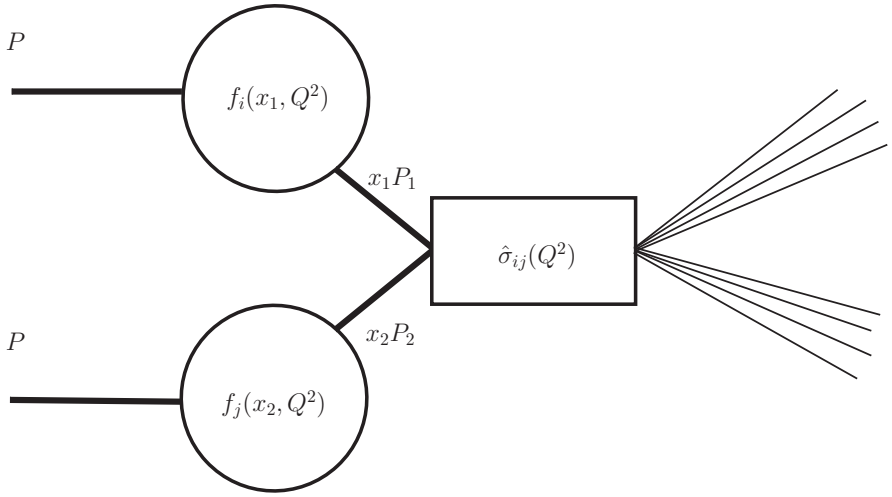

Figure 2.6: Diagram summarizing the main elements of the factorisation model approach for proton proton high energy collisions.

The *factorisation model* can be used to calculate the cross-section of any given process $P_1 + P_2 \rightarrow X$ where P_1 and P_2 stand for any two colliding hadrons and X is any system of particles obtained from the hard interaction. This model describes a collision between two hadrons as the individual interaction between two partons of species i and j belonging separatedly to the two different incoming hadrons with associated cross-section $\hat{\sigma}_{ij}$ and individual parton distribution functions $f_i(x_i, Q^2)$ and $f_j(x_j, Q^2)$ respectively for the two partonic species. The diagram in Figure 2.6 describes the factorisation approach where all the mentioned elements are accommodated together. The cross section can be factorised into two parts in the parton distribution functions corresponding to the partonic species of the two hadrons and the characteristic hard scatttering cross-section factor $\hat{\sigma}_{ij}$ that relies on SM parameters.

For example for $t\bar{t}$ production in hard-scaterring processes initialized with either $p\bar{p}$

or pp collisions the cross section from the factorisation model can be expressed as:

$$\sigma^{t\bar{t}}(\sqrt{s}, m_t) = \sum_{i,j=q,\bar{q},g} \int dx_i dx_j f_i(x_i, \mu^2) \bar{f}_j(x_j, \mu^2) \times \hat{\sigma}_{ij \to t\bar{t}}(\rho, m_t^2, x_i, x_j, \alpha_s(\mu^2), \mu^2) \quad (2.6)$$

the dependence of Equation (2.6) on the arbitrary scale μ^2, decreases when increasing the precision of the calculation. The convention $\mu^2 = Q^2$ is commonly used. Other additional scales could appear when increasing the precision of the calculation; by convention they are as well set equal to Q^2. The sum includes all partonic combinations $q\bar{q}$, gg and qg pairs. $\rho = \frac{4m_t^2}{\sqrt{\hat{s}}}$ the ratio between the minimum required energy to produce a top pair and the available energy, $\hat{s} = x_i x_j s$. $\hat{s}$ is the *effective* centre-of-mass-energy corresponding to the actual partonic collision. The production diagrams associated with the $t\bar{t}$ cross-section at Leading Order are discussed later and are displayed in Figure 6.1. A $t\bar{t}$ pair can be produced from either a $q\bar{q}$ annihilation process or gluon-gluon fusion.

The minimum energy needed to produce a pair of top quarks is $\hat{s} \geq 4m_t^2$. Then it follows that $x_i x_j = \frac{\hat{s}}{s} \geq \frac{4m_t^2}{s}$. According to the shapes of the PDF's in Figure 2.5 it can be noticed that x fraction values would more likely move to smaller values as possible. A threshold value for $t\bar{t}$ production can be estimated by considering $x_i \approx x_j \equiv x$. At centre of mass energies 1.8 TeV for Tevatron and 8 TeV for the LHC the $x \approx \frac{2m_t}{\sqrt{s}}$ for $t\bar{t}$ pair production takes the approximate values $x_{Tevatron} = 0.20$ and $x_{LHC} = 0.045$ for top pair production in the two accelerators. From Figure 2.5 we notice that at the LHC the x fractions giving rise to $t\bar{t}$ production corresponds mainly to gluon-gluon processes, with $\sim$ 90 % of the production rate, being dominant over $q\bar{q}$ production processes ($\sim$ 10 % of the production rate). At the Tevatron on the other hand $q\bar{q}$ production processes were dominant with a rate $\sim$ 85 %. The $t\bar{t}$ cross-section at the LHC increases by more than a factor of 100 compared to the Tevatron, which improves the statistical precision in the different measurements and searches involving top pairs. Figure 2.7 shows the cross section for different processes taking place from proton-proton collisions in current high energy experiments from collision energies from 8 TeV to 100 TeV. The $\sigma_{t\bar{t}}$ for $t\bar{t}$ production changes by

more than two orders of magnitude within this range. In this plot processes with two b-quarks in the final state or at least a jet with $p_T > 50$ GeV have the highest cross sections. Also at the bottom processes giving rise to Higgs production are shown. The most dramatic change in cross-section within this range corresponds to the final state $t\bar{t} + H$.

The number of events of interest produced in a hadron accelerator can be expressed as:

$$N = \sigma \int dt \mathcal{L}(t) \tag{2.7}$$

where $\mathcal{L}(t)$ is the *instantaneous luminosity*, usually expresed in units of $cm^{-2}s^{-1}$ and σ is the cross section for any given process, expressed in units of b, where 1 b $= 10^{-24}\ cm^2$. If beams with n_b bunches containing n_1 and n_2 particles respectively are circulated around the accelerator circumference to produce head-on colisions at the frequency f then the corresponding instantaneous luminosity is:

$$\mathcal{L}(t) = f \frac{n_b n_1 n_2}{4\pi \sigma_x \sigma_y} \tag{2.8}$$

where σ_x and σ_y are the rms values for the transverse dimensions of the beam. Then the instantaneous luminosity can be increased by increasing the number of bunches per beam. The integrated luminosity in L = $\int$Ldt is also a useful paramater.

During the time period from 1990 to 2010 the main attention in particle physics was focused on the operation of the Tevatron accelerator at Fermilab in Batavia, Illinois, United States and the LEP (e^+e^- collider) at CERN. The Tevatron was the first accelerator to produce collisions at an energy over 1 TeV and was responsible for the discovery of the top quark in 1995, but was unable to discover the Higgs particle with the produced data. The LHC started operation in 2010 being able to accelerate each of the hadron beams to energies over 1 TeV for first time in history producing

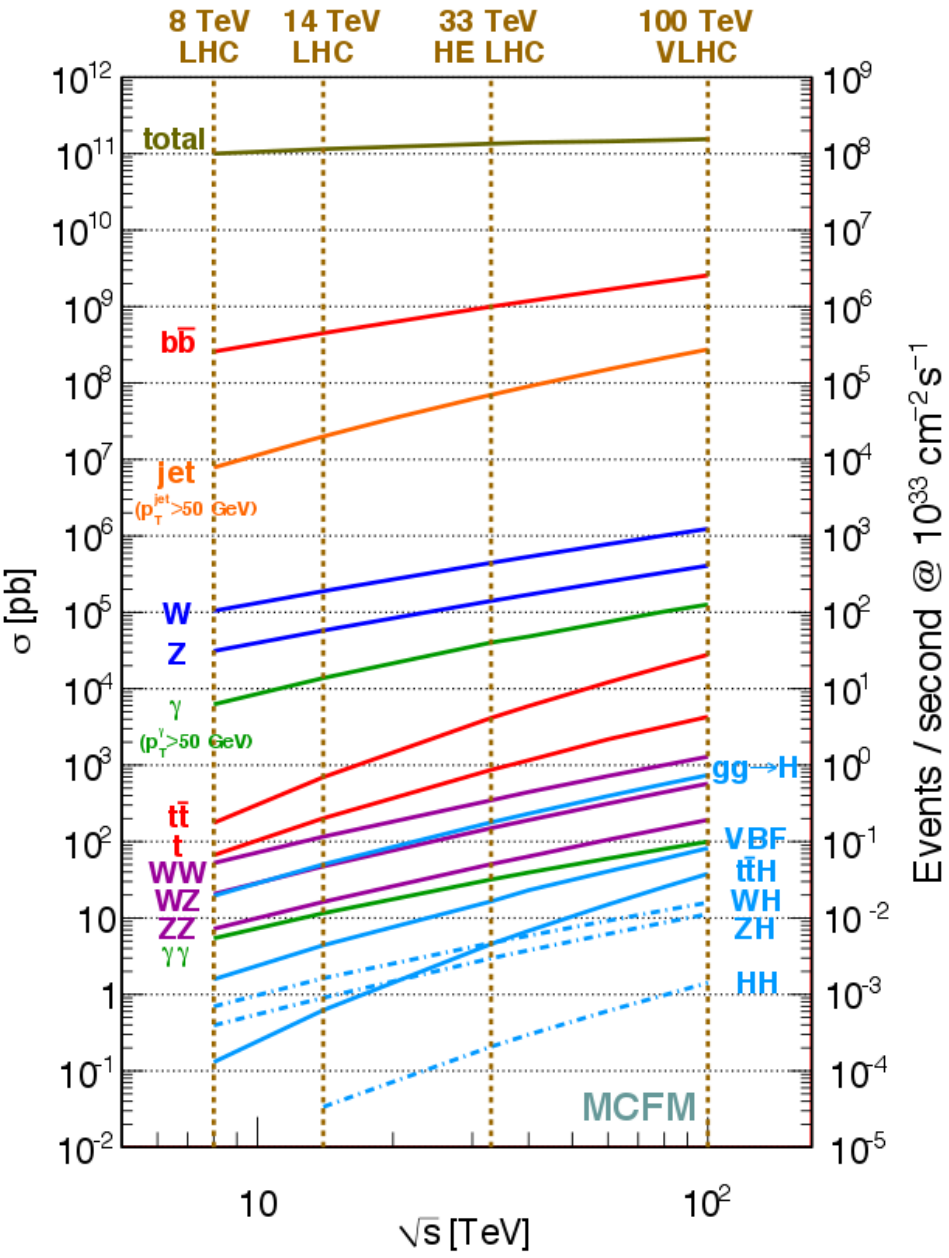

Figure 2.7: Predicted cross sections for different typical final states presented at the LHC in logarithmic scale. The plot shows the impact of increasing the collision energy from 8 TeV to 100 TeV for the different states. The cross section corresponding to $t\bar{t}$ events increases by more than two orders of magnitude within this range. HE-LHC and V-LHC stand for two proposed upgrades of the LHC so it can run with collisions at centre-of-mass energies of 33 TeV and 100 TeV respectively. From [11].

collision energies $\geq$ 7 TeV and then providing enough data to finally declare the discovery of the Higgs boson. Also the LHC experiments offer the possibility of exploring beyond the standard model theories. From hadron collider machines it has been possible to discover the $W^{\pm}$, Z^0, t and H. Precision measurements over SM parameters such as M_W and m_{top} have also been achieved.

2.6 Importance of the Top Quark

The top-quark was first observed by the CDF and D0 experiments at Fermilab in 1995 in $p\bar{p}$ collisions at a centre-of-mass energy $\sqrt{s}$ = 1.8 TeV [16], [17]. It is regarded as the weak-isospin partner of the bottom quark and since the discovery of the b-quark in bottomium states Υ in 1977 the top quark was expected to complete the third generation of quarks. Its huge mass, the highest value for any observed fundamental particle (up to now) suggests that it should play an important role in fundamental physics. Strong interactions can be probed by studying $t\bar{t}$ pair production, while the weak force is studied by analysing the different top decay channels. The SM parameters associated with the top quark are its mass m_{top} and the three elements in the CKM matrix involving top quark decays, both described in more detail in chapter 6. The value of the Z, W bosons, t-quark and Higgs boson masses are not independent in the SM. From the LEP and Tevatron accelerators it has been possible to measure the Z, W and top-quark masses and to set constraints on the Higgs mass.

The plot in the left of Figure 2.8 shows the history of top mass measurements from the year 1989. During the time period 1989-1995 before the discovery of the top the statistical uncertainties in the m_{top} measurement were really large, covering a range $>$ 100 GeV. From 1995 when the top was discovered the uncertainty in the measurement decreased drastically as is displayed in the plot and the measured value has been converging to the current average without large fluctuations since then. Fermilab experiments after the long campaign of the Tevatron operation were able

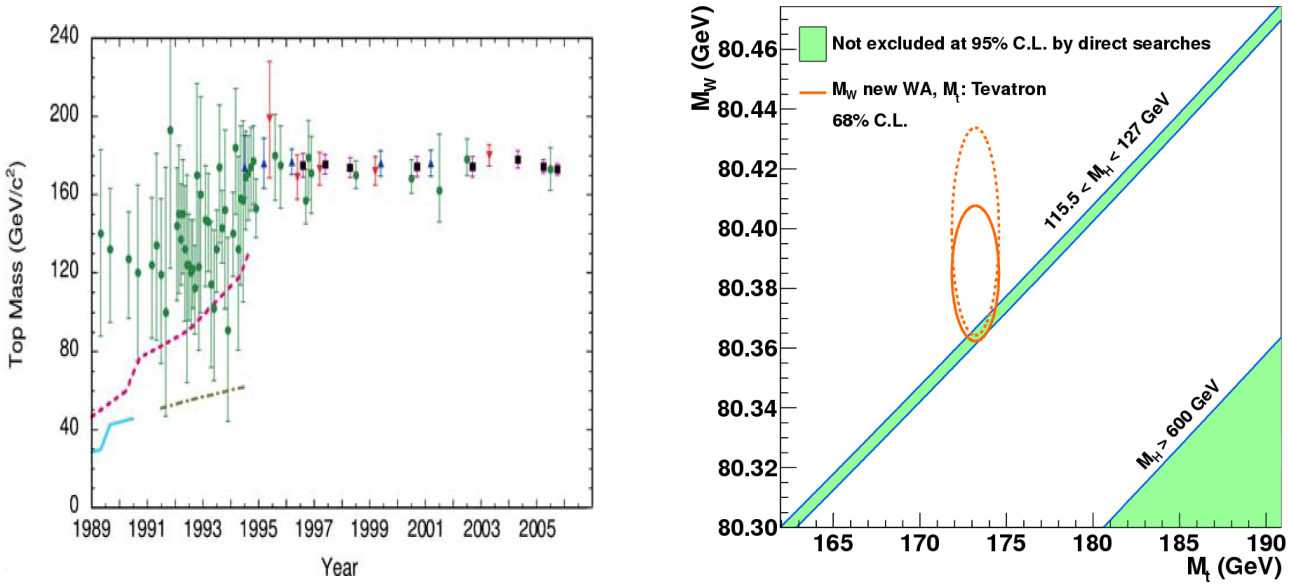

Figure 2.8: History of m_{top} measurements from the time period 1989 to 2005 showing a dramatic change in precision from the top discovery in 1995, (left) from [61]. SM prediction for the m_H given a relationship beween the m_W and m_{top} masses, (right) from [9], the predicted dependency is in agreement with what has been measured so far.

to understand sources of uncertainty very well and have shown comparable results to those delivered by the LHC experiments. A situation that should change during the LHC run-II due to better understanding of the detectors and the increase in statistics.

The plot in Figure 6.5 in chapter 6 shows the most recent measurements of m_{top}, the current world average and the latest combination from Tevatron experiments yielding a value $\sim$ 173.3 GeV with uncertainties smaller than 1 GeV. The world average measurement of the W-boson mass was used before the Higgs was discovered to set constraints on its mass still having uncertainties with large value $\sim$ 30 GeV. In the right side of Figure 2.8 the SM prediction for the Higgs mass given a set of measured values of the m_W and m_{top} is shown. The plot displays that the current world's averages are consistent with a Higgs mass value between 115.5 and 127 GeV in good agreement with the recent measurements of $m_{Higgs} = 126.0 \pm 0.4(\text{stat}) \pm 0.4(\text{sys})$ GeV [40].

2.7 Beyond the Standard Model

The plot in Figure 2.9 displays different cross-section measurements from ATLAS with corresponding theoretical predictions calculated at NLO or higher degree of precision. These measurements have been made for different final states in most cases with all the collected run-I data set showing in all cases perfect agreemment with the SM predictions. Still there are several proposed extensions for the SM that have to be tested to either exclude them or claim discovery of new physics. One of the most popular *beyond the standard model* ideas is the possibility for the existence of more than one Higgs boson each with a different mass value [19]. Another popular theory where actually most of the effort will be focused during LHC run-II is *supersymmetry*, SUSY. This theory suggests that each of the fermions we have observed so far has an associated super-symmetric massive boson partner and in the same way each boson has a supersymmetric fermion partner [20]. These massive particles still not observed, could be candidates for dark matter which has not yet been observed so far either. During LHC run I the different experiments have increased the range of exclusions for supersymmetric particles. Much more stringent limits will be placed with the LHC run II data.

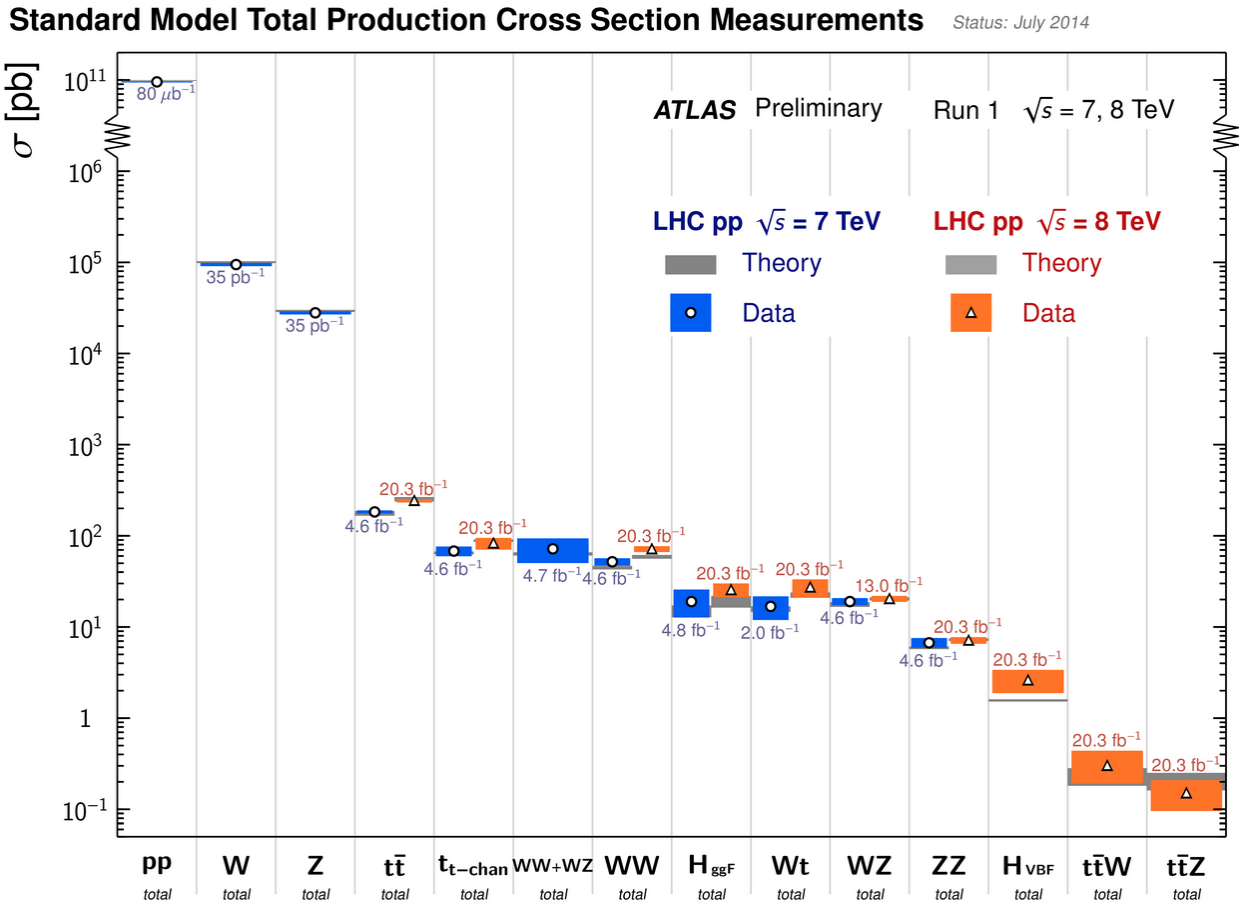

Figure 2.9: Summary plot from the ATLAS Standard Model group displaying several cross-section measurements for different final states processes with their corresponding theoretical prediction. From [55].

Chapter 3

High Energy Physics at CERN

This chapter is focused on the acceleration complex located at CERN, the European Laboratory for Particle Physics and its operation to provide high energy head-on collisions of protons or heavy ions at the different detectors located around its main accelerator the Large Hadron Collider (LHC), the largest accelerator of particles ever built. Collected data from these collisions are used for a huge diversity of particle physics studies. Section 3.1 provides general information about the laboratory and its facilities, section 3.2 describes the acceleration chain to the LHC and section 3.3 explains briefly the operation of the LHC. Information about the facilities and accelerators operation is based on references [21] and [22].

3.1 World's Largest Particle Physics Laboratory

The CERN laboratory comprises a range of experiments and accelerators used for fundamental research in particle physics. It directs the operation of the LHC which has a 27 km circumference that extends to both sides of the border between France and Switzerland as shown in Figure 3.1. This massive accelerator runs at unprecedented collisions energies being able to operate at a design luminosity of 10^{34} cm^{-2} s^{-1}. At design performance the protons are grouped in 2898 bunches making up each of the circulating beams travelling in opposite directions. Each of these bunches contain $\sim 10^{11}$ protons and are 25 ns apart from each other. At design luminosity there should be over 25 proton-proton interactions per bunch crossing. As the bunches of protons are approximately 5 cm long and 10 μm in diameter, these interactions form a distribution of 2.5 *cm* approximately along the beam line.

Massive detectors are located at different points around the LHC circumference to analyze the data produced from the collisions. Each detector was designed with different specific purposes as it is described in subsection 3.3.3. The laboratory also hosts additional smaller experiments that are within the scope of interest of nuclear and particle physics such as NA61-SHINE, NA62, COMPASS, CNGS, incorporated in the Super Proton Synchrotron (SPS) and TOTEM and LHCf incorporated in the LHC.

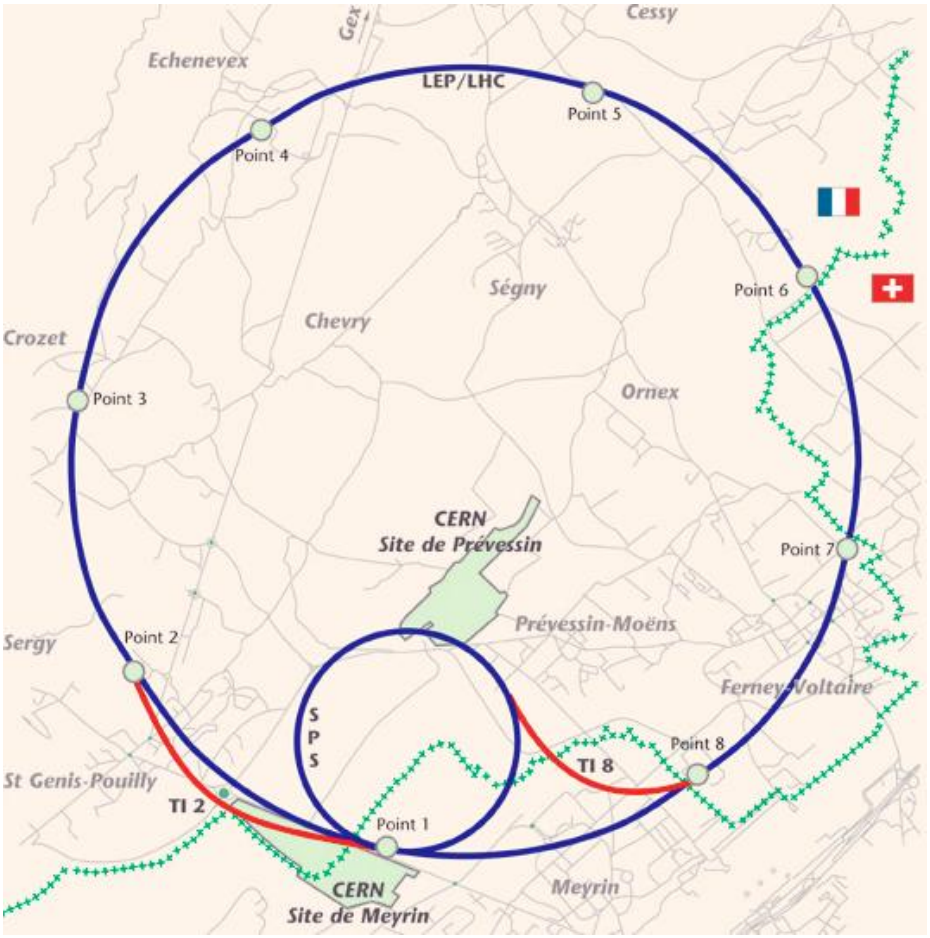

Figure 3.1: The LHC extends to both sides of the border between France and Switzerland. The ATLAS experiment is located at point 1, where the Super Proton Synchrotron (SPS) makes contact with the LHC. From [26].

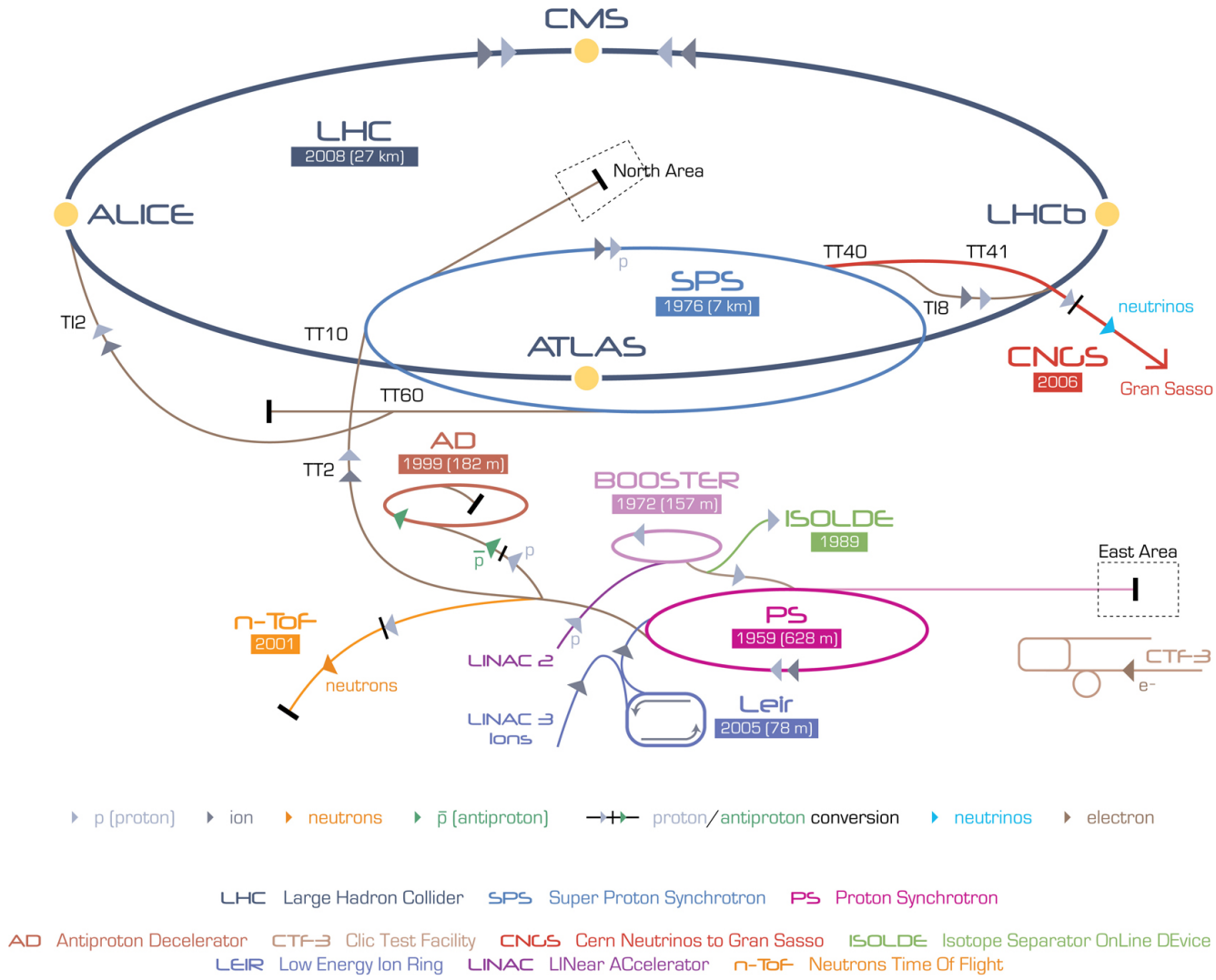

Figure 3.2: Acceleration complex at CERN. Proton bunches are produced at LINAC II and then split in the BOOSTER and accelerated in the PS and SPS sequentially before injection into the LHC. From [27]

3.2 Acceleration Chain to the LHC

Before reaching the LHC tunnel the proton bunches need to be accelerated in a series of smaller accelerators that push them to higher energies. Each stage is shown in the diagram in Figure 3.2 where additional facilities are displayed as well. In the acceleration process the proton bunches are collimated into beams travelling in a common direction. Two resulting proton beams are obtained travelling in opposite directions along the LHC circumference. In the first part of the acceleration process a hydrogen sample is ionized to obtain protons by using the LINAC II linear ac-

celerator, where the electrons are removed from the hydrogen atoms and remaining protons are accelerated to an energy of 50 MeV (31 % of the speed of light). This device has small quadrupole magnets that ensure protons remain in tight beams, 100 μm wide per pulse. The resulting beam is introduced into the Proton Synchrotron Booster (PSB), which splits the proton bunches producing 72 bunches out of every 6 bunches and accelerates them to an energy of 1.4 GeV (91.6 % of the speed of light). It is made up of 4 superimposed synchrotron rings and allows the following accelerator in the chain (the Proton Synchrotron) to receive 100 times more protons than it would from the LINAC directly.

After the PS booster the protons are injected into Proton Synchrotron (PS), which acelerates the protons to 25 GeV (99.93 % of the speed of light). This accelerator can as well be used to accelerate heavy ions from the Low Energy Ion Ring (LEIR), which is also shown in figure 3.2. LEIR has a length of 78 metres and receives ions from the LINAC 3 accelerator. The PS, which began operation in 1959 was CERN's first synchrotron. It has a circumference of 628 metres and it comprises 277 electromagnets including 100 dipoles. Additionally it can accelerate lead, sulphur nuclei, electrons, positrons and antiprotons.

The next accelerator in the sequence is the Super Proton Synchrotron (SPS), which receives beam from the PS. The SPS pushes the protons to 450 GeV (99.9998 % of the speed of light). It is currently the second biggest machine at CERN with a circumference of 7 km and it provides beams to the LHC and smaller experiments such as NA61/SHINE, NA62, COMPASS and CNGS. This accelerator started operation in 1976. It has 1317 electromagnets of which 744 are dipoles. In the early 1980's it was operated in $p\bar{p}$ collider mode, leading to the discovery of the W and Z bosons in 1983. Finally the protons are injected to the LHC which accelerates the protons at up to a design energy of 7 TeV (99.9999991 % of the speed of light), thus being able to produce proton-proton head-on collisions of up to 14 TeV of energy at a design luminosity of 1×10^{34} cm^{-2}s^{-1}.

3.3 The Large Hadron Collider

3.3.1 Overview

On December 1994 CERN's governing body voted to approve the construction of the LHC. The LHC started operation in 2008. The estimated cost to build the LHC and its experiments is $\sim$ £3.74 billion [90]. The LHC initial main goal was to run at higher collision energies with respect to the previous accelerator, the Tevatron at Fermilab, in order to increase the chances to generate unexpected events that could lead to new physics discoveries. The initial focus of the LHC was the discovery of the Higgs particle whose existence is predicted by the SM but whose mass was not known.

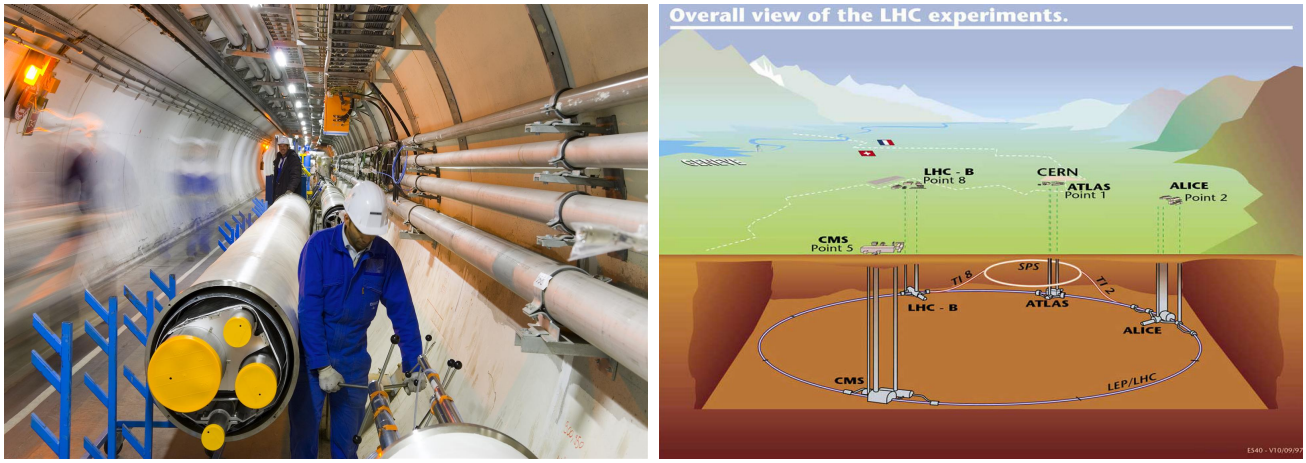

Figure 3.3: A person is standing inside the LHC tunnel with the beam pipe at his side (left). The LHC tunnel is located 100 metres underground (right). From [46].

Rather than being a perfect circle the LHC is made up of eight *insertion* straight sections of which four are dedicated to experiments, while one is used for radio frequency cavities used to accelerate the proton bunches, two for beam cleaning and one for beam dumping. The LHC also comprises eight arcs (*sectors*) joining these straight insertions. A total of 154 dipole magnets are in each of the arcs and are independently connected in series in the same continuous cryostat with its own power source as well.

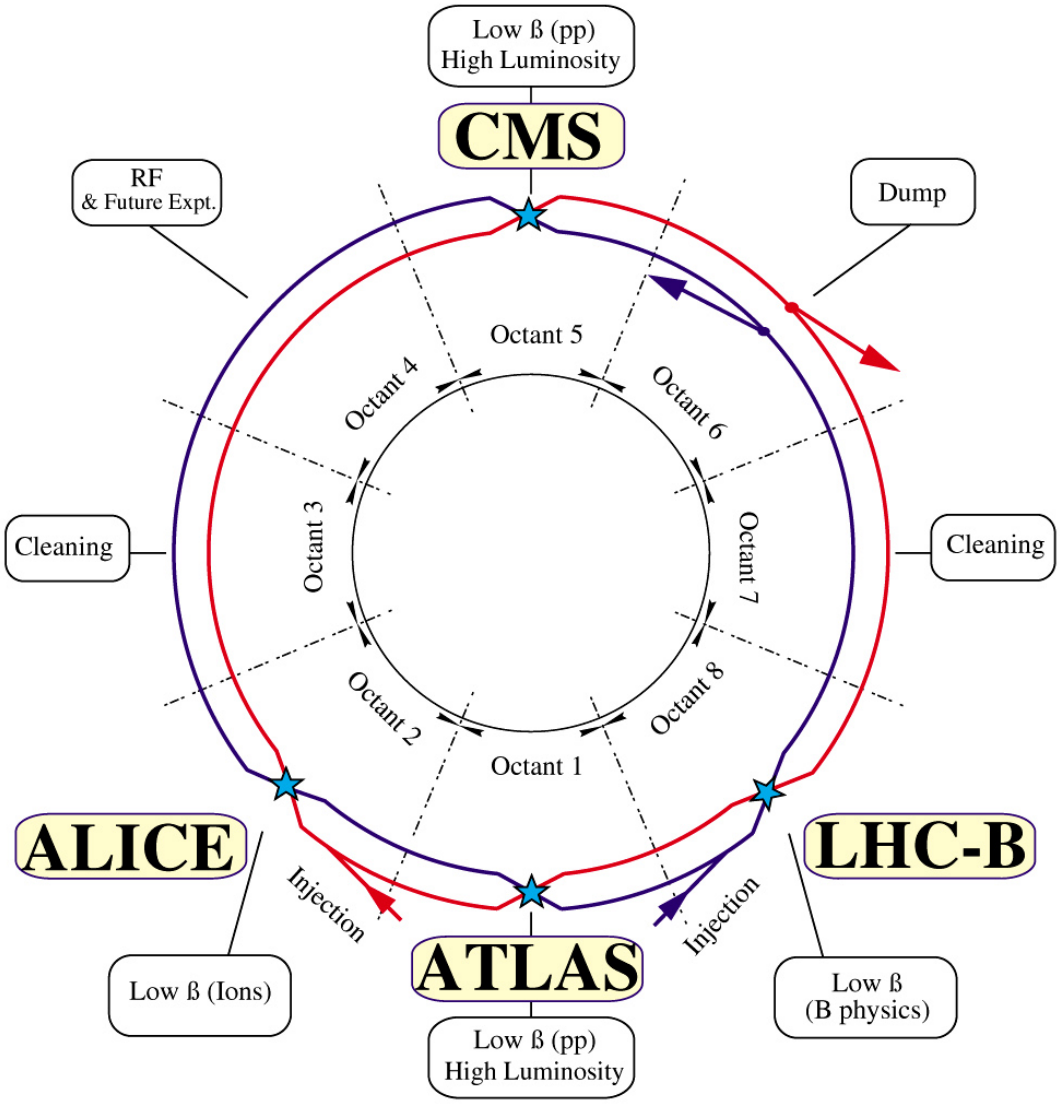

Figure 3.4: Distribution of LHC sectors. Beam one is directed clockwise and viceversa for beam two. Injection points are located in octants 2 and 8 close to the ATLAS detector in point 1. From [21].

An *octant* is defined as the region from the middle of an arc to the middle of the following arc spanning a full straight section.

The distribution of octants across the LHC can be seen in Figure 3.4 where the location of the main detectors along the circumference is shown and areas used for radio frequency emission, beam injection, beam cleaning and beam dumping are displayed as well. Excluding heavy ion collisions, protons were chosen over electrons as the colliding particles as have a much lower energy loss per turn through synchrotron radiation than electrons, which are much lighter. The LHC is located $\sim$ 100 metres underground as earth provides good shielding for radiation.

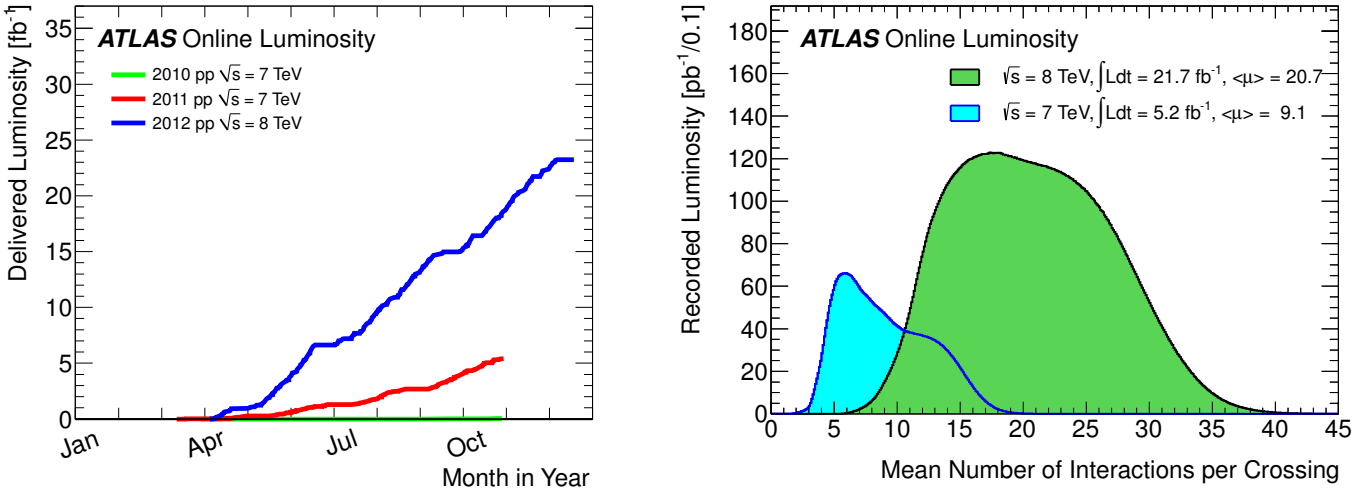

Figure 3.5: Integrated luminosity for three different campaigns recorded by ATLAS (left). Measured Pile-up levels by the ATLAS experiment for 7 and 8 TeV centre-of-mass collision energies (right). From [56].

The beam forms into bunches owing to the radio frequency acceleration scheme. As the protons pass through the acceleration cavities they are squeezed or expanded into bunches. The bunches are further squeezed by magnetic fields that manipulate the shape of the bunches close to the collision points. For example far from the collision points a bunch is $\sim$ 1 mm wide. Close to a collision point the bunch width reduces to $\sim$ 16 μm, where the bunch length is $\sim$ 5 cm.

Each bunch circulates $\sim$ 11.2 k times in 1 second which corresponds (considering a total of 2898 bunches per circulating beam) to a crossing rate of $\sim$ 40.0 MHz. Figure 3.5 shows on the left the total integrated luminosity accumulated by ATLAS in three different campaigns of the LHC and on the right the measured levels of pileup for different collision energies. The pileup increases with energy. If for example the level of pileup is $\sim$ 20 collisions per bunch crossing as with collisions at $\sqrt{s} = 8$ TeV, then the corresponding number of interactions is $6{\times}10^8$ per second. These events should be quickly analyzed by the data acquisition systems of the different detectors.

3.3.2 LHC Systems and Beam Control

3.3.2.1 Cryogenic System

The LHC has the largest cryogenic system in the world. It is able to operate at temperatures below 2 K to optimize the performance of the electromagnets and other components at the LHC which are immersed after a cooling process in liquid helium. The system is mostly limited by having to use previous LEP tunnel and refrigeration facilities. A total power of 150 kW is required to cool down a total of 3700 tonnes of material in cold masses holding magnets to a temperature of 4.5 K. Liquid nitrogen and refrigerator turbines are used in the first stage of the cooling down process. For the final stage of the cooling process down to 1.9 K, 20 kW of power is required. In this process cold masses are filled with liquid helium which at atmospheric pressure liquefies at $\sim$ 4.2 K and below $\sim$ 2.17 K becomes *superfluid*. As a superfluid it has special properties such as high thermal conductivity ideal for refrigeration and temperature stabilization. Cold masses have high specific heat (10^5 times that of the superconductor per unit of mass) and large heat conductivity. This allows fast recovery from fluctuations in temperature and pressure and resistive transitions of superconductors at different locations. A total of 120 tonnes of liquid helium is required: 60 % is used for magnets and 40 % for general refrigeration.

3.3.2.2 Vacuum System

Extreme vacuum conditions are required for LHC magnets, its helium Cryogenic Distribution Line (QRL), and beam pipes. In order to keep such low temperatures the cryogenic system is kept at $\sim 10^{-6}$ mbar. For the beam pipes the required vacuum conditions are more extreme. Here the pressure is expressed in terms of equivalent density of H_2 molecules per cubic metre. Usually for a beam with a life-time of 100 hours the density should be below $10^{15}\ H_2\ m^{-3}$, and around the collision points where the detectors are located the density should go below $10^{13}\ H_2\ m^{-3}$. The vacuum system for the beam pipes is divided into sectors.

3.3.2.3 Magnets and Beam Control

The LHC possesses a more powerful set of electromagnets of any other accelerator. A total of 1232 dipole magnets are installed around the LHC circumference made with the superconducting material *Niobium-titanium* (NbTi). Figure 3.6 shows the transverse section of a single dipole magnet. These electromagnets are 15 metres long and weigh 35 tonnes each one, and are kept at temperatures below 2 K, allowing helium to remain in a superfluid state. The magnets use NbTi as superconductor. The dipoles provide a magnetic field of $\sim$ 8.3 T over their length to keep proton bunches in their orbits. The distribution of magnetic field in a dipole magnet is shown in Figure 3.7.

Previous accelerators like Tevatron and HERA operated with the same material for the superconducting cables but at temperatures $\sim$ 4.2 K and then having a magnetic field $\sim$ 5 T. Decreasing the temperature by a factor of two approximately makes the heat capacity of the cable smaller by an order of magnitude, which reduces the energy deposition that can trigger a quench, which means that a tighter control of heat dissipation and dynamics of the cables is required.

A set of quadrupole magnets (5 - 7 metres long) focuses the beam down to the smallest size possible at collision points increasing the chance of two protons col-

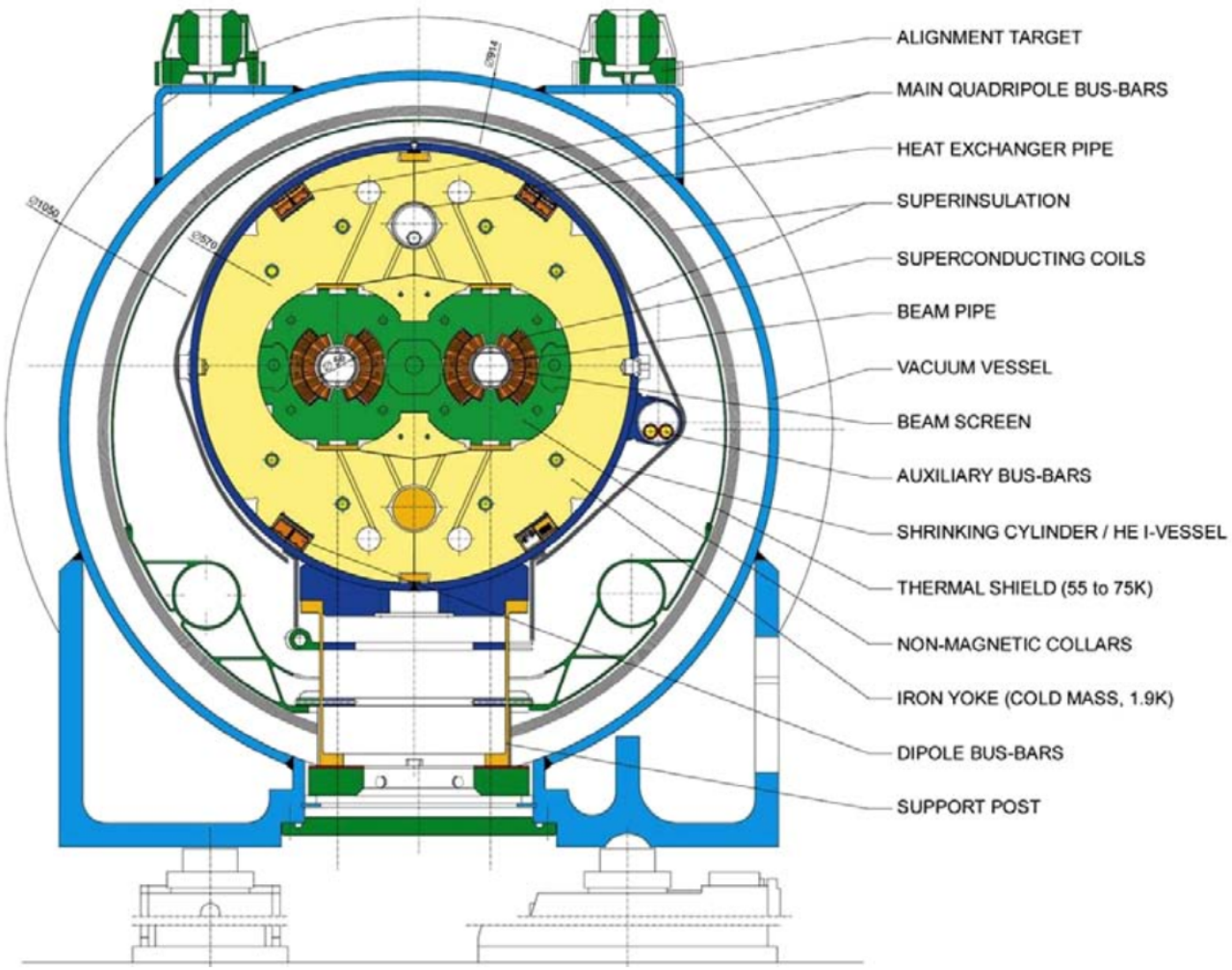

Figure 3.6: Transverse section, displaying the main components of the magnetic and vacuum systems of a dipole cryomagnet. A "two-in-one" design for the cable windings was chosen to keep costs as low as possible and save space within the tunnel, such design accommodates the windings generating the magnetic fields for both circulating beams in the same cold mass. From [21].

liding head-on with each other as it is displayed in Figure 3.8. Some quadrupoles focus the beam height and some of them the beam width. Additional systems of secondary sextupoles, octupoles, decapoles magnets are installed to optimize the beam optics bunches' trajectories at each of the sectors. There are in total 9600 magnets.

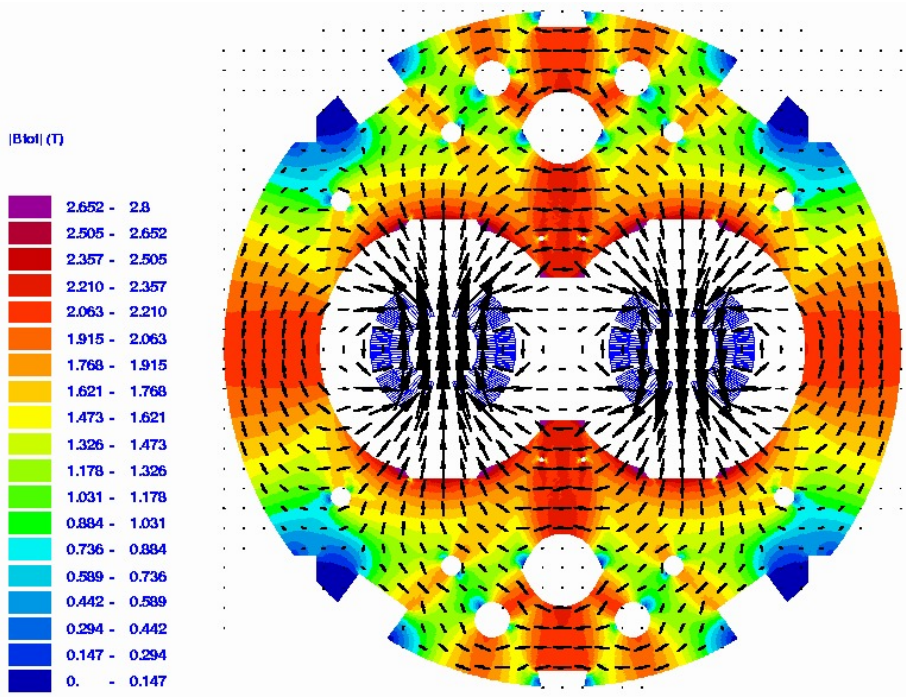

Figure 3.7: Distribution of the magnetic field in one of the LHC dipole magnets. Maxima occur at the two beam pipes with the field in opposite directions, keeping the counter-rotating proton beams within their orbits. From [21]

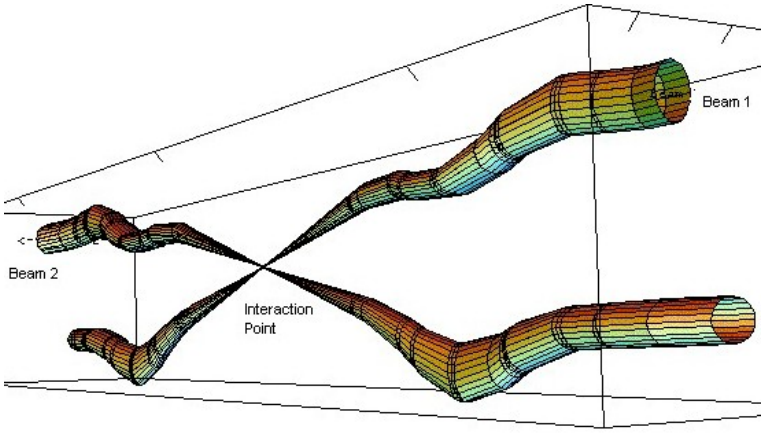

Figure 3.8: Diagram illustrating the effect of the quadrupoles over the beam close to the interaction points, where they are squeezed to the smallest transverse size as possible. From [21].

3.3.2.4 RF Cavities

A superconducting cavity system varies the electric field at radio-frequencies (RF), with a rate of ~ 400 MHz. These RF cavities accelerate the proton bunches, initially injected at 450 GeV into the LHC, to a design energy of 7 TeV. Cavities operate at a temperature of 4.5 K and require 275 kW/beam of power to accelerate the beams. Additional power is required by the beam control systems. The RF is used as well to correct errors in the beam injection process to the LHC. Usually the separation between the two beams along the LHC is $\sim$ 194 mm, but is increased to a value of 420 mm in the RF cavity, so that both beams can be accelerated independently in a more efficient divided system. Each of the protons oscillate around what is called the *synchronous particle state* which is the state of a particle that is in perfect synchrony with the variation of the electric field and gets no acceleration per turn (ignoring energy loses). What usually happens is that each proton is accelerated and deaccelerated continuously after each turn. The RF systems are located at point 4, between the ALICE and CMS detectors, close to the beam cleaning system as shown in Figure 3.4.

3.3.2.5 Safety

The LHC has many safety mechanisms that will be activated in case there is anomalous behavior [21]. For example in case of an unexpected emergency during the LHC operation or loss of control over the beams, the accelerator has at point 6 a beam abort system which would kick each of the beams horizontally into an additional iron septum magnet which would direct the beams away in a vertical direction from the LHC components against absorbers in a separate tunnel. Each beam has its own absorption system. Also for safety reasons liquid nitrogen is not used within the LHC tunnel, but is used only for the initial cooling process and with restricted quantities. The flux of liquid helium has to be kept to very low rates. It is carefully monitored during the cooling process at all times.

3.3.3 Experiments at the LHC

The aim of the particle detectors located around the LHC is to record and measure the particles produced in the *pp* collisions. The main detectors are briefly described in the following subsections. ATLAS is described in chapter 4.

3.3.3.1 ALICE: A Large Ion Collider Experiment

ALICE is a general purpose experiment, used to analyze particles from lead nucleus-nucleus, Pb-Pb, head-on collisions. These generate very dense matter states such as the *quark-gluon-plasma*. This state of matter, with very high temperature and densities where quarks are no longer confined, existed just after the Big Bang [96].

3.3.3.2 CMS: Compact Muon Solenoid

CMS has a large superconducting solenoid which produces a magnetic field of 4 T to deflect the produced particles as much as possible [94]. The main goals of this experiment are the verification of the Higgs boson existence and measurement of its properties. It also searches for massive particles predicted by Super Symmetry (SUSY) theory, where the main effort will be focused during the LHC Run-II from 2015. This type of detector can be used as well to make precision measurement of variables whose value is predicted by the SM as is done in areas such as top-quark physics and standard model physics. The CMS experiment along with ATLAS discovered the Higgs during the LHC Run-I [91]. The results from these two general purpose experiments can be combined in most of the cases.

3.3.3.3 LHCb: Large Hadron Collider Beauty Experiment

LHCb's main purpose is the identification of small asymmetries between matter and antimatter from interactions that involve B particles (particles that contain a b-quark). This detector is located in point 8 and is not symmetric. Its detectors

are located on one side of the interation point. It differs mainly from the general purpose experiments in having an excellent vertex detector and also being able to identify particles (π's, K's and p) from B-meson decays, using Cherenkov counters [95].

3.3.3.4 TOTEM: TOTal Elastic cross section Measurement

These detectors attempt to measure the effective size of the cross section of protons using 'Roman pots' [32] which are specially designed vacuum chambers, to identify protons produced at very small angles to the beamline. These chambers have shape of a 124 mm $\times$ 50 mm $\times$ 105 mm rectangular box. It also uses two tracking detectors T1 and T2 [32]. These detectors are spread along half a kilometre from the CMS detector, on both sides, along the LHC beamline. Also diffractive physics that is not accesible to general purpose experiments can be explored. This experiment is used as well to determine the luminosity of the LHC. TOTEM comprises 3000 kg of equipment, including 26 Roman pots and 2 particle telescopes.

3.3.3.5 LHCf: Large Hadron Collider Forward

This detector studies particles from pp collisions produced at very small angles to the beamline. These particles are used to gain information about cascades of particles from cosmic rays usually ocurring in the upper atmosphere, in order to calibrate large scale cosmic rays experiments. LHCf consists of two detectors 30 centimetres long 10 centimetres wide 80 centimetres high and weighing 40 kilograms [33]. These detectors are located 140 metres on either side from ATLAS, along the LHC beamline.

3.3.4 Main Goals for Run-II

The operation of the Tevatron has been stopped since September 2011. It delivered a total integrated luminosity of $\sim$110 pb^{-1} during its Run-I, and $\sim$ 11.5 fb^{-1} during

its Run-II to the CDF and DØ experiments [28], reaching a maximum centre-of-mass proton - anti-proton collision energy of $\sqrt{s} = 1.96$ TeV.

The LHC has run already with pp collision energies of $\sqrt{s} = 7$ and 8 TeV during its Run-I, larger by more than a factor of four with respect Fermilab accelerator. It delivered an integrated luminosity of 5.46 fb^{-1} and 22.8 fb^{-1} at 7 and 8 TeV, respectively. From these delivered integrated luminosities, about 4.57 fb^{-1} and 20.3 fb^{-1}, respectively, are good quality data for physics [56].

The LHC has recently started its Run-II, running at record collision energies of $\sqrt{s}$ = 13 TeV. The current plan is to extend Run-II until the end of 2017, delivering an integrated luminosity $\sim$ 100 fb^{-1}. During this second phase the collision energies could be increased further to 14 GeV. The LHC is then planned to restart operation in the middle of 2018 until the end of 2020, delivering an additional integrated luminosity of $\sim$ 200 fb^{-1}.

Several precision measurements performed previously at Fermilab have been already reproduced at the LHC experiments during Run-I, though data from the LHC experiments need to be understood better in order to achieve more precise results. Exclusion limits for candidate mass values of supersymmetric (SUSY), particles have been expanded. The goal now is to expand them further to identify or exclude these heavy particles during Run-II.

A Higgs-like particle has been already discovered by the ATLAS and CMS experiments, but it still needs to be explored to see if there is more than one Higgs boson and keep studying its different properties such as its width and spin, to make sure they are compatible with the SM. Also CP violation has been identified at the LHCb experiment, but the measured amount is not enough to account for the imbalance between matter and antimatter we see in the universe, a topic whose understanding will be hopefully expanded during Run-II. Several more analyses will become more interesting during Run-II, and one of the main challenges will be to have to deal with

a higher degree of pile-up whose average will be ~ 40 collisions per bunch crossing.

Chapter 4

The ATLAS Experiment

In this chapter the main features and potential of the ATLAS detector are described. An overview of the whole experiment and characteristic features are given in section 4.1; the system of magnets is described in section 4.2; the tracker, calorimeters, muon detectors and triggering systems are described in sections 4.3 to 4.6. Comments on physics and performance of the detector during run-I and preparation towards run-II are included in sections 4.7 and 4.8. Most of the material is based on the content of references [49] and [89].

4.1 Overview

ATLAS (A Toroidal LHC Apparatus) is the largest detector located around the LHC ring and weighs 7000 tonnes; its main components are displayed in Figure 4.1. As mentioned in the previous chapter the detector produces two independent magnetic fields around the collision point, in the inner section a superconducting Central Solenoid (CS) is used to bend all charged particles in a plane perpendicular to the beam before they reach the Electromagnetic Calorimeter (ECAL), and Hadronic Calorimeter (HCAL). In the outer section a superconducting air cored toroid surrounding the calorimeters, provides with a set of particle detectors before, inside and after the toroidal field, an excellent standalone muon identification. The ECAL registers the energy deposits from electromagnetic particles (such as electrons and photons) and the HCAL those from strong interacting particles. The tracker (or Inner Detector) is made of three subsystems: pixel, semiconductor tracker (SCT) and

a transition radiation tracker (TRT), located between 50 mm and 1.0 m from the beam pipe. These sub-detectors are designed to reconstruct very efficiently tracks of individual charged particles within this magnetic field. They also provide, along with the calorimeters, measurement of the transverse momentum of leptons; electron and photon identification; τ-lepton and heavy flavour identification.

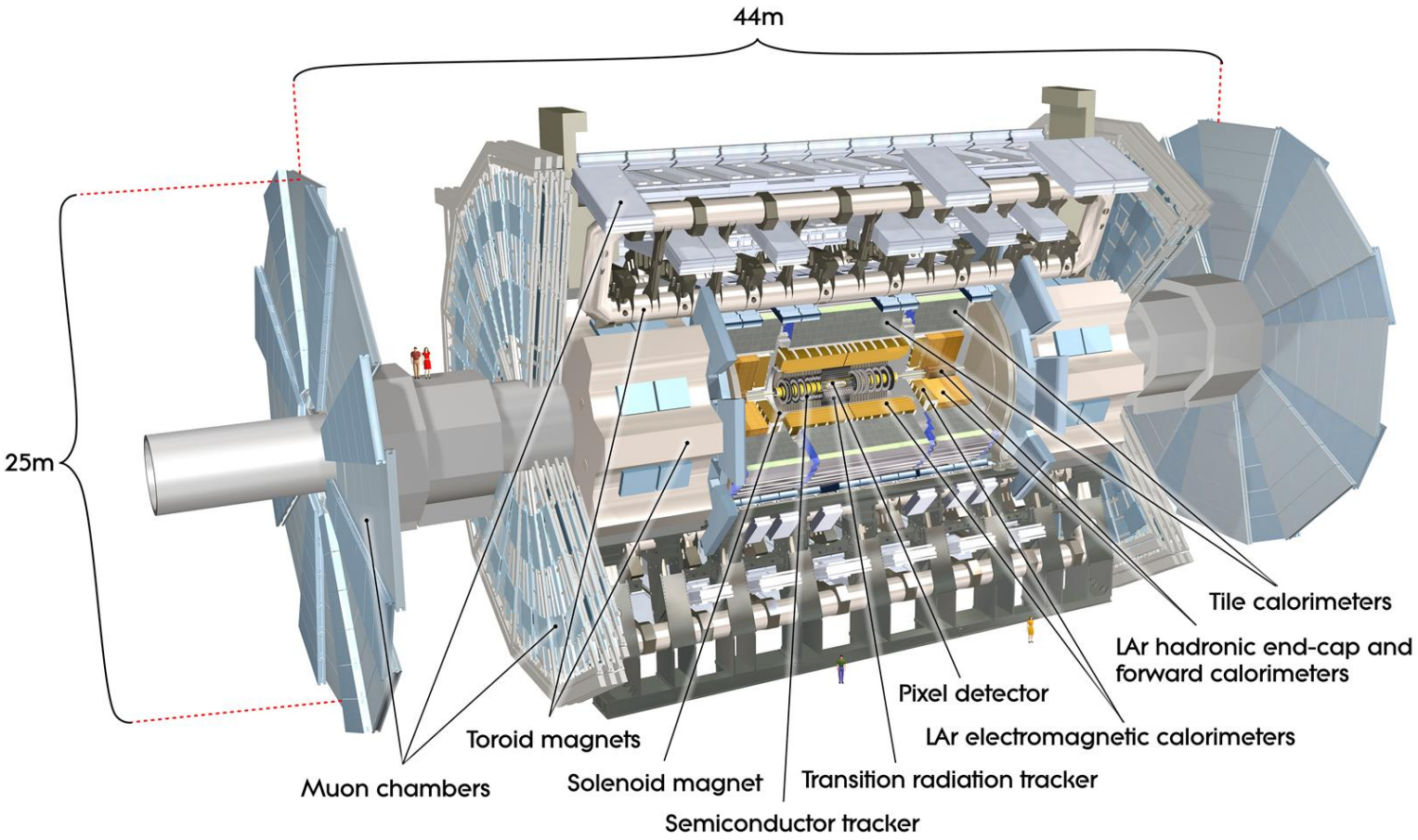

Figure 4.1: ATLAS detector at CERN and all its main components. From [47]

The detector allows the location of primary and secondary vertices, the identification of electrons, muons and showers of particles originating from quarks produced in the collision hard-scattering. These showers are regarded as jets and their definition is

included in chapter 7. Information from the inner detector is used in specialized algorithms to tag jets that potentially could have originated from a b-quark. All these elements are of crucial importance for indentification of events with top-quark decays, as described in chapter 6.

Figure 4.2 shows how the detector is aligned with the LHC beam pipe within its cavern. ATLAS also has an efficient triggering system and provides measurement of particles with low p_{T} thresholds. Due to its huge size and the diversity of sub-detectors ATLAS is a multipurpose detector able to catch data from a huge variety of events relevant for the different areas of particle physics. This detector can also be used to make studies with $^{208}_{82}$Pb - $^{208}_{82}$Pb nuclei head-on collisions at energies of up to 2.7 TeV per nucleon pair. ATLAS can operate at a design luminosity of up to $\sim 10^{27} cm^{-2} s^{-1}$ for these types of collisions.

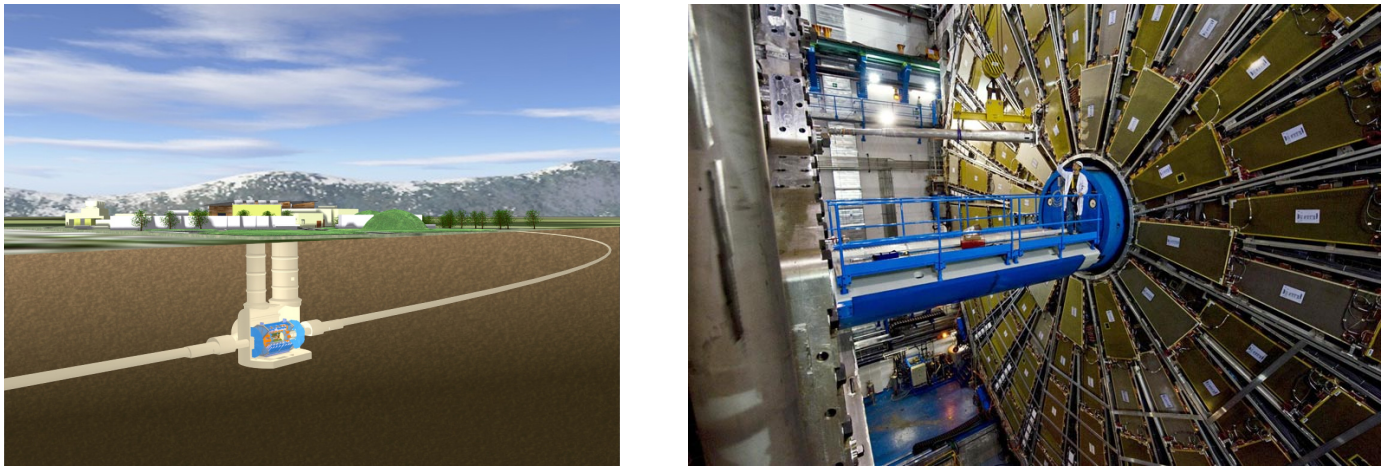

Figure 4.2: A schematic view of the ATLAS detector showing how it is accommodated within its assigned cavern along the LHC circumference (left), a photo of the transverse section of the detector showing the end-cap muon chambers (right). From [47].

The z-axis is used to indicate the position along the beam direction with the origin at the centre of the detector. The x-y plane is perpendicular to this axis, by convention the positive direction of x-axis is directed to the centre of the LHC and the perpendicular y-axis positive direction upwards to the sky. Along with this reference

system the angles (ϕ, θ) can be used to indicate the direction the different produced particles and physical objects travel through the detector. The ϕ variable is the *azymuthal angle* in the x-y plane measured from the x-axis and θ is the *scattering angle* from the beam z-axis. Instead of θ, the pseudorapidity, η is used, because in hadronic interactions particles are produced uniformly in η, though predominantly at small angle θ. The relationship between θ and η is indicated in Equation (4.1):

$$\eta = -ln[tan(\frac{\theta}{2})] \tag{4.1}$$

and their relative values are indicated in the left of Figure 4.3. Usually θ extends from an angle in radians $\sim$ 0.09 to 3.0, corresponding to the η range between -4.9 to 4.9. In the right of the figure it is possible to see the spacing in θ between equally spaced η values.

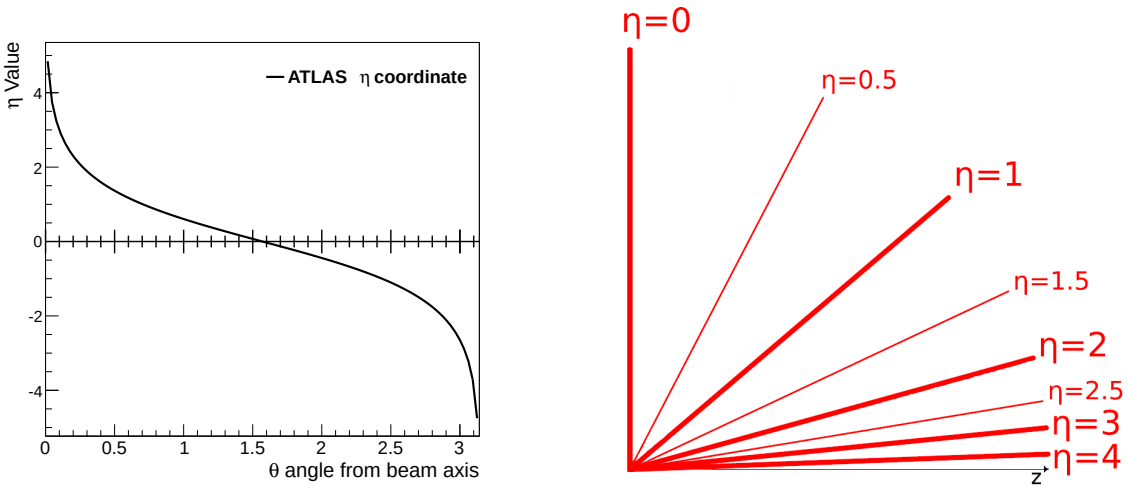

Figure 4.3: Atlas η angular coordinate as a function of θ angle from the beam axis (left), equally spaced η values. From [57]

If the momenta of all charged particles are measured and the energies and locations of all the electromagnetic and hadronic showers are as well measured in the calorimeters, then by conservation of momentum the x, y, and z components of

momentum should sum to zero within experimental errors. In the z direction, as the momenta of the incident partons are not known, the momentum sum $\sum p_z$ will not be zero. However in the transverse plane, the summed momentum in the x and y directions will be zero. Therefore any non-zero momentum in the transverse plane might indicate the presence of a neutral weakly interacting particle (e.g. a neutrino). Considering that the invariant mass of neutrinos is negligible with respect the value of their momenta, the difference from zero on the sum of momenta in the transverse plane is regarded as *missing energy* or E_{T}^{miss}, which is associated with presence of neutrinos if it surpasses certain threshold value $E_{\mathrm{T}}^{miss} > 25$ GeV.

Physical objects such as the ones defined in section 7.2 standing for individual particles or groups of particles travelling close to each other can be located in the different regions of the detector cylindrical shape by using the η-ϕ plane. The variable ΔR in Equation 4.2 is useful to determine the relative distance of the objects in the 2D cylindrical plane.

$$\Delta R = \sqrt{(\Delta\eta)^2 + (\Delta\phi)^2} \tag{4.2}$$

Other variables can be used to understand better the resulting tracks in the Inner Detector such as the transverse impact parameter d_o, defined as the transverse distance to the beam axis at the point where the extrapolated trajectory is closest to the interaction point or primary vertex. The longitudinal impact parameter z_o is defined as the z position of the track at the point where the extrapolated trajectory is closest to the main vertex.

4.2 Detector Magnet System

The systems of magnets of the detector and the produced fields are used to bend the charged particles trajectories. Figure 4.4 shows on the left all components of this system; the toroid magnet in the barrel (BT), is shown in red, the two End-Cap

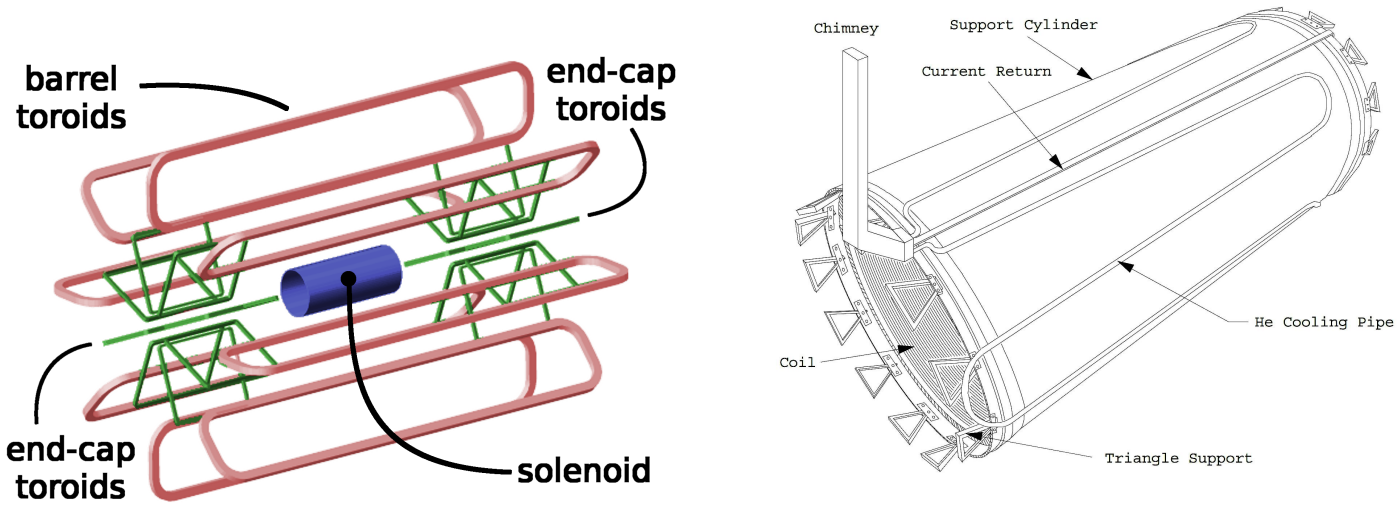

Figure 4.4: Arrangement of the coils in the ATLAS toroid in the barrel and end-cap, including the detector Central Solenoid in the inner section (left), [47], schematic view of the central solenoid (right) from [48].

Toroids (ECT), in green and the central solenoid (CS), in blue in the inner section. The CS is provided with 8 kA and produces in the inner detector a uniform magnetic field of 2 T, the arrangement of the coils is shown in in the right of the Figure 4.4. The CS has an inner diameter of 2.46 m and axial lenght of 5.80 m.

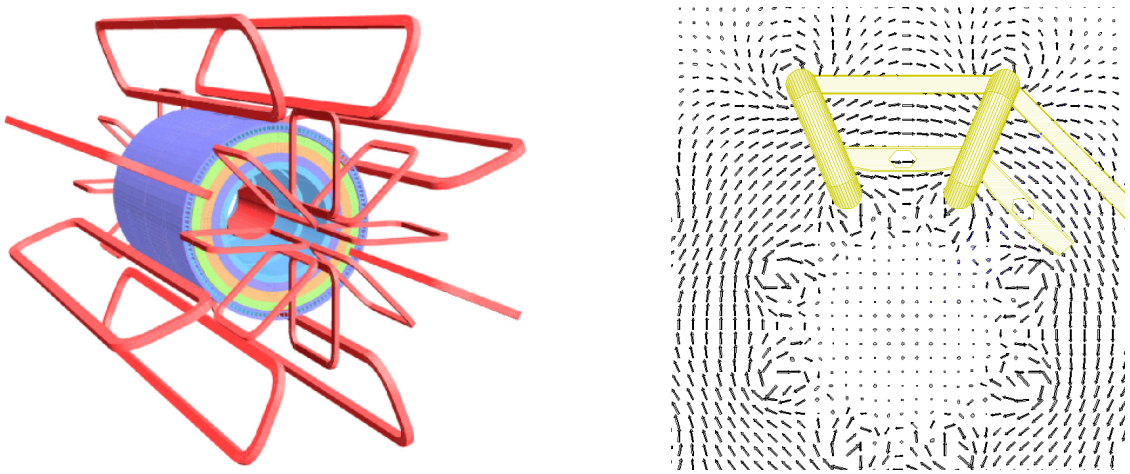

Figure 4.5: Arrangement of the coils in the ATLAS toroid in the barrel and end-cap (left), [47], magnetic field lines produced by the detector toroids (right) from [48].

The three toriods have eight coils connected in series, located in cryostats assem-

bled radially and with eightfold symmetry around the beam axis, just outside the calorimetry systems, as indicated in the left of Figure 4.5. They are designed to bend the trajectory of muons by producing magnetic field lines that follow a cylindrical geometry as indicated in the right in the same figure. A Muon Spectrometer (MS), is embedded in this toroidal field with strengths of 3.9 T and 4.1 T, in the barrel and end-cap, respectively. The bending power of the system is lower in the transition regions with pseudorapidity $1.3 < |\eta| < 1.6$. The entire system of magnets is 26 m long and with diameter of 20 m. The size of its elements can be appreciated from the photographies in Figure 4.6. The whole detector, as can be seen in Figure 4.1 is divided in three parts, with end-cap and barrel sections.

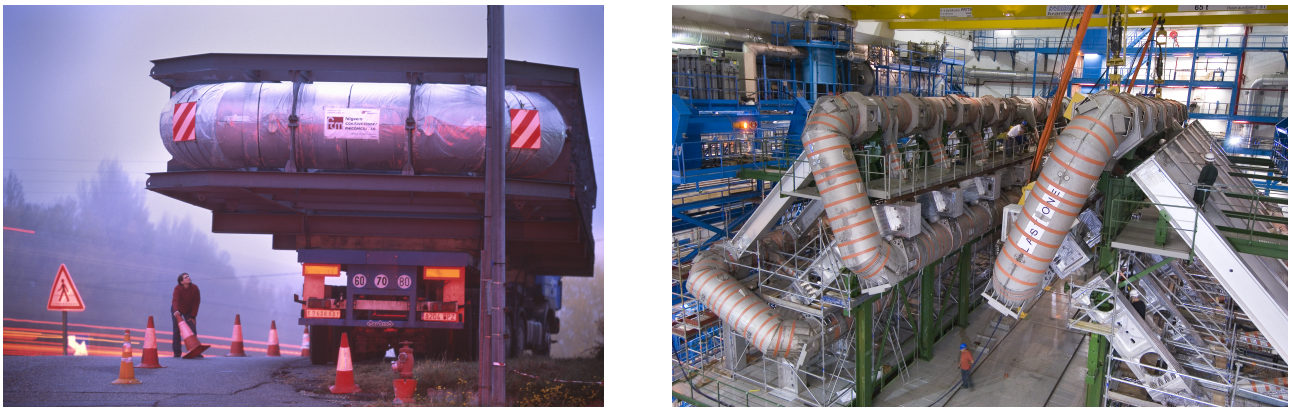

Figure 4.6: ATLAS toroid components being transported to Geneva from Spain (left). Assembly of ATLAS toroids at CERN (right). From [46].

4.3 Inner Detector

The Inner Detector (ID) data are used, after the application of pattern recognition algorithms, to measure the momentum of each charged particle, and for vertex location and electron identification. The ID is contained within a cylinder of length 7 m and radius 1.15 m bounded by the cryostat containing the LAr ECAL. The barrel length is 1.6 m while the end-caps occupy the remaining 5.4 m along the beam direction. In the barrel the detectors are mounted in concentric cylinders around the

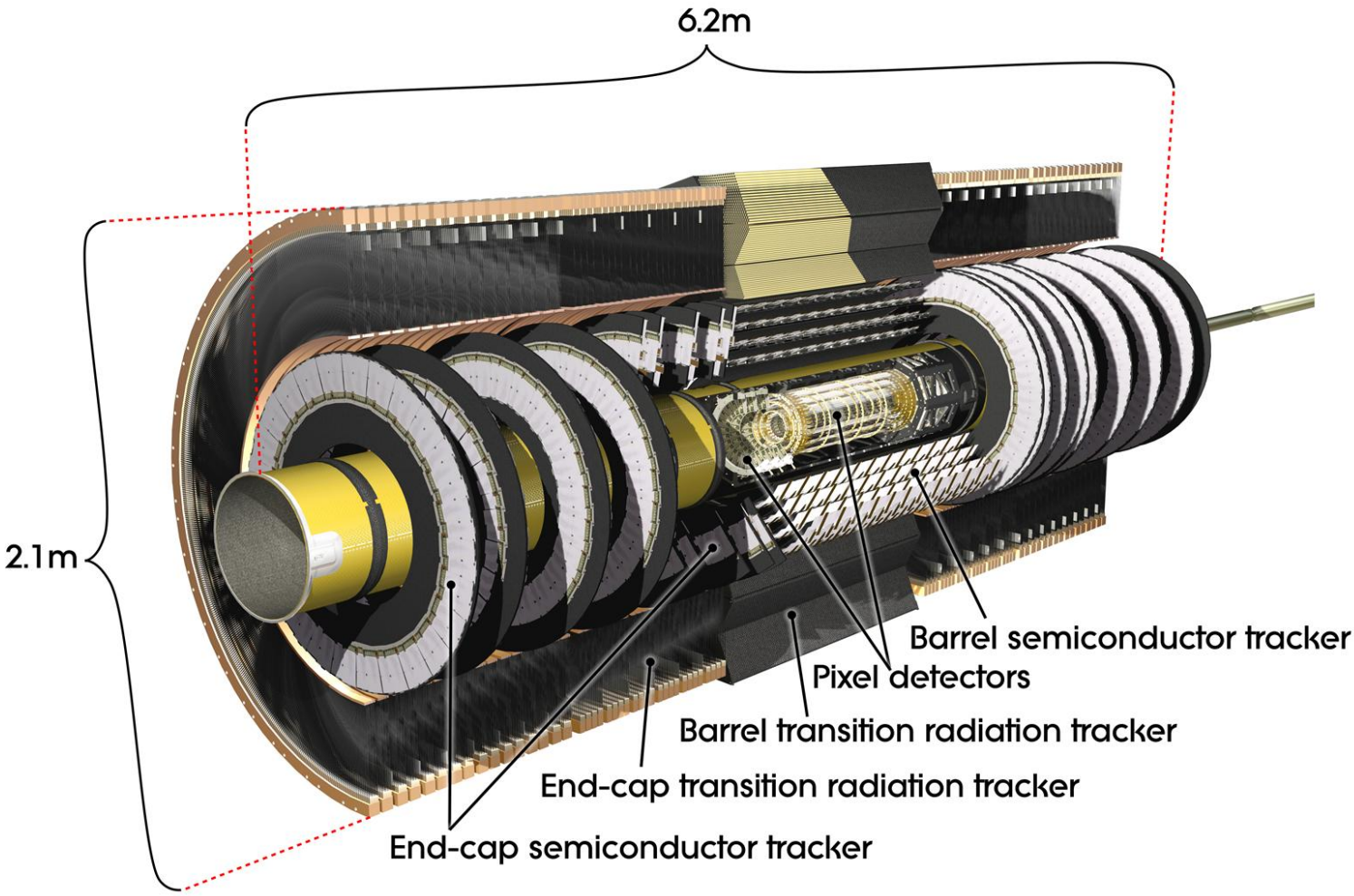

Figure 4.7: Inner Detector longitudinal view. From [47].

beam axis, and in the end-cap region they are arranged as disks perpendicular to the beam axis. The system comprises a high-resolution precision pixel detector and Semi-Conductor Tracker (SCT), within a radius of 56 cm followed by a continuous tracking system (TRT), and a support and service region. The large number of measurements in this outer part (complemented by the precise measurements by pixels and SCT) contribute to the identification of photon conversions and V^o decays and improve the electron identification efficiency. The whole system has coverage over the pseudorapidity range $|\eta| \leq 2.5$. On average each particle crosses three pixel layers, 8 SCT strips, and 36 TRT tracking points which provides enough information for high precision pattern recognition.

4.3.1 Pixel Detector

This section of the ID provides the highest-granularity and precision measurements close to the interaction point. It has three layers of pixels with radii: 5 cm, 8.8 cm and 12.2 cm respectively from the beam line in the barrel and five disks on each side, located between 11 and 20 cm from the interaction point in the beam direction. As it is the closest sub-detector to the interation point this section is crucial for the identification and location of secondary vertices. The development of b-tagging algorithms is fundamental to the analysis of top quarks whose decays involve the production of a b-quark. The first layer of pixels closest to the IP is known as the "B-layer".

In total there are 140 M pixel elements arranged into 1500 modules in the barrel and 700 in the disks, each module being 62.4 mm long and 21.4 mm wide. All the pixel modules are identical, having a minimum pixel size in ϕ-z of 50 $\times$ 400 μm^2. The intrinsic accuracies in the barrel are 10 μm and 115 μm in the ϕ and z directions respectively. The system has individual circuits for each pixel element that provide a buffering feature that makes possible storing the data until the level-1 trigger output.

4.3.2 Semiconductor Tracker

The SCT provides eight precision measurements per track as it comprises 4 two-sided barrels with radii: 30.0, 37.3, 44.7, 52.0 cm respectively and two-sided end-caps separated in three rings with three wheels, as shown in Figure 4.7. Each silicon sensor is 6.36 $\times$ 6.40 cm^2 with 768 read out strips each 80 μm wide. These silicon detectors are arranged in modules: four sensors are connected longitudinally in pairs, and each pair located at an angle to the other to produce a module 12.8 cm long as shown in Figure 4.8. The sensors are rotated with respect each other to give a resolution of 17 μm in the $r\phi$ coordinate and 580 μm in the z coordinate in the barrel and 12 μm and 580 μm in the $r\phi$ and z coordinates respectively, in the end-cap. The end-cap has strips that vary between 6 and 12 cm long to achieve an optimal coverage which

goes up to $|\eta| < 2.5$. In total there are 61 m^2 of silicon detectors in the whole structure with 6.2 M readout channels. Output signals are amplified and discriminated and then stored as binary bits passed to a binary pipeline that stores hits until level 1 trigger output.

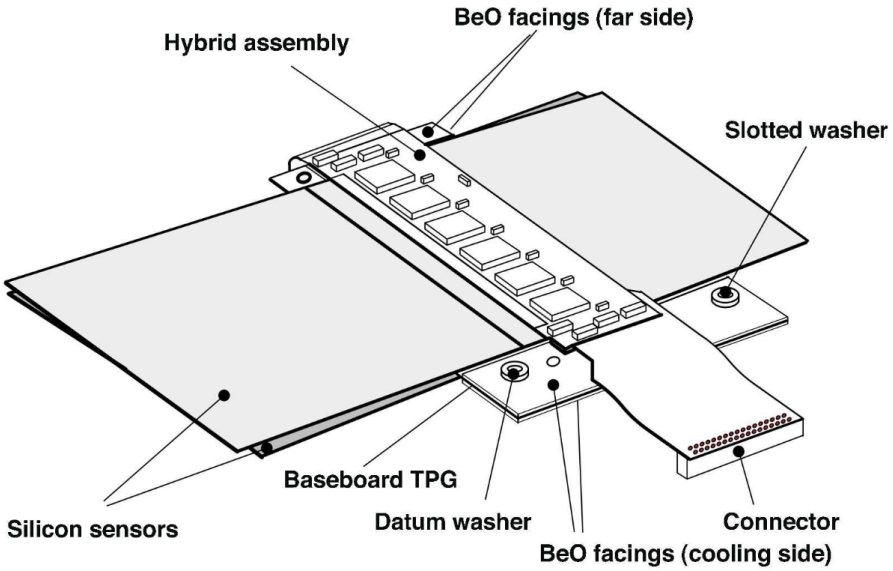

Figure 4.8: A barrel module of the SCT. The pair of sensors at the top is rotated by 20 mrad with respect the pair at the bottom. From [89].

Silicon microstrips are arranged along the barrel and end-caps, contributing to the measurement of impact parameter for each track, with a resolution of (22.1 ± 0.9) μm and a relative momentum resolution of $(4.83 \pm 0.16) \times 10^{-4}$ GeV$^{-1} \times p_{\mathrm{T}}$ [50]. Also the microstrips contribute to the vertex position measurement with resolution ~ 16 μm for primary vertices and enhance the good pattern recognition of the ID as it keeps high granularity at larger radii.

4.3.3 Transition Radiation Tracker

Transition radiation is electromagnetic radiation emitted as a consequence of a charged particle passing through the boundary between two different materials. The Transition Radiation Tracker TRT, is made up of a sequence of radiator foils made

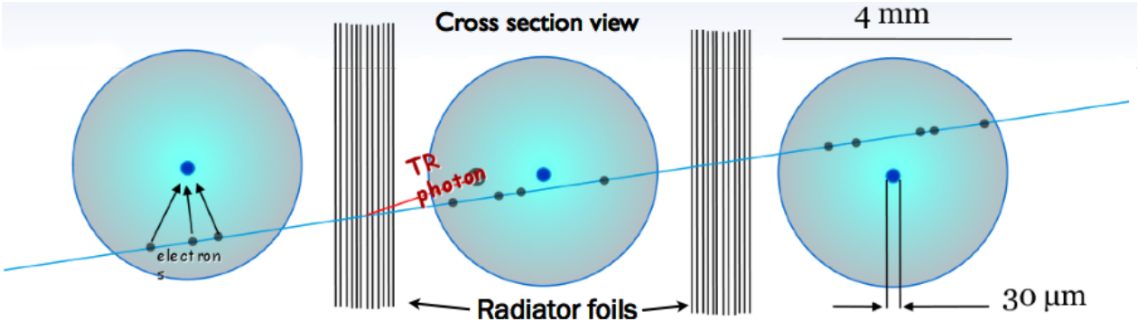

Figure 4.9: Transition radiation photons are produced from electrons crossing between materials with different dielectric constants. For the ATLAS TRT, radiation foils of CO_2 and polypropilene are used to produce transition radiation, From [52].

with polypropylene in a CO_2 atmosphere, followed by straw detectors as shown in Figure 4.9. A non-flammable gas combination of Xe (70%), CO_2 (20%) and CF_4 (10%) is used in the straw tubes. The xenon in particular absorbs the transition X-rays that are usually produced by electrons when passing through the radiation foils. The emission of transition radiation depends on the value of $\gamma = \frac{E}{m}$, and so is only significant for electrons. Therefore electrons produce larger signals in the tubes than the usual ionization left by a traversing charged particle.

The TRT as can be seen in the left of Figure 4.10 occupies most of the ID space. The straw detectors with diameter equal to 4 mm have a well isolated internal gold-plated W-Re wire with diameter equal to 30 μm and lengths up to 144 cm in the barrel that can operate at very high rate ($\sim$ 12 MHz) providing a continuous tracking system. The barrel contains 50k straws each of them divided in two halves at the centre and placed horizontal to the beam direction. The end-caps on the other hand contain 320k straws arranged radially in 18 wheels on each side making a total of 420 electronic channels. Each channel gives a drift time measurement with spatial resolution in $r\phi$ of 170 μm per straw. At the barrel, straws are arranged in individual modules with between 329 and 793 axial straws each extending from 56 to 107 cm radii. The 14 wheels at the end-caps closer to the IP cover a radial range of 64 to 103 cm while the remaining 4 extend to an inner radius of 48 cm to keep constant the number of crossed straws over the full acceptance. The TRT allows $\sim$

36 measurements per track.

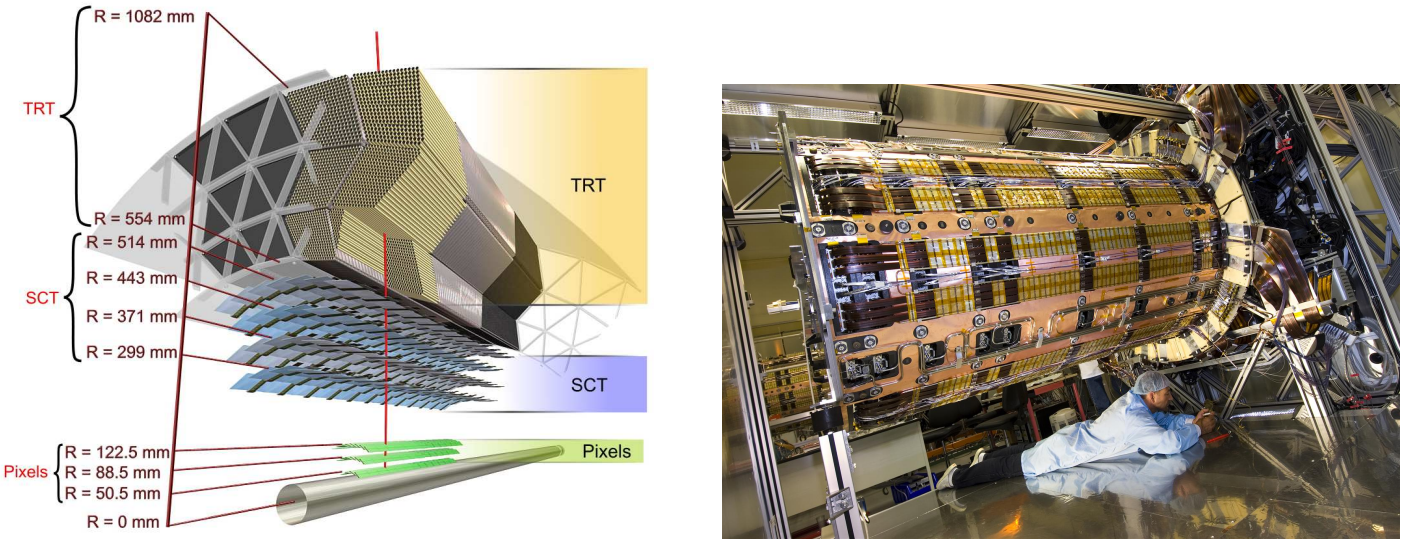

Figure 4.10: Transverse view of th ID showing its three sections (left), From [47]. Assembly of the ID at CERN (right), From [46].

4.4 Calorimetry Systems

In Figure 4.11 are displayed the main components of calorimetry systems in the ATLAS detector. The ECAL has a coverage of $|\eta| < 3.2$ and the HCAL has coverages of $|\eta| < 1.7$ (barrel), $1.5 < |\eta| < 3.2$ (end-caps) and $3.1 < |\eta| < 4.9$ (hadronic forward calorimeter, HFCAL). The ECAL provides an excellent electron and photon identification while the HCAL allows jet location and measurement of E_{T}^{miss}. The whole calorimetry system weighs 4000 tonnes. The LAr systems are contained in a cylinder 6.65 m long and with a radius of 2.25 m, while the scintillator-tile section extends to a radius 4.25 and total longitudinal length of 12.2 m.

4.4.1 Electromagnetic Calorimeter

Most particles will interact with the ECAL and so deposit some energy in it. Electrons and photons will be absorbed totally so that the energy deposited in the ECAL

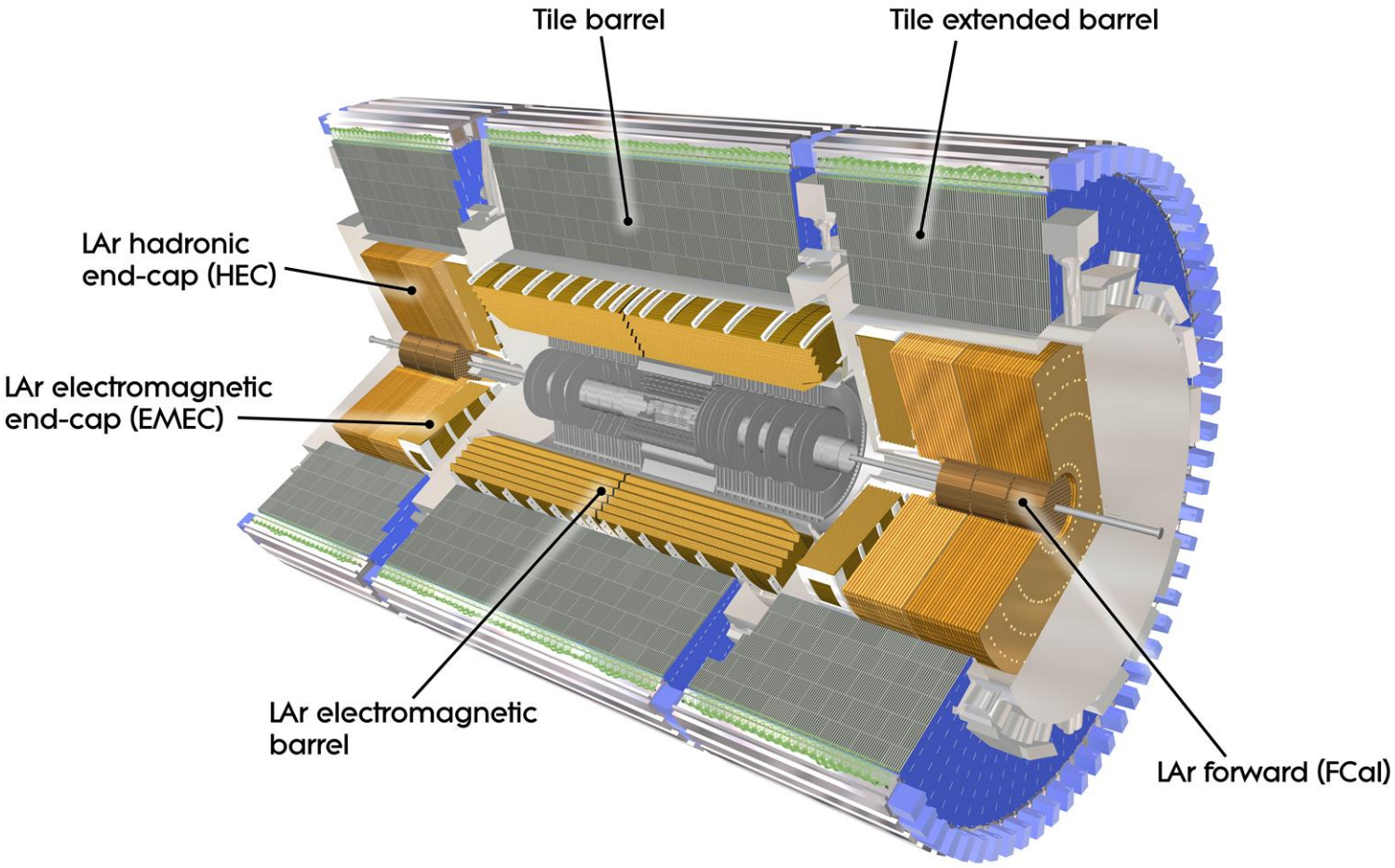

Figure 4.11: ATLAS calorimetry systems. From [46]

will correspond to their total energy. Other strongly interacting charged particles will deposit just a fraction of their energies in the ECAL.

The interaction of the incident particles with the layers of lead, the absorber material, produces an electromagnetic shower as illustrated on the left of Figure 4.12, which is measured by the liquid Argon (LAr) layers, the active material. The layers are arranged with accordion geometry to ensure azimuthal uniformity, as shown in the right of the figure, where also the dimensions of a barrel module are shown. The LAr provides radiation hardness, speed and uniformity of response [53]. The barrel which is divided in two halves separated by 6 mm, provides coverage up to $|\eta| < 1.475$ and the end-caps cover the range $1.375 < |\eta| < 3.2$. All the system

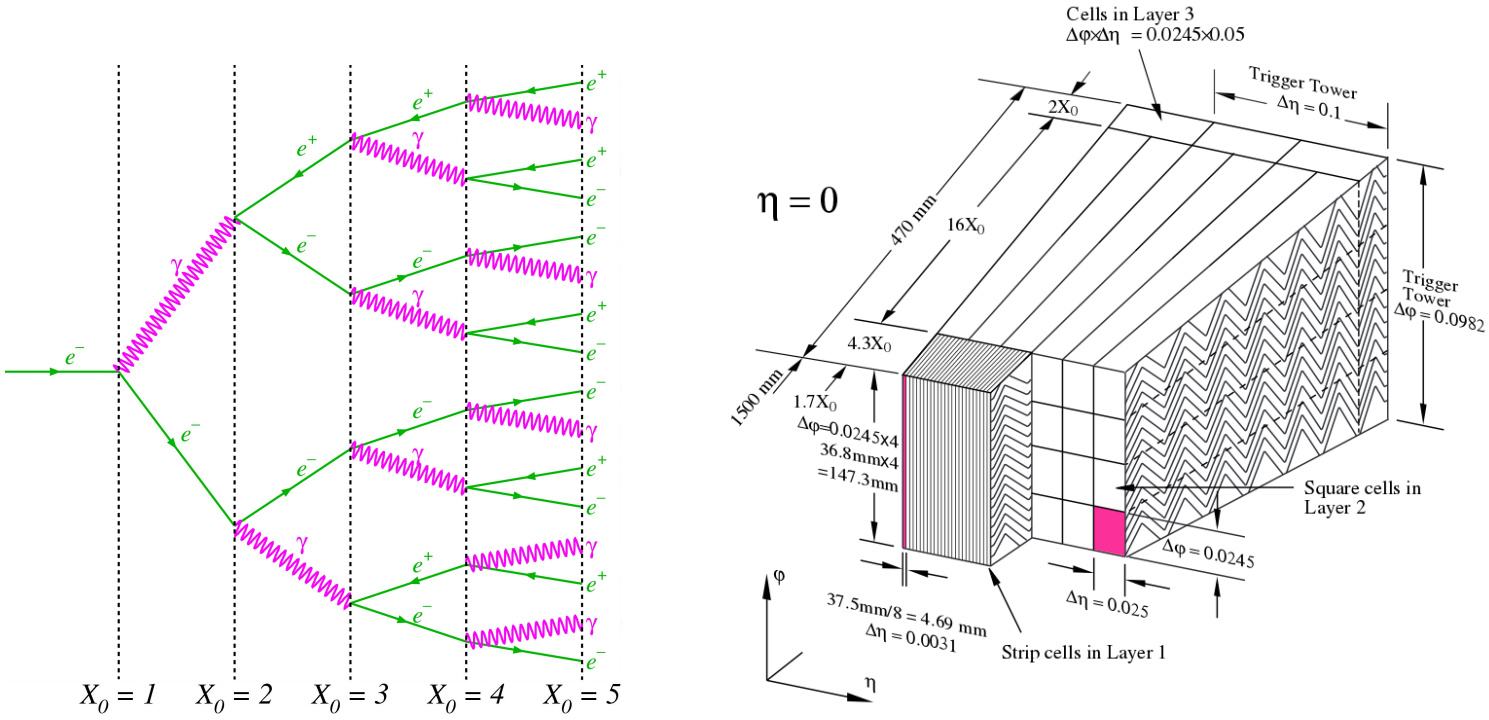

Figure 4.12: (left) Schematic representation of a electromagnetic shower in an electromagnetic calorimeter, in terms of radiation lengths X_o, from [138], (right) transverse view of a single barrel module of the ATLAS electromagnetic calorimeter, showing the distribution of LAr/Lead layers with accordion shape and radiation lengths, from [89].

is contained within a cylinder with an outer radius of 2.25 m and length 6.65 m. The calorimeter cells point towards the IP; in total there are 190k channels. The total thickness of the EM calorimeter is $\sim$ 24 radiation lengths, X_o, in the barrel as shown in the figure and $\sim$ 26 X_o in the end-caps [49]. The angular resolution is energy dependent, as $\sigma_\phi = \frac{50}{\sqrt{E}}$ mrad and energy fractional resolution as $\frac{10}{\sqrt{E}}$ % [29]. Signals are sent to a preamplifier then to analogue memories until the Level-1 trigger decision is taken (section 4.6). Then after the validation a digitization and data acquisition system is activated.

4.4.2 Hadronic Calorimeter

The Hadronic Calorimeter (HCAL), absorbs and measures the energy of strongly interacting particles just as the ECAL does to electrons and photons. The HCAL

barrel is divided in three sections: a central barrel and two identical extended barrels as can be seen in Figure 4.11. The barrel covers the range $|\eta| < 1.7$ with central barrel over $|\eta| < 1.0$ and extended barrels in $0.8 < |\eta| < 1.7$. Iron scintillating-tile technique is used in this region, which consists of layers 4 mm thick of plastic scintillator plates interleaved with layers of iron absorber 5 mm thick. The barrel is contained in a cylindrical region with inner and outer radii of 2.28 m and 4.25 m respectively. It is divided azimuthally in 64 modules with tiles placed radially and staggered in depth with the same pattern repeated in the z direction.

The end-cap, indicated in Figure 4.11 as LAr hadronic end-cap (HEC), consists of two wheels with outer radius 2.03 m located after the ECAL end-caps in the z axis. Each wheel has 32 modules of copper plates spaced by 8.5 mm thick LAr layers. The wheels are divided into two segments, with plates 25 mm thick (closer to the IP) and 50 mm respectively. This system provides the higher radiation resistance required for calorimetry systems located at higher pseudorapidities. The end-cap shares the cryostat used for the ECAL end-caps and also with the LAr forward calorimeter HFCAL, which extends the HCAL pseudorapidity coverage to 4.9. The end-caps cover the pseudorapidity range $1.5 < |\eta| < 3.2$ and the HFCAL the range $3.1 < |\eta| < 4.9$. The total thickness of the HCAL is 11 interaction lengths (λ) at $\eta = 0$ [89] and the fractional energy resolution is about $\frac{40}{\sqrt{E}}$ % [30].

4.5 Muon Spectrometer

The Muon Spectrometer (MS), comprises four different technologies used to track muons being bent by the magnetic field generated by the large superconducting air-core toriod magnets described in section 4.2. Figure 4.13 summarizes the arrangement of the chambers of the whole system. The Monitored drift tubes (MDTs), and the Cathode Strip Chambers (CSCs), are part of the precision-measurement tracking chambers system. The Resistive Plate Chambers (RPCs) and the Thin Gap Chambers (TGCs) are part of the trigger chambers system. All the chambers

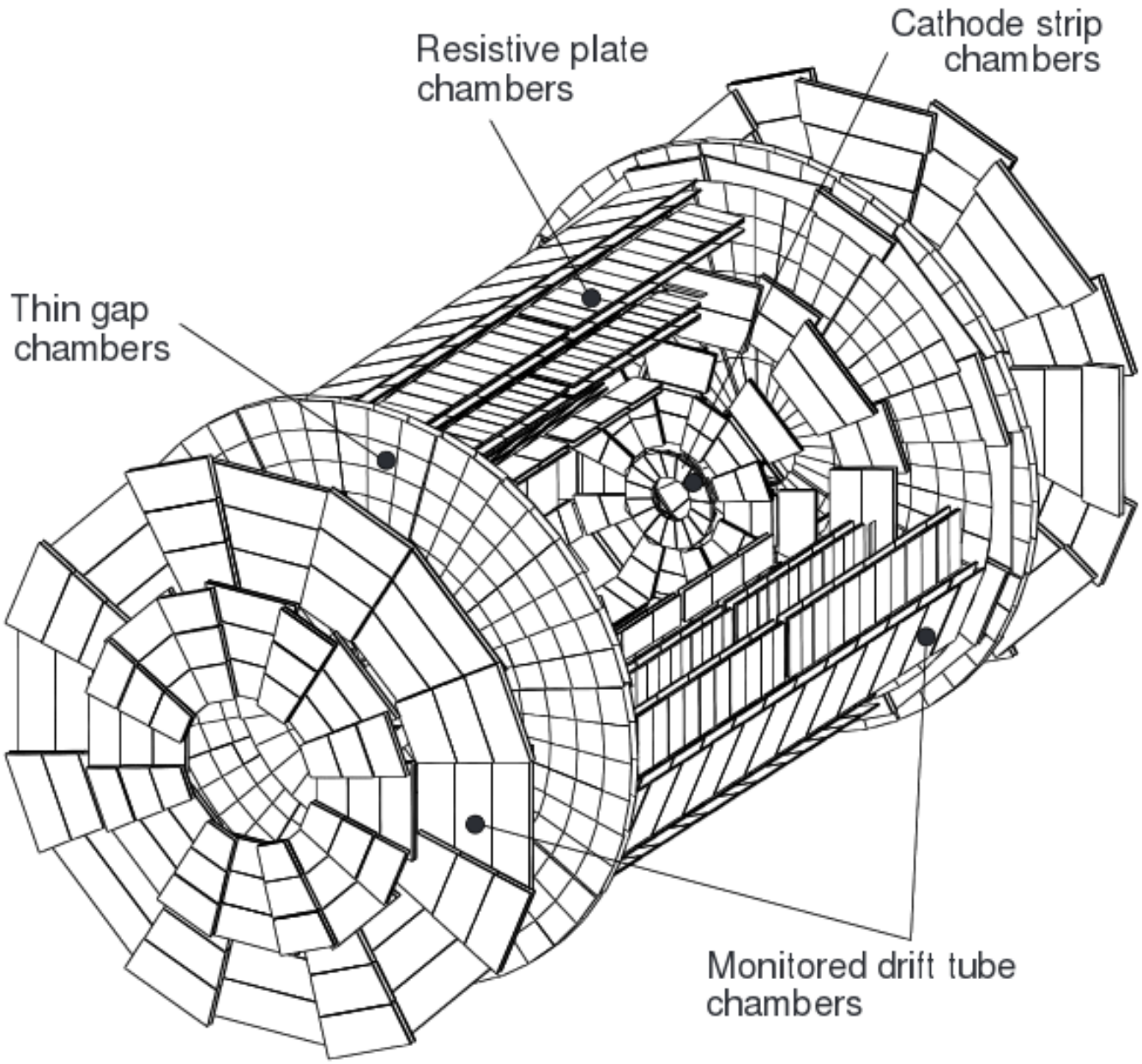

Figure 4.13: Over-all layout of the 4 muon chamber technologies, precision measurement chambers and trigger chambers. From [93]

combined give a coverage over the pseudorapidity range $0 < |\eta| < 2.7$. The MS has a barrel with total length of 25 m while the end-caps extend up to 22.5 m from the centre of the detector along the z-axis. The barrel (covering the range $|\eta| < 1.0$) has rectangular chambers with areas 2-10 m^2 that are arranged in three cylindrical layers with radii 5, 7.5 and 10 m respectively. The end-caps have trapezoidal-shaped

chambers arranged with vertical orientation with areas 1-10 m^2 in the range $1.4 < |\eta| < 2.7$. Each end-cap is made of 4 disks at 7, 10, 14, and 21-23 m from the IP along the z-axis. The pseudorapidity range $1.0 < |\eta| < 1.4$ is a transition region from barrel to end-cap; here vertical oriented chambers are located in the combined end-cap and barrel magnetic fields.

The trigger of the MS is crucial to suppress backgrounds associated with penetrating products from primary collision known as "punchthrough" and secondary decay products generated in calorimeters and shielding material. The MS includes its own trigger and high-precision chambers with very fast time response. The system has an opening at $|\eta| = 0$ to allow the entrance of cables and other services for the ID, CS and Calorimetry systems. The muon momentum resolution is expected to increase from 2 % to 10 % of the momentum value in a range from 10 to 1000 GeV [87].

4.5.1 Monitored Drift Tubes

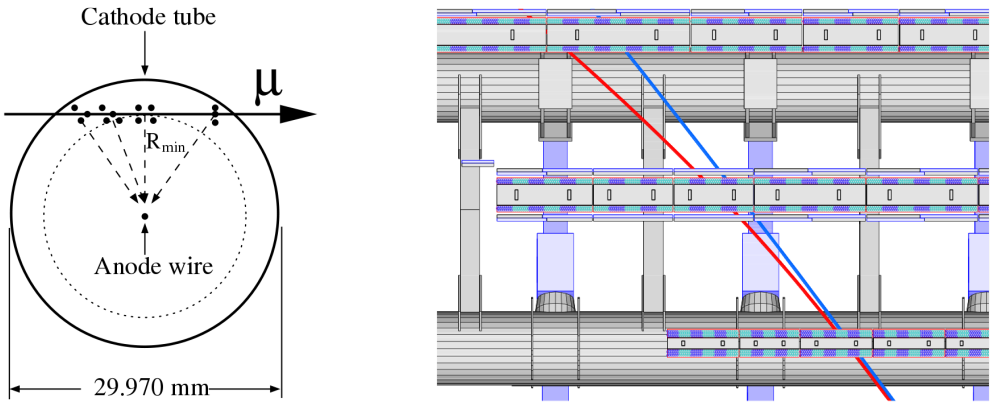

Figure 4.14: Cross-section of a single MDT element (left), trajectories of muons with momenta 4 GeV (red colour) and 20 GeV (blue colour) respectively through the magnetic field in the barrel of the MS, in general the tracks hit 3 layers of MDT modules (right) From [89].

The Monitored drift tubes (MDT), are used for precision measurement of the muon momentum in the MS. They are located in the MS barrel and end-caps, over most of the η range covered by the MS, as shown in Figure 4.13. The cross section of

a single MDT chamber is shown in the left of Figure 4.14, the tubes are made of aluminium with lengths varying from 70 cm to 630 cm and diameter of 30 mm. An internal 50 μm diameter W-Re wire is surrounded by a non-flamable mixture of Ar (93%), CO_2 (7%) ($\sim$ 3 bar absolute pressure). The electrons produced in the ionization are collected by the central wire. Two muon tracks crossing the three layers of MDTs in the MS barrel at radii 5, 7.5 and 7 m respectively, are shown in the right of the figure. The track with the highest momentum with blue colour has a smaller bending curvature. The system has a single-wire resolution of $\sim$ 80 μm. The tubes are arranged in groups 'monolayers' of 2×4 or 2×3 tubes and then in groups of four or three monolayers known as 'multilayers'. Each drift tube is read out by low impedance current preamplifier and then by a differential amplifier, and finally by a shaping amplifier and a discriminator. The tubes are constantly being monitored for mechanical deformation by a sophisticated optical system - hence its name. There is a system of four monitoring rays (2 parallel and two crossing diagonally) at every unit of area of (1 - 2 m) by (1 - 6 m).

4.5.2 Cathode Strip Chambers

The Cathode Strip Chambers provide the MS with higher granularity and higher rate capability. These chambers are located in the region of the detector subject to high flux, $2.0 < |\eta| < 2.7$, and are able to perform at counting rates about 1000 Hz/cm^2. These chambers are also supported by an optical alignment system as in the MDTs. The chambers are made with several anode wires with anode-cathode spacing as shown in Figure 4.15 where a single CSC module is shown in the left and an illustration of the arrangement of the cathode strips and the anode wires is shown in the right. Coordinates are obtained by measuring the charge in cathode induced by the 'avalanche in anode'. Cathode strips are orthogonal to anode wires and a position resolution of $\sim$ 60 μm is achieved. A second set of cathodes in the chamber are oriented parallel to the anodes, to measure the second transverse coordinate. The chambers use a non flamable mixture of Ar(30%), CO_2 (50%) and CF_4 (20%).

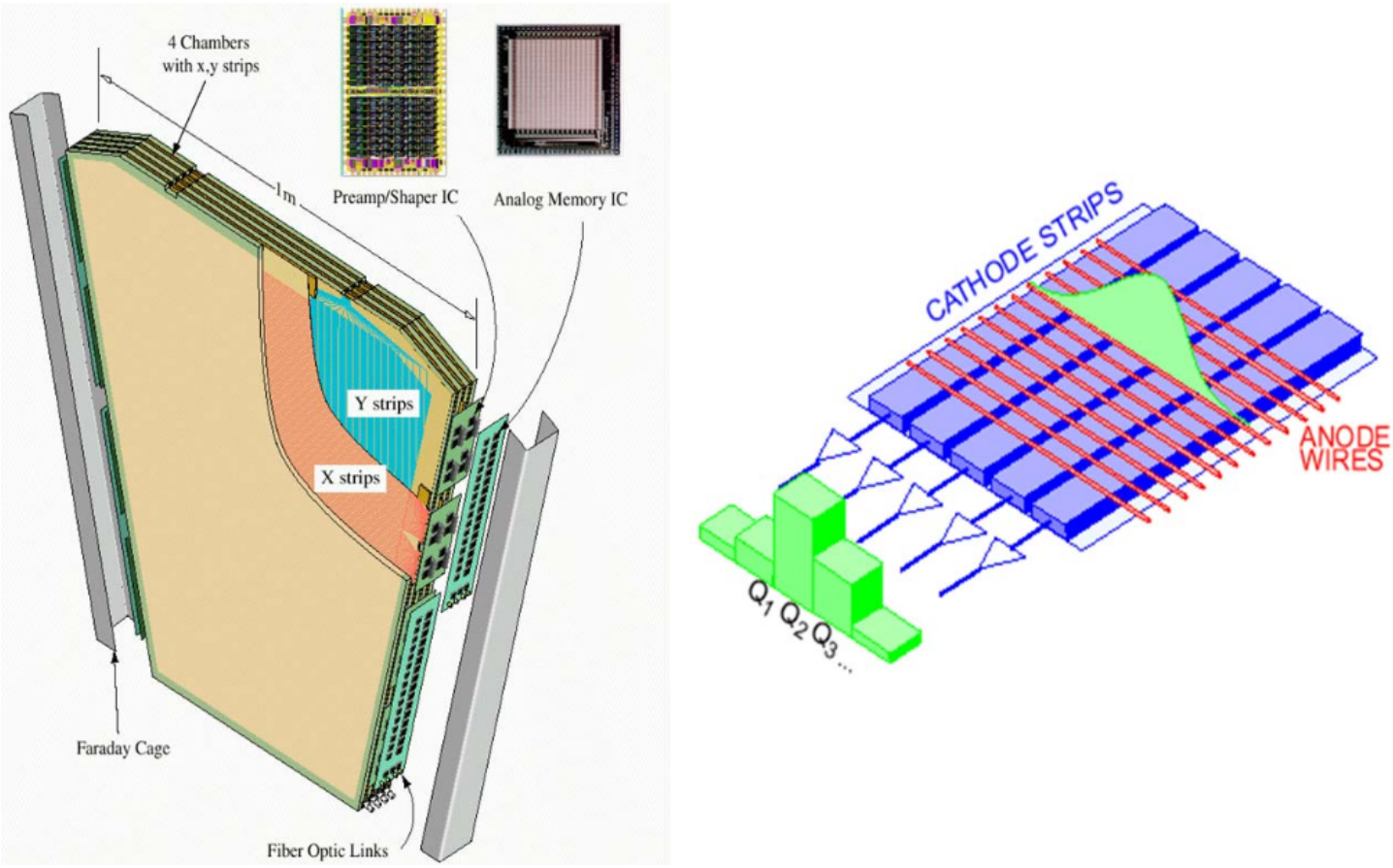

Figure 4.15: Schematic view of a single unit of CSC chambers (left), illustration of arrangement of cathode strips and anode wires in the CSC chambers (right). From [54].

4.5.3 Resistive Plate Chambers

The Resistive plate chambers provide the trigger system in the barrel and are arranged in three stations located inside the outer layer of MDTs in the barrel as shown in Figure 4.16. The outer layer permits selection of high transverse momentum tracks with values of p_T in the range 9 - 35 GeV, regarded as high p_T trigger and the remaining two inner layers allow the selection of tracks with low value of p_T in the range 6 - 9 GeV [89]. The RPCs provide a space-time resolution of 1 cm $\times$ 1 ns. They have a narrow gas gap (2 mm defined by polycarbonate spacers) formed by two bakelite (2 mm thick) plates. Ionizing electrons are generated from the muon hits and an electric field is applied over them so capacitance pulses are generated as charge is accumulated. The gas used for this chambers is $C_2H_2F_4$. Capacitive coupling is used to read the signal which is read out by a set of η-strips parallel to

MDT wires (bending view) and ϕ-strips parallel orthogonal to MDTs wires (second coordinate), each chamber has 2 detector layers and 4 readout strip panels.

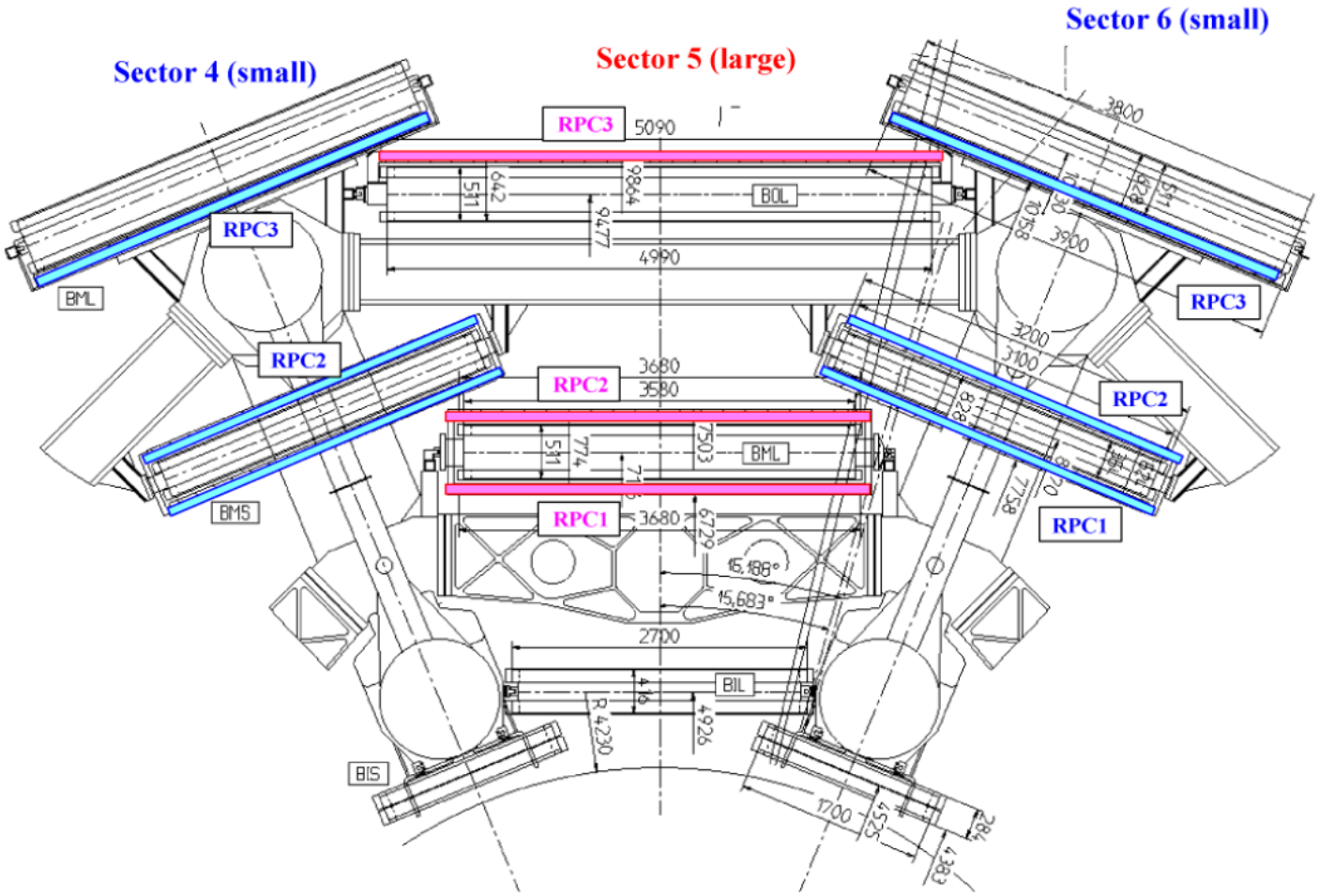

Figure 4.16: Trigger system in the MS barrel with three layers of RPCs. The first two layers, RPC1 and RPC2 straddle the middle layer of MDTs. The third layer RPC3 is above the outer layer of MDTs in the larger MS sectors and below in the smaller MS sectors. From [89].

4.5.4 Thin Gap Chambers

The Thin Gap Chambers provide the trigger system in the end-cap and are located close to the middle MDT layer and are separated in three stations that are also used to complement the angular measurements of the MDTs in the end-caps. Here as in the CSCs, multiwire proportional chambers are used but the wire-to-cathode distance of 1.4 mm is smaller than the wire-to-wire distance of 1.8 mm, graphite 1.6

mm G-10 plates are used for cathode strips [89]. An illustration of the arrangement of anode wires and cathode strips is shown in Figure 4.17.

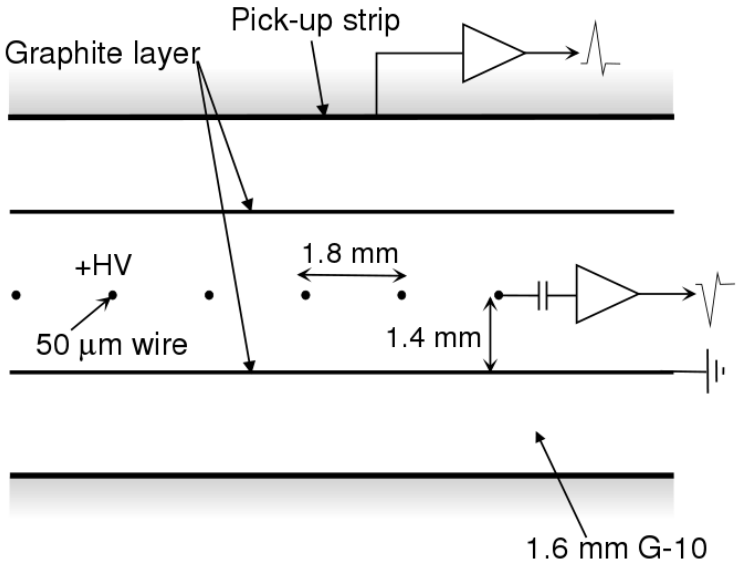

Figure 4.17: Schematic illustration of the configuration of anode wires and cathode strips in the TGCs. From [89].

There is a 2.8 mm thin separation between cathodes which yields to short drift time and good time resolution. Orthogonal copper strips provide measurement of second coordinate (similar structure as the CSCs). The highly flammable gas mixture CO_2 (55%), n-pentane (45%) is used for these chambers which are arranged in groups of two or three.

4.6 Data Acquisition and Selection Stages

The Data acquisition system (DAQ), in ATLAS is separated into three levels: Level 1, Level 2 and Event Filter for online event selection as illustrated in Figure 4.18, where the main stages of the event selection are shown. Each level decision is based on different observed signatures that characterize events of potential interest for the diffent physics analyses. Bunch crossing rates corresponding to head-on proton-

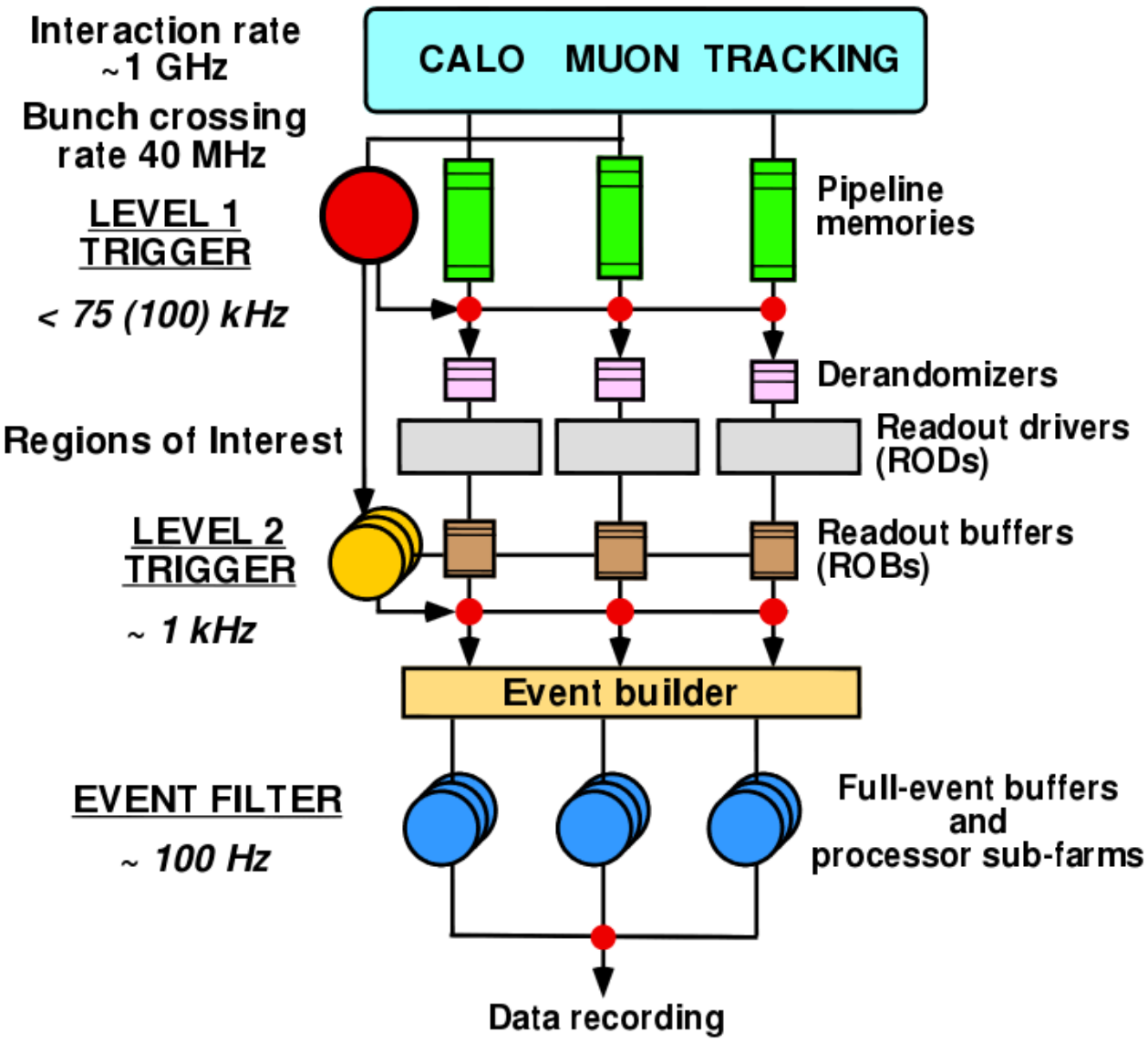

Figure 4.18: Diagram of Trigger and DAQ system, From [93]

proton collisions at 40 MHz (corresponding to design luminosity) should be reduced to $\sim$ 100 Hz for storage. Ignoring the pixel detector the total number of detector channels exceeds 10^7.

4.6.1 Level-1 Trigger

The Level-1 Trigger (LVL1), should identify a bunch crossing of interest (the bunch are separated by $\sim$ 25 ns). In general, information from a subset of detectors with low granularity is used at this stage e.g. the segmented regions of muon spectrome-

ter chambers. The calorimetry system trigger finds high p_T electrons and photons, jets and τ leptons decaying into hadrons (energy isolation cuts are applied) or large missing transverse energies. Trigger information is stored for different sets of p_{T} thresholds where conditions for certain objects are required in coincidence or veto. ATLAS can accept a maximum rate from LVL1 Trigger of 75KHz (which has been upgraded to 100kHz). Pipeline memories are used to store information from the event for up to 2.5 μs when the trigger decision is taken. Finally the data are transferred to readout buffers (ROBs) and kept there until the LVL-2 trigger decision is taken. Then the data are either erased or passed to the event filter.

4.6.2 Level-2 Trigger

The Level-2 Trigger (LVL2), uses regions of interest (RoI) from the event classified as primary and secondary. Primary RoIs are stored at the L1-trigger while secondary correspond to information not used for the L1-trigger decision. RoIs comprise the angular locations, η and ϕ, and transverse momentum p_{T} of muons, electrons, photons, τ candidates and showers of particles (jets) originating from quarks. Also the event missing energy $E_{\mathrm{T}}^{\mathrm{miss}}$ and scalar sum of total transverse energy $\sum E_{\mathrm{T}}$ are variables considered by the RoIs. For most of the cases data from only a small fraction of the detector are required for the LVL-2 decision as it is mostly guided by identification of few regions of interests. The LVL2 reduces the rate from 75 kHz to $\sim$ 1 kHz. The decision time of the LVL2 is around 1-10 ms.

4.6.3 Event Filter

The Event Filter (EF), is the final stage for the triggering process and event building where refined algorithms and methods adapted to the online environment, during event selection, are used. Information such as the alignment of detector components, calibration details and the magnetic field map are used at this stage. Sometimes the EF uses tighter p_{T} thresholds than those used in previous stages. All event data are available for this last stage. The selected events are written to the detector mass

storage and are available to be used for physics analyses. The output final rate is $\sim$ 100 Hz, corresponding to output data rate of $\sim$ 100MB/s (if full data are recorded). The Event filter is able to perform vertex location and track fitting. Considering the massive amount of data collected each year (in the order of Peta-Bytes) new methods of data reduction, data selection and data access are under study for future stages of the LHC.

Finally a preliminary processing is done of the raw data after the event filter in order to separate data into event categories. From this point data are available to be used directly for different studies and analyses.

4.7 Physics and Performance During Run I

The ATLAS detector has had a successful operation during Run-I, analysing events from proton-proton collisions at centre-of-mass energies of 7 TeV and 8 TeV. The detector recorded about 4.57 fb^{-1} and 20.3 fb^{-1} of good quality data for physics at 7 TeV and 8 TeV, respectively. The collaboration has analysed the collected data producing a total of 429 publications [58].

During Run-I the experiment has produced remarkable results such as the discovery of the Higgs boson and has set tighter limits for candidate values for masses of different theoretical supersymetric particles. It has also reproduced most of the measurements performed by the Tevatron experiments for analyses involving top quark and B-mesons decays, the former being described with more detail in chapter 6. These areas in particular will gain precision for the different measurements during Run-II as the detector and different sources of systematic uncertainties are understood better after the experience with Run-I. ATLAS has measured several cross section values of different processes. As shown in Figure 2.9 a good agreement between data and the SM predictions has been found.

Before moving towards Run-II the collaboration has cooperated with the CMS collaboration to make possible the combination of some of their results, mostly in analyses involving the measurement of Higgs properties increasing the precision of the results.

4.8 Collaboration Progress Towards Run II

As the LHC starts running again this time at proton-proton collisions with centre-of-mass energies of 13 TeV, the collaboration has started to upgrade its analysis software and MC simulations to prepare for the increase in collision energy. Internal studies on expected results have been performed. This new campaign provides an exciting time for physics in general as collisions with this record energy have not been analysed before and new interesting results could lie ahead during this new run.

Between the main upgrades performed over the ATLAS detector before the start of Run-II, is the successful insertion of the Insertable B-Layer subdetector (IBL), the innermost layer of pixels, which will improve significantly the detection of b-quarks. It is also expected to increase the tracking, vertex location and b-tagging efficiencies of the ID. This is the closest sub-detector of the ID to the beam pipe, reducing its radius by 4 mm and with its supporting tube just 1.9 mm from the pixel detector. It is made with pixels with size 50×250 μm, in the ϕ and z coordinates respectively, with total coverage $|\eta| < 3$ and just ~ 33 mm from the interaction point [59]. Also hardware and software improvements have been achieved for all the detector subsystems, allowing it to accommodate higher rates that will be present during Run-II.

Chapter 5

Atlantis; ATLAS Event Display

In this chapter the technical contributions from the service work completed by the author for the ATLAS experiment are summarized. Atlantis is a program that is used by the collaboration to display simulated and observed events from data using intuitive graphical objects. Its use is widespread in publications and in the collaboration control room at CERN in Geneva [143]. A simpler version of Atlantis called Minerva is used in particle physics masterclasses and outreach events around the world.

The author spent one year before the start of the physics analysis as a developer in the Atlantis group, in charge of the upgrades to the program and of giving tutorial talks at CERN about the use of this program. The ATLAS tutorial programme involved mostly students in their 1^{st} and 2^{nd} years of PhD who had just become members of the collaboration. Also this service task included assisting people from all over the collaboration with enquiries about the use of the program and addressing reports of small bugs identified in it. The Atlantis group comprises staff and students from the University of Birmingham and University College in London (UCL).

Atlantis is briefly introduced in section 5.1 and main developments of this program achieved by the author are discussed in section 5.2. Current projects under development by others, but initially started by the author, are described in section 5.3.

5.1 Introduction to Atlantis

Atlantis is a program written in the `Java` [145] programming language mostly used to develop programs that involve the use of graphical applications. It is a standalone ATLAS event display, which means that it can be run in any computer with the appropriate updated Java packages [146]. Its name is formed by taking some of the letters from the expression "ATLAs eveNT dISplay", which describes the main function of the program. Atlantis creates a visual representation of events that are produced when proton-proton collisions occur at the ATLAS detector. To accomplish this task it uses nine different 2D projections, briefly described in section 5.1.1.

Atlantis reads information from files with format `.xml`, produced by ATLAS software, `Athena` [147]. It uses as input the original files that store the recorded information from all the selected events by the experiment. The specific package that `Athena` uses to produce these files is called `JiveXML` [144], and can only be used by ATLAS members.

5.1.1 Atlantis Projections

In Figure 5.1 the x-y, η-ϕ and ρ-z projections are used to display a simulated $t\bar{t}$ event. The x-y projection in the left of the figure, is a transverse view of the detector, perpendicular to beam direction (here the end-cap information is hidden). Reconstructed jets are in general represented with white coloured cones; they are coloured blue if the jets originate from b-quarks.

Tracks of charged particles created in the inner tracker detector are represented with cyan colour. These tracks are the ones passing different selection cuts like transverse momentum and distance to primary collision vertex cuts. It is possible to colour tracks by different methods, for example they can be coloured by their values of transverse momentum p_T, as in Figure 5.8, where only the most energetic ones passing certain p_T cut are drawn. They can also be coloured by objects, so it can

be known if there is any track associated to an electron, a muon or a tau.

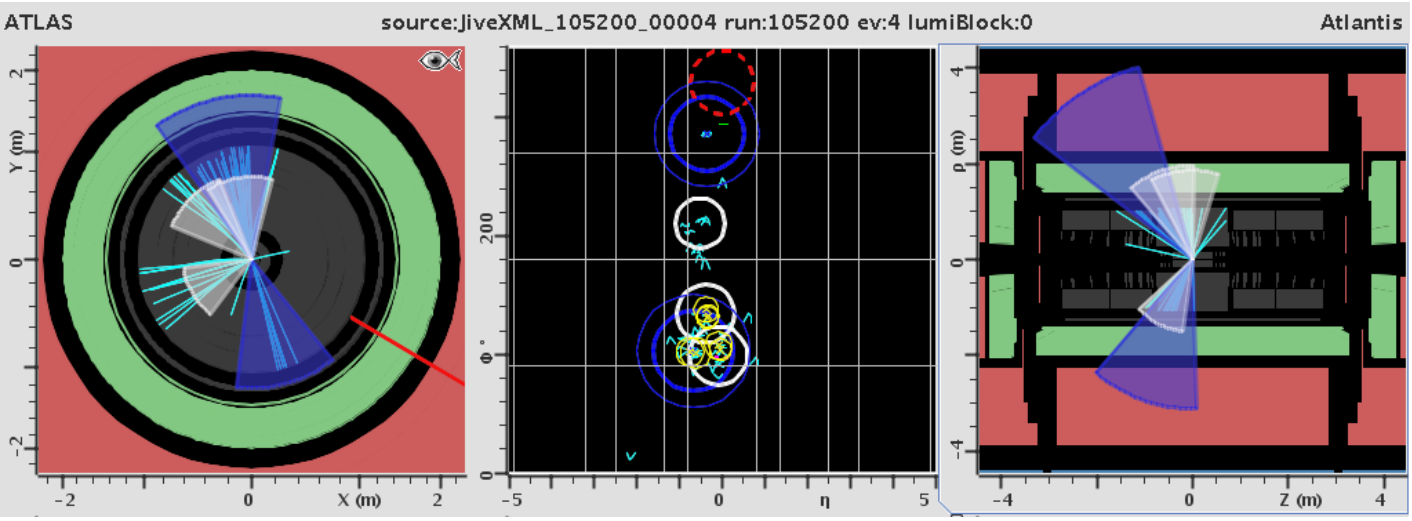

Figure 5.1: $t\bar{t}$ event displayed through the x-y, η-ϕ and ρ-z atlantis projections. For the x-y and ρ-z projections, jets are in general represented by white cones and are coloured blue if they are originated from b-quarks. They are represented by white and blue rings in the η-ϕ projection.

In the middle of Figure 5.1, the η-ϕ projection is shown, here η and ϕ are the detector angular coordinates described in section 4.1. This projection is useful to locate quickly in which region of the detector the interesting objects were produced. Physical objects (electrons, muons and taus) are represented by circles in this projection; reconstructed jets are represented with blue and gray circles while missing energy with a red dashed line. Electric charges of the different tracks are proportional to the height of the V-shape they form. Finally in the right side of Figure 5.1 the same event is displayed using the ρ-z projection which is a longitudinal view along the beam axis. Through this projection it is possible to have an over-all view of all the sub-detectors easily; in the figure are shown the hadronic calorimeter (red) and electromagnetic calorimeter (green) and all the objects within them.

Another set of projections that are not used very often within the collabotation are shown in Figure 5.2. The ϕ-ρ projection (left) is another transverse view of the

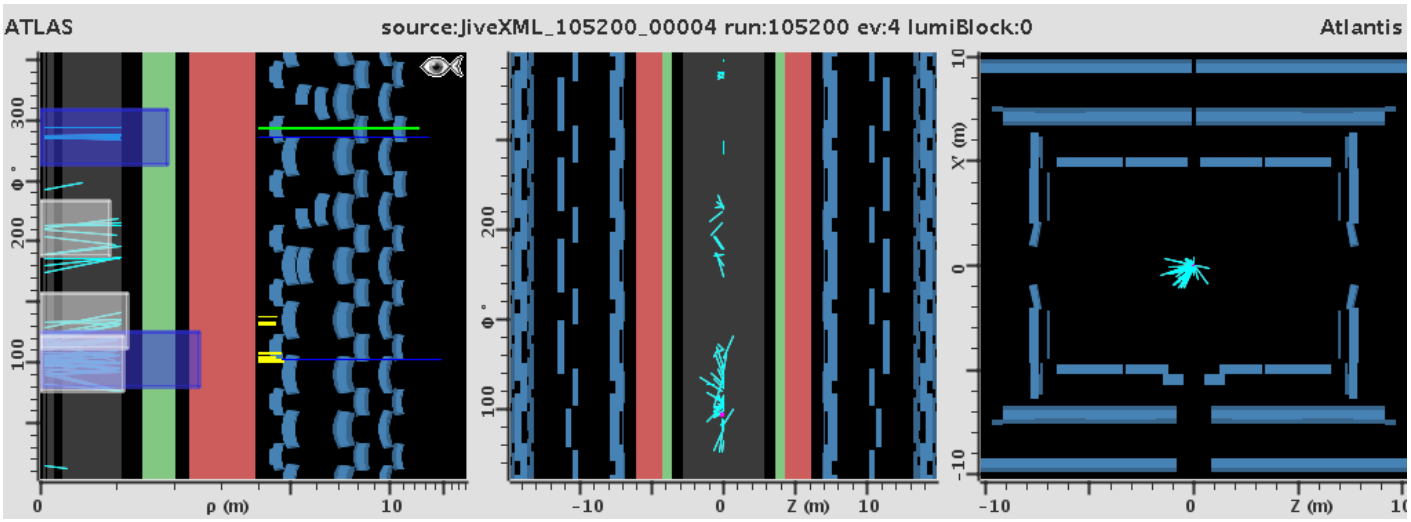

Figure 5.2: Same $t\bar{t}$ event displayed in Figure 5.1 using the ϕ-ρ, ϕ-z, x'-z Atlantis projections.

detector alternative to the x-y projection, using ϕ and ρ coordinates instead of x and y. The ϕ-z projection (in the middle) uses the ϕ and z coordinates and is much less intuitive than the rest of the projections. x'-z (right end) is another longitudinal view of the detector alternative to the ρ-z projection, that just shows tracks in the inner detector and the muon detector sections, so a rapid match between possible muonic tracks and spectrometer hits can be done.

Finally in Figure 5.3 are shown the rest of the available projections. y'-z (left) is another longitudinal view of the detector alternative to the ρ-z projection, but just showing the event tracks in the inner detector. In the middle of the figure, the lego plot is shown, which is a projection that, as with the η-ϕ projection, locates event signals using the η and ϕ angular coordinates, but additionally the lego plot shows the value of an extra coordinate, the objects' transverse energies, E_{T}. It displays the transverse energy deposited in calorimeters corresponding to a specific η-ϕ location through towers parallel to the E_{T} axis. Finally in the right-end of the figure there is an event information window that should be included when an event display is shown in an internal presentation or a scientific paper, as it indicates when the event was produced and if it is a real or simulated event.

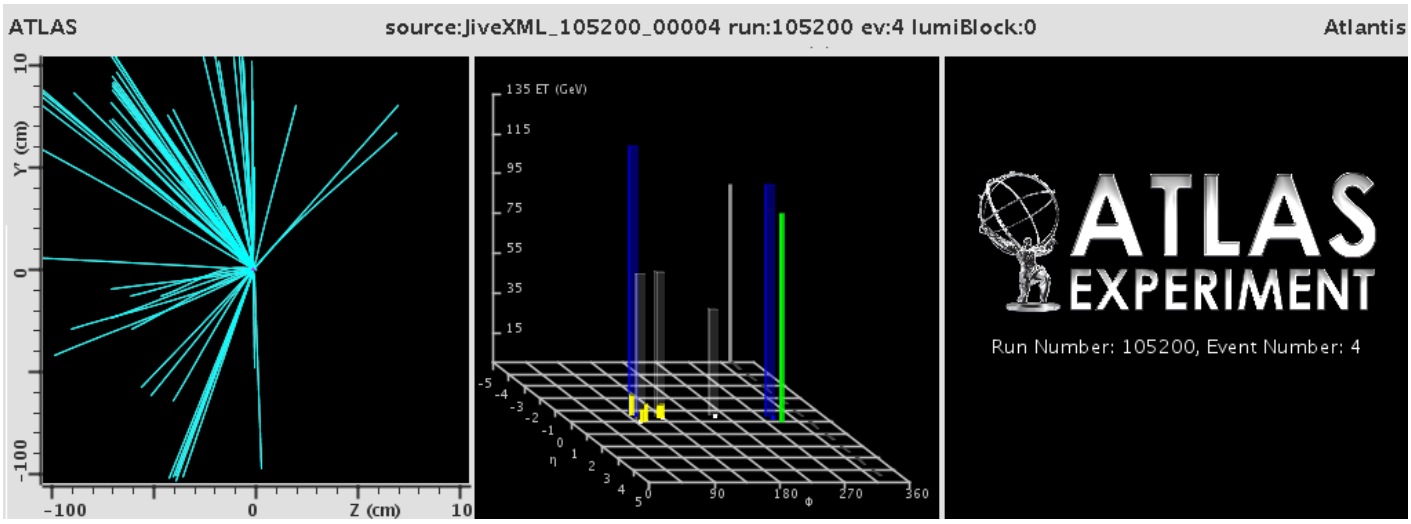

Figure 5.3: y'-z, lego-plot Atlantis projections and the event information window.

5.1.2 Available Tools to Analyse Events

When running Atlantis, a Graphical User Interface (GUI), menu is available, and is illustrated in Figure 5.4. The options at the top of the menu are useful to save the image of the display being shown or to open any input `.xml` file containing information from additional events located in specific URL addresses or locations in the computer memory.

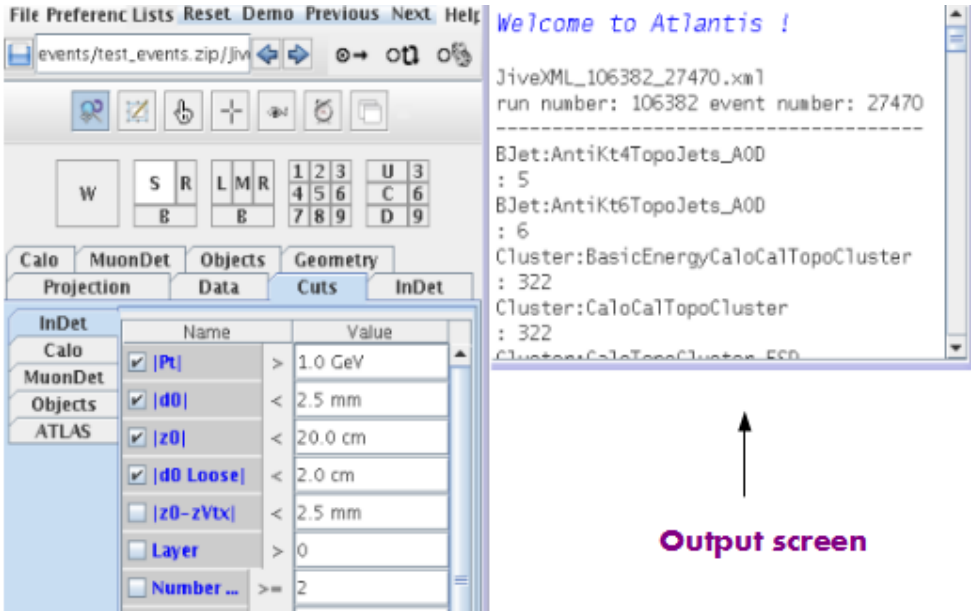

Figure 5.4: Atlantis Graphical User Interface (GUI).

Also with the GUI menu it is possible to change from one event to another one by using the buttoms “previous” and “next” and to reset to the default settings of the program or to create a list of selected objects in the event to perform a simple calculation. Below these top options, there is the interaction section, where it is possible to change the aspect of the selected projection. There is for example a zooming tool to observe closer a specific section of the detector or the fish eye tool which boosts the size of the inner-smaller regions of the detector. Below the interaction section there is a set of squares identified with letters. Here the user can select how all the selected projections will be distributed across the screen.

Finally at the bottom, there are labels that address different aspects of the event. For example with the option “cuts” the user can select a specific region of the detector like the inner detector or a specific physical object and can apply an available cut. Here the user can restrict the objects that will be displayed in the screen, for example a cut value for the p_T of tracks can be set. The option “projection" allows the selection of the different projections while the option “objects" gives the possibility to the user to decide how each object will be coloured.

5.2 Author’s Contributions to Atlantis

Contributions to the Atlantis program focused on the display of events that involve the production of jets and b-jets. Examples of such events are semi-leptonic $t\bar{t}$ events, described in chapter 6, where at least 4 jets are produced, of which at least two are b-jets. These contributions included changing the appearance of jets in the lego plot which are now represented by transparent towers rather than small circles and adding the feature to the program of colouring jets by “b-jet” using the output of b-tagging algorithms to discriminate these objects and colour them differently to ordinary jets. Also an option was added to the GUI to select the b-tagging algorithm of the user preference, and another slot was added to modify the b-tagging working point, defined in the following subsection. The aspect of all the objects

in general shown in the lego plot was improved using a Java transparency feature. These developments are described from sections 5.2.1 to 5.2.5.

Also small developments were done over the lego plot to improve the use of this projection for Level-1 electromagnetic calorimeter trigger studies, described in section 5.2.5. An aditional option to colour event vertices and tracks by vertex type was developed and is described in section 5.2.6

5.2.1 Jets and b-tagging Information

The ATLAS sofware `Athena` can run different b-tagging algorithms over the jet objects in the selected events using their recorded information. These algorithms determine how likely is each of the jets in the event to originate from a b-quark. Each of them will assign a `b-tagging weight` to the different jets. For each of the b-tagging algorithms there is a reference number that is called, "working point". If the b-tagging weight for a particular jet has a value over the working point, the jet is regarded as b-jet for a particular algorithm. Each working point will set an efficiency for b-jet identification, which is shown in Table 5.1 for three different b-tagging algoritms.

For research areas within experimental particle physics such as top quark physics the identification of b-jets with reasonable efficiency is crucial. In the event selection summarized in chapter 7, for example, two b-jet objects are required to be identified in each of the events by b-tagging algorithms. For this selection the MV1 algorithm in the table has been used as it has been the algorithm that has performed better in most of the analyses within the collaboration. An efficiency of 70 % has been selected, as if a higher efficiency is chosen several events are lost and large statistical fluctuations are introduced.

Code was added to the program so the b-tagging weights from the different b-tagging algorithms for each jet could be displayed on the Atlantis output screen, when a spe-

cific jet is selected with the mouse by the user. Figure 5.5 shows how the Atlantis oputput screen looks when a specific jet has been selected. The values corresponding to 9 different b-tagging algorithms are shown in the figure.

Table 5.1: Table presenting the different efficiencies for b-tagging identification corresponding to different working points and 3 b-tagging algorithms.

b-tagging Algorithm	Efficiency	Working Point
IP3DSV1		
	60%	4.55
	70%	1.70
	80%	-0.80
JetFitterCOMBNN		
	57%	2.20
	60%	1.80
	70%	0.35
	80%	-1.25
MV1		
	60%	0.91
	70%	0.60
	75%	0.40
	85%	0.07

5.2.2 b-tagging Colouring Function to Colour Jets

The following challenge was to allow the user to select any of the b-tagging algorithms contained in the input file and then select a specific working point. Jets with weight values higher than the working point value would be coloured blue, charateristic of *b*-jet objects. Additional code was written to add a new colouring function for jet objects and a drop-down menu to the GUI so the different available b-tagging

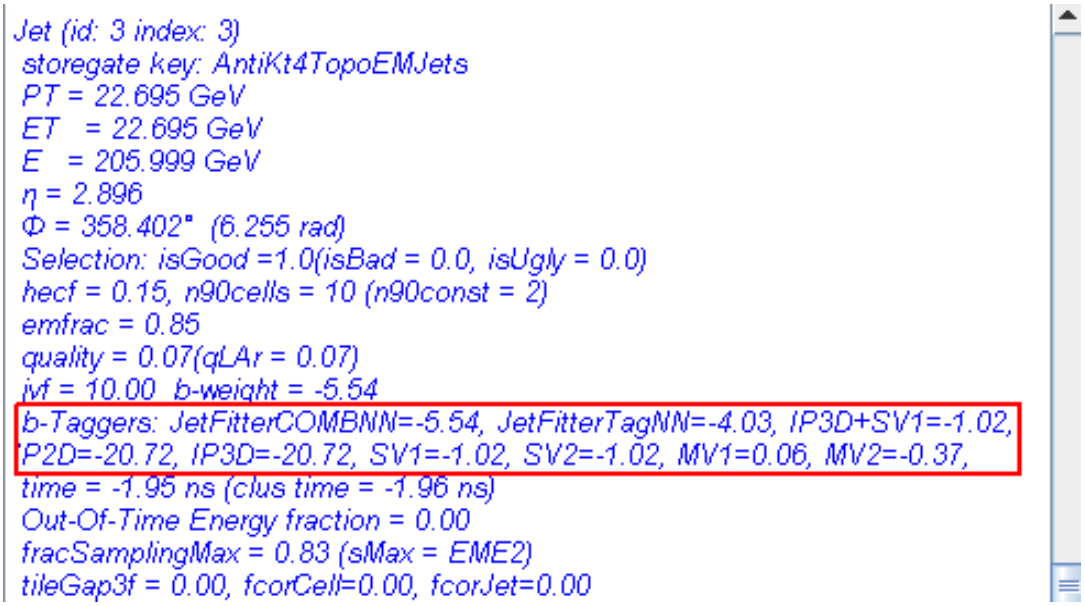

Figure 5.5: Atlantis output screen showing b-tagging weights from different algorithms for a specific selected jet.

algorithms could be shown as in Figure 5.6. For the event in the figure there are eight different *b*-tagging algorithms available. Once an algorithm has been selected the desired working point can be introduced into the GUI, as indicated in Figure 5.7.

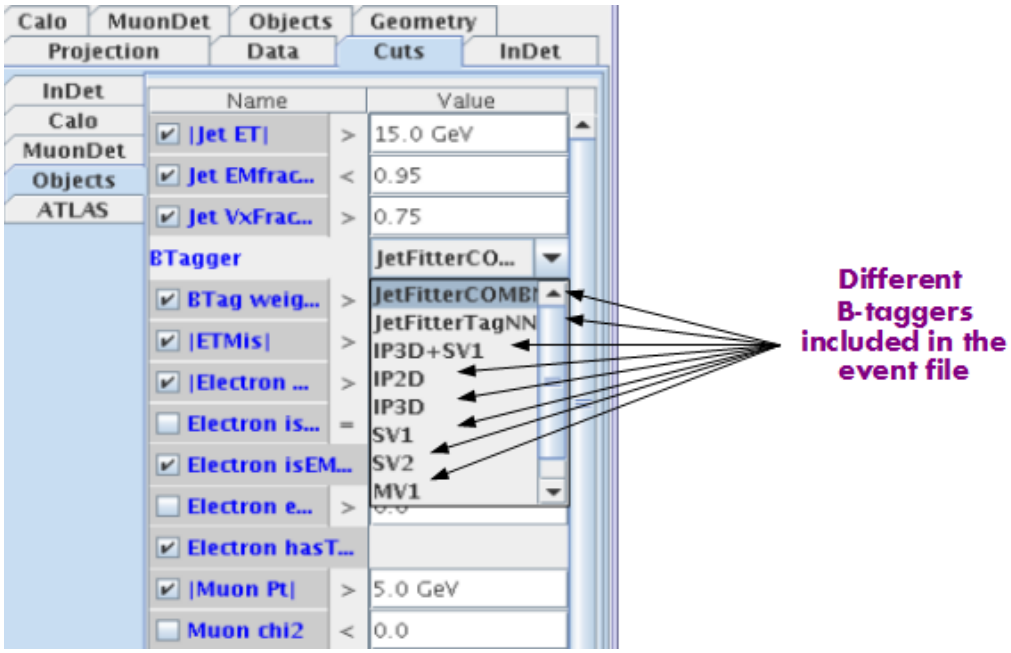

Figure 5.6: Added drop-down menu to the Atlantis GUI, showing the available *b*-tagging algorithms for each event jet.

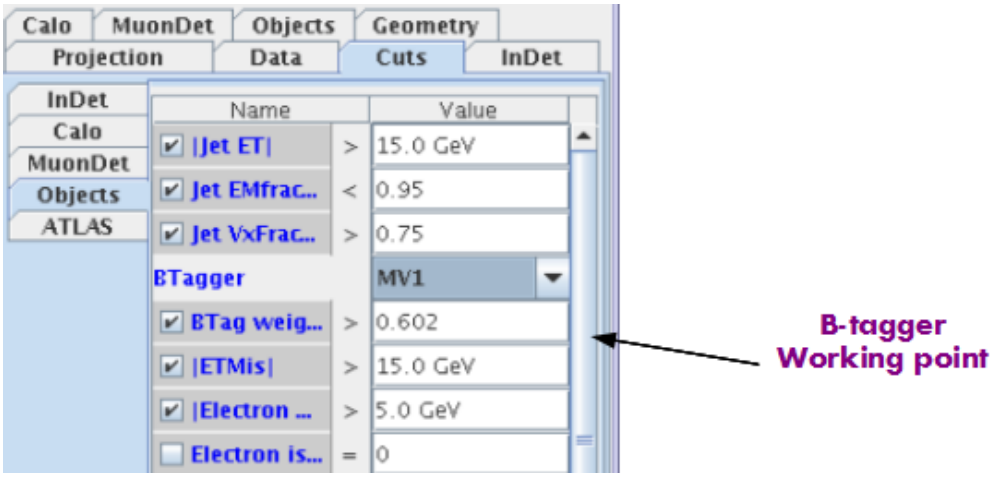

Figure 5.7: Once a *b*-tagging algorithm is selected, a working point can be set.

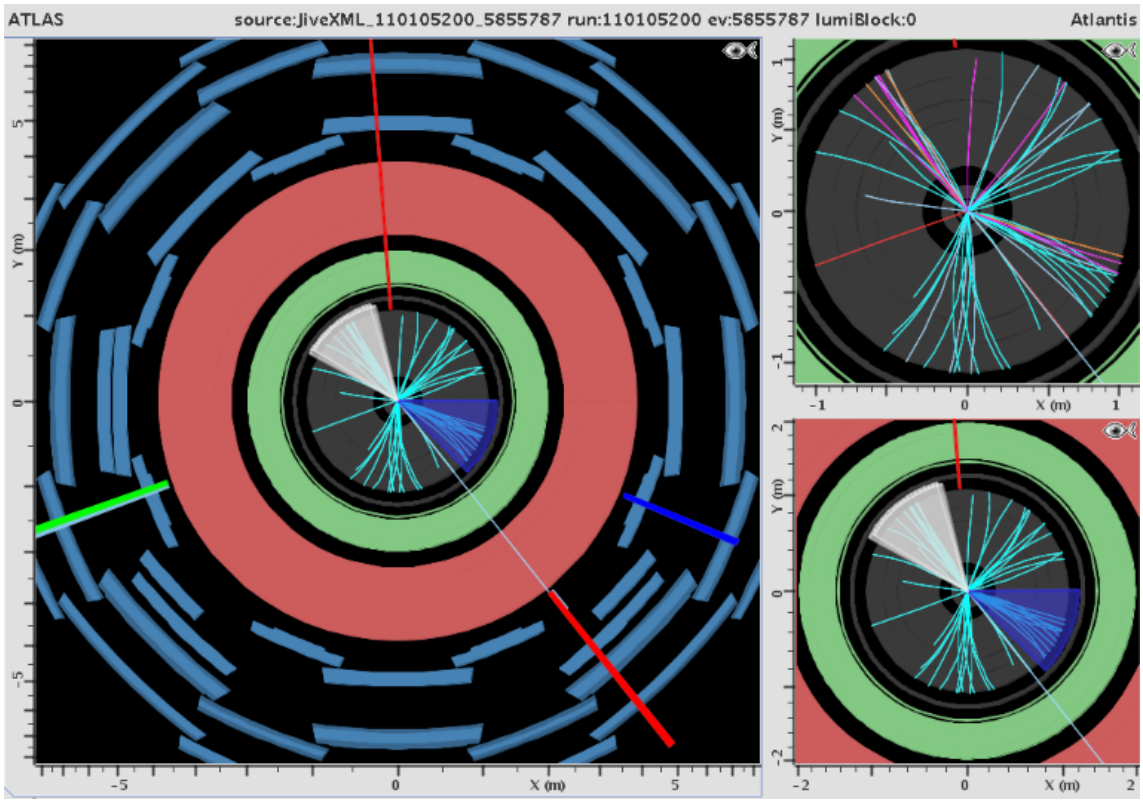

Figure 5.8: A typical look of the event jets being coloured according to their b-tagging weight values.

In Figure 5.7 for example, a working point of 0.602 for the MV1 tagger, corresponding to a efficiency of 70%, has been chosen. The new colouring function of jets was interfaced with the drop-down menu shown in the Figure 5.6, so that, if the user

selects an algorithm and a working point, this information is transmitted into the canvas automatically and the jets are coloured blue as b-jets if they pass the working point cut.

For the latest release of the program, to use this colouring feature for jets, the user has to select the “Objects" label in the GUI and then change the colouring function of jets to “BJets". Then the next step is to select the “Cuts" label, then the sub-label “Objects", and then a menu like the one shown in Figure 5.7 will appear. After the user has enabled the colouring by `BJets` function and adjusted the b-tagging preferences in the GUI, the event jets are coloured either as ordinary jets or as b-jets as shown in Figure 5.8, where two jets are produced, one of them being identified as a b-jet and coloured blue.

In Figure 5.8, it can be seen in the top right projection that the tracks in the inner detector have been coloured by their values of p_T. In this display the p_T values of tracks are: green $\rightarrow$ $p_T \sim 1$ GeV, pink $\rightarrow$ $p_T \sim 5$ GeV, orange $\rightarrow$ $p_T \sim 20$ GeV, red $\rightarrow$ $p_T \sim 70$ GeV. The track coloured in red corresponds to an electron object represented with a green bar coming from calorimenters. A muon object represented with a red bar coming from calorimeters has been identified as well and the red line going upwards represents the direction of the event transverse missing energy. This event is a simulated dilepton $t\bar{t}$ event and in this case the b-tagging algorithm identified only one of the event b-jets.

5.2.3 Jet Towers in Lego Plot

Another contribution consisted in changing the representation of jets in the lego plot and reducing the overlap between jets and electrons in the displays. In the bottom right of Figure 5.9 is shown how previously jets were represented in the lego plot by using circles. It was decided to represent the jets as towers just like the other objects in this projection. These towers needed to be transparent to avoid hiding any other object as the jets smear their energy into a wider area in the (η, ϕ) plane

than other objects.

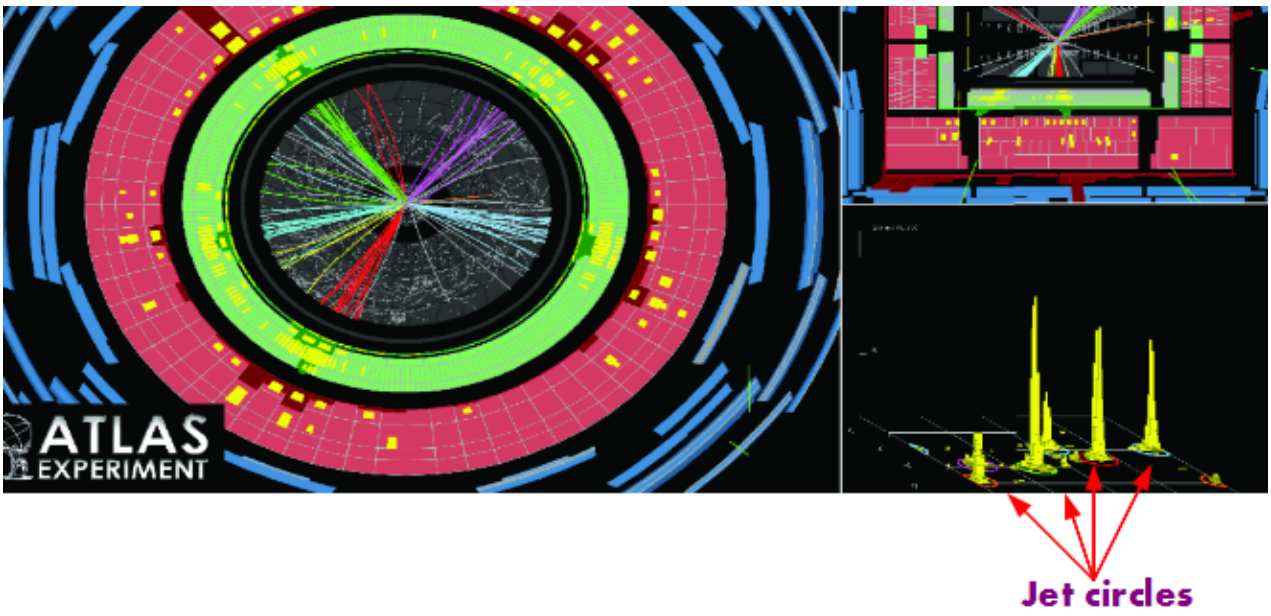

Figure 5.9: Event containing several jets, in the bottom right jets are represented by circles in the lego plot

Jets have associated electromagnetic and hadronic components for their energy deposits in the calorimeters. To avoid overlapping between jets and electrons and to avoid drawing the same object twice as an electron and as a jet, a new option was added into the GUI. Jets are drawn as electrons or jet objects depending on the value of their electromagnetic component. By default, if the electromagnetic component is over 95 %, then the object is considered an electron. The percentage of this overlap can be modified by the user with this new added option in the GUI. Figure 5.10 shows a display produced during the development of the jet towers in the lego-plot. In the right of Figure 5.10 a jet (white colour) has been overlapped by an electron (green colour). This problem was solved by adding the mentioned overlapping feature.

Initially the towers in the lego plot for the different objects did not have a 3D aspect, with their top and sides drawn with a squared shape instead of a single line. As can seen in the right side of Figure 5.10 a 3D aspect was given to all the towers, not just the ones corresponding to jets.

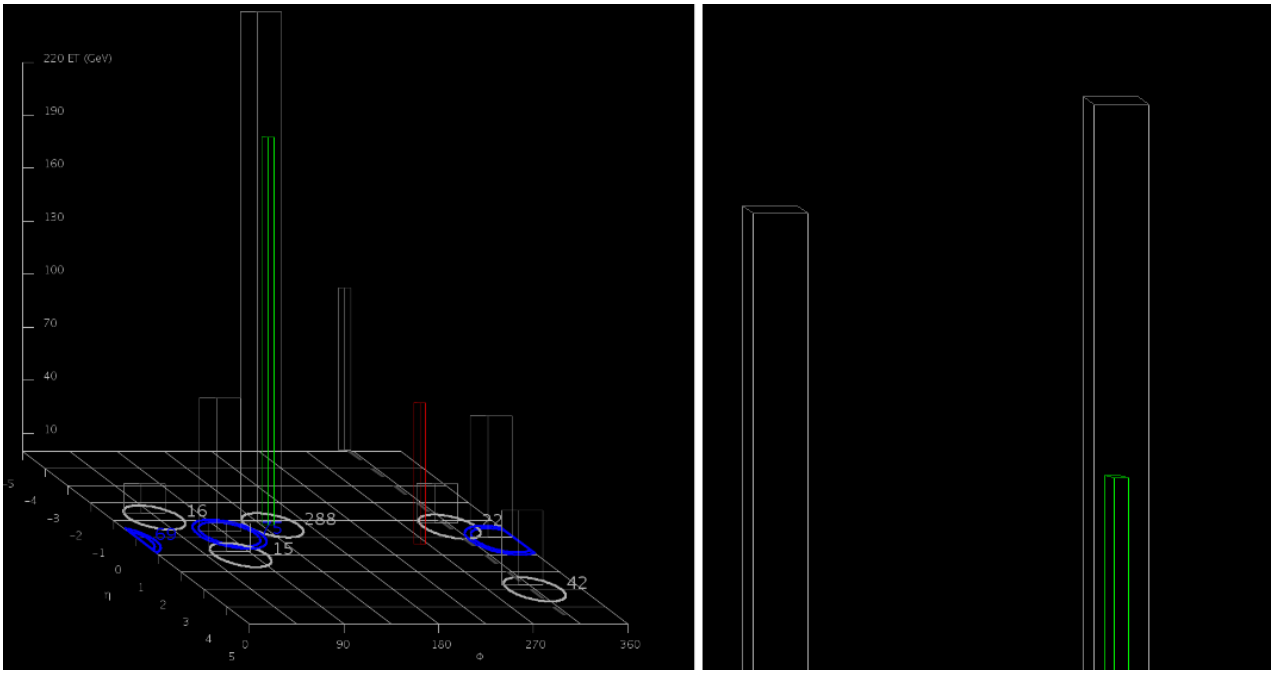

Figure 5.10: Initial attempt to produce the jet towers in Lego plot. In this plot the towers' sides have not been coloured, making it difficult to distinguish each of the towers. The towers with white lines represent jets, the tower with green colour represents an electron and the one with red colour represents a muon (left). Zoomed view of the same event to illustrate how one of the jets has been overlapped by an electron object (right).

In Figure 5.11 is shown one of the first advanced versions of the jet towers. Still all the towers specially the ones corresponding to jets had an "empty" look in the canvas, which has a black coloured background. So a transparency tool available for Java graphical applications was used to colour the walls of the towers with transparent colour. With this upgrade the towers look like in Figure 5.12, with a more solid aspect, but at the same time objects behind each of the towers can be identified.

In right of Figure 5.12, it can be seen that the degree of transparency for the towers corresponding to muons and electron objects is chosen to be higher as these objects are represented with narrower towers and the trasnparency is not required to be very low for these towers. In Figure 5.13 a multi-jet event observed in data from proton-proton collisions with centre-of-mass energy equal to $\sqrt{s} = 8$ TeV is being displayed using jet cones for the x-y projection and the improved towers for lego plot (all the features are visible).

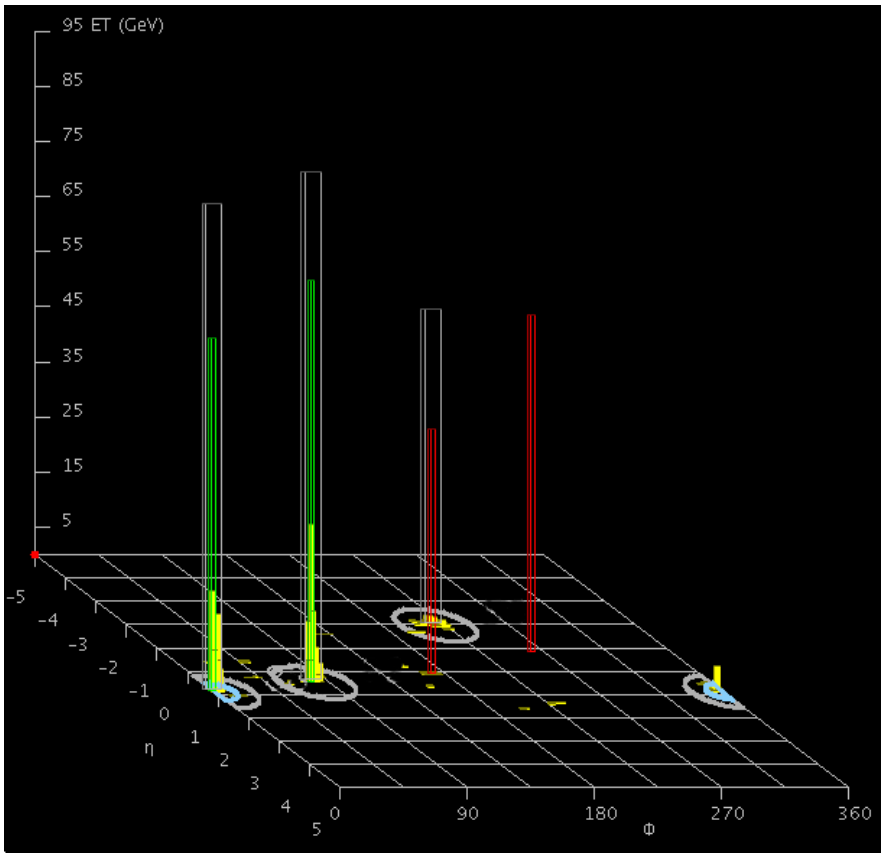

Figure 5.11: One of the first versions of the jet towers appearance in the lego plot. The towers with white lines represent jets, the towers with green colour represent electrons and the ones with red colour represent a muons. In this event two jets have been overlapped by two electrons. The gray circles were previously used to represent the jets. The towers with yellow colour represent energy deposits in the calorimeters in the transverse direction perpendicular to the beam line.

5.2.4 Propagating b-tagging Colouring to the Lego Plot

The colouring feature of jet objects by b-jet described in section 5.2.2 was initially only available for the x-y and ρ-z projections but not for the lego plot, which is a projection that comes from a separated set of classes within the program. So a substantial amount of code had to be added to the program to make this feature work also in the lego plot.

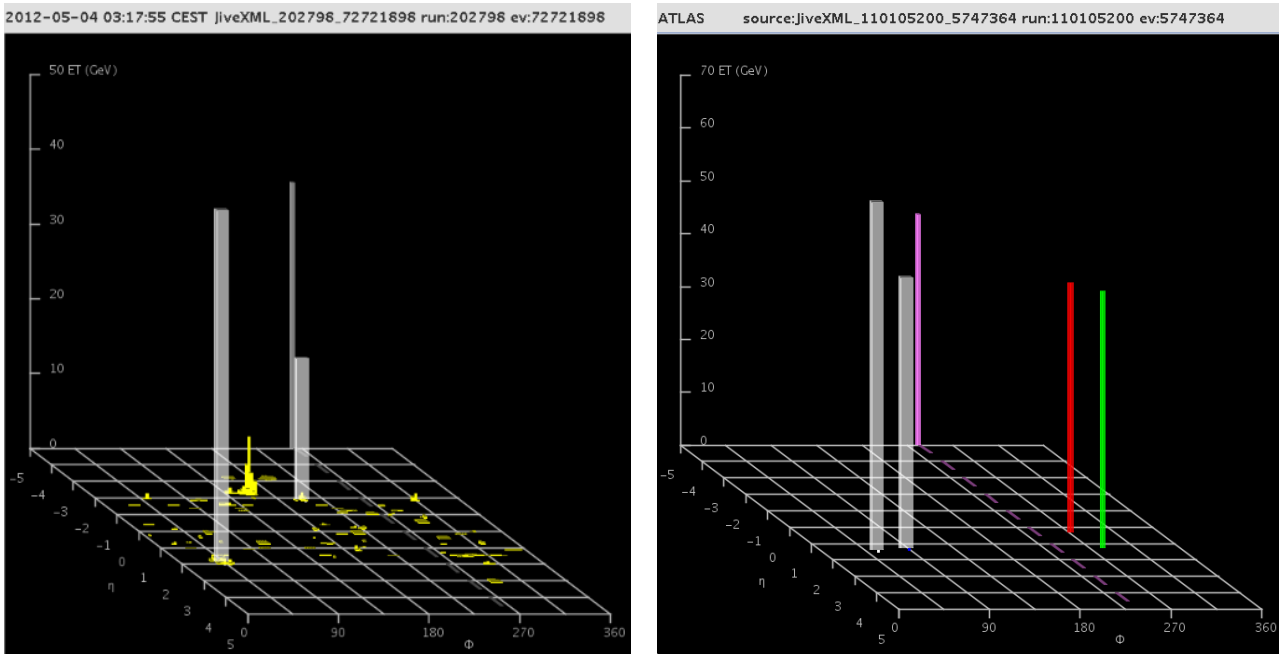

(a) Current aspect of Jet towers

(b) current aspect of all lego plot towers

Figure 5.12: Aspect of the towers in the lego plot projection with improved towers for jets (white), electrons (green) and muons (red) in the latest release of Atlantis. Two observed events are shown here corresponding to collisions at 8 TeV.

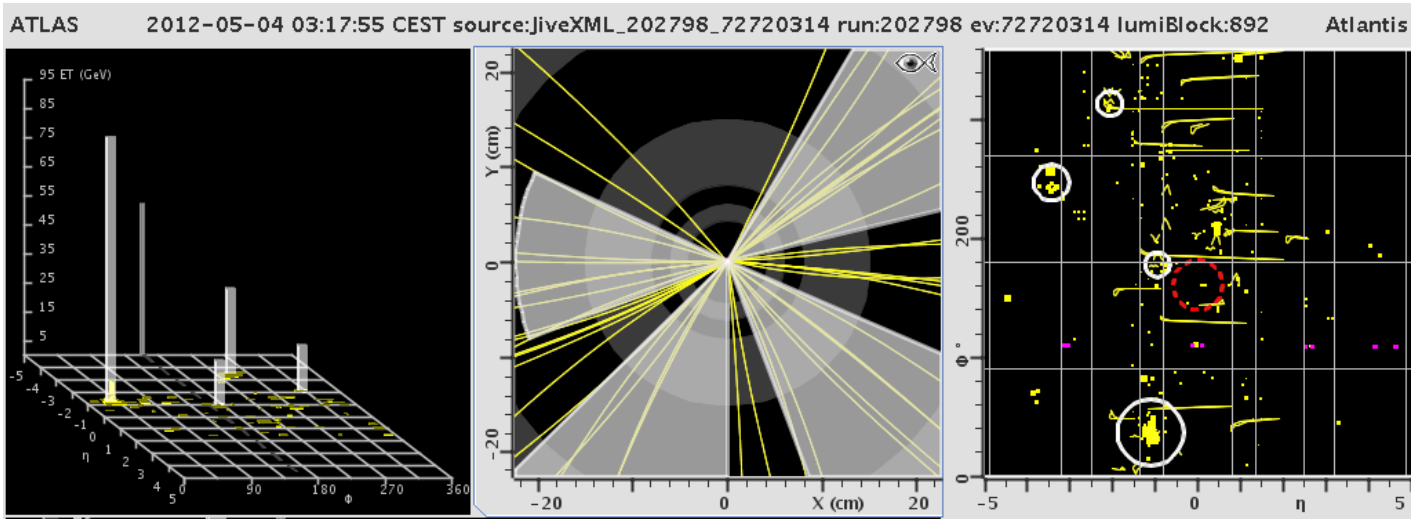

Figure 5.13: 2012 real multi-jet event being displayed using the jet cones and towers

Figure 5.14 shows the implementation of the colouring by b-jet over the towers associated to jets in the lego plot. The event shown in the figure is a simulated $t\bar{t}$ event, where two jets have been b-tagged and coloured blue by Atlantis. This figure sum-

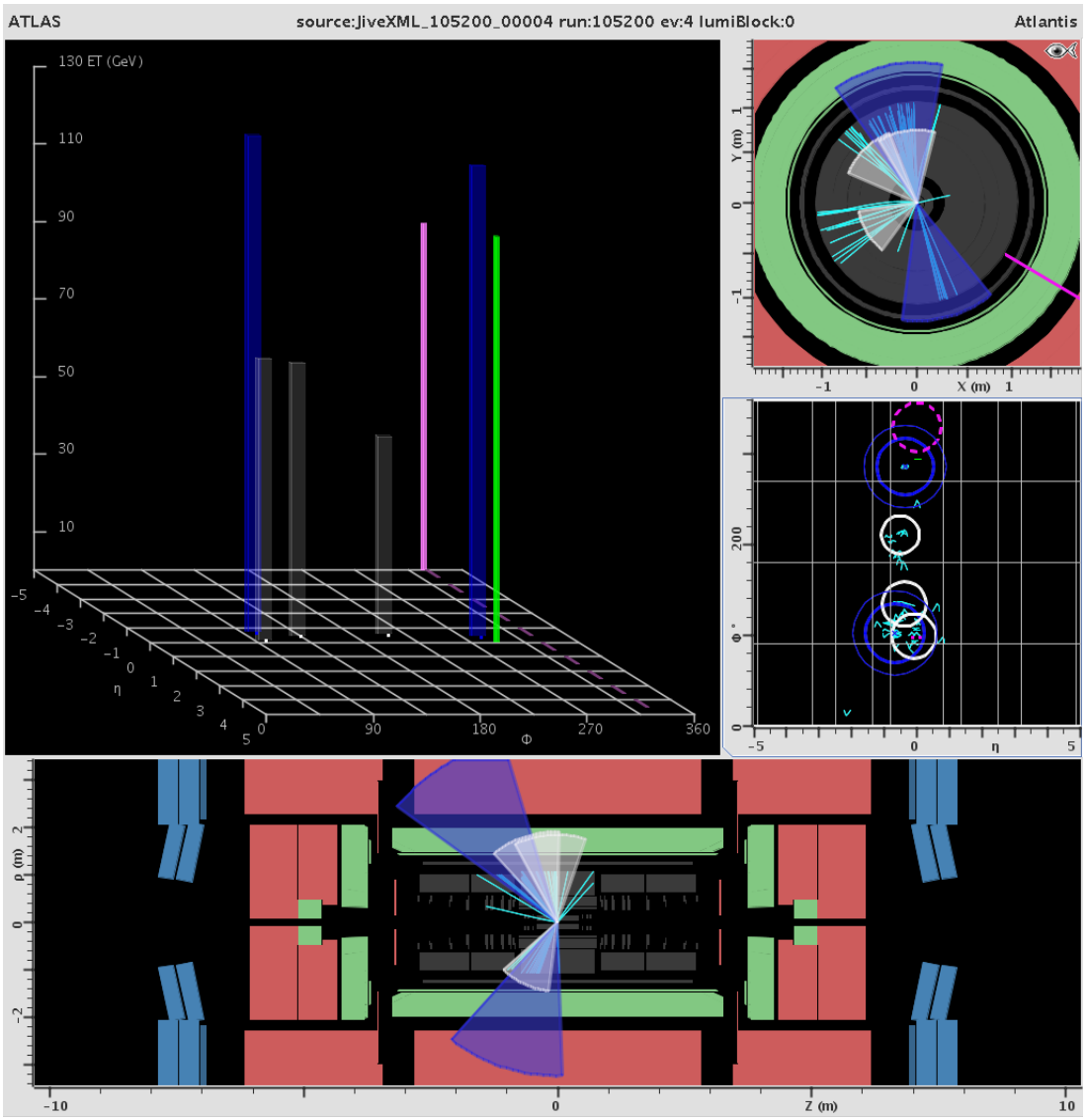

Figure 5.14: Application of the b-tagging colouring function in the lego plot over a semiletopnic simulated $t\bar{t}$ event.

marizes all the work done related with jet b-tagging described in section 5.2.2 and the improvements over the lego plot projection. These upgrades were well received within the collaboration and have been used very often since they were introduced to the Atlantis official release.

In Figure 5.15 recent simulated events are displayed using the improved lego plot and the b-tagging colouring feature. On the left a simulated $t\bar{t}$ event and in the right a simulated event with a Higgs boson decaying to four leptons.

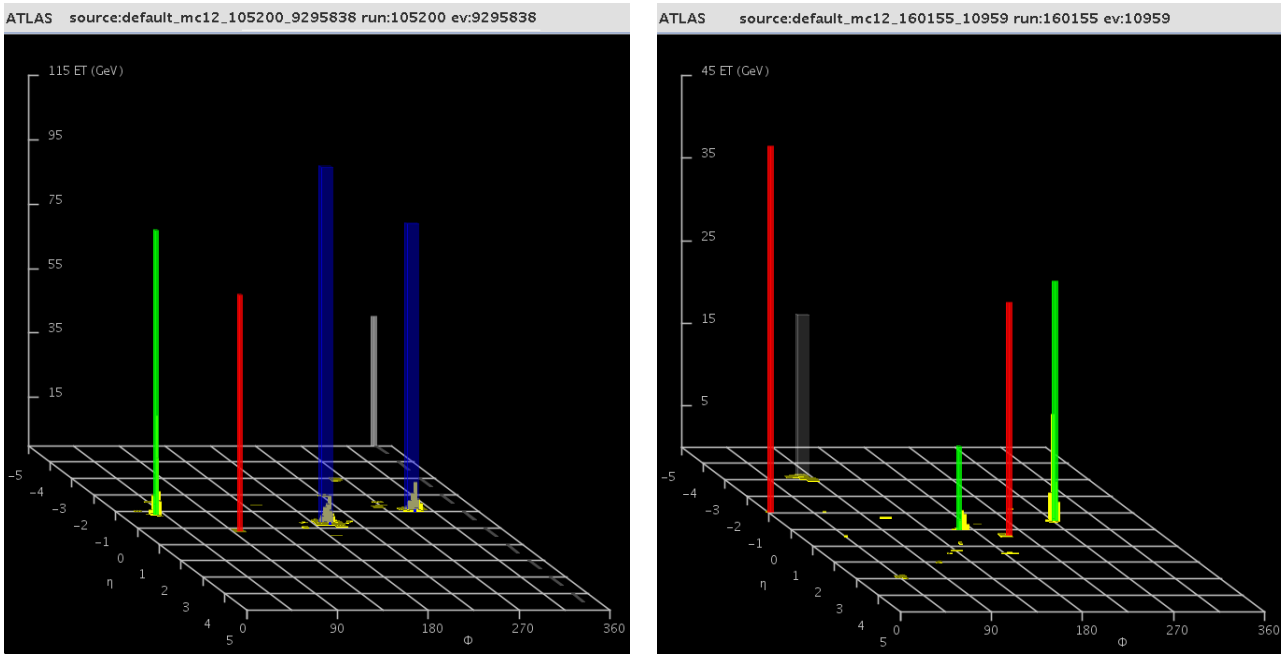

(a) Simulated $t\bar{t}$ event.

(b) Simulated $4l$ Higgs event.

Figure 5.15: Simulated events being displayed to test the upgrades over the lego plot projection and jet colouring by b-jet.

5.2.5 LVL1 Trigger and Jet Elements Towers

For studies involving the L1-Level Electromagnetic Calorimeter Trigger a specific configuration of Atlantis is used with three different versions of the lego plot called "calorimeter views". Each of the three views, shown in Figure 5.16, use towers representing the energy deposits in the calorimeters. The size of the tower elements was initially set to have the same value in the η and ϕ directions for the three views. An additional option was added into the Atlantis GUI so the granularity of jet towers could be modified by the user. If the granularity is very high then the energy deposits are separated in several small towers or "elements" as can be seen in the first view in the left. The granularity is decreased gradually for the view in the middle and in the right respectively, reducing the amount of towers. These feature allows the study of different isolation criteria implemented for this trigger. The resolutions used for the views in the middle and in the right end of the figure are called "LVL1TriggerTower" and "LVL1JetElement" criteria respectively.

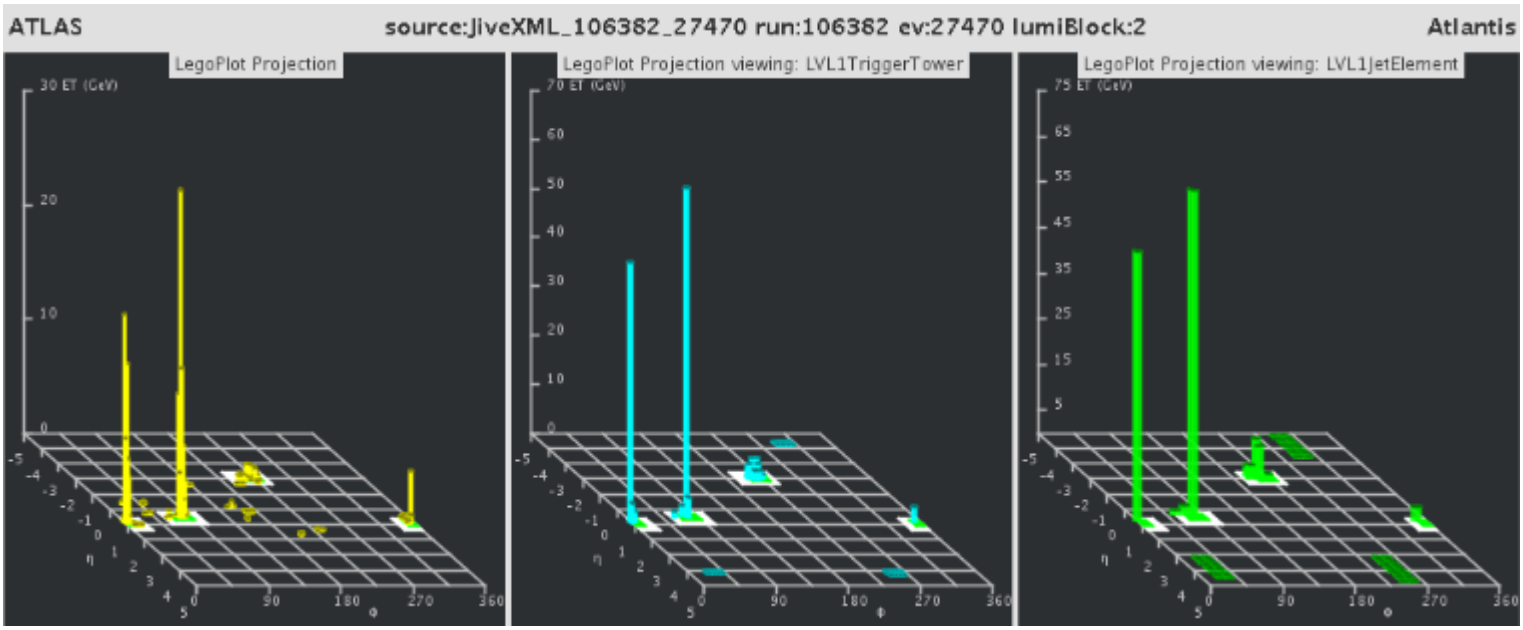

Figure 5.16: The towers sizes in the ϕ and η directions can be modified by the user, so the energy deposits are spread in tower elements with variable granularity.

5.2.6 Colour by Vertex Type Function

The last significant contribution added to the program was the addition of a new colouring option for tracks and vertex objects located within the inner detector. The event vertices are represented in Atlantis with small squares (or circles) and can be seen if one zooms-in enough when using x-y or ρ-z projections.

These vertex objects represent mostly regions where a proton-proton collision took place and several particles were released as a result. One of these reconstructed vertices is categorized as the “primary". When a b-quark hadronises, it generates a jet of particles that orginates in a vertex that is said to be of “secondary” type. These vertices are usually not aligned along the beamline with the rest of the vertices, as the b-quark hadronisation happens just after the collision takes place.

An additional function was created within the program to colour vertex objects by

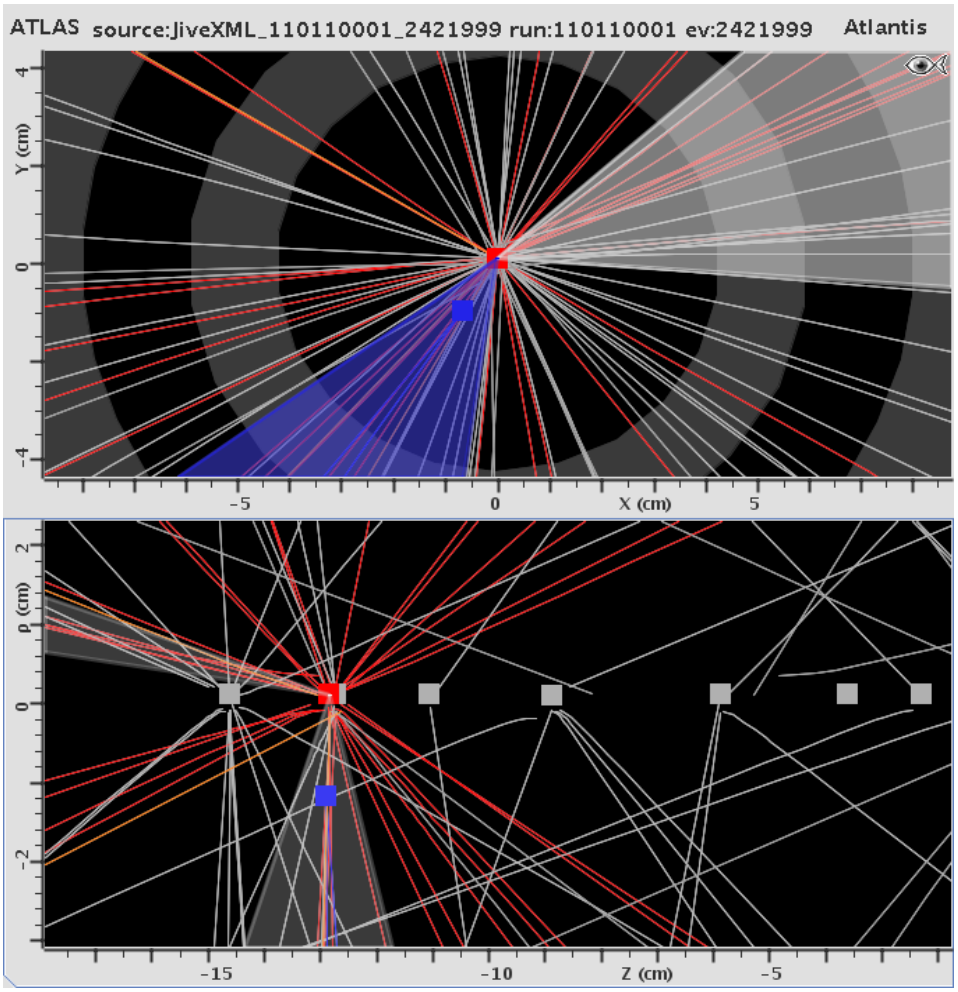

Figure 5.17: Implementation of the colouring of vertex objects and tracks by vertex type feature over a simulated dilepton $t\bar{t}$ event.

type: “primary", “secondary" or any of the remaining vertices with low interest. The chosen colours to represent these different types were red, blue and gray respectively. In Figure 5.17 the display at the top shows the x-y plot of the tracks and two jets that seem to come from a singular point. After zooming-in enough over this region the ρ-z display looks as in the bottom of the figure; the different tracks are actually coming from different vertex points. One of them was categorised as primary with red colour and one of them shifted down with respect all the aligned vertices was tagged as secondary and coloured with blue colour. The rest of them are tagged as vertices of low interest and have been coloured with gray colour.

The user can also colour the different tracks by the type of vertex they are coming from as it is shown in the figure. The jet that was b-tagged seems to be coming

from the secondary vertex and then it is very likely that the b-jet identification was sucessful for this event. These features can be enabled in the GUI by changing the colouring mode of vertices and tracks to the option "by vertex type".

5.3 Projects Under Development

A configuration file within Atlantis sets how the display will look when the user starts the program. It determines which projections and objects will be shown by default and which cuts will be applied over the different physical objects in the event. A particular configuration file is selected by the user when starting Atlantis. The choice depends on which aspects of the events are required to be presented.
A project that is in progress is the generation of a configuration file that could show by default only physical objects without including tracks or hits in the different sub-detectors. These type of displays would be useful to illustrate different processes under interest for the different analyses without showing background tracks or detector hits, especially ideal to display $t\bar{t}$ event candidates.

Another project in progress that has been developed so far by the author is to expand the feature of colouring of vertices and tracks by vertex type described in section 5.2.6, so the user can cut as well tracks and vertices by vertex type. This expansion would allow to show only the vertices of interest and the objects originated from them. A preliminary version of this code has been prepared but is currently under test.

Finally another task under development concerns jet cones, which are currently set to be drawn from a common central point in the x-y and ρ-z projections, but they should be originated from the vertices they are associated with. This upgrade would allow a more realistic display when zooming in enough so the vertex objects in the event are visible.

Chapter 6

Top-Quark Properties

In this chapter the main physical properties that can be measured from top quark decays are discussed focusing on the top quark width. Important features about the top quark, as described in the SM, are reviewed in section 6.1. Section 6.2 introduces $t\bar{t}$ pair production. Results from top properties' analyses from ATLAS during run I are included in section 6.3. Section 6.4 is dedicated to the top quark width and the SM prediction of this parameter is shown. Current limits from analyses performed by the CDF and CMS collaborations with two different methodologies are described.

6.1 The Standard Model Top Quark

$$\begin{pmatrix} d' \\ s' \\ b' \end{pmatrix} = \begin{pmatrix} V_{ud} & V_{us} & V_{ub} \\ V_{cd} & V_{cs} & V_{cb} \\ V_{td} & V_{ts} & V_{tb} \end{pmatrix} \begin{pmatrix} d \\ s \\ b \end{pmatrix} \tag{6.1}$$

According to the SM the top quark is a spin - $\frac{1}{2}$ fermion with electric charge + $\frac{2}{3}$ e (where e is the electron charge). It is the weak isospin parter of the bottom quark and transforms as a colour triplet under the group SU(3) of strong interactions. The SM states that the top quark decays via the electroweak interaction to an on-shell W-boson plus one of the down-type quarks. The up-type quarks: u, c and t decay to the weak eigenstates d', s' and b', which are a combination of the mass eigenstates d, s and b, standing for the down-type quarks. In Equation (6.1) the weak eigenstates

are related to the mass eigenstates via the Cabibbo-Kobayashi-Maskawa (CKM), matrix or quark mixing matrix. The CKM matrix determines the branching rates for the different decays from any of the up-type quarks to any of the down-type quarks.

$$V_{CKM} = \begin{pmatrix} 0.97428 \pm 0.00015 & 0.2253 \pm 0.0007 & 0.00347^{+0.00016}_{-0.00012} \\ 0.2252 \pm 0.0007 & 0.97345^{+0.00015}_{-0.00016} & 0.0410^{+0.001}_{-0.0007} \\ 0.00862^{+0.00026}_{-0.00020} & 0.0403^{+0.0011}_{-0.0007} & 0.999152^{+0.000030}_{-0.000045} \end{pmatrix} \tag{6.2}$$

The numerical values for the CKM matrix elements are shown in Equation (6.2). They are obtained from a global fit that uses several theoretical and experimental results [64], the squared values of the three terms on the bottom row of the matrix $|V_{td}|^2$, $|V_{ts}|^2$ and $|V_{tb}|^2$ are proportional to the rate of decay of the top quark into the d, s and b quarks. It is possible to conclude from the numerical values in the matrix that according to the SM the top quark decays almost exclusively (with a rate equal to ~ 99 %) to a W-boson + b-quark.

A deviation from these predicted rates for top decays could indicate beyond the SM processes involving contributions from unobserved heavier quarks. Some possible extensions of the SM allow V_{td} to have smaller values than that predicted by the SM [86] as processes producing a charged Higgs via top decays like t $\rightarrow$ b H^+ are allowed. However recent searches for charged Higgs bosons show no deviations from the SM predictions [66]. Also exclusion results from the search of heavier generations of particles [67] support that this matrix should indeed be 3×3.

Due to its large mass and small lifetime the top quark is involved in very fundamental phenomena like the electroweak symmetry breaking [60] that separated the electroweak unified force into two separated forces, the weak and the electromagnetic. It is also involved in fundamental processes associated with possible extensions of the SM as has been already mentioned. It is then crucial to measure precisely all the properties of the top quark.

6.2 $t\bar{t}$ Pair Production and Decays

Top quark pair $t\bar{t}$ decays are used to study different processes and observables constrained by the SM. The LHC experiments have already collected an unprecedented amount of data as the production cross sections of the different processes increases with the pp collision energy as was shown in Figure 2.7. So far the different studies performed during run-I at the LHC with collision energies at 7 and 8 TeV have given results in agreement with the SM predictions. Several analyses will be reproduced during run-II with a collision energy equal to 13 TeV. In run-II even higher statistics will be obtained and results will be more precise as the sources of systematic uncertainty will be understood better.

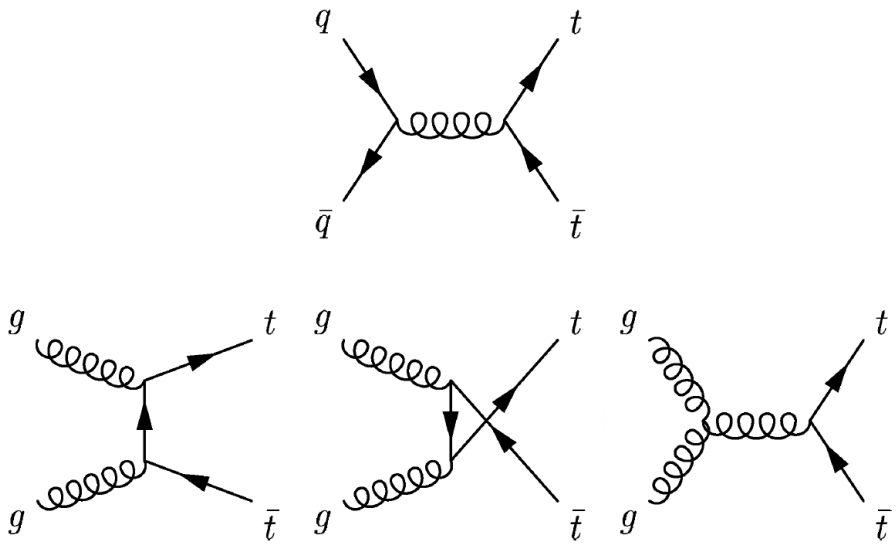

Figure 6.1: $t\bar{t}$ production Leading Order (LO) Feynman Diagrams: from $q\bar{q}$ annihilation in the upper diagram and gluon-gluon fusion in the lower diagrams.

Figure 6.1 displays the Feynman diagrams corresponding to proceses contributing at Leading Order (LO) approximation to $t\bar{t}$ production. The diagram at the top accounts for q-$\bar{q}$ annihilation while the three diagrams at the bottom correspond to gluon-gluon fusion processes giving rise to a $t\bar{t}$ pair. As explained in section 2.5 at the LHC (collision energies $\geq$ 7 TeV) $t\bar{t}$ production via gluons is much more likely

to happen (with a rate $\sim 90\%$) as described in section 2.5.

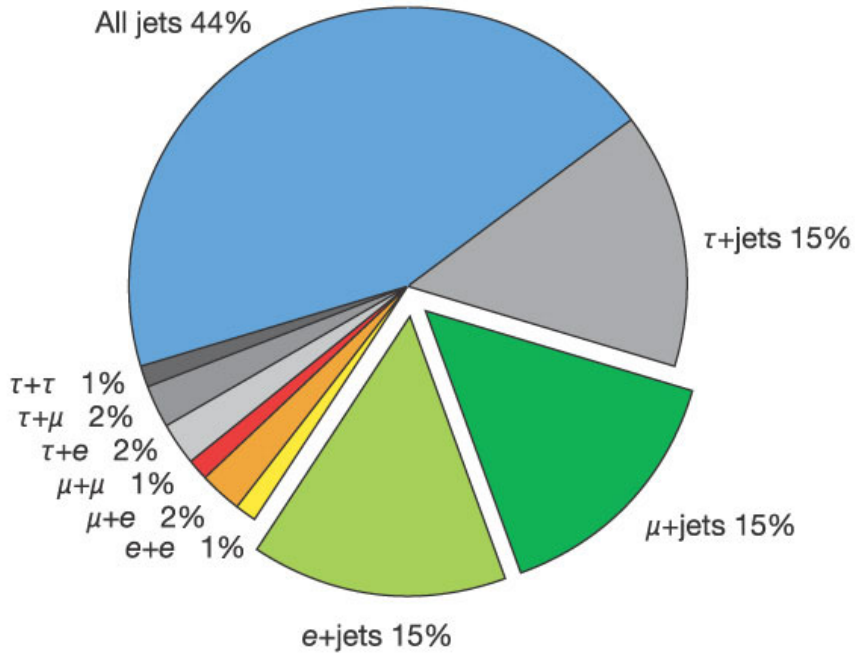

Figure 6.2: Diagram displaying the different categories for $t\bar{t}$ decays. All Jets channel and Lepton + Jets share a rate value of $\sim 44\%$ while the Dilepton channel has a branching ratio $\sim 11\%$. From [62].

Figure 6.2 shows the different channels for $t\bar{t}$ decays and the relative decay rates. These channels are set considering that each top quark decays to a b-quark and a W-boson. The W-boson can decay to a quark-antiquark pair which is known as *hadronic* decay, or can decay to a lepton + neutrino pair: a neutrino and an a up-type lepton (electron, muon or tau). In the hadronic decay of W, the quarks will manifest themselves as jets of particles. The diagram shows that in ~ 45 % of the events the two W-bosons decay hadronically, ~ 10 % of the decays are dileptonic and ~ 45 % are semileptonic where one of the W's decays hadronically and the other leptonically. Though the all-hadronic or "all jets" channel has a large branching ratio, it is challenging to use these events as it is difficult to assign each jet to the correct initial quark. Dileptonic events on the other hand can be selected and reconstructed easily as they have two leptons with two different electric charges

with different signs but the branching fraction for this channel is the smallest. The semileptonic channel has a large rate (same as hadronic channel), but it has both, a hadronic and a leptonic side which is a good discriminant for the event selection against backgrounds. For the selected events in this channel there should be at least 4 jets accounting for the 2 b-quarks and 2 light quarks from the W-boson decay plus one up-type lepton with a neutrino from the other W-boson decay. With proton collisions at 8 TeV and a collected integrated luminosity ~ 20.3 fb^{-1} (ATLAS record), ~ 4.8 M $t\bar{t}$ events are expected to be produced, of which ~ 1.4 M are semileptonic events (with an electron or muon).

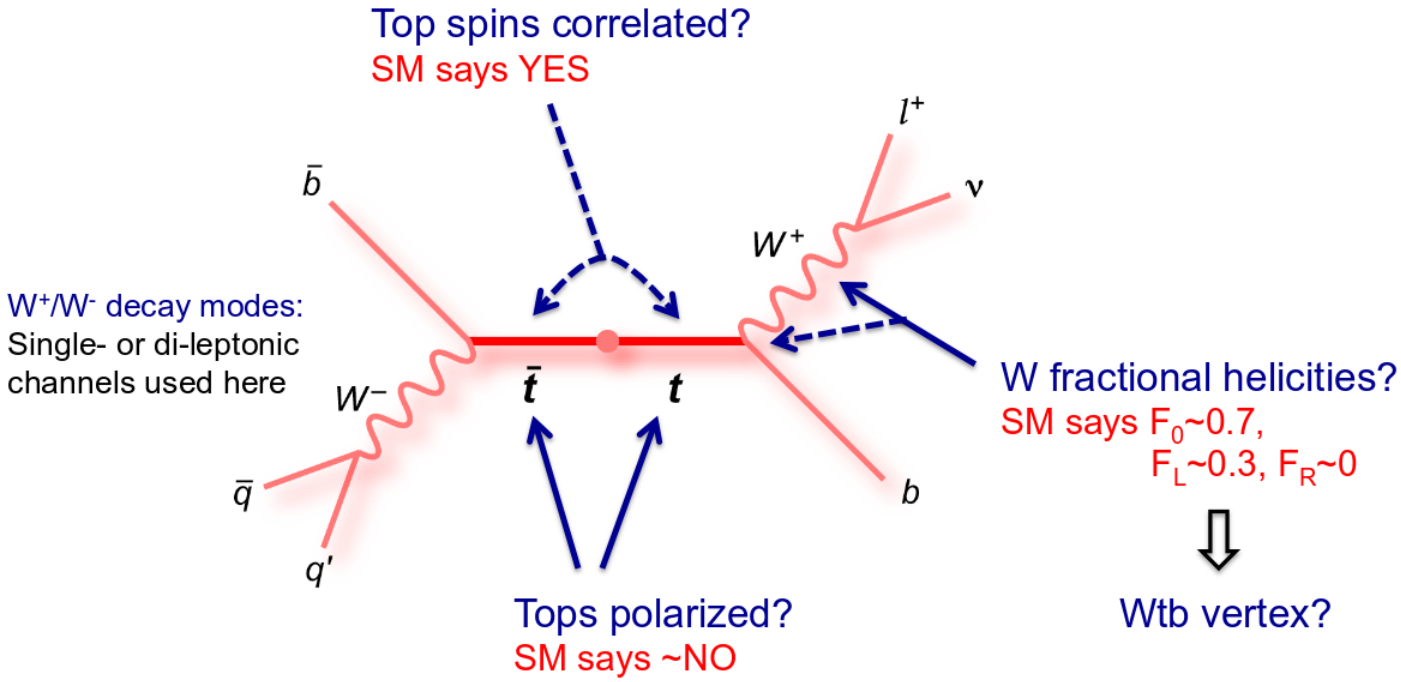

Figure 6.3: Different properties that can be studied with $t\bar{t}$ events, From [73]

6.3 Top Properties Measurements from $t\bar{t}$ Decays at ATLAS

Different properties can be measured from $t\bar{t}$ processes as illustrated in the diagram in Figure 6.3, where a $t\bar{t}$ diagram is shown including the main decay products and some of the main variables that can be studied. One of the properties whose mea-

surement puts under test the SM is the degree of spin correlation between the two top quarks in the event. The degree of spin correlation in $t\bar{t}$ pairs is defined as in Equation (6.3), where the different terms represent the number of events where the spins of the top and antitop quarks are in the same or opposite direction. The direction of motion of the top quark in the $t\bar{t}$ rest frame is used as the reference axis. The SM predicts a degree of spin correlation of $A_{SM} = 0.31$ at NLO accuracy in p-p collisions at 8 TeV.

$$A = \frac{N_{\uparrow\uparrow} + N_{\downarrow\downarrow} - N_{\uparrow\downarrow} - N_{\downarrow\uparrow}}{N_{\uparrow\uparrow} + N_{\downarrow\downarrow} + N_{\uparrow\downarrow} + N_{\downarrow\uparrow}} \tag{6.3}$$

In the plot in the left of Figure 6.4 it can be seen the latest result obtained by ATLAS in agreement with the SM using the full 8 TeV data set. For this analysis the dilepton channel was selected due to its high purity. The $\Delta\phi$ distribution between the two event leptons is sensitive to different values of the spin correlation and the measured variable is the fraction of the predicted SM spin correlation, f_{SM}. The final result is $f_{SM} = 1.2 \pm 0.05$ (stat.) $\pm$ 0.11 (syst.) including the SM prediction at 95 % C.L. [74]

The polarisation state of the W-boson is defined by the value of the coefficients (F_R, F_L, F_0) in Equation (6.4), where F_R, F_L and F_0 are known as *helicity fractions*. θ^* in the equation is the angle between the event lepton and its corresponding parent top in the W-boson rest frame. Therefore the semileptonic and dileptonic channels can be used. The equation sets the probability distribution of this angular variable.

$$\frac{1}{N}\frac{dN}{dcos\,\theta^*} = \frac{3}{4}sin^2\theta^* F_0 + \frac{3}{8}(1 - cos\,\theta^*)^2 F_L + \frac{3}{8}(1 + cos\,\theta^*)^2 F_R \tag{6.4}$$

The helicity fractions are the parameters of interest for this analysis and their values are predicted by the SM. For this measurement the $\cos\theta^*$ distribution with variable helicity fractions is fitted to the observed data, to obtain a set of measured helicity fractions. The plot in the right of Figure 6.4 shows the result of this analysis

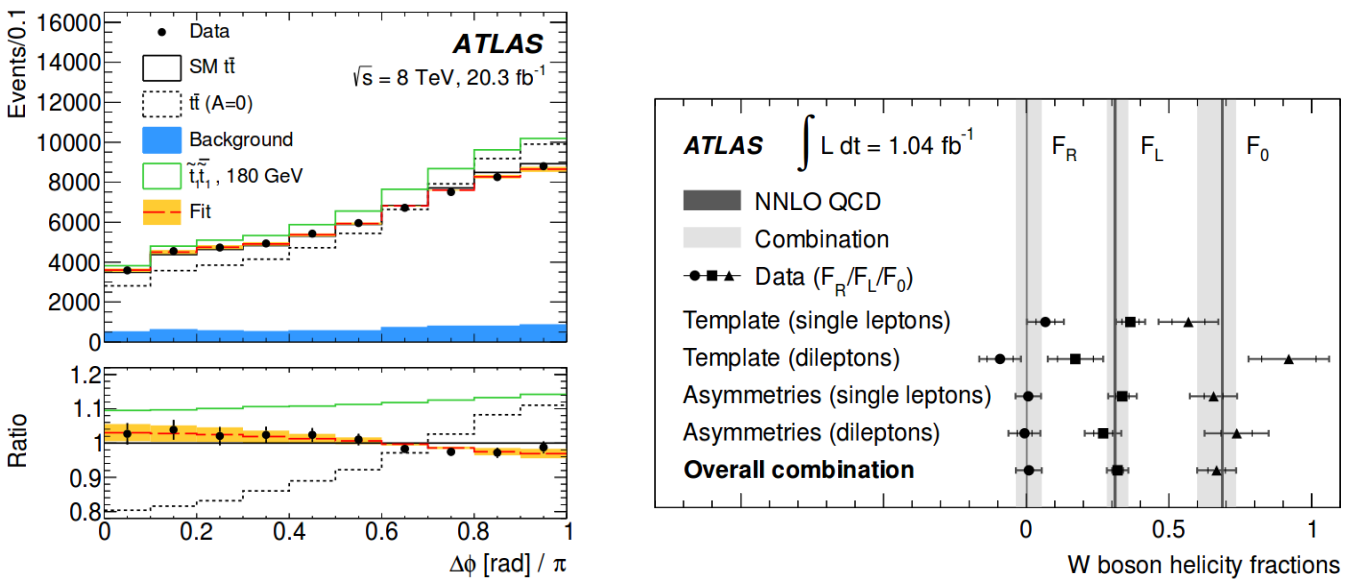

Figure 6.4: Final fit of the data $\Delta\phi$ distribution to templates with different f_{SM}, From [74] (left) and results for helicity fractions describing polarisation of W-boson, From [75] (right).

using fraction of the 7 TeV data with two different methods and displaying the overall combination, which converges for the three parameters to the SM prediction [75].

The top quark is the heaviest known fundamental particle; it is $\sim$ 35 times more massive than the second most massive quark, the b-quark. Its mass is a parameter of great interest in particle physics as it can be used to constrain the possible Higgs mass values within the SM expectation and some other fundamental processes. The evolution of the measured m_{top} from different published analyses is displayed in figure 6.5, where two results published by ATLAS with the l + jets and all jets channels respectively are shown [77], [78], having the lastest one the smallest systematic uncertainty. The current overall world's combination is 173.34 $\pm$ 0.95 GeV and there is a recent combination from Tevatron experiments equal to 174.34 $\pm$ 0.64 GeV that uses the full data set collected by the CDF and DØ experiments and should affect the world's combination slightly.

The top quark has a lifetime of $\sim 5 \times 10^{-25}$ s, smaller than the time it takes for a quark to *hadronise*, therefore several properties of this heavy quark can be measured, as its properties are transferred directly to its decay products.

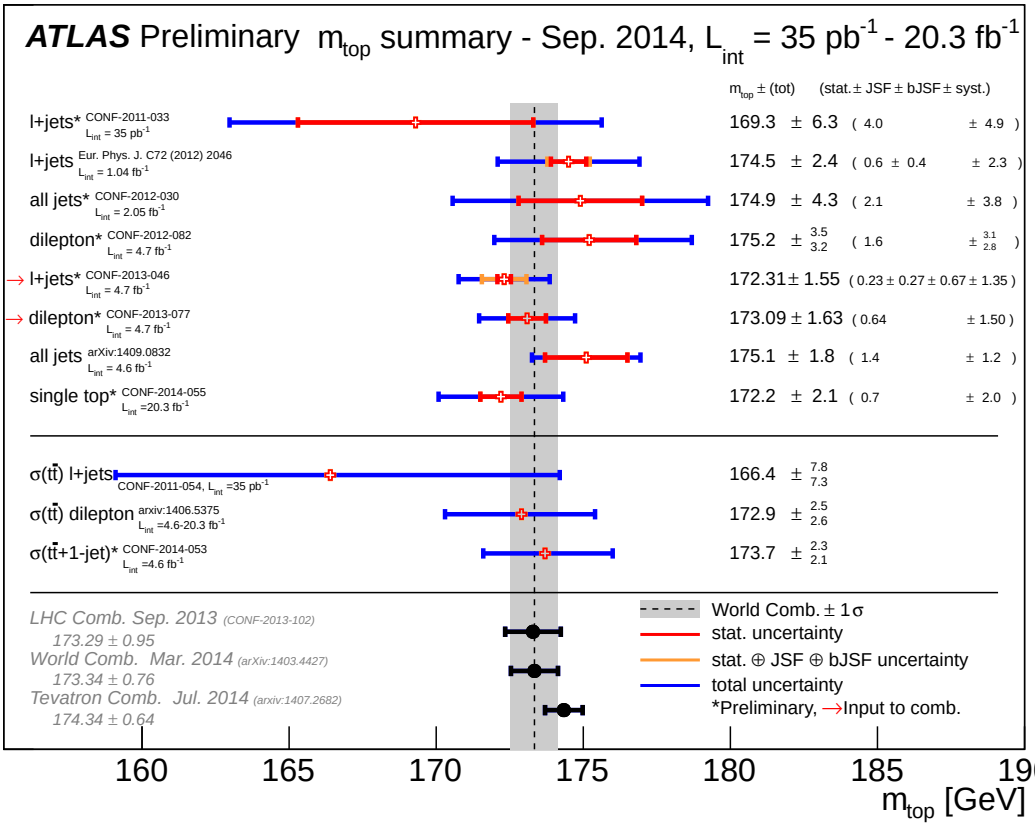

Figure 6.5: Recent evolution of top mass measurements, From [76]

Asymmetries associated with the difference between the top and antitop mass and electric charge can be measured. So far ATLAS has obtained results in agreement with the SM expectations [79], [80]. More analyses are still in progress using $t\bar{t}$ decays, to measure at 8 TeV the $t\bar{t}$ cross section and the degree of CP violation, test several color flow models and to search for $t\bar{t}$ resonances.

6.4 The Top Quark Width

6.4.1 Standard Model Prediction

A measurement of m_{top} and top width (Γ_{top}) with high precision puts under test the SM. The top mass and width are introduced in the theory through the position of the single pole m^*_{top}:

$$m^*_{top} = m_{top} - i\frac{\Gamma_{top}}{2} \tag{6.5}$$

in the perturbative quark propagator [63]. m_{top} appears in the *top yukawa coupling*, $y(\mu)$ shown in Equation (6.6), where μ is the measured signal strength of the Higgs boson mass distribution. $y(\mu)$ determines the SM behaviour of the Higgs coupling to the top quark with the signal strength for a specific Higgs mass value M_h.

$$y(\mu) = 2^{3/4} G_F^{1/2} m_{top}(1 + \delta_t(\mu)) \tag{6.6}$$

where $\delta_t(\mu)$ accounts for radiative corrections [69] and G_F is the Fermi constant. At next-to-leading order (with QCD and electroweak corrections and with aproximately 1 % of precision) the relationship predicted by the SM between the top width Γ_{top} and m_{top} is shown in equation (6.7) [70]. In the left of Figure 6.6 this relationship is plotted for a range of m_{top} values from 170 to 175 GeV, corresponding to a variation in Γ_{top} from 1.27 to 1.41 GeV. For a mass value equal to 172.5 GeV, which is used as input default m_{top} for most of the simulations that involve top production, there is an associated width of 1.33 GeV, which is regarded as the SM prediction. With the increase in the precision in the m_{top} measurements, it is natural to consider the Γ_{top} measurement as a cross-check of this SM predicted relationship. However the precision achieved for Γ_{top} measurements has been much lower.

$$\Gamma_{top}(m_{top}) = \frac{G_F m_{top}^3}{8\pi\sqrt{2}} \left(1 - \frac{m_W^2}{m_{top}^2}\right)^2 \left(1 - \frac{2m_W^2}{m_{top}^2}\right) \left[1 - \frac{2\alpha_s}{3\pi}\left(\frac{2\pi^2}{3} - \frac{5}{2}\right)\right] \tag{6.7}$$

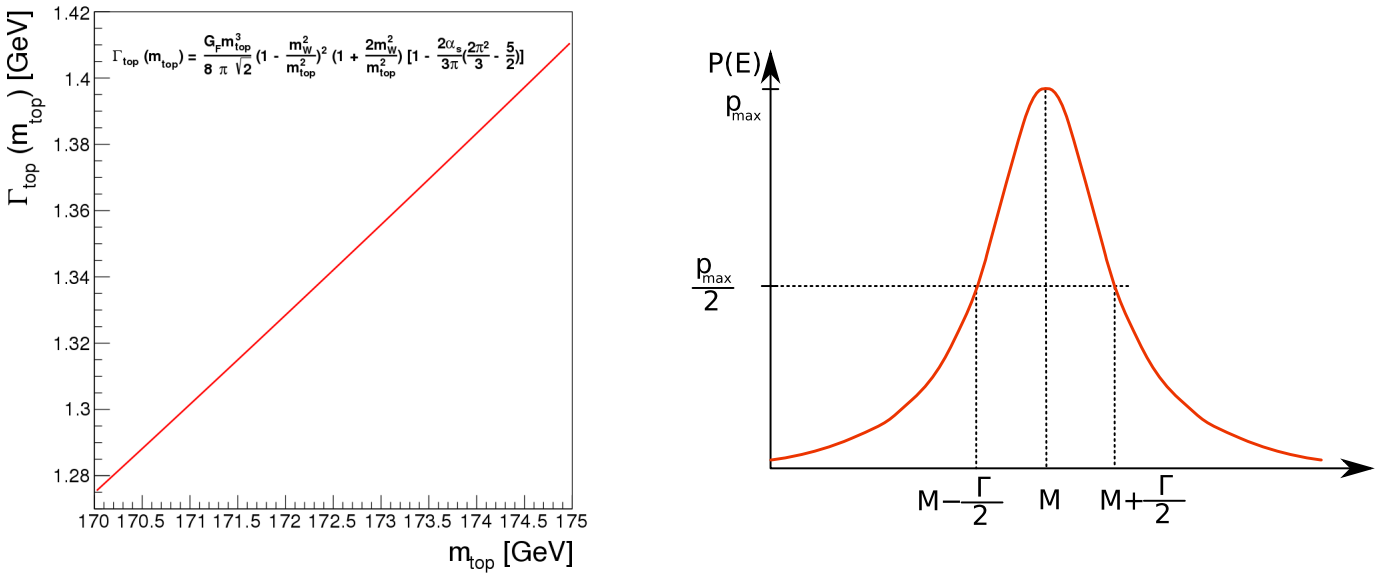

Figure 6.6: Relationship between Γ_{top} and m_{top} predicted by the SM (left), from [71] (left), shape of the m_{top} Breit-Wigner resonance with half width $\frac{\Gamma_{top}}{2}$ at truth particle level (right), From [64].

The measurement of Γ_{top} ensures that the modelling of the top quark production in the Monte Carlo simulations is reasonable [71]. At truth particle level without any radiation or detector effects, the shape of the m_{top} resonance looks like the plot in the right of Figure 6.6. This resonance is usually modelled with a relativistic Breit-Wigner shape with mean at m_{top}, and where the width of the curve is directly associated with Γ_{top}. According to the Heisenberg uncertainty principle, Γ_{top} is related to the top-quark lifetime (τ) by the relationship shown in Equation (6.8):

$$\Gamma_{top} = \frac{\hbar}{\tau_{top}} \tag{6.8}$$

An indirect measurement of the top lifetime τ_{top} which is expected to have the smallest value for all fermions can be obtained by measuring Γ_{top}. Another reason why a measurement of Γ_{top} is important is that all the fundamental particles are lighter so

there could be a chance that the top decays into any of them. A deviation from the SM prediction could indicate the presence of beyond the SM decay channels with perhaps non-standard couplings. This might show up anomalies in the top quark production and decays, such as decays through a charged Higgs boson, through supersymmetric top quark partner (stop s-quark) [74] or via flavor changing neutral currents [86].

6.4.2 Current World's Benchmark Limits for Γ_{top}

The Fermilab collaborations CDF [81] and DØ [82] have measured Γ_{top} following two different methodologies which are briefly explained in this section. The CMS collaboration at CERN has published the first result from LHC experiments [72] using a similar technique to the one used by the DØ collaboration. All the reported current limits for Γ_{top} are in agreement with the theoretical expectation.

6.4.2.1 Direct Measurement of Γ_{top}

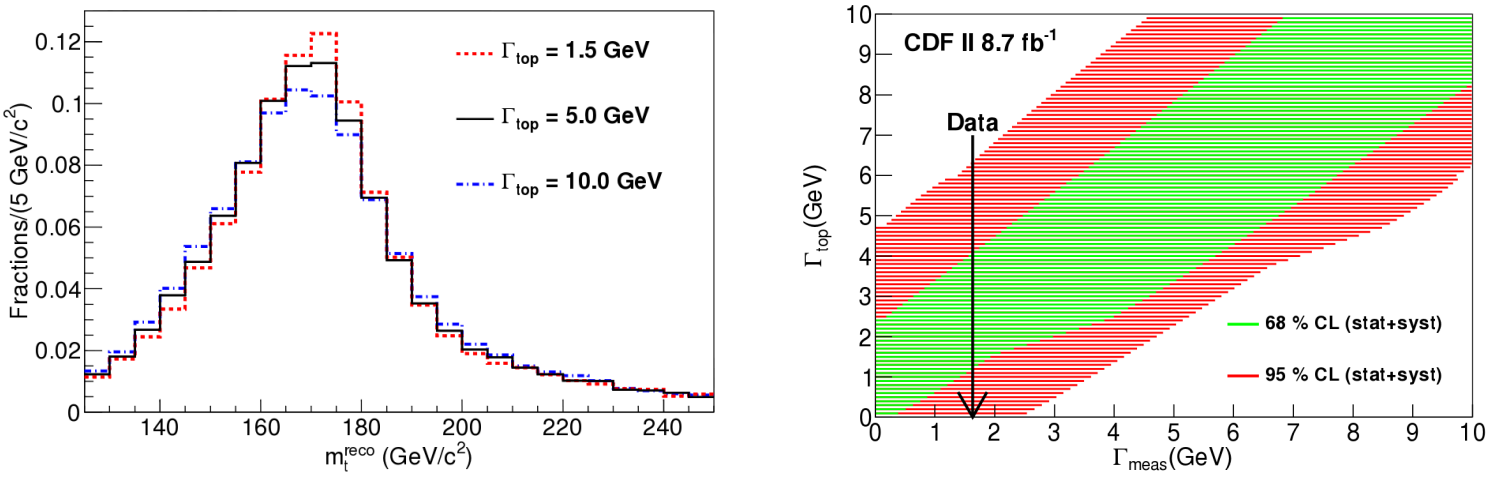

Figure 6.7: m_{top}^{reco} distribution for different values of Γ_{top} in the simulation (left), summary of statistical + systematic uncertainties for different values of Γ_{top} (right). From [68]

The CDF collaboration has measured Γ_{top} using the m_t^{reco} variable [68] plotted on

the left of Figure 6.7 where this variable is shown for Γ_{top} values of 1.5, 5.0 and 10 GeV. From the plot it is possible to see that the variation of the width has a small effect on the distribution, which produces large statistical and systematic uncertainties. The plot on the right shows the uncertainties obtained for a range of Γ_{top} values from 0 to 10 GeV. The measured Γ_{top} value with the observed data is shown with the vertical arrow.

The CDF result can be summarized as $1.10 < \Gamma_{top} < 4.05$ GeV at 68 % confidence level and $\Gamma_{top} < 6.38$ GeV at 95 % confidence level. The analysis presented in this thesis uses a similar technique and more detailed information about this method is included in the following two chapters.

6.4.2.2 Indirect Measurement of Γ_{top}

In the indirect approach the measured and theoretical cross-sections of the single top production mechanism W + $b \rightarrow t$ (an example diagram is shown on the left of Figure 6.8 below), are combined with measured variables from $t\bar{t}$ decays. This method relies on there being no contributions from new processes to the top decays apart from $t \rightarrow$ W + q processes, where q stands for any of the down-type quarks (d, s or b). This approach is actually centred on the measurement of the branching fraction R shown in Equation (6.9) below in $t\bar{t}$ decays, preferably with the dilepton channel as it is possible to achieve the highest degree of purity:

$$R = \frac{B(t \rightarrow W + b)}{B(t \rightarrow W + q)} \tag{6.9}$$

where the denominator includes a sum over all the decays of the top to down-type quarks and this is expected to have a value close to one. On the right of Figure 6.8 is the summary of the measurement of the R ratio from CMS collaboration performed with the $t\bar{t}$ dilepton channel. For this analysis the b-tagged jet multiplicity

distribution from data is fitted to templates produced using different values of the parameter R, which is a free parameter in the simulation. This distribution is obtained by counting how many jets per event are likely to have originated from a b-quark produced in the hard scattering (see object definitions in chapter 7). The dilepton channel is used as in these events the $t\bar{t}$ pair decays to two leptons, which can be either an electron or muon, two neutrinos and two b-quarks, so the jets that are found in the event are very likely to have originated from a b-quark. Once the measured value is obtained a similar procedure to what is described in the previous sub-section is followed to set limits on the R parameter. The result from CMS is R = 1.0114 ± 0.003 (stat.) ± 0.032 (syst.) and requiring R ≤ 1, a lower limit R > 0.955 at 95 % C.L. and a corresponding lower limit on the CKM matrix element $|V_{tb}| > 0.975$ are obtained. Measurement of R with $t\bar{t}$ decays is combined with the single top-quark cross-section measurement to obtain an indirect measurement of Γ_{top} following SM formula:

$$\Gamma_{top} = \frac{\sigma_{t-channel}}{B(t \to W + b)} \times \frac{\Gamma_{th}(t \to W + b)}{\sigma^{theory}_{t-channel}} \tag{6.10}$$

where the $\sigma_{t-channel}$ is the measured single top cross section that can be extracted from the most recent CMS measurement [85] and $\sigma^{theory}_{t-channel}$ is the theoretical prediction of the single top cross section and is taken from [83]. According to the SM, for a top quark mass of 172.5 GeV, the partial decay width $\Gamma_{th}(t \to W + b) = 1.329$ GeV. This is the point where it is assumed that $\sum_q$ B(t → W + q) = 1 which leads to R = B(t → W + b). Then R can be written in terms of Γ_{top} and a new fit can be performed using the latter as a free parameter. The result from CMS is Γ_{top} = 1.36 ± 0.02 (stat.)$^{+0.14}_{-0.11}$(syst.) GeV in agreement with the theoretical expectation and with a previous result from DØ using a similar procedure [82].

From these two results it is possible to conclude that a more precise measurement is obtained from the indirect approach. However this method relies on the assumption that $\sum_q$ B(t → W + q) = 1, not allowing additional processes beyond the SM pre-

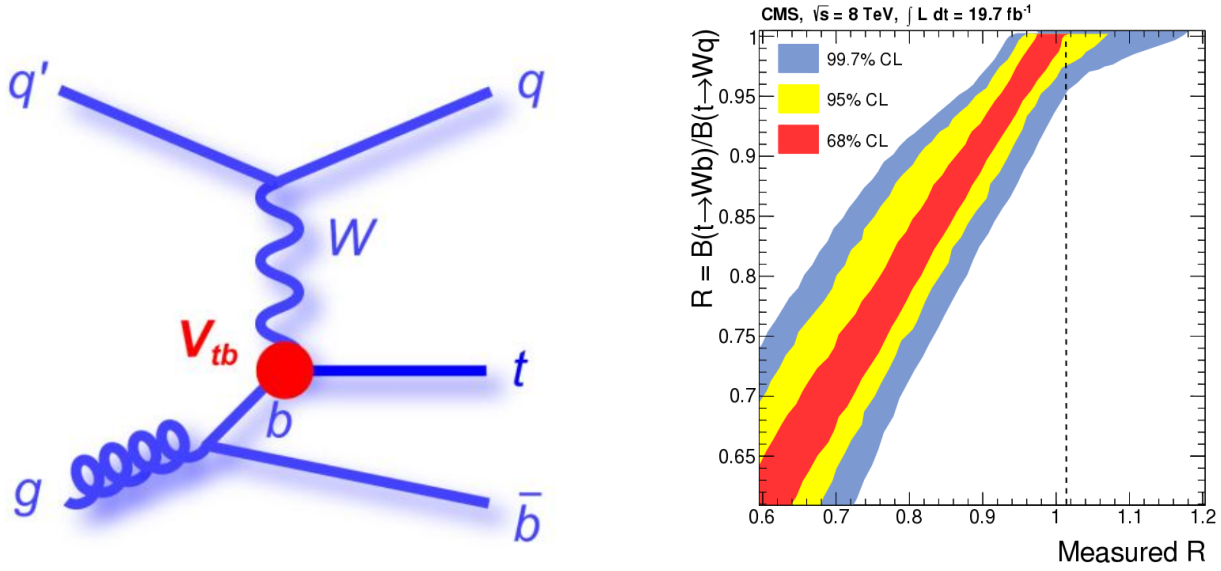

Figure 6.8: Example of single top quark production diagram (left) and confidence limits for different input values for the measured variable R by CMS (right), From [72].

dictions. The direct approach on the other hand does not rely on any assumption, but the small effect of the variation of the top width over the distribution used for the measurement gives very large uncertainties.

Chapter 7

Event Selection and Analysis Techniques

In this chapter the procedures involved in the different stages of the analysis are outlined, with final uncertainties and measurements being shown in chapter 8. Computing tools and packages used throughout the analysis are mentioned in section 7.1. Definition of physical objects from proton-proton collisions are included in section 7.2. Data and simulation are explained in sections 7.3, 7.4 and 7.5. The analysis comprises: event selection (section 7.6), studies at truth level and the production of templates (section 7.7), event reconstruction techniques including detector effects (section 7.8), fitting techniques to extract the parameter of interest Γ_{top} and computation of statistical and systematic uncertainties (section 7.9). Finally in section 7.10 an alternative strategy that includes fitting to a second parameter, the Jet Energy Resolution (JER), is briefly explained. A brief summary is included at the end of the chapter.

7.1 Analysis Tools

The `ROOT` interactive analysis framework [99] was used throughout all the analysis work presented in this thesis. `ROOT` provides several tools to store, process and analyse the selected events from the MC simulations and from the actual data from collisions at the LHC. It also offers an environment to perform a huge variety of mathematical calculations and produce instructive plots from the selected events. This package has the convenient feature that is written as a library of the `C++`

programing language which allows interfacing with other useful packages such as `RooFit` [127], [129] which offers a wide range of tools to perform statistical calculations. These are used to compute the analysis uncertainties, described in more detail in section 7.7.

Data and simulation events were initially processed using a package generated within the Top Physics group in the ATLAS collaboration known as `AnalysisTop version 1.8.0`. This is a software package used in all the top physics analyses in ATLAS to make easier the matching in yields for selected events for the common part of the selection shared between the different analyses.

Final stages of the selection were processed using another package widely used for physics analyses known as `SFrame` (A ROOT data analysis framework) [133], which is completely compatible with the `ROOT` environment. With `SFrame` the author developed and implemented the event reconstruction, producing distributions of general kinematic variables and also variables sensitive to the top quark width, Γ_{top} parameter, described in section 7.8.

Additionally the author created a suite of `C++` programs to analyse events after the final selection. These programs are implemented from within `ROOT` and `RooFit`.

To process the data and simulation samples with the above mentioned AnalysisTop sofware the CERN grid service known as `LXPLUS` [135] was used mostly through the Job Execution and Definition Interface, (JEDI). This interface allows CERN users to submit several tasks using the power of different computing grids located around the world. This interface was mostly used for the standard part of the event selection common for most top physics analyses within the collaboration. For these computing facilities, the SLC6 (Scientific Linux CERN 6) operating system is used. These facilities were also used to store temporarily processed events, to run auxiliary software to produce event displays and to compute some of the systematic uncertainties.

The Particle Physics group at University of Birmingham provides as well to all its postgraduate students with an efficient computing facility, known as `eprexa` and `eprexb`, which uses the `Fedora-20` operating system. Through this facility it is possible to execute intensive jobs efficiently, producing output files that can be easily manipulated locally. This local system was used to perform the event reconstruction, calculation of the analysis uncertainties and the final measurement.

Additional packages were used throughout the analysis such as `LHPDF` [134] which allows the calculation of the systematic uncertainty accounting for Parton Distribution Funtions (PDF), described in the following chapter.

7.2 Object Definition

Physical objects are the elements present in each of the selected events from proton-proton collisions that are used for the analysis. The objects are reconstructed following the definitions outlined in this section. The definitions include: Muon, Electron, Jet, Missing Energy and b-Jet. These definitions are standardized throughout the ATLAS Top Group for the different analyses. The correct implementation of the different definitions results in agreement in yields for the selected events in data and simulation between the different analyses. Such comparisons of event yields with other internal analyses for observed data and simulation were performed to cross-check that the final selected events were chosen properly.

7.2.1 Muons

Muon identification is performed online at the trigger level and also offline using reconstruction algorithms and appropriate selection requirements. For this analysis muons are required to have passed additional offline selection. The offline algorithm used to reconstruct muons is called `muid` and the selection criteria are those set by the ATLAS Muon Combined Performance (MCP), group:

- Muons are required to be within the detector acceptance $-2.5 < \eta < 2.5$
- Muons are required to have $p_{\mathrm{T}} > 25$ GeV, a momentum range with high single trigger muon efficiency
- Muons are required to pass special inner detector quality cuts set by the MCP group, such as requiring that the muon object has an associated track in the ID that has produced > 0 hits in the pixel detector and > 4 hits in the SCT
- In order to be associated with the primary vertex, muons are required to have a z_0 value (defined in section 4.1) < 2mm.
- A mini isolation criteria is required; for tracks with a ΔR distance (Equation 4.2) from the muon $\Delta\mathrm{R} < 10/p_{\mathrm{T}}^{\mu}$, the sum of the tracks' p_{T} divided by the transverse momentum of the muon should be < 0.05
- Any jet with $p_{\mathrm{T}} > 25$ GeV is required to have a ΔR distance from the muon > 0.4

Also the selected muons should match the associated online trigger objects, which were reconstructed by online algorithms. The efficiency of the algorithms and the selection has been measured in Z-boson events (i.e. $\mathrm{Z} \to \mu\mu$ events). From these studies, additional scale factors have been obtained to correct the simulated reconstruction and a propagation of the systematic uncertainties over the muon reconstruction has been provided by the ATLAS top group for the use in the different analyses.

7.2.2 Electrons

In a similar way electron identification has trigger and offline level components which should match each other. Electrons are reconstructed in the central region

using energy deposits in the EM calorimeter associated with tracks in the inner detector. As with the muons there are some additional requirements:

- Energy deposits used for the reconstruction are required to be $|\eta| < 2.47$ excluding the transition region between $1.37 < |\eta| < 1.52$ (section 4.4.1)
- Transverse momentum of the reconstructed object is required to satisfy $E_{\mathrm{T}} > 25$ GeV which is defined as the energy of the cluster over $\cosh(\eta_{track})$ where η_{track} is the pseudorapidity associated with the matched track in the inner detector
- Energy deposits in the EM calorimeter should satisfy an isolation criteria called `tight`$^{++}$. It involves calorimeter and inner tracker selection cuts. Further cuts are applied over combined variables containing information from the tracker and the calorimeter, which improve the identification between electron and jet energy deposits in the calorimeter
- Additional isolation criteria are required for electrons that constrain the separation of the tracking and calorimeter hits in the η-ϕ plane. This requirement helps to suppress the QCD multijet background.

Also an *overlap removal* procedure is performed; the jet closest to the electron within a $\Delta\mathrm{R} < 0.2$ radius is removed from the event. If another jet with $p_{\mathrm{T}} > 20$ GeV is found to be within a radius $\Delta\mathrm{R} < 0.4$ the electron is rejected. In the same way as with muons, the efficiency of the isolation and selection criteria is tested with $\mathrm{Z} \rightarrow ee$ events and then the correction scale factors are applied to the MC reconstruction.

7.2.3 Jets

Jets are recontructed with the anti-k_t algorithm [100] which uses topological clusters from energy deposits in the calorimeters. Clusters are classified as electromagnetic or hadronic and by degree of isolation, energy density and depth of the deposits within the calorimeters. Jets are calibrated by using MC simulation and applying

extra corrections from data. Also a Jet Vertex Fraction, (JVF) cut is applied to remove jets generated from errors in the detector hardware or clusters originating from LHC beam gas interactions, and showers induced by cosmic rays.

7.2.4 Missing Energy

Transverse Missing Energy, ($E_{\mathrm{T}}^{\mathrm{miss}}$) or MET, reconstruction uses energy deposits from the calorimeters, hits from the muon spectrometer and track information from the inner detector (section 4.1). The energy deposits in the calorimeters are usually associated with a physical object like a jet or an electron, however deposits not associated with any objects are tagged as soft contributions. Uncertainties over MET rely on the resolution of the different variables associated with the different physical objects.

7.2.5 B-tagging

All jets in the selected event are passed through a b-tagging algorithm known as MV1 b-tagger [101], which takes the weights from three different algorithms known as JetFitter, IP3D and SV1 [102] and the jet p_{T} and η values as inputs to a multivariable discriminant algorithm to determine a final b-tagging weight value that is used to discriminate b-jets with certain efficiency. The input weights are obtained individually focusing on either reconstructing the secondary vertex where the b-jet is supposed to originate or focusing on analyzing the impact parameter values of the tracks associated with the jet object. The working point corresponding to a b-tagging efficiency of 70% is used.

7.3 Monte Carlo Samples

Monte Carlo simulated event contributions from proton-proton collisions at $\sqrt{s} = 8$ TeV corresponding to the semileptonic l + jets channel are separated into $t\bar{t}$ signal

events and the background contributions, which produce a similar topology to the usual $t\bar{t}$ event with a single lepton. As has been mentioned in the previous chapter, in a semileptonic $t\bar{t}$ event at least 4 jets are produced, originating from two quarks produced by one of the W-bosons in the event and 2 b-quarks originating directly from the top and anti-top quarks respectively, give rise two to b-jets, and also a lepton pair is produced from the remaining W-boson (either a muon or an electron + its neutrino). The background processes briefly described in section 7.3.3 produce a similar topology to the one obtained from a semileptopnic top quark pair decay. Some of the events produced from these processes manage to pass the event selection described in section 7.6, so these background contributions need to be modelled reasonably well. However, for this analysis background processes contribute with less than 10 % of the final set of selected events.

The available MC samples within the collaboration correspond to the internal MC production, prepared by the ATLAS Monte Carlo samples production team. The latest version of the MC production for 8 TeV analyses is known as `MC12a`, which was used for the analysis presented in this thesis. The selected MC samples (sections 7.3.2 and 7.3.3) accounting for background and signal events, were chosen following internal recomendations from the collaboration top group. The recommended samples have given best performance modelling of the observed data events for different control kinematic variables. As can be seen in section 7.6.2 data are resonably well modelled for all the control variables produced from the selection. Also additional samples and re-weighting tools are provided to improve the Monte Carlo simulation predictions. All the samples are weighted down to the total integrated luminosity recorded by the ATLAS experiment from collisions at $\sqrt{s} = 8$ TeV, of 20.3 fb^{-1}.

7.3.1 Simulation Chain

MC simulated predictions include description of the following processes that take place in a collected event from a proton-proton collision. These processes are illustrated in Figure 7.1:

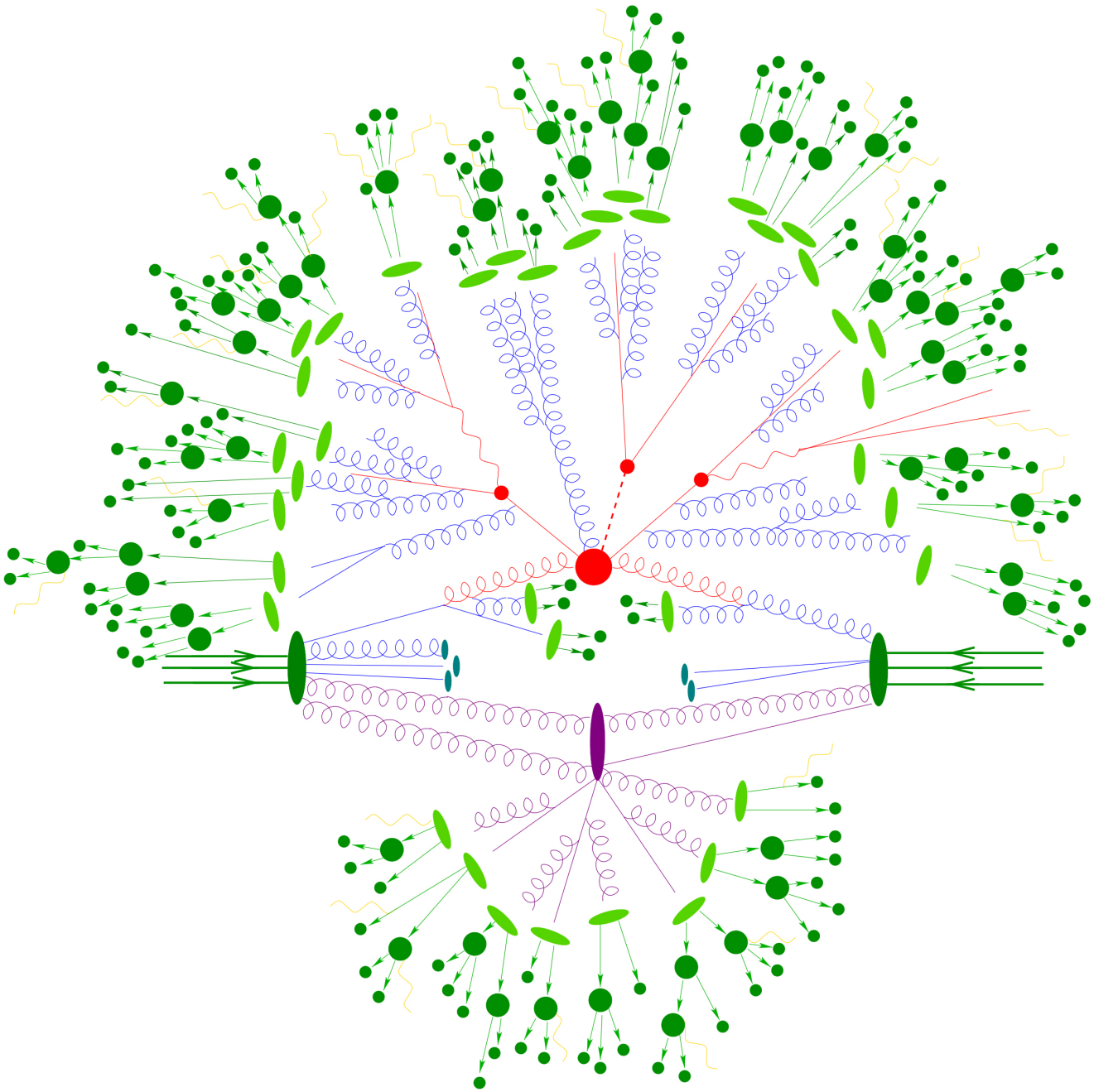

Figure 7.1: Diagram representing the processes involved after a hard interation between two partons from two different protons has taken place, which is represented with the large red circle produced by two gluons represented with red curly shapes. ISR and FSR radiation is represented with blue curly gluon shapes, the resonance decays are represented with the small red circles while the multiple interactions are indicated by the purple oval. From [140].

- The hard scattering processes occur between partons from two different protons. These partons can be either quarks or gluons. This interaction contains the most important part of the event as it determines the topology that is measured in the detector. This interaction is described with a matrix element calculation. The hard scattering is represented with the large red circle in Figure 7.1.

- Also quarks and gluons can experience *QCD bremsstrahlung* processes, where gluons are emitted before (Intial State Radiation, ISR) and after (Final State Radiation, FSR) the hard scattering, adding more partons into the decay chain. This radiation is illustrated with blue curly gluon shapes in the same figure.

- Resonance decays consists in decays of unstable particles produced in the hard scatter to daughter particles, such as the top decay to a W-boson and a b-quark or the decay of the W-boson to a couple of quarks or a couple of leptons. These decays are represented in the figure with small red circles.

- Multiple Parton Interactions, MPI account for additional pairs of partons generating additional secondary interactions. Secondary interactions carry less energy and are usually known as soft QCD interactions and are shown in the figure by the purple coloured oval.

- After all the above processes have ocurred, the event chain is left with a mixture of quarks, leptons and gluons. Quarks and gluons cannot stay in an isolated state as they carry colour and QCD just allows systems with a colourless state. Quarks and gluons are confined into a system of colourless hadrons travelling in the same direction as the original partons, and these composite

particles are the ones that are measured in the detector. This process of going from partons to composite hadrons is known as hadronisation. It is represented with green ovals decaying to green circles in the figure. Additional electromagnetic radiation emitted from charged particles is shown.

7.3.2 Signal Shape

The MC sample used to simulate $t\bar{t}$ signal events is produced from the `POWHEG` generator for parton shower interfaced with the `PYTHIA` generator for the underlying event: `POWHEG` with PDF set, CT10, and `PYTHIA` with PDF set, CTEQ6L1. These provide full simulation with a Next to Leading Order NLO, level of accuracy [103]. Samples exclude all-hadronic $t\bar{t}$ events as the analysis requires events to have a well isolated lepton. For these samples the top quark has a mean top mass value equal to $m_{top} = 172.5$ GeV and Standard Model top width $\Gamma_{top} = 1.33$ GeV.

7.3.3 Background Shape

The backgrounds considered for this analysis produce a combination of physical objects that have a similar topology to that of a $t\bar{t}$ event decaying to a single lepton as shown in Figure 6.3.

An important contribution to the background comes from single top events; some representative diagrams for these processes are displayed in Figure 7.2. In these events a single top is produced decaying to a b-quark and a W-boson which produces half of the elements obtained in a usual l + jets $t\bar{t}$ event. An additional b-quark is obtained in the production process which means this background makes the biggest contribution even after applying 2 b-tags as discussed later in Table 7.1. The contribution from single top processes was produced by interfacing the simulation `AcerMC` version 3.5 (PDF set: CTEQ6L1) with `PYTHIA` version 6.426 with P2011C tune (PDF set: CTEQ6L1) [130].

Figure 7.2: Processes giving rise to a single top quark and additional light quarks and b-quark producing extra light and heavy jets. An overall topology similar to a $t\bar{t}$ l + jets is obtained. From [136].

Another important contribution to consider is QCD multijet background, which is a result of reconstructing a lepton when there is no real or prompt lepton in the event. This background is illustrated on the left of Figure 7.3, where a quark giving rise to a jet may be confused with an electron. This background shape is obtained by re-weighting the events observed in data using a Matrix Method [114], as it is difficult to model this background directly from a MC generator.

To estimate the QCD multijet background the quality cuts for lepton objects described in subsections 7.2.1 and 7.2.2 for muon and electrons respectively are reduced, producing *loose* lepton objects. Efficiencies of loose to tight leptons are measured for prompt lepton (ϵ^{real}) and fake lepton (ϵ^{fake}) samples. To calculate the efficiency for prompt leptons a 'tag and probe' method is used with a sample containing known prompt leptons from Z $\rightarrow l^+l^-$ events. One of the leptons (also passing the tight requirements) is tagged as the 'tag' and the other lepton (the 'probe') is used to calculate the efficiency ϵ^{real}. To calculate the fake leptons to tight efficiency, ϵ^{fake}, a sample requiring at least one jet with $p_T > 25$ GeV and one loose lepton is used. To make sure that the sample has sufficient fake leptons the event missing energy is required to satisfy $E_{\mathrm{T}}^{\mathrm{miss}} > 20$ GeV. As the sample still contains a reduced amount of prompt leptons after the event selection, an estimated number of remaining events is substracted. As before ϵ^{fake} represents the fraction of loose leptons that pass the tight quality cuts.

Once the efficiencies ϵ^{real} and ϵ^{fake} are calculated they can be used to set the relationship between the real and fake events present at the loose stage N^{real}_{loose} and N^{fake}_{loose}, respectively, with respect the total observed events at the loose and tight stages N_{loose} and N_{tight} respectively, as shown in Equation (7.1):

$$\begin{pmatrix} N_{loose} \\ N_{tight} \end{pmatrix} = \begin{pmatrix} 1 & 1 \\ \epsilon^{real} & \epsilon^{fake} \end{pmatrix} \begin{pmatrix} N^{real}_{loose} \\ N^{fake}_{loose} \end{pmatrix} \tag{7.1}$$

From this matrix is is possible to solve for the number of fake events after tight cuts are applied $N^{fake}_{tight} = \epsilon^{fake} N^{fake}_{loose}$, in terms of the efficiencies ϵ^{real} and ϵ^{fake} and the observed total events N_{loose} and N_{tight} at the loose and tight stages respectively as shown in Equation (7.2):

$$N^{fake}_{tight} = \epsilon^{fake} N^{fake}_{loose} = \frac{\epsilon^{fake}}{\epsilon^{real} - \epsilon fake}(N_{loose}\epsilon^{real} - N_{tight}) \tag{7.2}$$

where N^{fake}_{tight} is the estimation of the number of events for the QCD multijet background. The efficiencies ϵ^{real} and ϵ^{fake} are parametrized in η and p_T in order to obtain the weights $N^{fake}_{tight}/N^{tight}$ for each location to produce the corresponding distributions of different variables for this background by weighting data events with single leptons passing the *loose* requirements.

Events with two bosons producing a single lepton as shown on the right of Figure 7.3 are also considered, the three possible combinations for the pair of weak bosons being W-W, W-Z and Z-Z. The contribution from diboson processes was produced by interfacing the `POWHEG` version V2 (PDF set: CTEQ6L1) and `Herwig` version 6.520.2 with AUET2 tune (PDF set: CTEQ6L1) simulations [103].

Events with a W-boson or a Z-boson and at least one additional jet as shown in Figure 7.4 are regarded as W + jets or Z + jets events. These two processes contribute

to the background for this analysis as both processes produce a similar topology to semileptonic $t\bar{t}$ events, when the W or Z bosons decay into a pair of leptons.

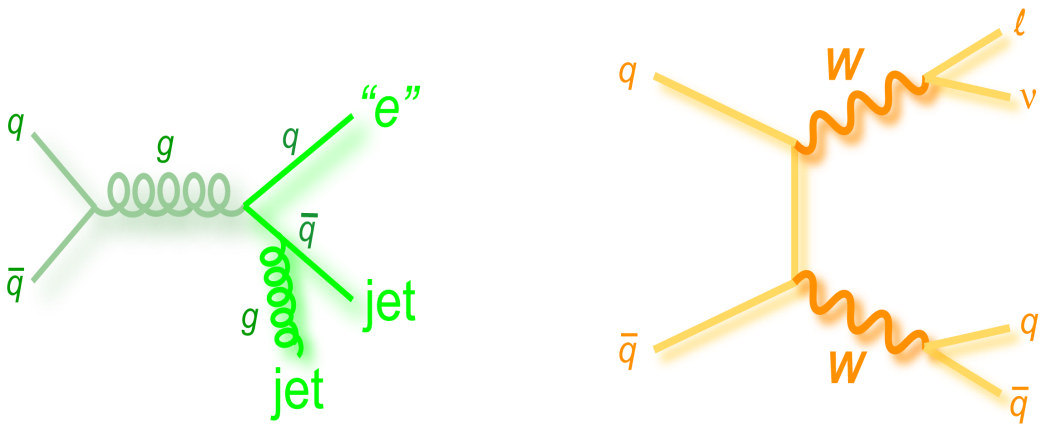

Figure 7.3: Production diagram for a possible QCD multijet event (left) and a diboson event in this case with a couple of W-bosons (right). From [136].

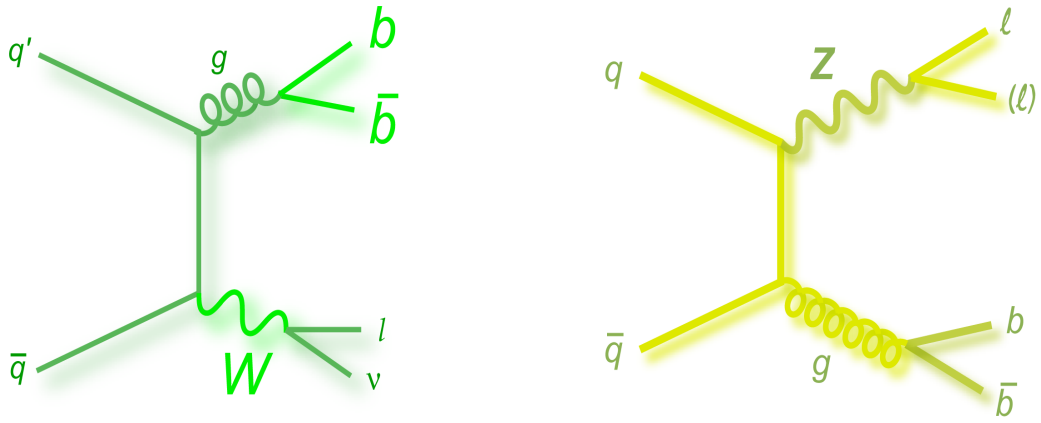

Figure 7.4: Diagrams standing for processes where a single W-boson (left) or a Z-boson (right) plus a couple of additional quarks are produced. The latter ones being produced in a strong interaction. From [136].

However contribution from W/Z + jets to the background is very reduced with respect to the contributions introduced by the single top and QCD multijet processes

as it is discussed in section 8.1. The W + jets contribution was produced from the SHERPA generator version 1.4.1 (PDF set: CT10) [131] and the Z + jets processes by interfacing the ALPGEN version V2.14 (PDF set: CTEQ6L1) and PYTHIA version 6.426 with P2011C tune (PDF set: CTEQ6L1) simulations [103].

7.4 Detector Simulation

All the MC samples are processed with the GEANT4 [105], [106], [139] simulation of the ATLAS detector to evaluate the detector response and are passed through an identical selection process as data. This simulation includes multiple primary vertices (pile-up) effects. MC events are weighted so that average number of interactions per bunch crossing matches what is obtained from data.

7.5 Data Sample at $\sqrt{s} = 8$ TeV

This analysis uses proton-proton collision data produced with centre-of-mass energy of $\sqrt{s} = 8$ TeV, corresponding to an integrated luminosity of 20.3 fb^{-1} collected by the ATLAS detector. The data were recorded with all detector subsystems being operational as recorded in the collaboration's Good Run List file (GRL). The observed yields for the different stages of the selection for observed events match what other analysis teams within the ATLAS Top Physics group have reported.

7.6 Standard Event Selection

The $t\bar{t}$ topology that was selected for the analysis corresponded to events with a single lepton, either a muon or an electron. As mentioned in the previous chapter this channel has a large decay rate corresponding to a fraction of $\sim 44\%$, and for this analysis it is crucial to catch as high a proportion of these events as possible. These $t\bar{t}$ events contain a hadronic and leptonic top decay. This provides a good

discriminant against the background contributions.

7.6.1 Selection Requirements and Yields

Analyses using the same event channel usually adopt a same common standard pre-selection of events before applying an analysis particular constraint. A summary of the standard $t\bar{t}$ lepton + jets channel pre-selection is therefore included in this subsection. In this analysis a further constraint is applied using a variable that can be obtained from the reconstruction such as a χ^2 value or a Likelihood value that judges the quality of the reconstruction for a particular event. This is described in more detail in section 7.8.

- The electron or muon online trigger is required to have fired. Exactly one reconstructed lepton is required to match the object reconstructed online by the fired trigger. The lepton is required to have transverse momentum $p_{\mathrm{T}} >$ 25 GeV, and pseudorapidity $0 \leq |\eta| \leq 2.5$. Here electron stands for an electron or a positron and a muon for a positively or negatively charged muon.

- There are events where a muon and electron are reconstructed and both are associated to the same track in the inner detector, and their location in the ϕ-η plane almost overlaps. These events are tagged as having an electron-muon overlap and are removed from the selected events.

- Events are required to have at least 4 jets with a transverse momentum $p_{\mathrm{T}} >$ 25 GeV and pseudorapidity values $0 \leq |\eta| \leq 2.5$. These jets account for our required two b-jets and two light jets produced in lepton + jets $t\bar{t}$ events.

  To reduce the QCD multijet backgrounds and suppress diboson and weak bosons + jets backgrounds, the following requirements are added to the event selection:

- Missing transverse energy should have a value $E_{\mathrm{T}}^{\mathrm{miss}} > 30$ GeV for the e + jets channel and over 20 GeV for the μ + jets channel.

- The reconstructed hadronic W-boson transverse mass is defined as: $M_{\mathrm{T}}(\mathrm{W}) = \sqrt{m_W^2 + p_x^2 + p_y^2}$ [37], where m_W is the invariant mass of the W-boson and p_x and p_y its x and y momentum components. $M_{\mathrm{T}}(\mathrm{W})$ is required to satisfy $M_{\mathrm{T}}(\mathrm{W}) > 30$ GeV for the electron channel and $M_{\mathrm{T}}(\mathrm{W}) + E_{\mathrm{T}}^{\mathrm{miss}} > 60$ GeV for the μ channel.

  These final requirements are tighter for the electron channel as QCD multijet events have a higher contribution for the electron channel, as jets are confused with electrons more often than with muons.

- The number of b-tags in an event is defined as the number of jets identified as b-jets using the multivariable discriminant MV1, described in section 7.2.5 and set to yield a 70% b-tagging efficiency. To further reduce the background contributions, each event is required to have at least two b-tags.

Table 7.1: Data and simulation yields from standard lepton + jets channel preliminary selection. All the simulation yields are normalized to the collected integrated luminosity of 20.3 fb^{-1} at 8 TeV.

Process	μ: ≥ 1 b-tag	μ: ≥ 2 b-tags	e: ≥ 1 b-tag	e: ≥ 2 b-tags
Single top	$12640\ ^{+900}_{-910}$	$5122\ ^{+310}_{-320}$	$8599\ ^{+710}_{-630}$	$2971\ ^{+230}_{-190}$
W + jets	$31066\ ^{+3200}_{-2840}$	$1031\ ^{+96}_{-82}$	$5051\ ^{+600}_{-470}$	$1613\ ^{+170}_{-130}$
Z + jets	$2215\ ^{+340}_{-230}$	$365\ ^{+53}_{-29}$	$2125\ ^{+410}_{-250}$	$331\ ^{+63}_{-37}$
Diboson	$857\ ^{+69}_{-64}$	$64\ ^{+6}_{-3}$	$598\ ^{+50}_{-46}$	$47\ ^{+6}_{-4}$
QCD Multijet	$8300\ ^{+2600}_{-2600}$	$1905\ ^{+570}_{-560}$	$8146\ ^{+2500}_{-2500}$	$2525\ ^{+860}_{-820}$
$t\bar{t}$	$163042\ ^{+8200}_{-8200}$	$82982\ ^{+4000}_{-4000}$	$107731\ ^{+6000}_{-6000}$	$47580\ ^{+2500}_{-2500}$
Expected	$218119\ ^{+9300}_{-9100}$	$91470\ ^{+4100}_{-4100}$	$132250\ ^{+6600}_{-6600}$	$55068\ ^{+2700}_{-2700}$
Observed	216406	91565	131621	56714

Table 7.1 shows the data and MC yields for the number of selected events corresponding to the above selection requirements, which is a preliminary standard

selection used by most groups analyzing the $t\bar{t}$ l + jets channel.

7.6.2 Correction Scale Factors

Additional correction scale factors are obtained from independent studies within the ATLAS top group by matching data to the simulated events. These account for pile-up, electron and muon identifications effciencies, trigger performance, vertex location efficiency and b-tagging efficiency.

7.6.3 Selection Control Plots

In this sub-section are shown distributions corresponding to different kinematic variables whose values were constrained in the event selection described in section 7.6.1. The total prediction is broken down into different processes already listed in table 7.1, where their yields and uncertainties are shown. After requiring 2 b-tags the background is reduced significantly, amounting to a contribution of $\sim$ 10 % for the electron and muon channels.

7.6.3.1 μ + jets channel

The distributions for event jet multiplicity n_{jet} are shown in Figure 7.5 for the μ + jets channel. The jet multiplicity is given by the total number of observed jets in an event that match the conditions stated in the selection requirements (section 7.6.1). Events are required to have $\geq$ 4 jets as these plots indicate. In these distributions the data dots are compared with the total prediction obtained from adding all the background contributions together. The hatched areas in the plots in Figure 7.5 indicate the total uncertainty of the prediction (statistical + systematic). Sources of systematic uncertainties are discussed in section 8.2. From the distributions it can be seen that the fractional contribution of W + jets background, reduces dramatically after requiring 2-b-tags (from 14.2 % to 1.1 %).

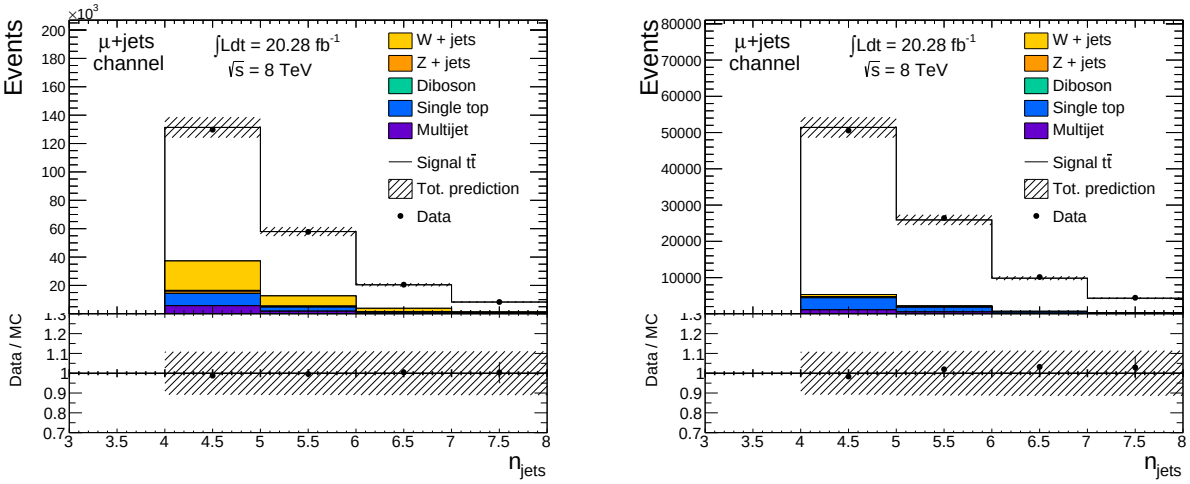

Figure 7.5: Distributions for jet multiplicity n_{jet} for the μ + jets channel at the stage of 1 (left) and 2 (right) b-tags required respectively.

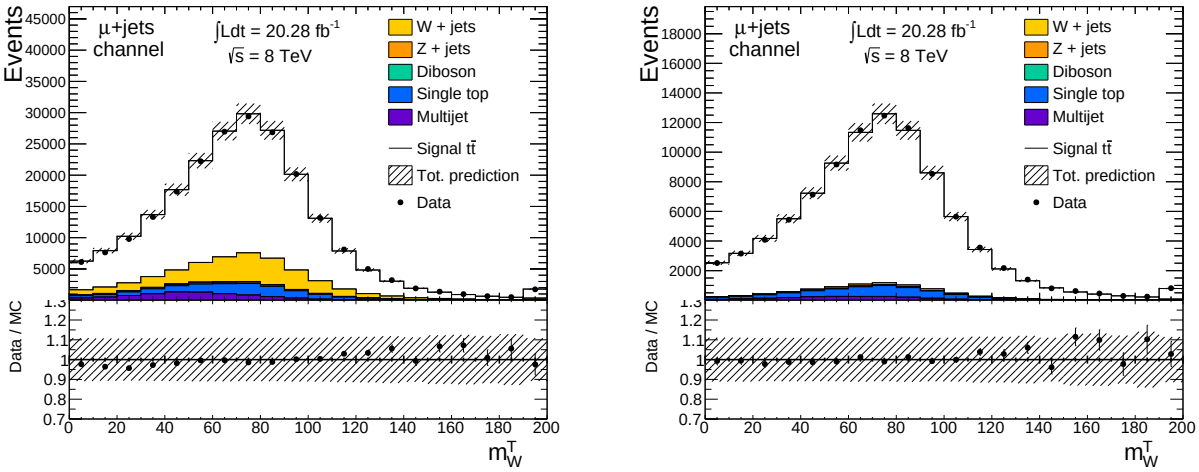

Figure 7.6: Distributions of the W-boson transverse mass (section 7.6.1) for the μ + jets channel at the stage of 1 (left) and 2 (right) b-tags required respectively.

Another important distribution to consider is the reconstructed value for the W-boson transverse mass displayed in Figure 7.6 for the μ + jets channel. These distributions are initially used as reference to determine agreement with data, as to reconstruct the W-boson two ordinary jets are required. So the resulting m_W^T distribution is not biased by the performance of the b-tagging algorithms.

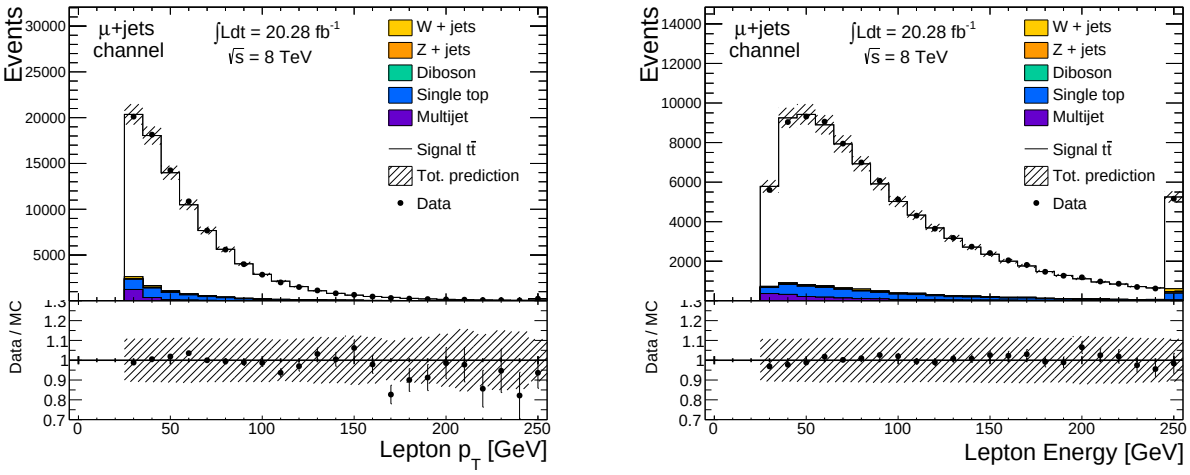

Figure 7.7: Lepton transverse momentum p_{T} (left) and lepton energy (right) for the μ + jets channel after requiring 2 b-tags.

Distributions for lepton transverse momentum p_{T} and lepton energy are shown in Figure 7.7 for the μ + jets channel. These distributions keep very good agreement with observed data for the regions with most of the statistics and keep within the systematic uncertainty bands for bins with few events.

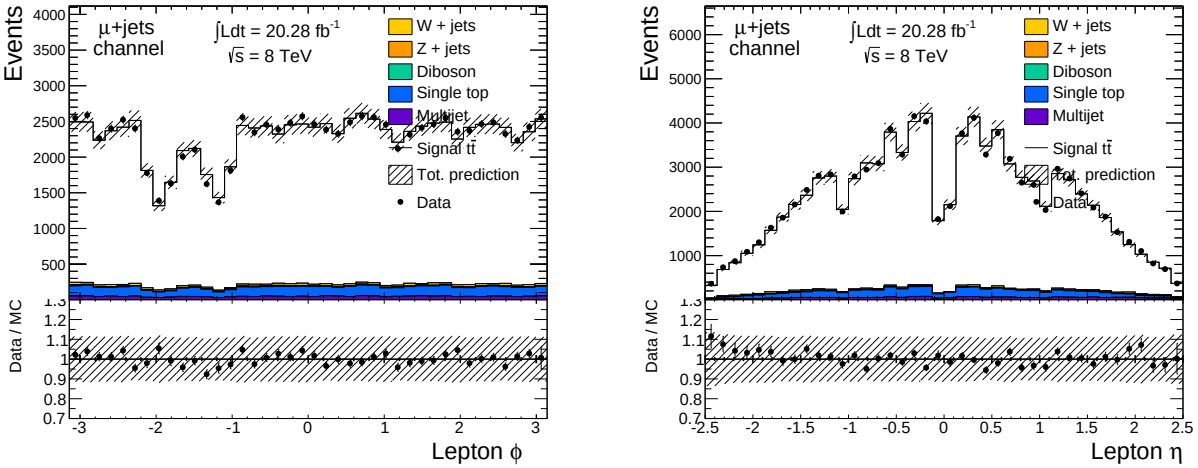

Figure 7.8: Lepton ϕ (left) and pseudorapidity η (right) angular variables for the μ + jets channel after requiring 2 b-tags.

Additional lepton angular variables ϕ covering the range $[-\pi, \pi]$, describing the

distribution of leptons in the transverse direction of the detector and pseudorapidity with range [-2.5, 2.5] are shown in Figure 7.8 for the μ + jets channel. The second variable describes the distribution of leptons in the longitudinal direction of the detector as described in Figure 4.4 in chapter 4. In both plots, good agreement between data and the prediction for all bins is observed. The pseudorapidity plot in the right has an abrupt reduction in number of entries around the region with values ~ 0, which corresponds to the azimuthal location $\phi \sim$ -π in the left. The reason for this is that around that region several electronic cables are passed from within the detector to the outside through the muon spectrometer, reducing the ability of the detector to record muons around this region.

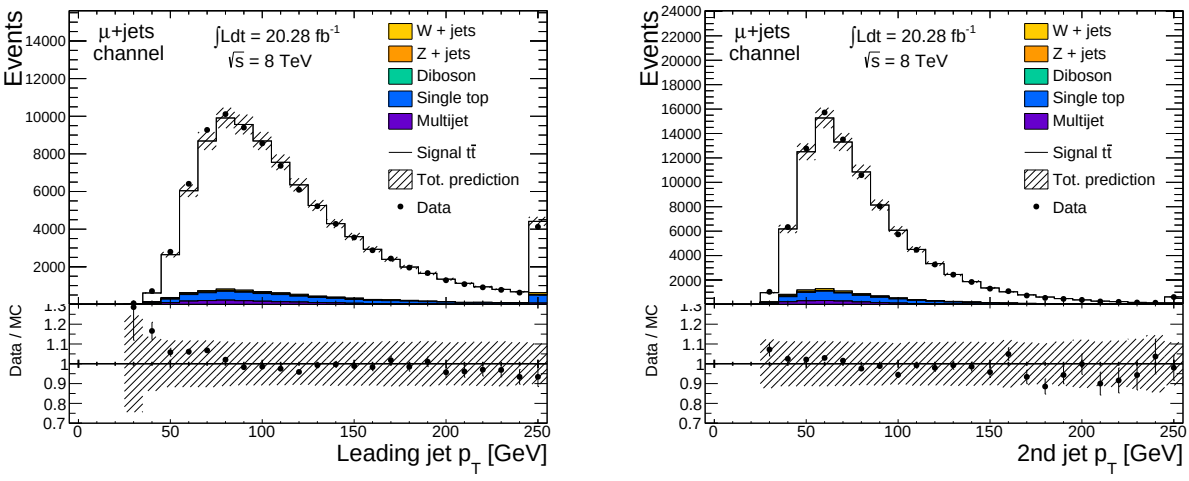

Figure 7.9: Transverse momentum p_{T} of the event leading jet (left) and second leading jet (right) for the μ + jets channel after requiring 2 b-tags.

Figure 7.9 displays the transverse momentum p_{T} of the event leading jet and second leading jet. These are the two jets with highest value of p_{T} in the event and are usually likely selected for the top quark reconstruction between all the jet candidates.

The precise contributions of each of the backgrounds for the final set of selected events is discussed in the first section of the following chapter.

7.6.3.2 e + jets channel

In a similar way the same control distributions are shown for the electron channel. From Table 7.1, we see that this channel has 40 % fewer events than the muon channel as the detector rejects events where the electron is overlapped with other objects and also the event selection is tighter for the electron channel as described in section 7.6.1. For this channel, the W + jets background has a similar contribution of $\sim$ 1.5 % as in the muon channel for the final set of selected events. The QCD multijet background comprises a larger fraction of the selected events of 4.5 % after two b-tags compared to 2.0 % in the muon channel.

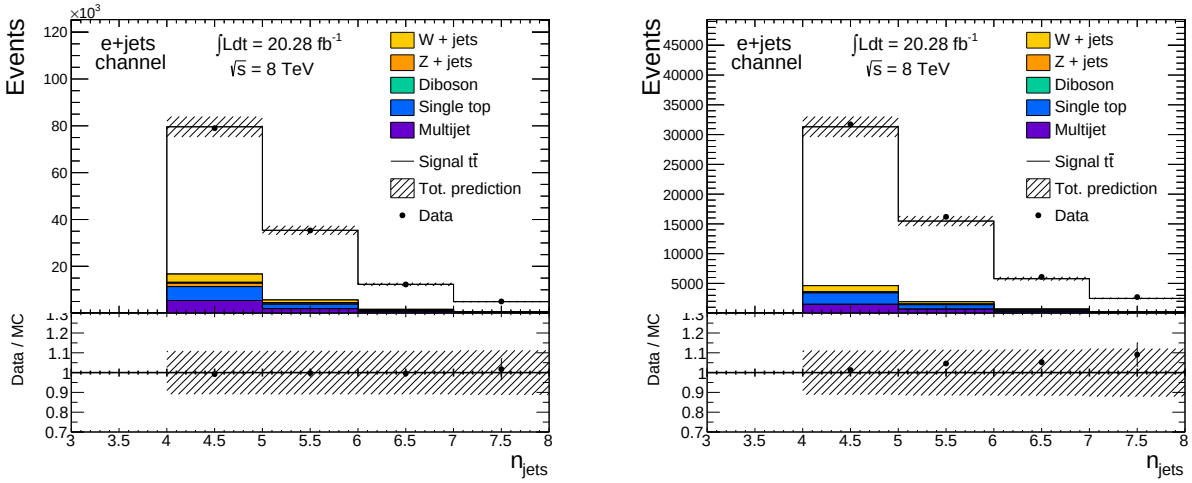

Figure 7.10: Distributions for jet multiplicity n_{jet} for the e + jets channel at the stage of 1 (left) and 2 (right) b-tags required respectively.

The distributions for event jet multiplicity n_{jet} are shown in Figure 7.10 for the e + jets channel. For this channel the W + jets background keeps a constant fraction of $\sim$ 2.9 % between the 1 and 2 b-tags requirements. Distributions of the reconstructed value for the W-boson transverse mass are displayed in Figure 7.11. For this channel the cut $m_{\mathrm{W}}^{\mathrm{T}} > 30$ GeV is clearly visible.

Distributions of lepton transverse momentum p_{T} and lepton total deposited energy

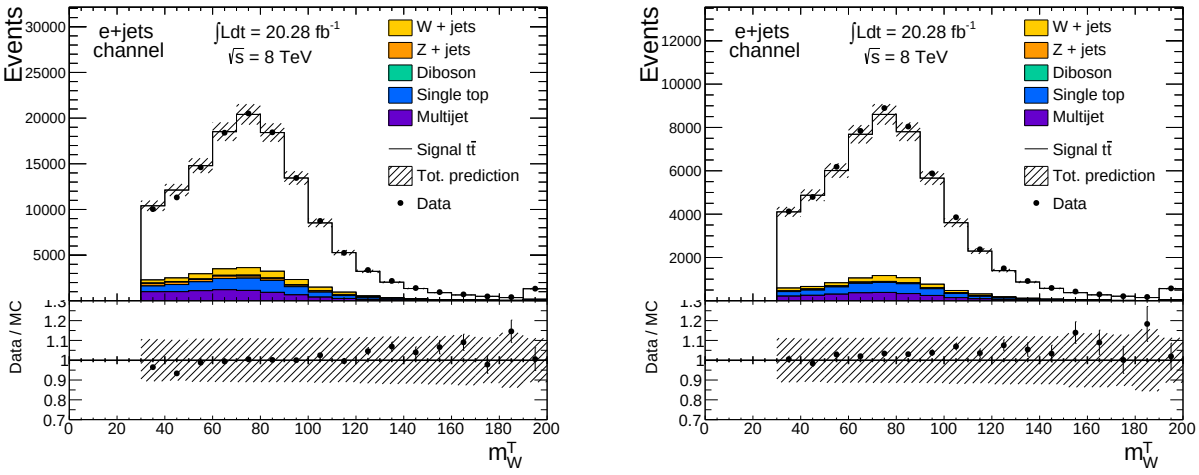

Figure 7.11: Distributions of the W-boson transverse mass for the e + jets channel at the stage of 1 (left) and 2 (right) b-tags required respectively.

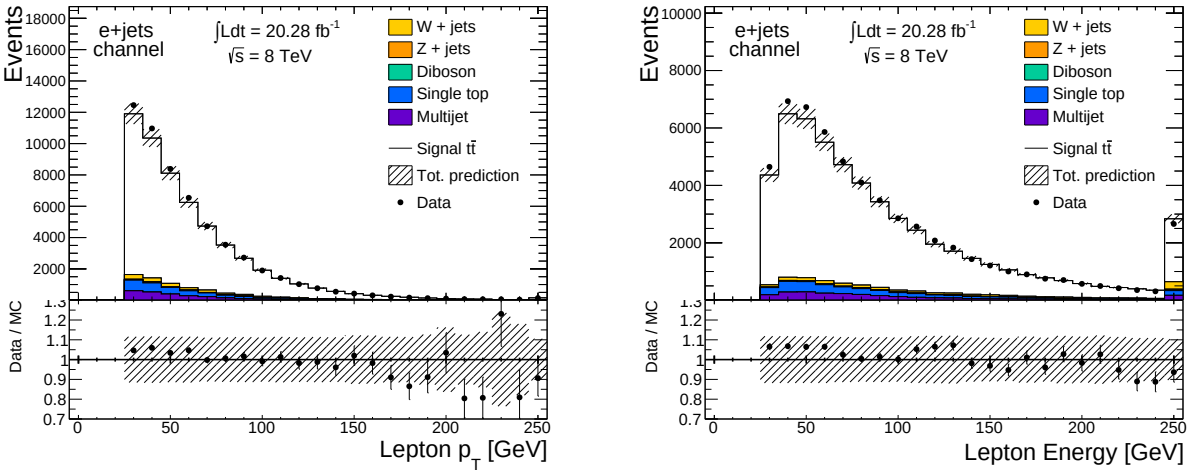

Figure 7.12: Lepton transverse momentum p_{T} (left) and lepton energy (right) for the e + jets channel after requiring 2 b-tags.

are shown in Figure 7.12. These distributions are in a reasonable agreement with observed data. The predicted event yields are slightly above the observed ones for bins located in the range 25 to 60 GeV for both plots in the figure. However all the variations are within the statistical + systematic uncertainties tolerance. As with the muon channel, the lepton angular variables ϕ and pseudorapidity are shown in Figure 7.13 for the e + jets channel. In this case the pseudorapidity plot in the

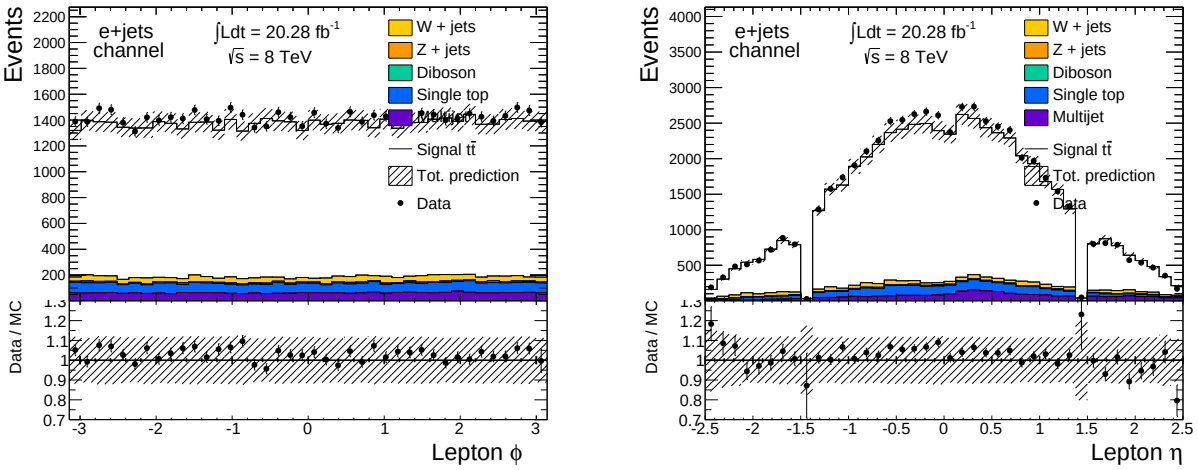

Figure 7.13: Lepton ϕ (left) and pseudorapiduty η (right) angular variables for the e + jets channel after requiring 2 b-tags.

right has almost zero entries for pseudorapidity values ~ 1.5, a transition region in the detector where the calorimeters are unable to record energy deposits, as already described in section 4.4. Finally Figure 7.14 displays the transverse momentum p_{T} of the event leading jet and second leading jet for the electron channel. The observed events have been modelled well within the uncertainties of the data and simulation.

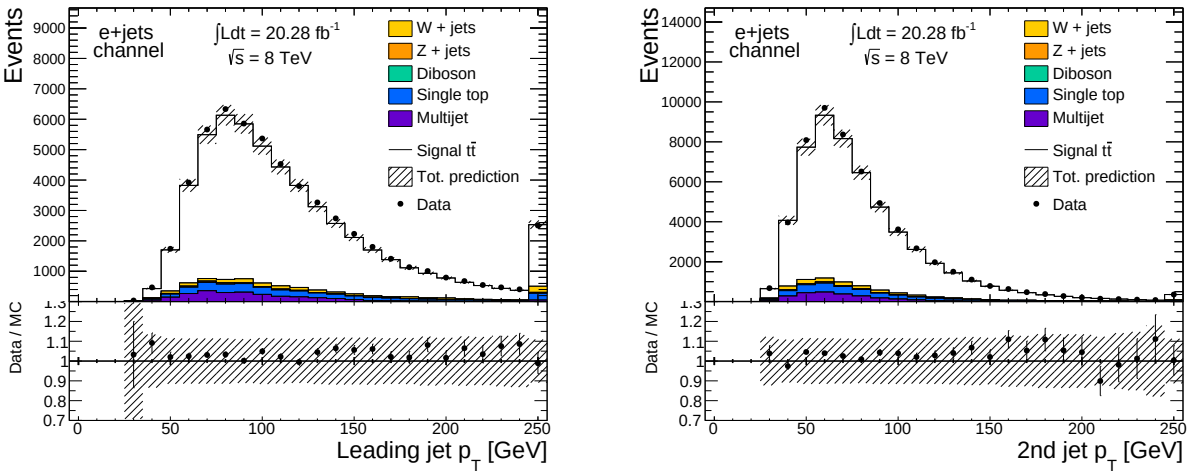

Figure 7.14: Transverse momentum p_{T} of the event leading jet (left) and second leading jet (right) for the e + jets channel after requiring 2 b-tags.

7.6.3.3 Number of Primary Vertices

As mentioned before the simulated events are weighted so that the average number of interactions per bunch crossing matches what is obtained from data. Figure 7.15 shows the distributions for simulation and data for the number of primary vertices per bunch crossing which reflect the degree of pile-up. These plots show that the simulated events have been weighted correctly and their distribution has the same mean as the data distribution. The number of primary vertices has a mean value of ~ 9.4 for the muon and electron channels with data at centre-of-mass collision energies of $\sqrt{s} = 8$ TeV.

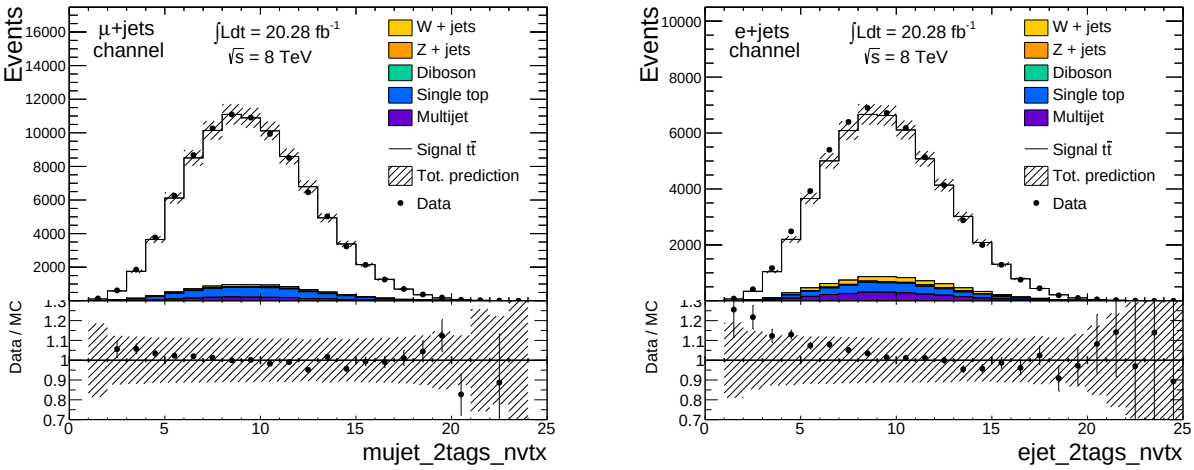

Figure 7.15: Number of primary vertices after weighting the simulated distribution so its average matches the mean value observed in data for electron (left) and muon (right) channels.

7.7 Templates With Different Γ_{top}

This analysis requires the production of templates with different underlying values of the top quark width Γ_{top} parameter. The templates are versions of the distributions of the reconstructed variables described in section 7.8 with different value of Γ_{top}. Once these templates are obtained, statistical studies, calculation of uncertainties

and measurement with data can be achieved.

Based on previous limits on top quark width set by the CDF experiment, previously described in section 6.4.2.1, Γ_{top} was studied in the range 0 to 10 GeV in steps of $\sim$ 0.1 GeV, which implied at least a total of 100 templates. Generating all the required samples with different Γ_{top} values directly from generators as described in section 7.3, covering the required range and spacing was not possible during the course of this analysis. The reason for this is that the request for production of additional samples within the collaboration is limited to a few samples which are not generated with all the features and amount of statistics as the $t\bar{t}$ sample described in section 7.3.2. Therefore a re-weghting procedure was implemented to generate the templates, based on techniques applied in similar analyses, such as measurement of W-boson polarisation within the collaboration. This method has the advantage that any template for a particular Γ_{top} value can be generated and any desired amount of templates can be produced within the indicated range. A verification that the weighting procedure works successfully is shown in this section.

The re-weighting method is based on the fact that the distribution of the generated on-shell top quark at truth particle level m_{top}^{truth} in the signal $t\bar{t}$ sample is modelled with a *Relativistic Breit-Wigner shape* shown in Equation (7.3):

$$f(m) = \frac{k}{(m^2 - m_{top}^2)^2 + m_{top}^2\Gamma^2}, \quad k = \frac{2\sqrt{2}m_{top}\Gamma\gamma}{\pi\sqrt{m_{top}^2 + \gamma}}, \quad \gamma = \sqrt{m_{top}^2(m_{top}^2 + \Gamma^2)} \quad (7.3)$$

On-shell here means that the selected top quark satisfies the physical relatioship between invariant mass and momentum shown in Equation 2.3. In the event generator it also means that this selected top quark decays to a W-boson + a b-quark. The Breit Wigner shape has an associated mean m_{top}, equal in this case to the top mass $m_{top} = 172.5$ GeV and a variable width Γ_{top} is the top quark width.

The plots in Figure 7.16 show a relativistic Breit-Wigner distribution fitted to the

m_{top}^{truth} distribution in the signal $t\bar{t}$ sample for both the e + jets and μ + jets channels respectively. These fits output in both cases the SM relationship that was chosen in the simulation for these parameters, $m_{top} = 172.5$ GeV and $\Gamma_{top} = 1.33$ GeV for top mass and top width, and then confirm the modelling of the top mass resonance at truth level with the relativistic Breit-Wigner shape.

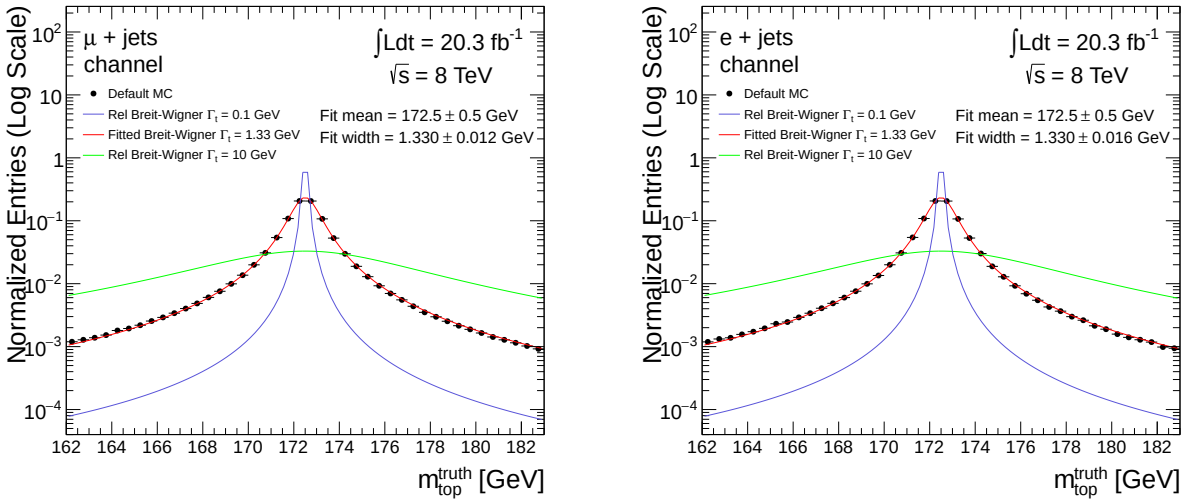

Figure 7.16: Relativistic Breit Wigner shape (red colour) has been fitted to the truth top mass distributions m_{top}^{truth} (black dots) for both channels μ + jets (left) and e + jets (right). In both cases the SM relationship between m_{top} and Γ_{top} is recovered confirming the modelling of this resonance with the shape in Equation (7.3). Additional curves with Γ_{top} values 0.1 GeV and 10 GeV have been added to illustrate the effect of the variation of the parameter.

After making sure the MC sample for $t\bar{t}$ signal events is modelled with the relativistic Breit-Wigner shape, several curves with different values of Γ_{top} are produced, keeping the mean top mass constant at the input value in the MC sample $m_{top} = 172.5$ GeV. These curves are shown in Figure 7.17.

The weights to produce the templates with variable Γ_{top} are obtained by dividing the value of the Breit Wigner curve with the desired width, over the value of the reference curve with $\Gamma_{top} = 1.33$ GeV (the SM prediction) at the required value of

m_{top}^{truth}. These weights are computed for width values within the range [0, 10] GeV. In the plot at the bottom of Figure 7.17 the shape of the weights as a function of the event m_{top}^{truth} value is shown.

Once the weights for different widths are computed for the value of the event m_{top}^{truth}, histograms of the reconstructed variables with different Γ_{top} are filled applying the appropiate weights.

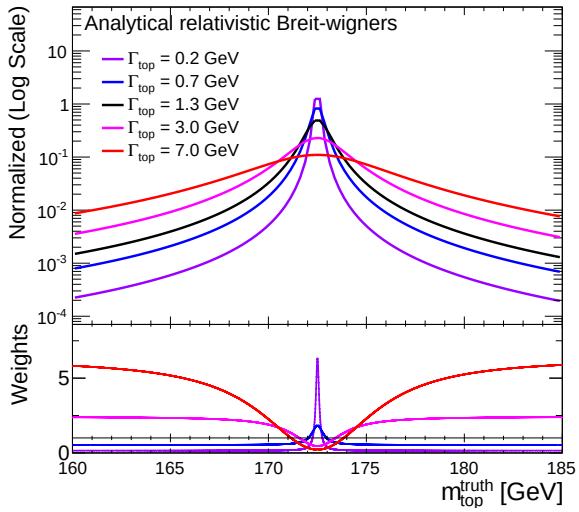

Figure 7.17: Several Relativistic Breit Wigner curves (Equation 7.3) corresponding to the same mean top mass m_{top} = 172.5 GeV and different top width values Γ_{top}. These curves are used obtain the templates with variable Γ_{top}.

The resulting templates obtained by implementing the re-weighting method are displayed in Figure 7.18, where the different weighted m_{top}^{truth} distributions are shown corresponding to different values of Γ_{top} for both channels μ + jets and e + jets respectively. Both $t\bar{t}$ and single top background samples were weighted with the same procedure as in the single top events a top quark is produced with variable width. Though for this analysis the effect of the single top background shape is minimal as it has a contribution of just $\sim$ 4 % of the total simulated prediction.

In order to cross-check the weighting procedure worked sucessfully, different Breit-Wigner curves are fitted over the obtained m_{top}^{truth} templates. For these fits a χ^2

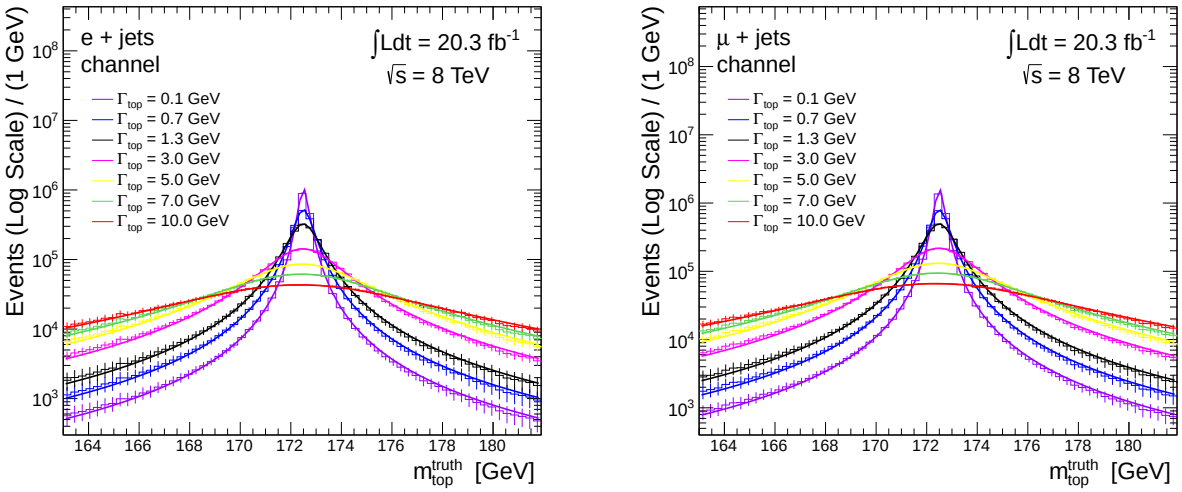

Figure 7.18: Produced templates at truth level from the re-weighting method with different values of underlying Γ_{top} for the μ + jets channel (left) and the e + jets channel (right).

minimization method from the `MINUIT` package [128] implemented in the `ROOT` environtment is used. This method outputs the ratio of the minimized χ^2 value over the number of degrees of freedom (NDF). The χ^2 value adds the squared differences between the fitted curve and the original histogram entries over the bin uncertainties, the χ^2 value and NDF should then satisfy $0.75 < \chi^2$ / NDF < 1.25 for a reasonable fit. The fitted values of m_{top} and Γ_{top} parameters listed in Table 7.2 for the different templates in the μ + jets channel. The table shows that the correct values of both parameters are recovered for the different templates with varying Γ_{top} and constant m_{top} within the uncertainties. The uncertainties over the fitted values are really small and have been considered in the calculation of the systematic uncertainties.

Column 4 in the same table shows the χ^2 / NDF ratios for each fit, which in general are close to 1 with average value ~ 0.95. Table 7.3 shows the fitted values for the different templates in the e + jets channel having similar results than the muon channel. Additionally the produced templates were compared with a set of independent samples corresponding to a few width values produced directly from MC generators. The weighted templates agreed with the MC distributions within

Table 7.2: Determined values of mean m_{top} and Γ_{top} from fitting Breit-Wigner curves to the m_{top} templates with different values of Γ_{top} from the re-weighting method in the μ + jets channel.

Template Γ_{top} Value [GeV]	Fitted Mean m_{top} [GeV]	Fitted Γ_{top} [GeV]	χ^2 / NDF
0.1	172.4 ± 0.6	0.11 ± 0.05	0.92
0.5	172.4 ± 0.5	0.51 ± 0.04	0.93
1.0	172.5 ± 0.4	1.03 ± 0.04	0.95
1.3	172.5 ± 0.5	1.33 ± 0.01	0.95
3.0	172.5 ± 0.5	3.04 ± 0.06	0.94
5.0	172.4 ± 0.5	5.01 ± 0.04	0.95
7.0	172.4 ± 0.4	7.02 ± 0.05	0.93
10.0	172.3 ± 0.5	10.03 ± 0.05	0.93

Table 7.3: Determined values of mean m_{top} and Γ_{top} from fitting Breit-Wigner curves to the m_{top} templates with different values of Γ_{top} from the re-weighting method in the e + jets channel.

Template Γ_{top} Value [GeV]	Fitted Mean m_{top} [GeV]	Fitted Γ_{top} [GeV]	χ^2 / NDF
0.1	172.5 ± 0.6	0.10 ± 0.05	0.94
0.5	172.5 ± 0.5	0.52 ± 0.05	0.95
1.0	172.5 ± 0.5	1.04 ± 0.04	0.95
1.3	172.5 ± 0.5	1.33 ± 0.02	0.96
3.0	172.5 ± 0.5	3.00 ± 0.06	0.96
5.0	172.4 ± 0.5	4.97 ± 0.04	0.94
7.0	172.4 ± 0.5	7.03 ± 0.05	0.94
10.0	172.3 ± 0.5	10.04 ± 0.05	0.93

their statistical + systematic uncertainties. As the generated samples have less than third of the statistics of the weighted templates, they were just used for validation purposes.

7.8 Event Reconstruction Techniques

Reconstruction techniques are used to match the physical objects, with detector effects included described in section 7.2, with the truth particles produced in the hard scattering. In this case the process of interest is the production of $t\bar{t}$ pairs and the particles to match are the ones produced in semileptonic decays as shown in section 6.2. The matched objects are used to obtain per-event variables such as invariant masses and kinematic variables like the lepton transverse momentum p_{T}, that are useful to compare the simulated events with the observed data.

The event reconstruction is limited by the detector resolution on the reconstructed variables and the ability to match the different objects in the event with their associated particles at truth level i.e. as they were produced in the hard scattering. For the case of the $t\bar{t}$ event decaying to a semileptonic topology (Figure 6.3), two b-quarks at truth level should match two b-jets, a pair of quarks either (u, d) or (s, c) should match two jets and a muon or an electron with the reconstructed lepton.

A χ^2 minimization technique described in section 7.8.1 is used for the main analysis presented in this thesis. Another reconstruction technique, based on per-event kinematic likelihood maximization method known as KL-Fitter, is briefly described in section 7.8.2.

7.8.1 χ^2 Minimization Method

The χ^2 minimization technique consists in constraining the value of a set of reconstructed variables associated with the $t\bar{t}$ system with a χ^2 expresion. All the possible permutations of objects in the event are matched to the $t\bar{t}$ topology, selecting the combination of objects that give the smallest χ^2 value, χ^2_{min}. After all the selected events have been analysed, just the ones having a χ^2_{min} below a certain value are

selected. Several χ^2 expressions were tested and the expression that gave optimal results for this analysis is shown in Equation (7.4), this expression was also used for the $t\bar{t}$ resonances search analysis and W-boson polarisation measurement in ATLAS.

$$\chi^2 = \frac{((m_t - m_W) - (m_{bjj} - m_{jj}))^2}{\sigma^2_{diff}} + \frac{(m_W - m_{jj})^2}{\sigma^2_W} + \frac{(m_t - m_{\nu lb})^2}{\sigma^2_{top}} \tag{7.4}$$

m_{bjj} stands for the invariant mass calculated with a permutation of two jets and a b-jet known as reconstructed hadronic top mass, m_{jj} is similarly the reconstructed hadronic W-boson mass with two jets and $m_{\nu lb}$ is the reconstructed leptonic top mass using the reconstructed muon or electron and one of the b-jets. The neutrino momentum p_x and p_y components in this last term, are set to be equal to corresponding components of the transverse missing energy $E_{\mathrm{T}}^{\mathrm{miss}}$. The p_z component is fitted to the value inside the range (-100000, +100000) GeV that minimizes the χ^2 expression. m_t is similarly allowed to float within the range (0, 2000) GeV, selecting the value that minimizes the χ^2 expression. σ_{diff}, σ_W and σ_{top} are the detector resolutions associated with each of terms in the expression respectively. Their calculated values are shown in section 7.8.1.1.

The first term constrains the reconstructed mass difference between the hadronic top mass and hadronic W-boson mass, $m_{bjj} - m_{jj}$. The second term contraints the reconstructed hadronic W-boson mass m_{jj}, separately (compared with $m_W = 80.4$ GeV). The third term constrains the leptonic top mass $m_{\nu lb}$. All the possible permutations are obtained using all the jets and b-jets present in the event. After the minimization process is over, either of the reconstructed variables m_{bjj}, m_{bjj}/m_{jj} and $m_{\nu lb}$ or the fitted variable, m_t can be used as observables for the analysis selecting at the end the variable that offers the smallest statistical uncertainty or highest sensitivity to the top width Γ_{top} parameter. An optimization study over these variables and secondary variables defined as combinations of them such as the $m_{bjj} - m_{jj}$

difference and the ratio m_{bjj}/m_{jj} was performed and is briefly described in section 7.9.4.1. The aim of this study was to select which variable was more sensitive to the parameter Γ_{top}. In fact the fitted m_t variable showed the highest sensitivity to the Γ_{top} compared with the other variables.

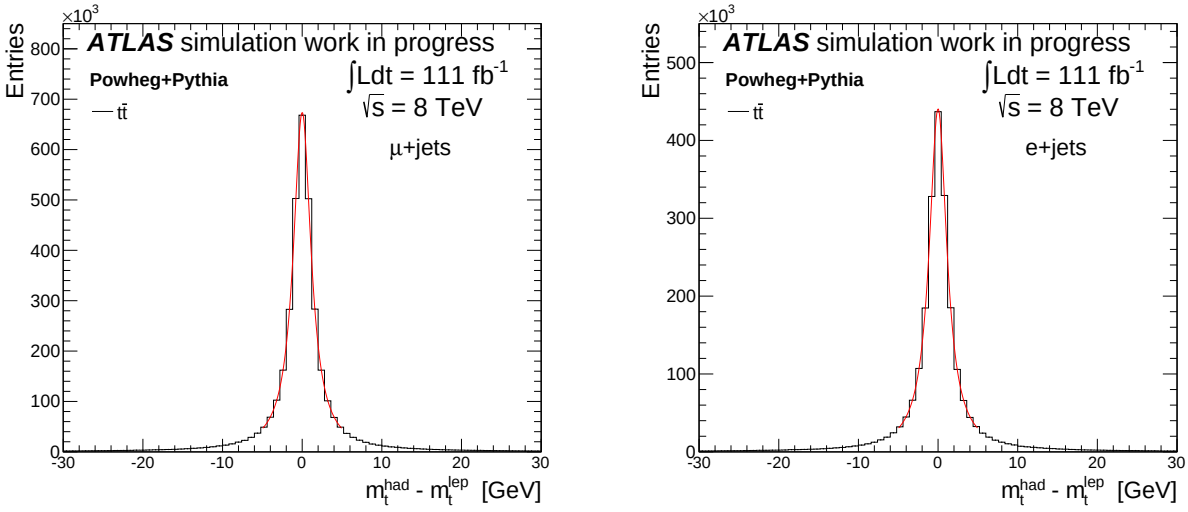

Figure 7.19: Distributions for the difference between the per-event truth values of top mass and anti-top mass in the μ + jets channel (left) and e + jets channel (right). The difference gives a average value of zero and typically these two masses have similar values in each of the events.

In principle the χ^2 expression could have two fitted variables like m_t, one for the hadronic side and one for the leptonic. Figure 7.19 shows the distributions for the difference between the truth leptonic and hadronic top masses for both channels. The difference of these two masses does not go beyond the detector resolution for the reconstructed top mass variables. The effect of adding a second fitted variable to the χ^2 expression in Equation (7.4) was studied. The obtained distributions from adding the additional fitted variable are indentical to the ones obtained with a single fitted variable, as the per-event difference between the truth leptonic and hadronic top masses is on average zero. Adding an extra fitted variable makes the per-event reconstruction substantially slower, therefore one fitted variable is used for this analysis. A similar global fitted variable was used for the width measurement performed

by CDF experiment [81].

An additional test was performed to see the effect of varying the transverse momentum of jets and transverse missing energy, within an uncertainty of 10 % of their values, during χ^2 minimization. However this variation does not affect the sensitivity of the obtained distributions to the top width. Adding such variations makes the per-event reconstruction substantially slower, therefore the χ^2 expression in Equation (7.4) is used for the analysis.

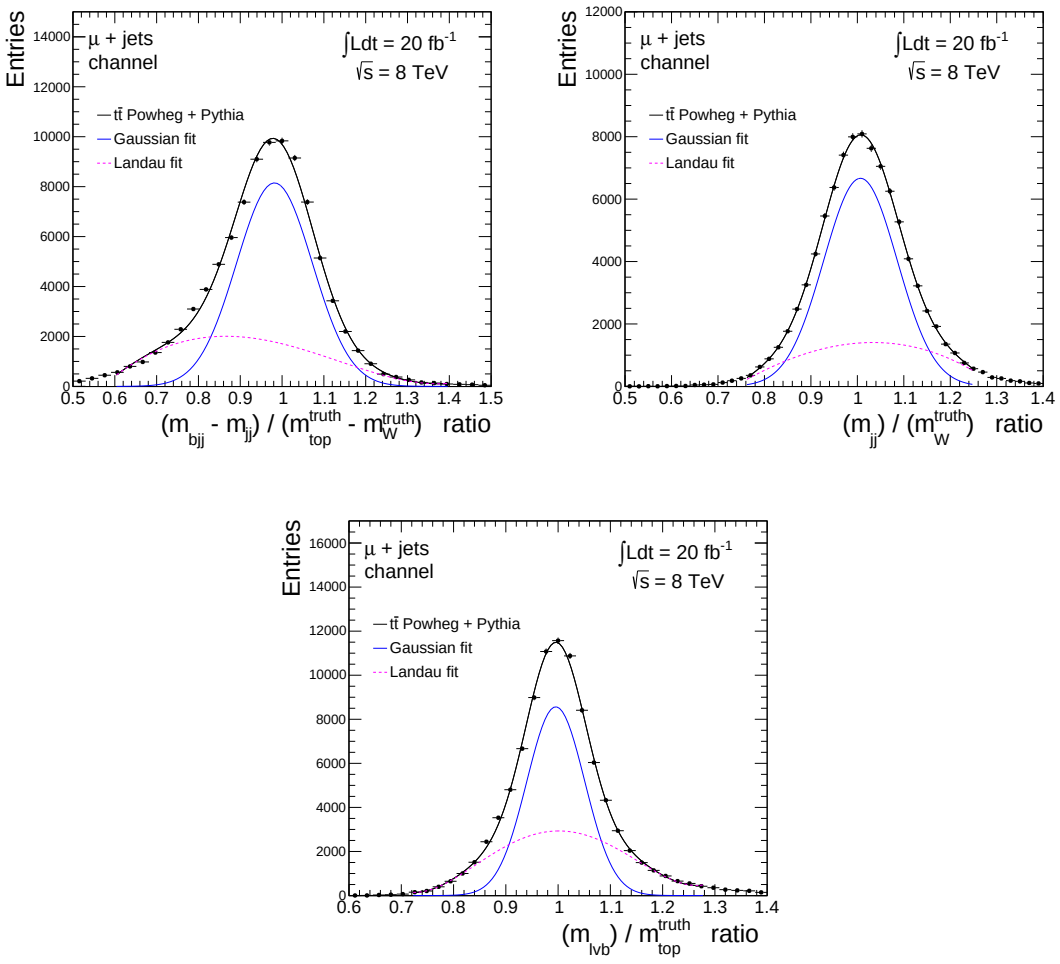

Figure 7.20: Distributions for per-event comparison between reconstructed and truth values of the variables $m_{bjj} - m_{jj}$, m_{jj} and $m_{\nu lb}$ respectively in the μ + jets channel, from these distributions it is possible to extract the detector resolutions associated with such variables.

7.8.1.1 Detector Resolutions

In order to calculate the sigma resolution values σ_{diff}, σ_W and σ_{top} for the χ^2 expression in Equation (7.4) the values for the constrained reconstructed variables $(m_{bjj} - m_{jj})$, m_{jj} and $m_{\nu lb}$ are required to be compared with their corresponding values at truth particle level. The mean values of the truth distributions of each of these variables are: 172.5 GeV - 80.38 GeV = 92.12 GeV for the $m_{bjj} - m_{jj}$ variable, 80.38 GeV for the m_{jj} variable and 172.5 GeV for the $m_{\nu lb}$ variable, where 80.38 GeV is the mass of the W boson [107] and 172.5 GeV stands for the mass of the top quark.

A *truth matching criteria* is implemented to make possible the extraction of accurate resolution values for these variables. The criteria select events where the ΔR distance (Equation 4.2) between each of the selected event jets (2 jets and 2 b-jets) with their associated quarks at truth level is ≤ 0.4 and also where $\Delta R \leq 0.2$ for the event lepton and its associated truth lepton. The signal sample containing $t\bar{t}$ events without background contributions is used to measure the σ resolution values for the χ^2 expression as for each of the reconstructed events the corresponding truth information is available.

Figure 7.20 shows the three distributions for the ratio of each of the three constrained variables in the χ^2 expression with respect to their corresponding truth values in the μ + jets channel selecting just the events that have passed the matching criteria. These three distributions peak around the value 1.0 as on average the reconstructed value is close to its corresponding truth value for the matched events. A Gaussian + Landau shape is fitted to the matched distributions, from where the sigma value of the fitted Gaussian gives the detector resolutions for each of the constrained variables after multiplying by the expected mean values of the variables at truth level.

The same distributions and fits were performed for the electron channel and are displayed in a similar way in Figure 7.21. The distributions for the electron channel have slightly worse resolution than the μ + jets channel ones and this is reflected in a slightly higher value for the σ values for the electron channel. All the resolution

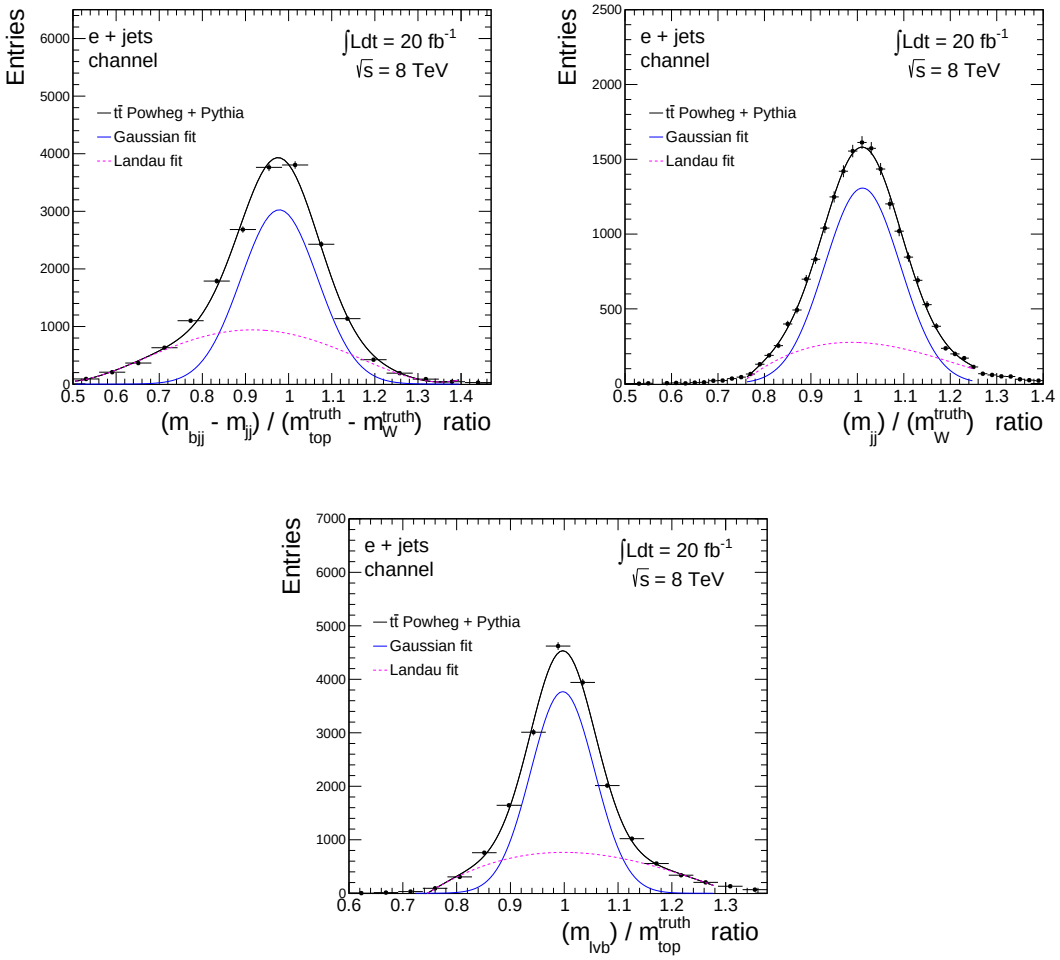

Figure 7.21: Distributions for per-event comparison between reconstructed and truth values of the variables $m_{bjj} - m_{jj}$, m_{jj} and $m_{\nu lb}$ respectively in the e + jets channel, from these distributions it is possible to extract the detector resolutions associated with such variables.

values are listed for both channels in Table 7.4. The best detector resolution corresponds to the reconstructed variable m_{jj} for both channels and the worst resolution to the $m_{\nu lb}$ variable as it involves the calculation of the p_Z momentum component of the neutrino and uses the selected leptonic b-jet. As mentioned before, during the χ^2 minimization the neutrino p_x and p_y components are set to be equal to the corresponding components of transverse missing energy $E_{\mathrm{T}}^{\mathrm{miss}}$, which is reasonable for events satisfying $E_{\mathrm{T}}^{\mathrm{miss}} > 30$ GeV as events with random small imbalances in transverse momentum not associated with neutrinos are rejected. The p_z component is then fitted to the value that minimizes the χ^2 value.

Table 7.4: Detector resolutions for constrained variables in χ^2 minimization method

Variable	μ + jets channel [GeV]	e + jets channel [GeV]
$m_{bjj} - m_{jj}$ (σ_{diff})	8.347	9.040
m_{jj} (σ_W)	6.353	6.524
$m_{\nu lb}$ (σ_{top})	9.541	10.360

7.8.1.2 Reconstruction Efficiency

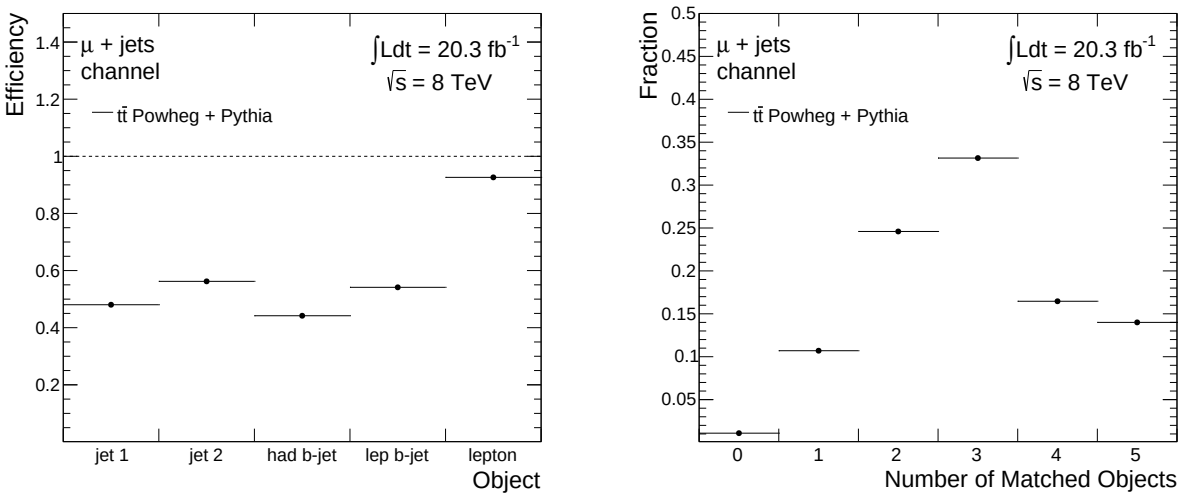

Figure 7.22: Matching efficiencies obtained by using the χ^2 method for the selected events separated by the individual objects (left) and by number of sucessfully matched objects (right) for the μ + jets channel.

The efficiency of the χ^2 reconstrution method described earlier is discussed in this section. For this analysis it is required to produce distributions sensitive to Γ_{top} in order to perform a fit to data.

For each of the selected events, the objects described in section 7.2 that are aimed to be selected correctly are: two b-jets should match two b-quarks at truth level, two jets should match with a pair of truth quarks either (u, d) or (s, c) and the event

reconstructed lepton with a truth muon or electron.

The signal sample containing just $t\bar{t}$ events without background contributions is used to test the reconstruction method efficiencies in a similar way to the previous sub-section. The efficiencies are defined as the fraction of events where the object has been matched correctly with its corresponding truth particle. In the plot in the left of Figure 7.22 efficiencies obtained from the χ^2 minimization method for the different objects are shown in the μ + jets channel. The efficiencies for the jet objects oscillate around 55% and the lepton efficiency surpasses 90%. The reason for this is that the selected leptons have already passed several isolation requirements and also just a single lepton is required for the selected events. The hadronic b-jet is slightly less likely to be matched than the leptonic b-jet as it has a higher chance to be confused with the other light-jets. In this case jet 1 corresponds to jets originating from quarks with absolute value of PDG ID equal to 1 and 4 (d and c quarks) and jet 2 corresponds to values 2 and 3 (u and s quarks) [37]. The plot in the right in the same figure shows the efficiency in terms of the per-event number of sucessfully matched objects. This distribution peaks at a value of 3 matched objects with 30% and the region ≥ 4 matched objects contains as well 30% of the events. This latter set of events introduce most of the sensitivity to Γ_{top}. All the columns in this plot add to 1.

In Figure 7.21 the same efficiencies are shown for the e + jets channel which have similar values for the individual objects and by number of matched objects to those in the μ + jets channel.

7.8.1.3 Reconstructed Variables Sensitive to Γ_{top}

The distributions for the per-event minimimized χ^2 values are shown in Figure 7.24 for both channels, where the total simulated prediction is compared with what is obtained from data. The selected events are located in the region $\chi^2_{min} < 7$, this constraint optimizes the statistical uncertainty as it is described in section 7.9.4.2. Additionally the reconstructed hadronic W-boson mass $m^{reco}_{W_{had}}$, is required to satisfy

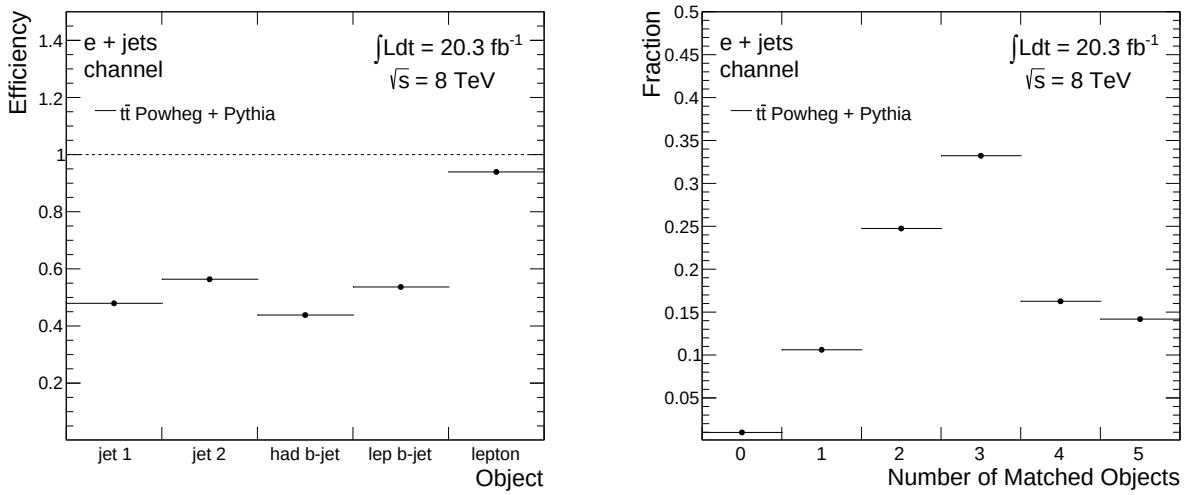

Figure 7.23: Matching efficiencies obtained by using the χ^2 minimization method for the selected events separated by the individual objects (left) and by number of sucessfully matched objects (right) for the e + jets channel.

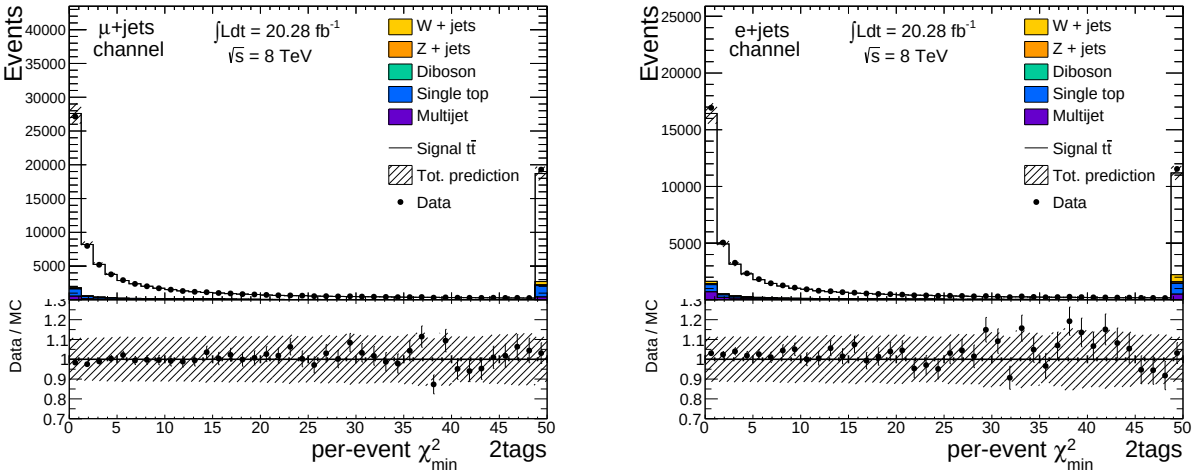

Figure 7.24: Distributions for per-event recorded minimized χ^2_{min} values for both channels muon + jets (left) and electron + jets (right). An optimal constraint of $\chi^2_{min} < 7$ is applied to decrease the statistical uncertainty.

the constraint 60 GeV $< m^{reco}_{W_{had}} <$ 80 GeV to reduce combinatoric errors.
The yield numbers for the final set of selected events are listed in table 7.5 for total simulated prediction and data from the ATLAS experiment at 8 TeV centre-of-mass collision pp energies. The observed number of events in data are within the statisti-

cal + systematic uncertainties of the total prediction for both channels. Tables 8.1 and 8.2 in the following chapter are expansions of Table 7.5 with all the background contributions included.

Table 7.5: Final set of selected events after applying χ^2 constraint and m_W^{reco} window. A more detailed set of yields is shown in Table 8.1.

Channel	μ + jets channel	e + jets channel
$t\bar{t}$	$45732\ ^{+2600}_{-2800}$	$26359\ ^{+1600}_{-1700}$
Total prediction	$49180\ ^{+2600}_{+2800}$	$29500\ ^{+1600}_{+1700}$
$t\bar{t}$ significance	0.93	0.89
Data	48502	30345

For the final set of selected events, the distribution significance is defined as in Equation (7.5):

$$\mu = \frac{S}{S+B} \tag{7.5}$$

where S stands for selected signal events and B for events corresponding to background contributions. The $t\bar{t}$ significance has the value ~ 0.93 and ~ 0.89 for muon and electron channels respectively, which indicates that the MC prediction for both channels is dominated by the $t\bar{t}$ distribution. The bigggest contributions to the backgrounds at this stage come from QCD multijet and single top backgrounds for both channels. All fractional contributions of the different backgrounds are shown in Table 8.2

As mentioned before in section 7.8.1 the variables sensitive to Γ_{top} extracted from the χ^2 reconstruction that can be used for the measurement are: m_{bjj}, $m_{\nu lb}$, $m_{bjj} - m_{jj}$, m_{bjj}/m_{jj} and the fitted variable m_t. Figure 7.25 includes the distributions for

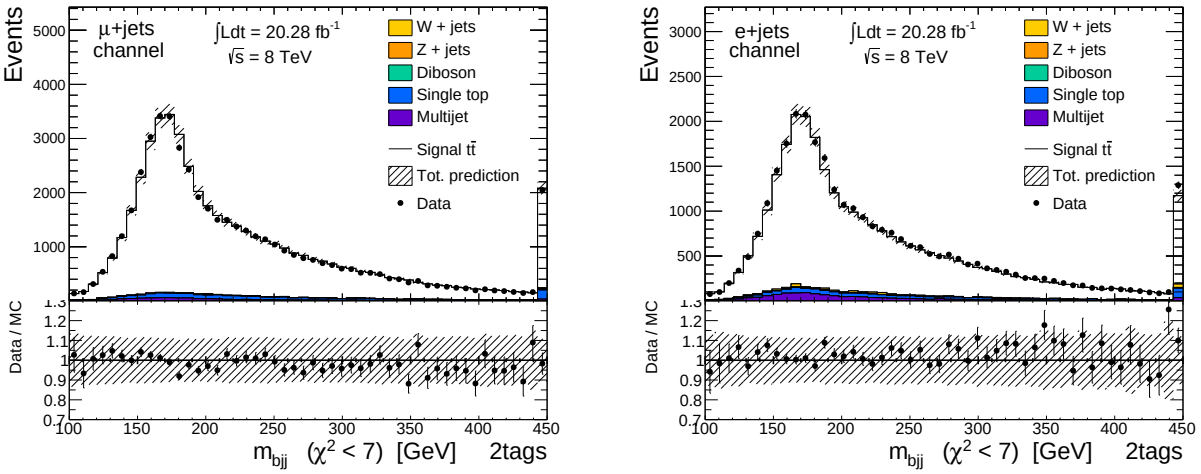

Figure 7.25: Distributions for the m_{bjj} hadronic top invariant mass with peak around 172.5 GeV in the μ + jets (left) and e + jets (right) channels respectively after applying a χ^2_{min} constraint and a reconstructed hadronic W-boson mass window cut.

hadronic reconstructed top quark mass m_{bjj}, for both channels which is produced by calculating the invariant mass of the selected hadronic jet triplet. The plots in Figure 7.25 include the signal $t\bar{t}$ distribution with the expected SM width Γ_{top} = 1.33 GeV, and the different background contributions for the final set of selected events. The distribution obtained from data is also included. A comparison between the total MC prediction and data distributions is included in the comparison at the bottom of the plots, which shows that the data distribution agrees well with the simulated events with Γ_{top} = 1.33 GeV.

A similar distribution corresponding to the reconstructed leptonic top mass $m_{\nu lb}$, is shown in Figure 7.26 with peak around the mean top mass value 172.5 GeV, here the fitted momentum p_Z component is required to calculate the invariant mass.

The $m_{bjj} - m_{jj}$ difference variable is shown in the plots in Figure 7.27 which is plotted in the range [0, 350] GeV and has a similar shape and comparison between data and MC as the previous variables.

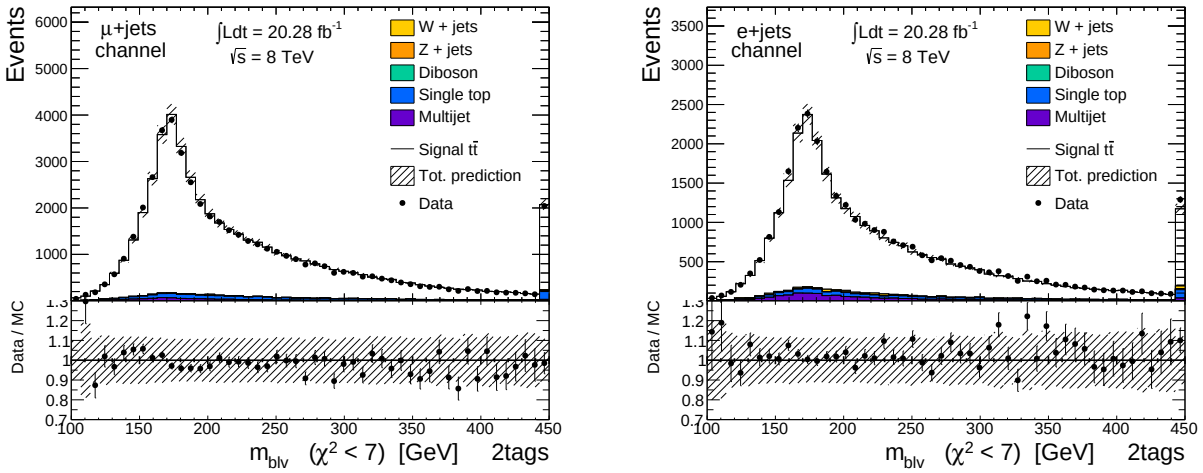

Figure 7.26: Distributions for the m_{blv} leptonic top inviariant mass with peak around 172.5 GeV in the μ + jets (left) and e + jets (right) channels respectively after applying a χ^2_{min} constraint and a reconstructed hadronic W mass cut.

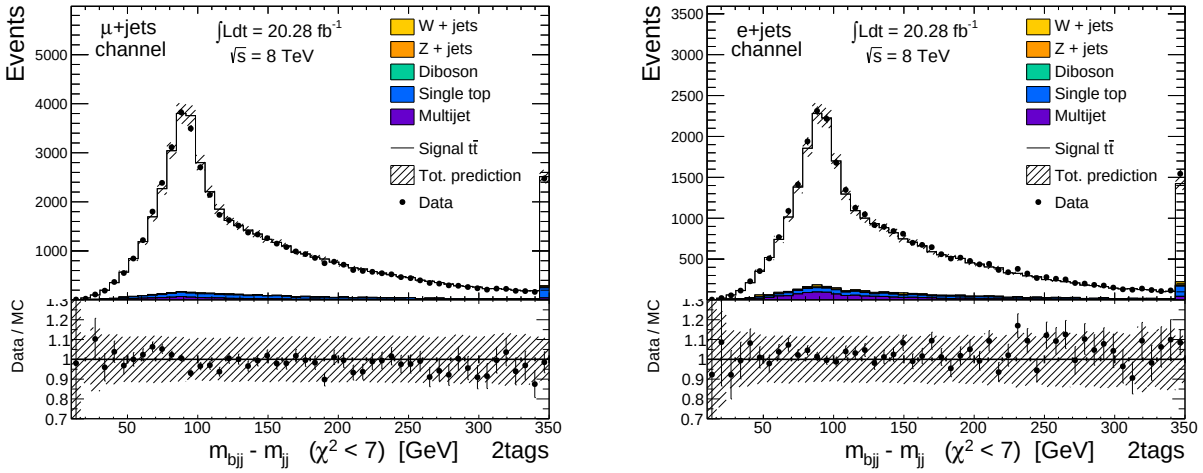

Figure 7.27: Distributions for the $m_{bjj} - m_{jj}$ hadronic difference with peak around 92.1 GeV in the μ + jets (left) and e + jets (right) channels respectively after applying a χ^2_{min} constraint and a reconstructed hadronic W-boson mass window cut.

Another alternative variable can be built by taking the ratio between invariant mass of the hadronically decaying top quark and the hadronic W-boson invariant mass obtained from the minimization, expressed as: m_{bjj}/m_{jj}. The distribution for this

ratio is shown in Figure 7.28 for both channels in the range [0, 6] with peak around the value 2.1 as expected, and with similar shape as the other variables.

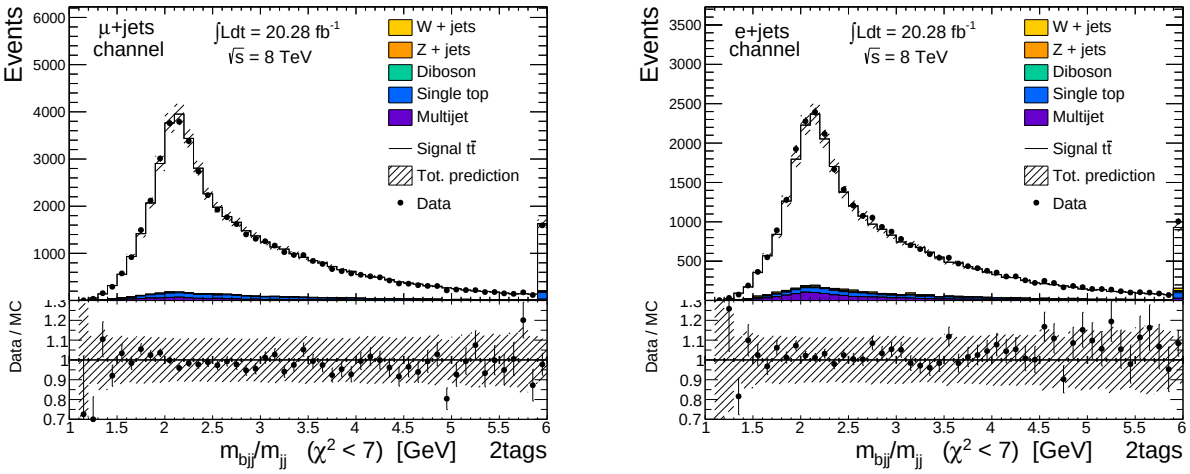

Figure 7.28: Distributions for the m_{bjj}/m_{jj} hadronic ratio with peak around the value 2.1 in the μ + jets (left) and e + jets (right) channels respectively after applying a χ^2_{min} constraint and a reconstructed hadronic W-boson mass window cut.

The distribution of the m_t fitted variable is shown similarly for both channels in Figure 7.29. From the plots in figures 7.25 to 7.29 it can be seen how data match well with the shape corresponding to the expected SM top quark width, $\Gamma_{top} = 1.33$ GeV used for these simulated distributions.

An optimization of the analysis uncertainties based on pseudo-experiments was performed as described in section 7.9.4.1. From this study as shown in table 7.7, the m_t distribution resulted in being the optimal variable to be used for the analysis as it provides the smallest statistical uncertainties for both channels. In other words this variable is the most sensitive to the variation of the Γ_{top} values.

7.8.1.4 Truth Matching and Sensitivity to Γ_{top}

From the selected distributions shown in Figure 7.29 the events where the reconstructed physical objects match their corresponding particles at truth level in the $t\bar{t}$

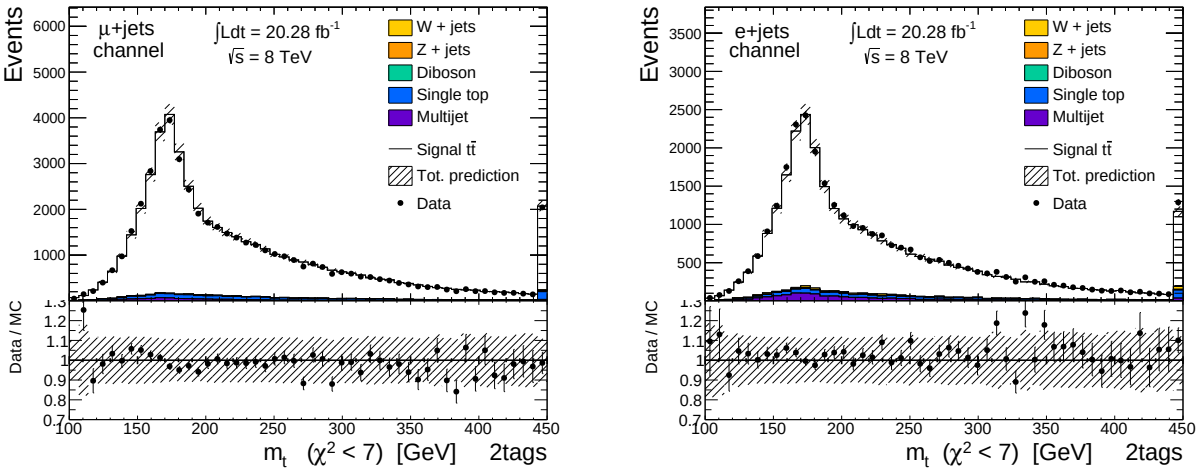

Figure 7.29: Distributions for the m_t fitted variable with peak around the value 172.5 GeV in the μ + jets (left) and e + jets (right) channels respectively after applying a χ^2_{min} constraint and a reconstructed hadronic W-boson mass window cut. This variable was selected as optimal to perform the measurement.

signal shape can be separated to visualise better the fraction of the total distribution that introduces sensitivity to the Γ_{top} parameter. Details about the truth matching criteria are described in section 7.8.1.1.

Table 7.6: Gaussian sigma values for matched m_t distributions with different Γ_{top}

Γ_{top} [GeV] / Channel	Gaussian Sigma (e + jets) [GeV]	Gaussian Sigma (μ + jets) [GeV]
0.7	13.48	13.47
1.3	13.66	13.66
3.0	14.15	14.18
5.0	14.73	14.85
7.0	15.31	15.52
10.0	16.14	16.49

Figure 7.30 displays the m_t distribution that just includes the truth-matched events for both channels. This is the part of the main distribution that mostly differenciates the templates with different underlying values of Γ_{top}. A Gaussian function was

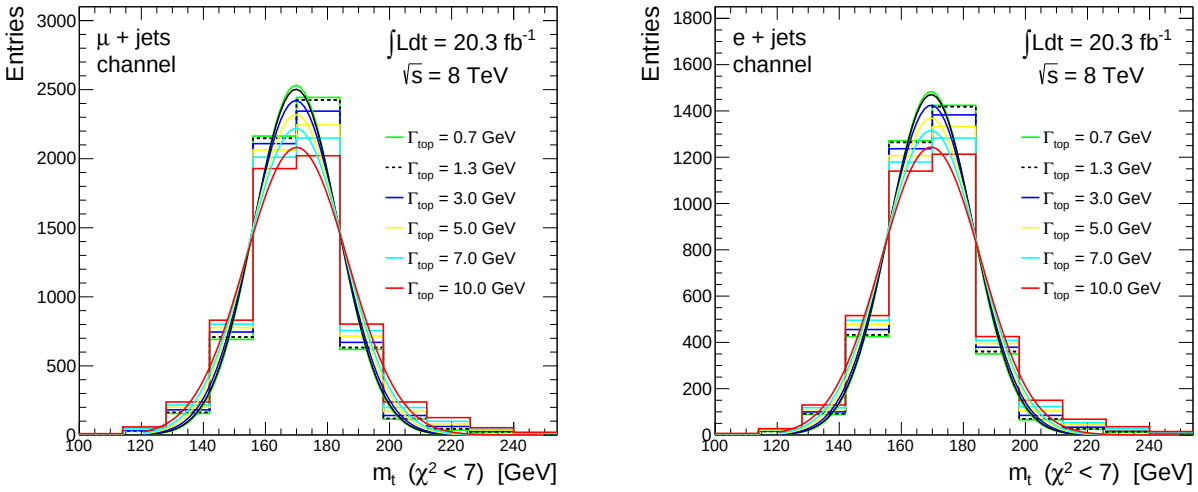

Figure 7.30: Distributions of the fitted m_t variable for the selected events where reconstructed objects perfectly match their associated particles at truth level for the μ + jets (left) and e + jets (right) channels respectively. These are the events that introduce most of the sensitivity to Γ_{top}.

fitted to these distributions as can be seen in the figure, the Gaussian sigma values corresponding to each width are listed in Table 7.6 for both channels.
As expected, the distributions become narrower as the width is decreased. The distribution shapes for both channels look consistent with each other.

7.8.1.5 Additional Kinematic Variables

Additional variables can be constructed from jet assignmment in the event reconstruction such as the ΔR distance between the event lepton and the reconstructed hadronic W-boson. This distribution is shown in the left of Figure 7.31 for the muon channel, which clearly peaks at a value of 3.14 when the lepton and the hadronic b-quark are recorded to be approximately back-to-back with respect each other in the x-y plane with almost no momentum components along the z-axis.
This variable could be used to set an extra constraint for the event selection. The plot in the right in the same figure displays a similar variable, the distance between the hadronic W-boson and the b-jet assigned to the leptonic side of the $t\bar{t}$ system

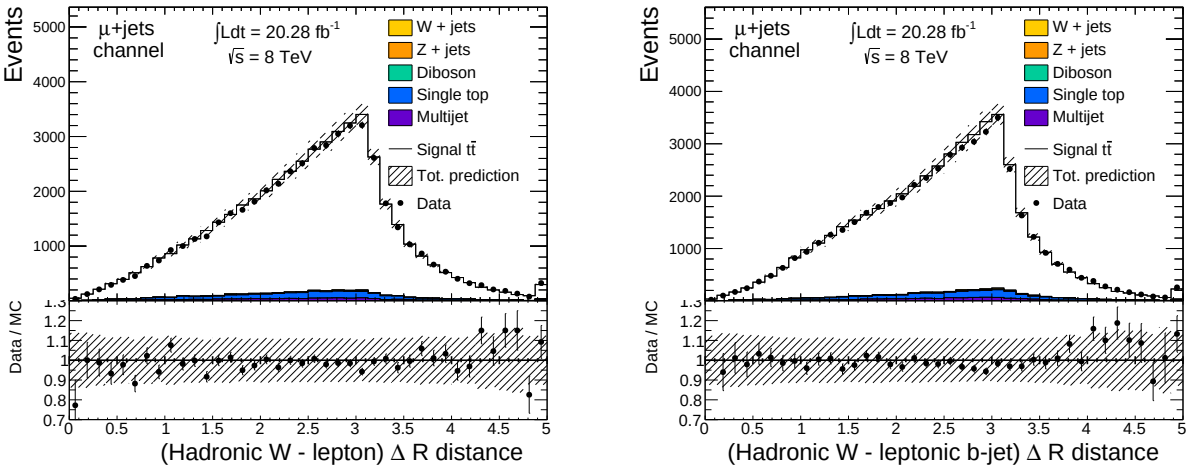

Figure 7.31: Recorded ΔR distance between the event lepton and reconstructed hadronic b-jet, peaking at a value of 3.14 when the leptonic and hadronic sides are aproximatelly back-to-back with respect each other (left). A similar variable the distance between the selected b-jet and the lepton with similar shape (right). Both distributions for the muon channel.

in the event reconstruction. As the lepton has been replaced by a b-jet the peak around 3.14 loses some resolution with more entries at smaller ΔR.

The distribution corresponding to the ΔR distance between the two selected event b-jet objects (event $b\bar{b}$ pair) is shown in the left of Figure 7.32. This distribution in a similar way has a peak around the value 3.14, but is less defined than in the two previous distributions as for this variable only information from selected b-jets is used. This carries more uncertainty as there is a possibility to confuse one of the b-jet objects with any of the ordinary jets in the events. In the right of the figure is the same distribution for the electron channel which looks similar.

Unfortunately these variables could not be used for this analysis, as additional cuts on the selected events affect the sensitivity of the m_t distributions to Γ_{top} significantly. However they could potentially be used for the $t\bar{t}$ analyses during LHC run-II with 13 TeV pp collisions, as more statistics will be delivered and additional constraints could be applied without affecting the sensitivity of the distributions to

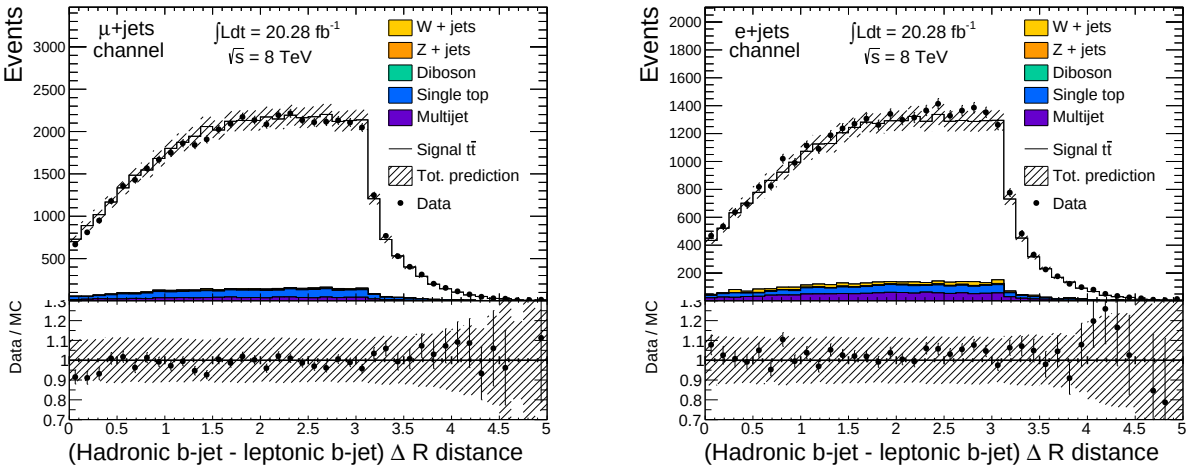

Figure 7.32: ΔR distance between the selected event b-jet and $\bar{b}$-jet, the peak around 3.14 is less defined as the distribution gains more contributions for low ΔR values, due to combinatoric errors in the selection of the b-jet objects, in the μ + jets (left) and e + jets (right) channels respectively.

the different parameters. For example only the events with $\Delta R(l, \mathrm{W}_{had}) > 1.5$ could be selected, where l is the event lepton and W_{had} is the reconstructed hadronic W-boson. These events would have the hadronic and leptonic sides back-to-back with respect to each other, reducing the combinatoric errors in the event reconstruction, as the jets reconstructing the hadronic top quark would be well separated from the event lepton and the b-jet originating from the leptonic top quark.

7.8.2 KL-Fitter Reconstruction

The KL-Fitter reconstruction method for $t\bar{t}$ event object assignment makes use of a likelihood-based reconstruction algorithm [110]. The algorithm is used to reconstruct the $t\bar{t}$ topology with a single lepton, by performing a per-event likelihood scan over the different possible permutations of hadronic jets reconstructing the hadronically decaying W-boson and the pair of b-jets, so the combination that maximizes the likelihood distribution is selected. The likelihood expression that is maximized with this method is in Equation (7.6) [110]:

$$
\begin{aligned}
L = & B(m_{q_1q_2q_3}|m_{top},\Gamma_{top}) \times exp[-4 \times ln(2) \times \frac{(m_{q_1q_2} - m_W)^2}{\Gamma_W^2}] \\
& \times B(m_{q_4\ell\nu}|m_{top},\Gamma_{top}) \times B(m_{\ell\nu}|m_W,\Gamma_W) \\
& \times \prod_{i=4}^{4} W_{jet}(E_{jet,i}^{meas}|E_{jet,i}) \times W_\ell \\
& \times W_{miss}(E_x^{miss}|p_x^\nu) \times W_{miss}(E_y^{miss}|p_y^\nu)
\end{aligned}
\tag{7.6}
$$

where the functions B represent Breit-Wigner functions. The free parameters are the mass of the top quark, m_{top}, the jet energies $E_{jet,i}$ (i = 1, ... , 4), the energy of the charged lepton, E_ℓ and the three momentum components of the neutrino assuming that the leptonic W-boson invariant mass can be espressed as $m_W^2 = (p_\nu + p_\ell)^2$, where p_ν and p_ℓ. The expressions $m_{q_1q_2q_3}$, $m_{q_1q_2}$, $m_{q_4\ell\nu}$ and $m_{\ell\nu}$ are the invariant masses of the reconstructed hadronic top quark, hadronic W-boson, leptonic top quark and leptonic W-boson respectively. The particle's energies are constrained in the last two terms based on the measured energies, using transfer functions with gaussian shape. These functions are obtained from matching the MC events with truth particles, the functions represent then the detector resolution. The top quark and W-boson widths are fixed to the values Γ_{top} = 1.3 GeV and Γ_W = 2.1 GeV [110].

Distributions of different variables obtained from this reconstruction method were used to make preliminary statistical studies described in section 7.9.4.3. Similar values for the statistical uncertainties were obtained by using the distributions from the KL-Fitter to those obtained from χ^2 method. It takes much longer to process each of the events with the KL-Fitter method than the χ^2 minimization method, which turned out to be impractical during the course of the analysis, considering the size of the MC and data samples to be processed each time the analysis software had an upgrade of its scale factors and calibrations. Therefore it was decided to complete this analysis with the χ^2 method. However the KL-Fitter reconstruction was tested and could be used for future measurements once the collaboration anaysis software

reaches its final version for 8 TeV analyses.

The author started and supported an effort to expand the analysis so the Jet Energy Resolution (JER), is measured along with the Γ_{top} parameter using the KL-Fitter reconstruction (section 7.10). Such collaboration has progressed sucessfully but slowly and this 2-dimensional analysis is currently in progress with main support from colleagues at Goettingen University.

In Figure 7.33 the distribution of the m_t variable from KL-Fitter is shown on the left, this is a fitted variable like the m_t fitted variable from the χ^2 method, this clearly spreads the events within a smaller range $\sim$ [130, 210] GeV than observed with the χ^2 method (Figure 7.29). However the templates with different Γ_{top} obtained with KL-Fitter do not gain any separation or sensitivity with respect to the distributions from the χ^2 method as can be seen from the comparison plot at the bottom of the plot, which can be compared with the relationship between templates from the χ^2 method in Figure 7.34.

On the right of Figure 7.33 the reconstructed hadronic W-boson mass distribution is shown for different values of the Jet Energy Resolution. The templates with different JER value are produced as described in section 8.2.4.2, where the JER systematic uncertainty is described. These distributions from KL-Fitter were also used to perform preliminary statistical studies towards a 2-dimensional analysis that includes the JER as a second parameter of interest. More details about this study are included in section 7.10.

7.9 1-Dimensional Fit with Γ_{top} as Parameter

In this analysis Γ_{top} is the single parameter of interest. The methodologies to perform likelihood fits and extract uncertainties are described in section 7.9.1. The

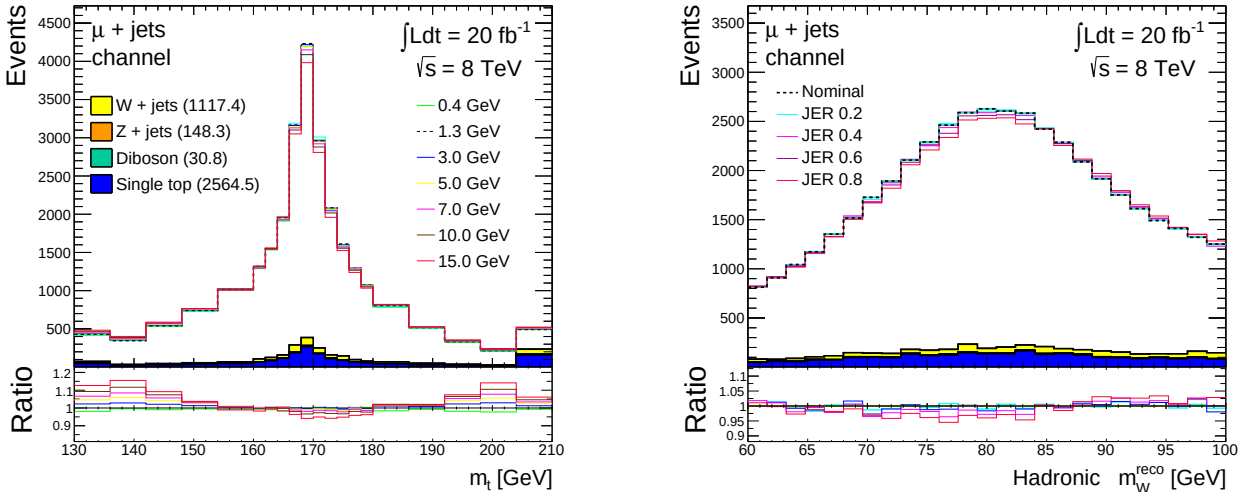

Figure 7.33: Reconstructed distributions from KL-Fitter reconstruction. Distribution of m_t variable spreading mostly within the range [130, 210] GeV, The comparison ratio at the bottom has been made with respect the template with the SM width $\Gamma_{top} = 1.33$ GeV (left), and W-boson mass distribution width different values of JER, the ratio at the bottom of the plot is taken with respect the template with nominal JER (right).

procedure to obtain confidence intervals for the different Γ_{top} values is described in sections 7.9.2 and 7.9.3. Results from optimization studies are included in section 7.9.4, where the selection of the variable from the χ^2 method with the highest sensitivity to Γ_{top}, and also the optimal χ^2_{min} cut are described.

As described in the following chapter the systematic uncertainty corresponding to Jet Energy Resolution, has a relatively large contribution compared with the rest of the uncertainties for the 1-dimensional measurement. This led to the idea recently of increasing the amount of analysis person-power within the collaboration to expand the 1-dimensional analysis produced by the author to a 2-dimensional analysis that gives measured Γ_{top} and JER as result. Preliminary studies performed by the author towards a 2-dimensional measurement are described in section 7.10.

7.9.1 Likelihood Scans

The package `RootFit` is used to calculate the statistical and systematic uncertainties for this analysis. It is written as a library of C++ programing language, compatible with the ROOT environtment. This package is widely used in different analyses throughout particle physics. It is very straightforward to run and allows the execution of several kinds of statistical studies. Details of the different objects and techniques that can be used with RooFit are in references [127] and [129].

In Figure 7.34 the distributions of the optimal variable m_t (section 7.9.4.1) obtained from the χ^2 reconstruction after applying a $\chi^2_{min} < 7$ cut and a hadronic W-boson mass window (section 7.8.1.3), are displayed for different values of Γ_{top} in both channels. The Γ_{top} templates are produced as described in section 7.7. This time the common part of the background for the different width templates has been filled with light blue colour and separated from the signal shape including the $t\bar{t}$ distribution and the single top distribution both with varying Γ_{top}. The bin sizes of the distributions have been customized to reduce statistical fluctuations mostly in the regions with low statistics as can be seen by comparing with the distributions shown in Figure 7.29 with smaller bin sizes but with the same events. Most of the sensitivity for the Γ_{top} parameter is within the region $\sim$ [100, 240] as shown in Figure 7.30.

For each of the templates with varying Γ_{top} shown in Figure 7.34 a histogram Probability Density Function (PDF), with exactly the same shape called `RooHistPDF` [132] can be produced with `RooFit`. This function is the same histogram normalized to one within its range and is represented as $P(m_t|\Gamma_{top})[i]$ as shown in Equation 7.7:

$$\sum_i P(m_t|\Gamma_{top})[i] = 1 \tag{7.7}$$

where m_t is the variable used to produce the distributions and Γ_{top} is the value of the top quark width associated with the distribution. This histogram PDF indicates the

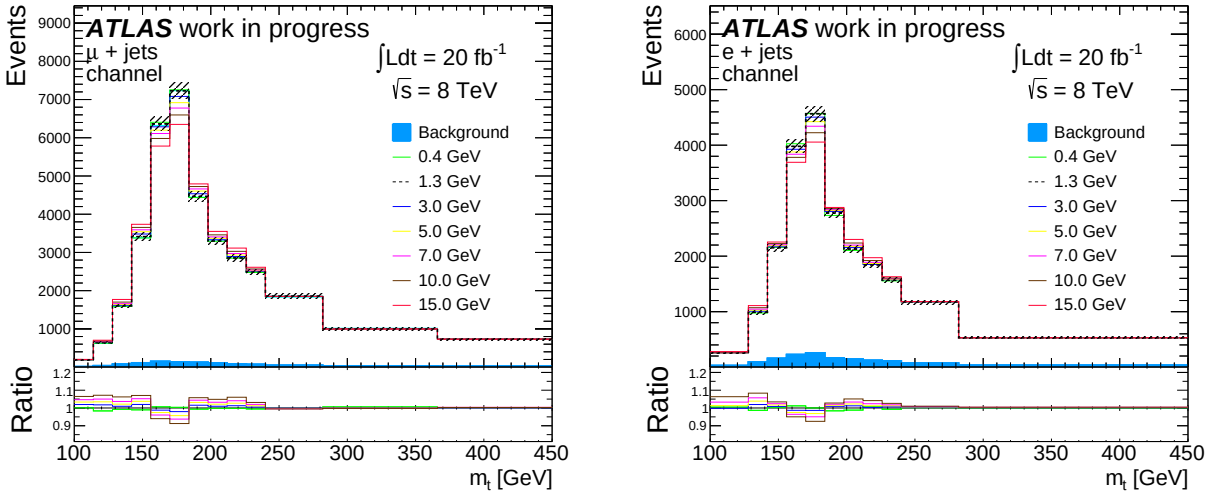

Figure 7.34: Different simulated templates with different underlying Γ_{top} for the m_t optimal variable. The common part of the background has been filled with blue. The comparison ratio at the bottom has been made with respect the template with the expected SM width $\Gamma_{top} = 1.33$ GeV.

probability of obtaining a m_t value within certain bin number i given an input width value Γ_{top}. The sum is performed over the histogram bins. Two separated histogram PDF's are generated for each of the Γ_{top} templates, one for the signal distribution and one for the background distribution. These two separated PDF's are added together into a main `RooHistPDF` histogram specifying the fraction of the shape that corresponds to the background shape for each of the Γ_{top} values. This main PDF histogram satisfies Equation (7.7). The background and signal shapes are separated like this because `RooFit` allows the production of random pseudo-data sets out of the original templates, producing separated events for background and signal shapes.

To compare any arbitrary m_t distribution corresponding to an unknown top width value Γ_{top}, with the same configuration of bins as shown in the Figure 7.34 a *binned likelihood* shape, $\mathcal{L}_{shape}$ is defined as in Equation (7.8):

$$\mathcal{L}_{shape}(m_t|\Gamma_{top}) = \prod_{i=1}^{nbins} P(m_t|\Gamma_{top})[i] \times n_i \tag{7.8}$$

where n_i are the bin entries of the arbitrary histogram for the bin i and the product is taken over the total number of bins of the corresponding template with width value Γ_{top}. The random m_t distribution with bin entries n_i is the input distribution. Equation 7.8 gives a single point of the likelihood distribution corresponding to a particular Γ_{top} value in the range (0, 10) GeV. The whole likelihood distribution is obtained when repeating the same procedure with the different histogram PDF templates with varying values of Γ_{top} but using same input m_t distribution with the same bin entries n_i.

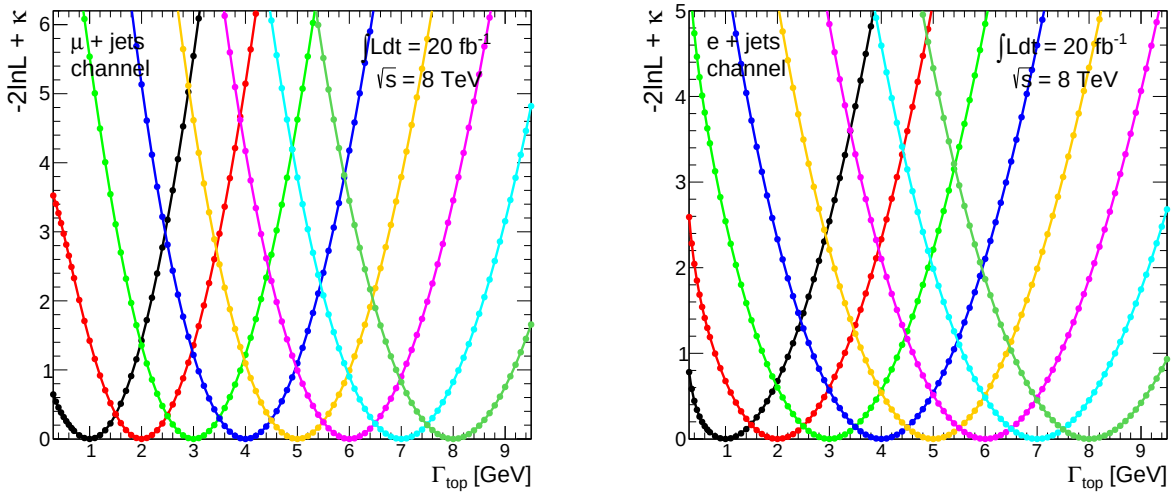

Figure 7.35: -2ln($\mathcal{L}_{shape}$) + κ distributions for different values of input Γ_{top} equal to 1.0, 2.0, 3.0, 4.0, 5.0, 6.0, 7.0 and 8.0 GeV in the μ + jets (left) and e + jets (right) channels respectively. The minimum of each distribution is located where the input Γ_{top} value is located, returning in each case the expected value.

Any of the produced templates (Figure 7.34) with width value Γ_{top} within the range [0, 10] GeV can be used as input distributions in the same way using Equation 7.8. The Γ_{top} value of the template that is selected as the input distribution is the input

top width, Γ_{top}^{input}. The binned likelihood distributions obtained by using different templates as input distributions are shown in Figure 7.35. Here rather than plotting $\mathcal{L}_{shape}$ directly, (-2) $\times$ ln($\mathcal{L}_{shape}$) + κ is plotted. The multiplication by -2 inverts the distribution shape and the κ shift value is set so the minimum of the resulting distribution is located at zero. It can be seen from the plots that the minimum of each of the obtained distributions is exactly where the input Γ_{top}^{input} value is located for each of the cases, which means the templates can be distinguished well from each other. So the likelihood distributions produced from Equation (7.8) can be used successfully to obtain the Γ_{top} value corresponding to any arbitrary m_t histogram.

Each of the template `RooHistPDF` histograms can be used as well to generate a random toy pseudo-data set originated from the original input histogram as prototype, by varying its shape and normalization [132]. This is done by generating a random poisson variation over each of the bin contents of the original m_t histogram. The original bin contents are the expected values for each of the bins. This variation is done over the background and signal histograms separately and the produced events are added together afterwards obtaining a particular random data set.

Figure 7.36 shows the produced -2ln($\mathcal{L}_{shape}$) + κ distributions obtained by using as input for the likelihood calculation in Equation (7.8), different random pseudo-data sets produced out of the template histogram corresponding to width value Γ_{top} = 5 GeV. In this case the minima of the distributions are located at values around the expected input value, 5 GeV for each of the generated random pseudo-data sets.

Figure 7.37 shows on the left the -2ln($\mathcal{L}_{shape}$) + κ distribution obtained by using the original template with width Γ_{top} = 3 GeV as input, having minimum exactly at 3.0 GeV. The black and green lines can be used as first estimations of the statistical uncertainties at 68 % and 95 % C.L. [38], though for this analysis all the uncertainties are calculated via pseudo-experiments. In the right a distribution corresponding to a random data-set derived from the Γ_{top} = 3 GeV template is shown, having a minimum around 3 GeV.

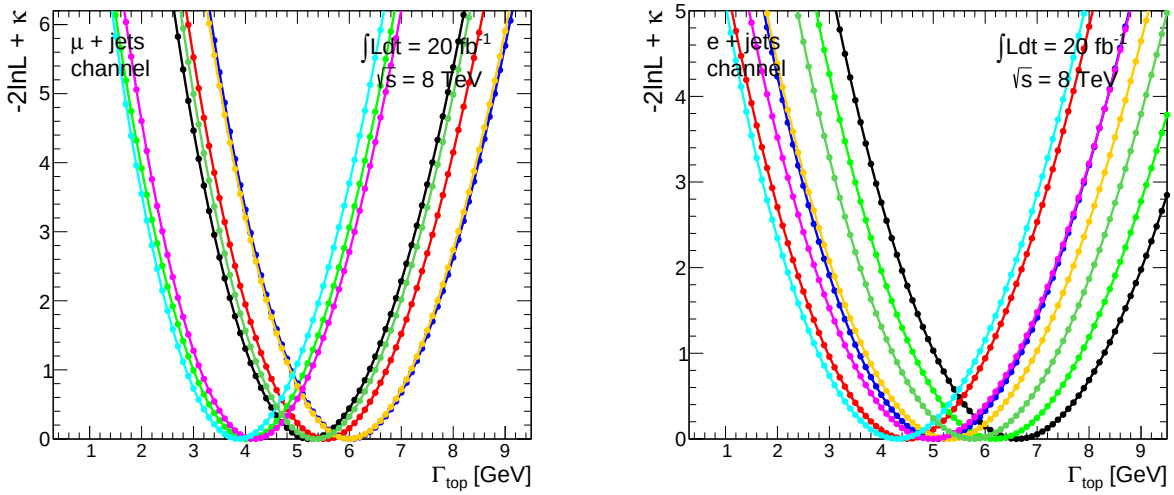

Figure 7.36: -2ln($\mathcal{L}_{shape}$) + κ distributions obtained by comparing random pseudo-data sets obtained from the histogram with Γ_{top} = 5 GeV with the rest of the templates using Equation (7.8) in the μ + jets (left) and e + jets (right) channels respectively. Each colour corresponds to a different pseudo-data set.

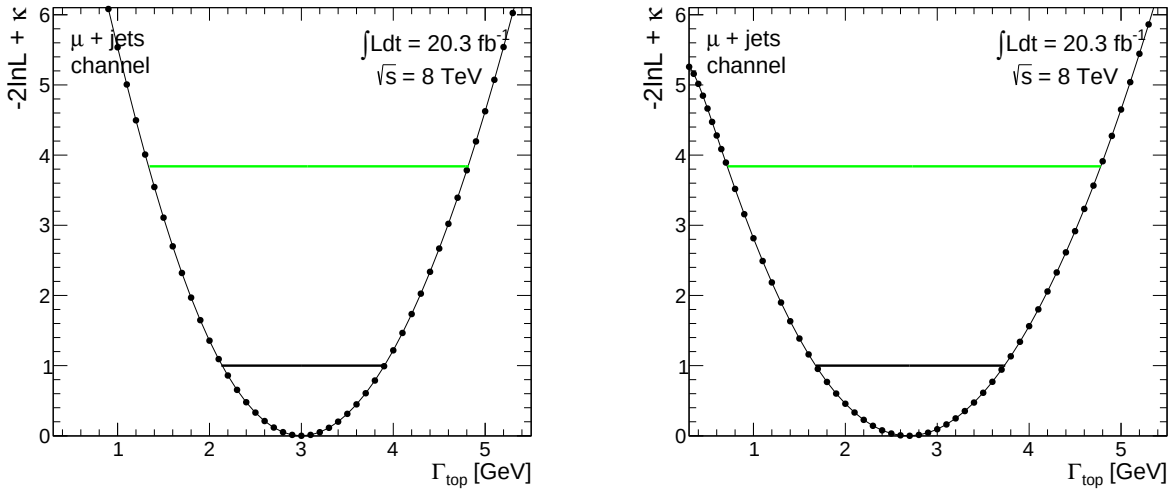

Figure 7.37: -2ln($\mathcal{L}_{shape}$) + κ distributions obtained by using Equation (7.8), comparing the original template histogram with Γ_{top}^{input} = 3 GeV with the rest of the templates (left), and comparing a random pseudo-data set derived from the template with Γ_{top} = 3 GeV with the rest of the templates (right).

7.9.2 Pseudo-Experiments

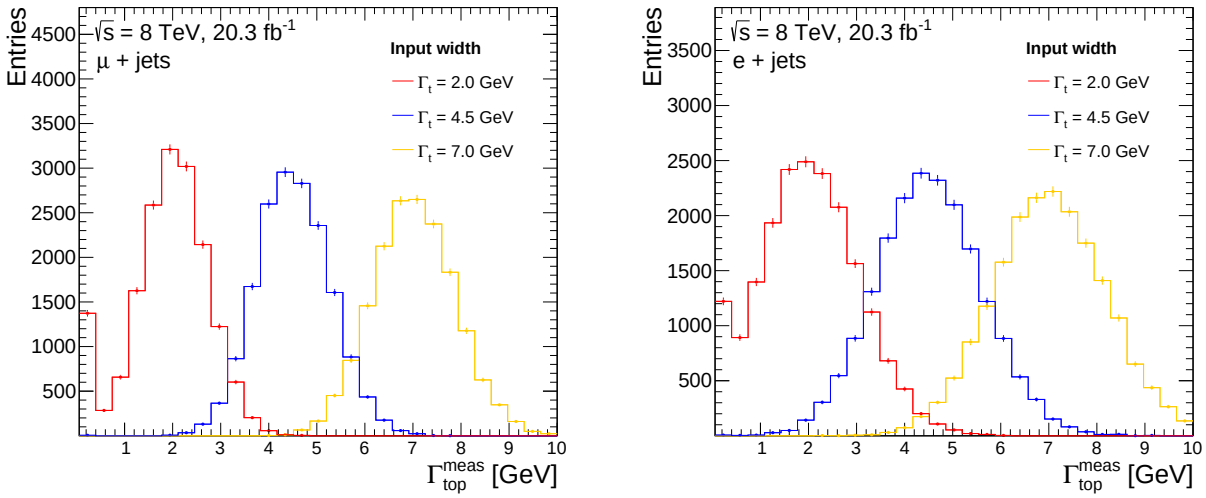

Figure 7.38: Distributions of the minimum of the $2\ln(\mathcal{L}_{shape}) + \kappa$ distribution from 20K pseudo-experiments using different input Γ_{top}^{input} values for both channels, μ + jets (left) and e + jets (right).

The distributions in Figure 7.36 are examples of pseudo-experiments, where a random data-set is produced out a particular template histogram and the minimum of the corresponding -2ln($\mathcal{L}_{shape}$) + κ distribution is recorded as measured width Γ_{top}^{meas}. If many random pseudo-experiments are performed ($\sim$ 20K) and the obtained Γ_{top}^{meas} are filled into a histogram, distributions like the ones shown in Figure 7.38 are obtained.

These distributions spread around the input width value that was used to generate the pseudo-data sets for each of the cases. In the figure, the input width values Γ_{top}^{input} = 2, 4.5 and 7 GeV were used. The distributions have a gaussian-like shape, though that was not required. The fluctuations of measured values to lower or higher values of Γ_{top}^{meas} are stored in inclusive bins at the end of the range at Γ_{top}^{meas} values 0 GeV and 10 GeV.

7.9.3 Feldman Cousins and Acceptance Intervals

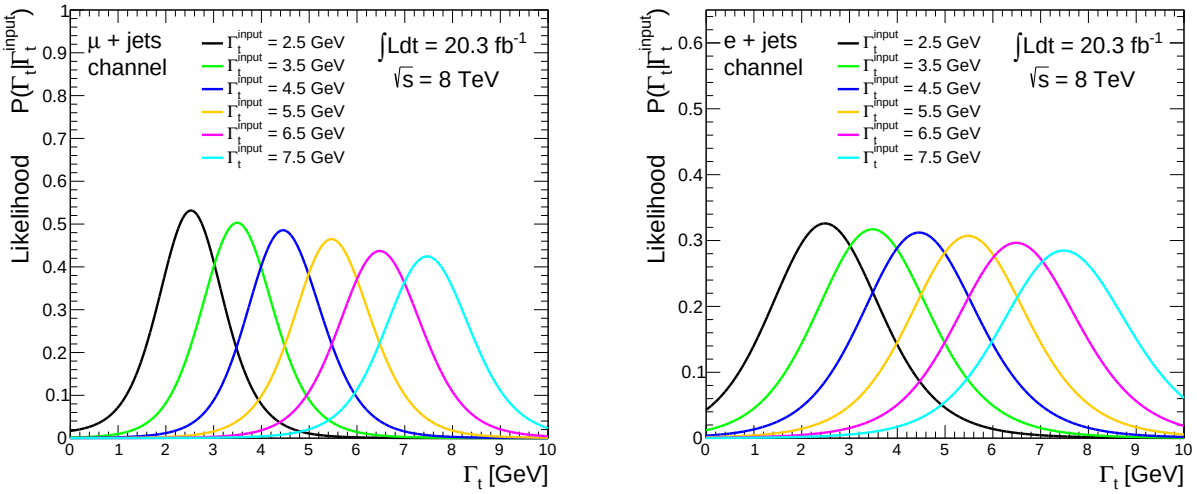

Figure 7.39: Output distributions in pseudoexperiments for different input Γ_{top}

In order to obtain a probability density $P(x|\Gamma_{top}^{input})$, giving the probability of obtaining a particular measured width x given an input width Γ_{top}^{input}, a Kernel Density Estimation (KDE) shape [141] is built from the pseudo-experiments. These functions are built by convoluting a gaussian function at the location of each of the measured widths Γ_{top}^{meas}, in the pseudo-experiments. This produces non-parametric functions with shapes similar to the distributions in Figure 7.38, but these functions are continuous. The obtained functions are shown in Figure 7.39.

These functions are used to generate confidence intervals for each of the input widths Γ_{top}^{input}. Confidence intervals are regions in those functions where there is a confidence or confidence level (with certain associated percentage between 0 % and 100 %) that if any random measured Γ_{top}^{meas}, falls within this region, then it is likely that the random-data set is derived from input widths that contain this Γ_{top}^{meas} in their confidence interval. Intervals corresponding to confidence levels C.L. 68 % and 95 % are used for this analysis.

Two values x_1 and x_2 for a particular input width Γ_{top}^{input} will limit a confidence interval, satisfying Equations (7.9) and (7.10), where it is required that the x_1 and x_2

values contain 68 % and 95 % respectively of the measured values in the pseudo-experiments for each of the distributions. Following this procedure confidence intervals at 68 % and 95 % C.L. can be set for each of the input Γ_{top} values.

$$\int_{x_1}^{x_2} P(x|\Gamma_{top}^{input}) = 0.68 \tag{7.9}$$

$$\int_{x_1}^{x_2} P(x|\Gamma_{top}^{input}) = 0.95 \tag{7.10}$$

However there could be several pairs of values x_1 and x_2 that can satisfy the conditions in Equations (7.9) and (7.10), so another condition is required to obtain a unique answer. To establish a second condition the Feldman-Cousins technique is used. Details about this technique and justification are included in this reference [111]. Through this technique the limits of the confidence intervals are set so they are not over or under-estimated. To set the additional condition an ordering principle is required which is defined as in Equation (7.11):

$$R(x) = \frac{P(x|\Gamma_{top}^{input})}{P(x|\Gamma_{top}^{best})} \tag{7.11}$$

The ratio R(x) produces an additional distribution for a particular input Γ_{top}^{input}. $P(x|\Gamma_{top}^{input})$ are the values of the probablity distributions with input width Γ_{top}^{input} at $x \in$ (0, 10) GeV range, and $P(x|\Gamma_{top}^{best})$ is the maximum value reached by any distribution P at the value x with associated width value Γ_{top}^{best}.

The obtained $R(x)$ distributions from this ordering principle, corresponding to different Γ_{top}^{input} values, are shown in Figure 7.40. Each of them has a maximum at 1. The second condition to set confidence intervals from the Feldman-Cousins technique is shown in Equation (7.12).

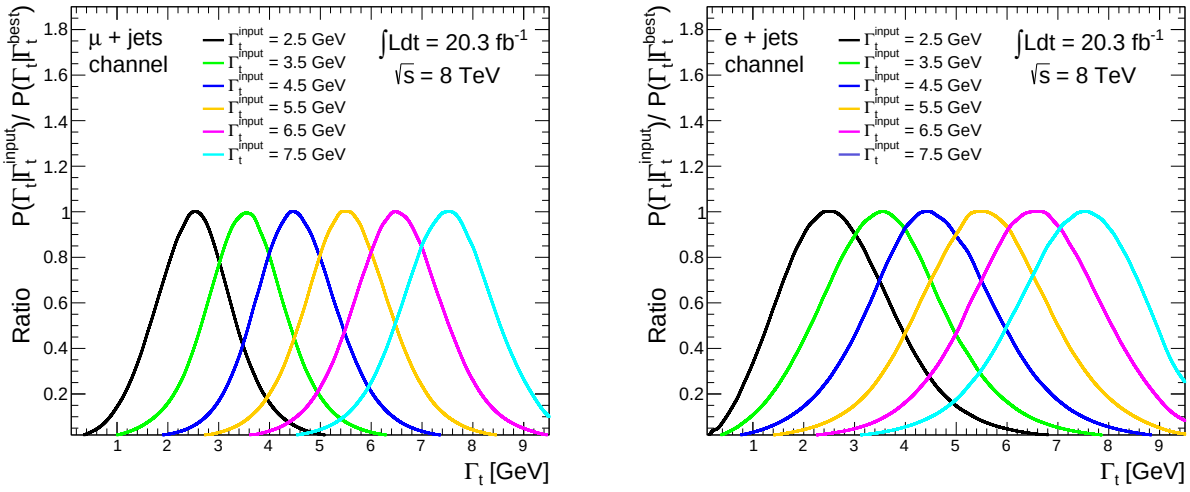

Figure 7.40: Output distributions in pseudoexperiments for different input Γ_{top}

$$R(x_1) = R(x_2) \tag{7.12}$$

Then to obtain the confidence intervals for the different Γ_{top} values, the limits x_1 and x_2 are required to satisfy Equations (7.9) and (7.12) for a 68 % confidence interval and Equations (7.10) and (7.12) for a 95 % confidence interval. The obtained confidence intervals following this technique without systematic uncertainties are shown in Figure 7.41 for both channels. The green colour indicates the 68 % confidence interval and the yellow colour indicates the 95 % confidence interval respectively for different input widths Γ_{top} which are read in the vertical axis. The confidence intervals for the electron channel in the right are slightly larger as will be shown numerically in the following sections.

7.9.4 Optimization of Variables and Constraints

The selection of the variable and the χ^2 cut with highest sensitivity to Γ_{top} was based on pseudo-experiments (described in sections 7.9.2 and 7.9.3). The methodology consisted in producing versions of the templates with different Γ_{top} as in figure

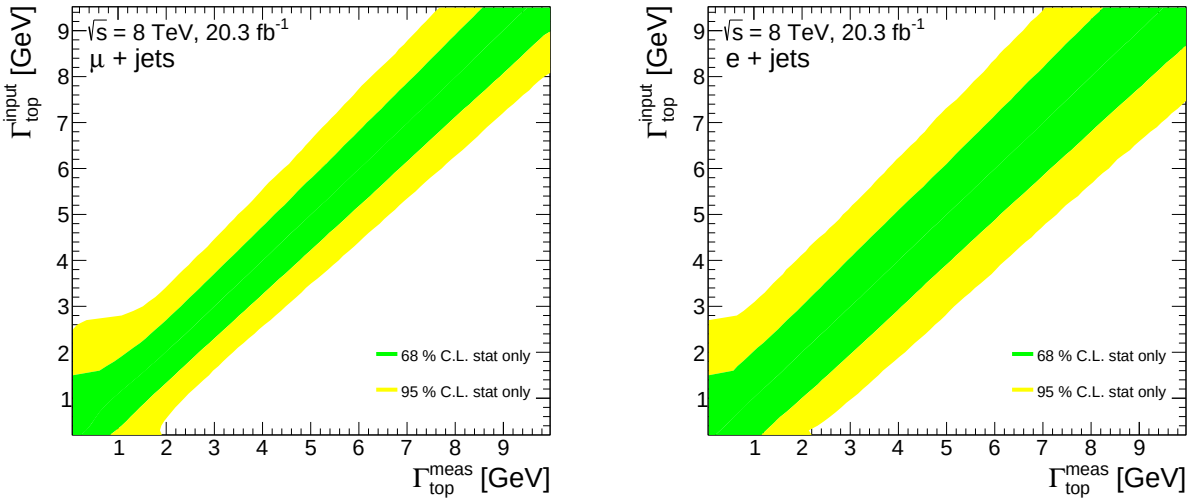

Figure 7.41: Final confidence belts for both channels showing the relative sizes of statistical and systematic uncertainties for different input Γ_{top}

7.34, but this time producing the distributions with different variables (m_t, m_{bjj}, $m_{bjj}-m_{jj}$, m_{bjj}/m_{jj} and m_{blv}) or applying a different χ^2_{min} cut. Pseudo-experiments can be performed using a particular width as input (in this case $\Gamma^{input}_{top} = 5.0$ GeV was selected) with the different versions of templates. Each of them will produce a different gaussian-like distribution like in Figure 7.38. The distributions with the smallest confidence interval size (section 7.9.3) or smallest statistical uncertainty determined the optimal χ^2_{min} cut value and variable to be used for the analysis.

7.9.4.1 Reconstructed Variables from the χ^2 Method

As described in section 7.8.1 the variables that can be used for the Γ_{top} measurement obtained from the χ^2 reconstruction are m_{bjj}, m_{blv}, $m_{bjj} - m_{jj}$, m_{bjj}/m_{jj} and m_t. Table 7.7 lists the sizes of the obtained confidence intervals for the different variables after performing 20k pseudo-experiments to ensure they converge to a single value. The variable that minimizes the statistical uncertainty or that is more sensitive to the variation of the Γ_{top} parameter for both channels is the fitted variable m_t from the χ^2 expression in Equation (7.4). The ratio variable m_{bjj}/m_{jj} showed slightly

Table 7.7: χ^2 Method Variable Optimization. Confidence Intervals Sizes at 68% / 95% C.L. [GeV]. 20k Pseudo-experiments were performed to obtain each of the confidence intervals to ensure they converge to a single value. The uncertainties on the limits have values up to ± 0.05 GeV, which is the precision on Γ_{top}^{meas} in each pseudo-experiment.

Variable	μ + jets channel	e + jets channel
m_t	1.56 / 3.14	2.20 / 4.43
m_{bjj}	2.10 / 3.46	3.11 / 4.67
$m_{bjj} - m_{jj}$	1.69 / 3.15	2.32 / 4.51
m_{bjj}/m_{jj}	1.57 / 3.29	2.23 / 4.61
m_{blv}	1.75 / 3.31	2.41 / 4.59

less sensitivity than the m_t variable. So the m_t variable is the optimal variable to be used for the measurement.

7.9.4.2 Minimized χ^2 Constraint

Using a similar procedure, rather than changing the variable for the different templates, the per-event minimized χ^2 cut value was modified. The different χ^2_{min} cut values that were used for the study are listed in Tables 7.8 and 7.9 for the μ + jets and e + jets channels respectively, from which it was concluded that the $\chi^2_{min} < 7$ cut was optimal to reduce the statistical uncertainties to the lowest possible value for both channels. As the χ^2 expression has three terms, this cut allows each of the terms to vary roughly within $< \frac{\sqrt{7}}{3} \sim 0.88\sigma$, where σ is the resolution associated with each term in the χ^2 expression in Equation (7.4).

As the χ^2_{min} cut value is reduced the event yields in column 2 of Tables 7.7 and 7.8 decrease while the $t\bar{t}$ signal significance in column three increases slightly. Though a really tight cut corresponds to a significant loss of statistics, source of additional fluctuations which increase the uncertainties after the cut value is decreased from the optimal cut value $\chi^2_{min} = 7$.

Table 7.8: χ^2_{min} cut constrain optimization for μ + jets channel. 20k Pseudo-experiments were performed to obtain each of the confidence intervals to ensure they converge to a single value. The uncertainties on the limits have values up to ± 0.05 GeV, which is the precision on Γ^{meas}_{top} in each pseudo-experiment.

χ^2_{min} cut value	Selected events	$\frac{S}{S+B}$	band size (68% / 95% C.L.) [GeV]
3	35601	0.95	1.72 / 3.22
4	39008	0.94	1.65 / 3.19
5	41673	0.94	1.65 / 3.19
6	43879	0.93	1.58 / 3.16
7	45732	0.93	1.56 / 3.14
8	47386	0.93	1.57 / 3.17
9	48807	0.93	1.65 / 3.23
15	54756	0.93	1.76 / 3.23
25	60468	0.93	1.99 / 3.28
40	65477	0.93	2.03 / 3.33

7.9.4.3 KL-Fitter Log-Likelihood Constraint

As the KL-Fitter method uses a likelihood function for the reconstruction a per-event log-likelihood value is obtained for each of the reconstructed events whose distribution is shown in the left of Figure 7.42. A cut over this variable is applied as events with higher log-likelihood value are more likely to be matched correctly. In the plot a clear tall peak can be seen with mean around the value -35 falling down to zero to the right after the value -36 and extending to the left to the value -40, where the distribution is divided into a shoulder-like shape which spreads to the left for the rest of the range.

In order to find the optimal cut value for this variable the same procedure followed

Table 7.9: χ^2_{min} cut constrain optimization for e + jets channel. 20k Pseudo-experiments were performed to obtain each of the confidence intervals to ensure they converge to a single value. The uncertainties on the limits have values up to ± 0.05 GeV, which is the precision on Γ_{top}^{meas} in each pseudo-experiment.

χ^2_{min} cut value	Selected events	$\frac{S}{S+B}$	band size (68% / 95% C.L.) [GeV]
3	20519	0.91	2.32 / 4.54
4	21572	0.90	2.26 / 4.47
5	23912	0.90	2.24 / 4.44
6	25284	0.89	2.21 / 4.44
7	26359	0.89	2.20 / 4.43
8	28847	0.89	2.22 / 4.45
9	31867	0.89	2.27 / 4.49
15	34511	0.89	2.29 / 4.53
25	37726	0.89	2.31 / 4.52
40	37739	0.89	2.36 / 4.55

in the two previous sub-sections to find the optimal variable and cut for the χ^2 reconstruction was used. The plot on the right of Figure 7.42 shows the different distributions from the pseudo-experiments corresponding to different log-likelihood cut values, it can be seen that a really tight cut, bigger than -50 reduces the statistics substantially so templates cannot be differentiated very well. In Table 7.10 are listed the obtained uncertainties for the different cut values and from the uncertainties in column 3 it can be seen that the optimal cut is $>$ -60.

Confidence intervals were also obtained using the mass shapes in left of Figure 7.33 from KL-Fitter. Figure 7.43 shows on the left the distributions obtained from pseudo-experiments using different width Γ_{top} values as inputs. These distributions as the distributions from the χ^2 method have a gaussian-like shape. The summary of confidence intervals for different input widths in the range (0, 7) GeV is shown in the

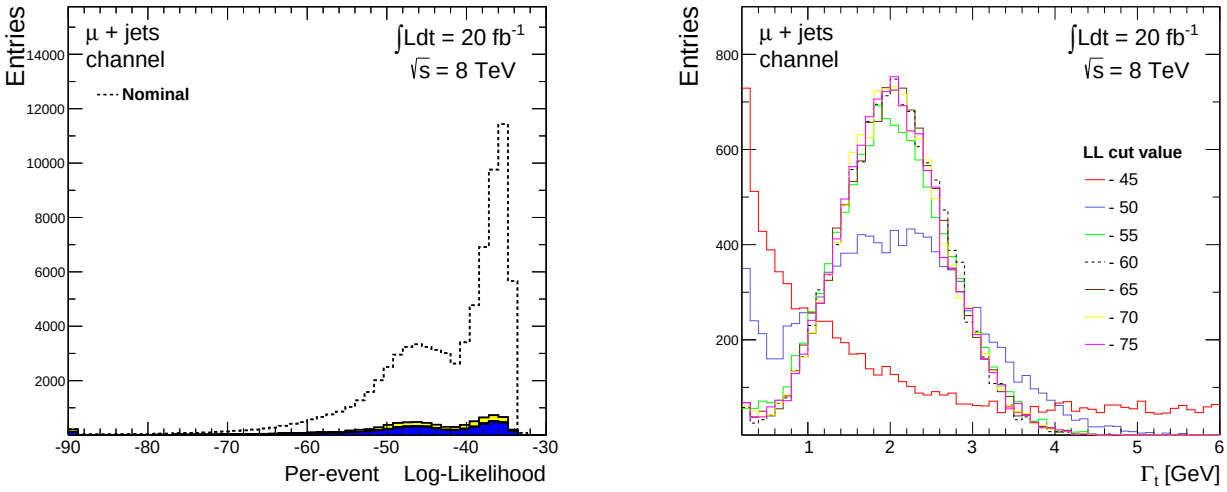

Figure 7.42: Distribution for the log-Likelihood values obtained for each of the events from the KL-Fitter reconstruction (left), distributions obtained from pseudo-experiments corresponding to different log-likelihood cut values (right).

Table 7.10: KL-Fitter Log-likelihood cut optimization, a value around -60 seems to give the smallest uncertainties at 68 % and 95 % C.L. 20k Pseudo-experiments were performed to obtain each of the confidence intervals to ensure they converge to a single value. The uncertainties on the limits have values up to ± 0.05 GeV, which is the precision on Γ_{top}^{meas} in each pseudo-experiment.

LL cut value	Events	65% Interval Size [GeV]	95% Interval Size [GeV]
-45	8610	6.15	11.87
-50	37573	2.37	3.91
-55	44062	1.49	3.34
-52	47782	1.34	3.24
-60	51708	1.33	3.17
-65	53653	1.35	3.18
-70	54117	1.35	3.23
-75	54276	1.36	3.24
-80	54340	1.36	3.24

right in the same figure, where the green colour limits the 68 % confidence intervals and the yellow colour the 95 % confidence intervals for the different width values. This plot can be compared with the one on the left of Figure 7.41 corresponding to the χ^2 reconstruction. The KL-fitter uncertainty shows a smaller uncertainty by $\sim$ 0.2 GeV for the 68 % confidence interval and a similar uncertainty for the 95 % confidence interval. This difference is not really significant considering the sizes of the statistical and systematic uncertainties for this analysis so both reconstructions give comparable sensitivity to the variation of the Γ_{top} parameter.

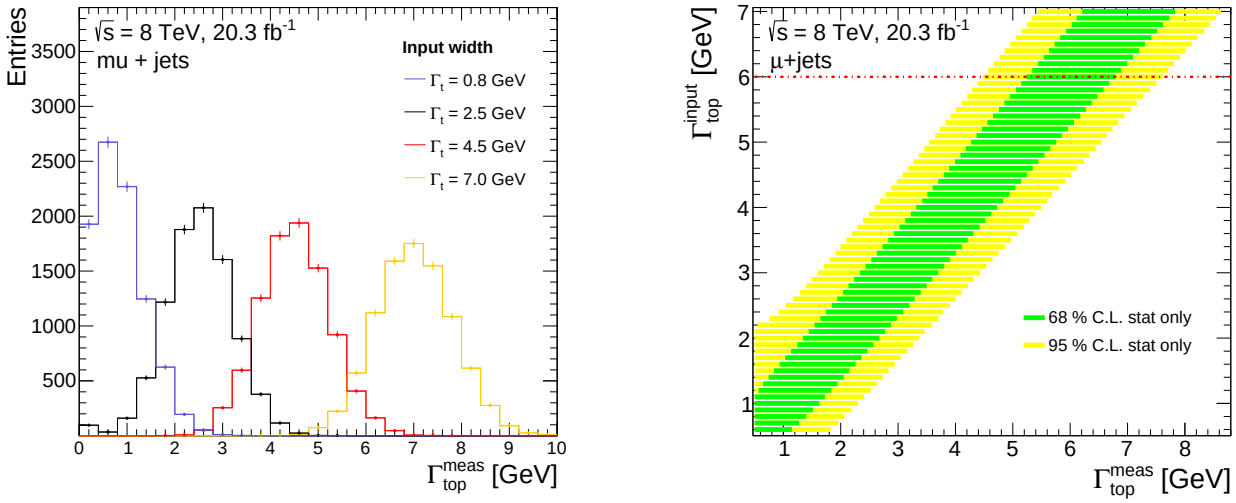

Figure 7.43: Distributions with gaussian-like shape from the pseudo-experiments from KL-Fitter (left), confidence intervals corresponding to different input width values Γ_{top}^{input} for the KL-Fitter reconstrcution (right).

7.9.5 Analytical Cross-Check

7.9.5.1 Expected Performance in Pseudo-Experiments

Ignoring the detector effects and statistical fluctuations an analytical study was performed to cross check the behaviour of the distributions obtained from pseudo-experiments. To simulate the final reconstructed shape a Voigt function [108] which is a convolution of a Gaussian and a Breit-Wigner curve is added to a Landau shape.

The latter shape accounts for combinatoric errors and backgrounds. The Gaussian determines the detector resolution and the Breit Wigner curve sets the value for the underlying Γ_{top}. The resulting analytical shapes are shown in the left of Figure 7.44 for different Γ_{top} values. The Voigt function at the bottom which introduces the sensitivity to the top width, has been separated from the Landau shape with dashed line. The curves have similar shapes to the histograms for the m_t variable obtained from the χ^2 reconstruction shown in figures 7.29 and 7.30. In the right in Figure 7.44 the distributions obtained from performing pseudo-experiments with these curves are shown. Each distribution corresponds to a different input width Γ_{top}^{input}. These distributions look like the ones obtained from the χ^2 and KL-Fitter reconstruction in Figures 7.38 and 7.43.

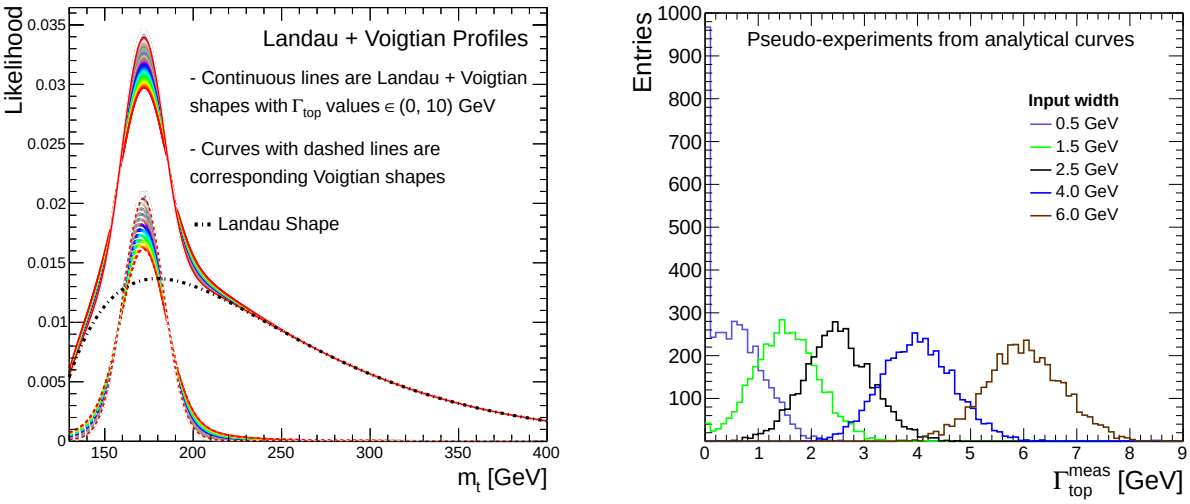

Figure 7.44: Analytical curves produced by adding Landau shapes standing for the combinatoric errors and a convolution betwen a Gaussian curve and a Breit-Wigner curve (voigt curve), introducing the former the detector resolution and the latter the Γ_{top} value (left), distributions from pseudo-experiments obtained by using different input width values Γ_{top}^{input} (right).

Finally Figure 7.45 shows the summary of confidence intervals for different input widths which are read in the vertical axis. As these intervals are obtained from perfectly smooth and continuous analytical shapes the confidence intervals have smaller

size than the confidence intervals corresponding to the $\chi 2$ and KL-Fitter reconstructions shown in Figures 7.41 and 7.43. However the behaviour of the distributions and confidence intervals obtained from both reconstruction methods look comparable with the analytical results.

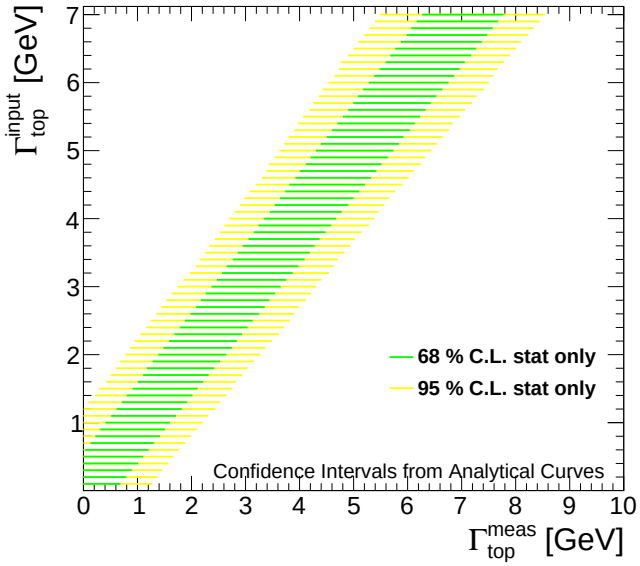

Figure 7.45: Summary of confidence intervals obtained with the analytical templates for different input width values Γ_{top}^{input}, which are read in the vertical axis.

7.10 2-Dimensional Fit with Γ_{top} and JER as Parameters

Preliminary analysis code was developed by the author using `RooFit` to expand the analysis to a 2-dimensional analysis aiming to measure the Jet Energy Resolution additionally to the Γ_{top} parameter. Adding this parameter to the analysis implies the use of 2-dimensional histogram templates that are built from the mass distributions shown in Figure 7.33 from KL-Fitter. The reconstructed W-boson mass m_W^{reco} distribution with a corresponding JER value and a reconstructed top mass m_{top} distribution corresponding to the same JER value and a width value Γ_{top} are

used to produce the 2-dimensional templates, which in this case in `RooFit` are called `RooProdPdf` objects. The templates are used to calculate the likelihood distribution defined as in Equation 7.13, which is an expansion of the likelihood shown in Equation (7.8).

$$\mathcal{L}_{shape}(m_W^{reco}, m_{top}|\Gamma_{top}, JER) = \prod_{j=1}^{nbins}\prod_{i=1}^{nbins} P_{top}(m_{top}|\Gamma_{top}, JER)[i]\times P_W(m_W^{reco}|JER)[j]\times n_i\times n_j \tag{7.13}$$

$\mathcal{L}_{shape}(m_W^{reco}, m_{top}|\Gamma_{top}, JER)$ in the equation indicates that each 2-D template has two associated distributions m_W^{reco} and m_{top} with parameters Γ_{top} and JER. The multiplication in the equation is performed over all the bin contents of the two associated distributions. The methodology to produce the likelihood distributions or generate pseudo-data is similar to that described for the 1 dimensional analysis. An example of a 2D likelihood distribution produced from Equation 7.13 and using input width value Γ_{top} = 5.0 GeV and JER = 0.4, is shown on the left of Figure 7.46 where each of the -2$\mathcal{L}_{shape}$ + κ points have now 2 coordinates as (Γ_{top}, JER). The JER values are numered from 0 which corresponds to the nominal JER value in the MC samples and any higher value implies higher degree of smearing of the energy of the jets or less resolution as described in section 8.2.4.2 This distribution can be used to obtain continuous contours shown on the right in the same figure which join the points that are located 2.30 above the minimum to estimate the uncertainty at 68 % C.L. and 5.99 from the minimum for the uncertainty at 95 % C.L. [38].

Additionally this 2-dimensional distribution can be separated into two 1-dimensional -2$\mathcal{L}_{shape}$ + κ distributions corresponding to the Γ_{top} and JER parameters separately so their measurements are performed separately. This is achieved by building what are called profile likelihood scans. The profile likelihood distributions in Figure 7.47 are built for example for the Γ_{top} parameter, by taking the minimum value of the likelihood in the vertical axis at each Γ_{top} value, spanning over all the JER values vertically. The distribution of these minimum values is shown in the left of Figure

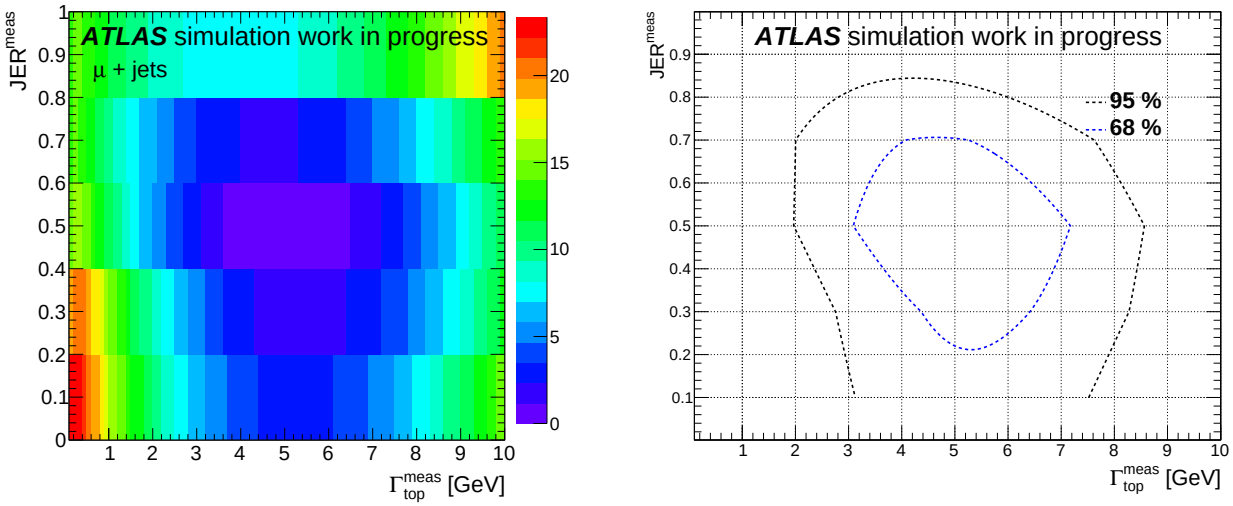

Figure 7.46: -2$\mathcal{L}_{shape}$ + κ 2-dimensional distribution corresponding to input Γ_{top} = 5.0 GeV and JER = 0.4 values (left), 2-dimensional countours that estimate the uncertainties at 68 % and 95 % C.L. (right).

7.47, from where it can be seen that the input Γ_{top}^{input} value that was used for this likelihod distribution has a value equal to 5 GeV. The same profile likelihood can be built using the same procedure for the JER parameter obtaining the distribution on the right in the same figure having minimum at 0.4 which is the JER value that was used as input.

Once these profile likelihood distributions have been obtained the rest of the procedure is similar to the 1-dimensional analysis that is producing pseudo-data sets, obtaining the minimum values for Γ_{top} and JER out of the profile likelihood distributions separately for both parameters and then obtaining confidence intervals for both parameters at 68 % and 95 % C.L. Finally a single 2D scan is done for the measurement with data, which is again separated into two profile likelihood distributions as in Figure 7.47 to obtain separated measurements for Γ_{top} and JER parameters.

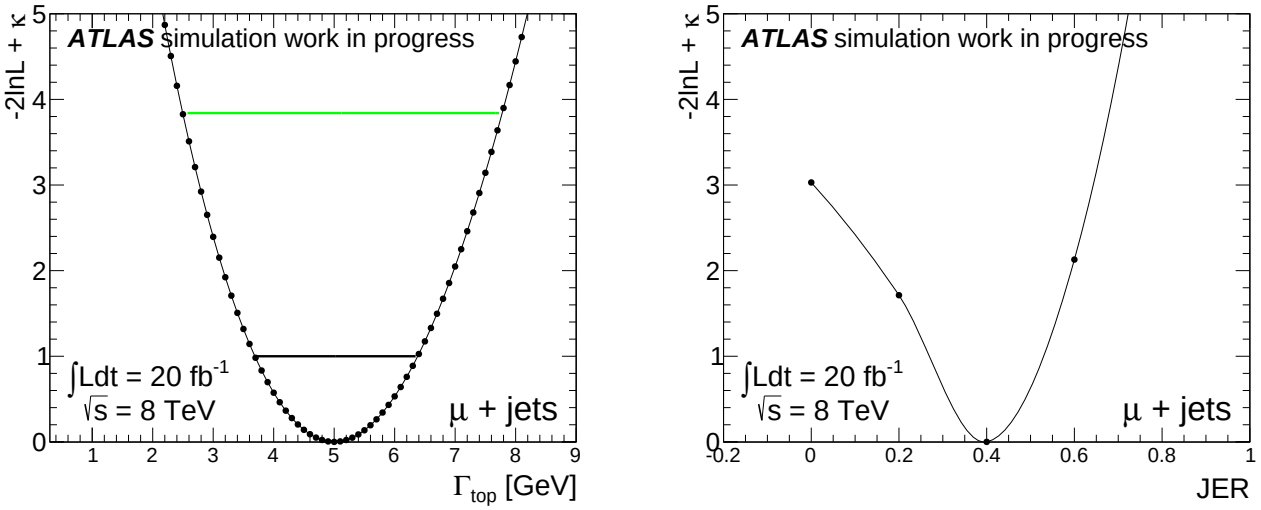

Figure 7.47: Profile likelihood scan corresponding to the parameters Γ_{top} (left) and JER (right).

7.11 Summary

An analysis infrastructure has been built to measure the Γ_{top} parameter with data recorded by the ATLAS experiment at centre of mass proton-proton collision energies of $\sqrt{s} = 8$ TeV. Physical objects have been defined and used to set an event selection aimed to reduce the backgrounds to $t\bar{t}$ signal events as much as possible. A well defined set of MC samples have been briefly described accounting for the different background and signal contributions.

Two event reconstruction techniques have been tested: χ^2 minimization and KLFitter, giving both of them comparable results in the statistical studies described in section 7.9, though it was more suitable for the author to finalize the analysis using distributions produced from the χ^2 minimization during the course of the PhD. Measurement with data and systematic uncertainties are described in the following chapter.

Chapter 8

Analysis Results and Measurement

Throughout this chapter the analysis results obtained by implementing the techniques and tools described in the previous chapter 7 are presented. The m_t distribution sensitive to Γ_t produced from the χ^2 method (section 7.8.1), produced by using the final set of selected events from MC simulation is described in section 8.1. The signal $t\bar{t}$ shape is separated from the different background contributions. The m_t distribution with the observed events in data from proton-proton collisions at $\sqrt{s} = 8$ TeV is also shown.

Different sources of systematic uncertainties are outlined in section 8.2, describing the methodology for the calculation of the contributions from the different sources and finally presenting a total systematic uncertainty. The dependence of the total systematic uncertainty on the parameter of interest Γ_t, is discussed in section 8.3. Section 8.4 presents the measurement with the observed data set for both channels. A summary of total statistical and systematic uncertainties is presented in section 8.5, showing confidence intervals for the different Γ_t values including the measured values with data. Section 8.6 shows the obtained measured Γ_t value for both channels plus the corresponding upper confidence limits. Finally section 8.7 includes a summary of the chapter.

8.1 Selected Events for Measurement

The final set of selected events is obtained by applying the selection requirements described in section 7.6.1 and by applying an additional constraint from the reconstruction performed using the minimized χ^2 variable described in section 7.8.1. An optimized constraint of $\chi^2_{min} < 7$ is applied. The procedure to perform such optimization is described in section 7.9.4.2

Table 8.1: Data and simulation event yields after applying the final χ^2 constraint and a m_W^{reco} window. These are the events that are considered for the final fit with data presented in this chapter. The different background contributions are listed at the top of the table with their yield systematic uncertainties. Each of the values have been rounded to integers.

Process	μ + jets channel	e + jets channel
Single top	$2048\ ^{+129}_{-168}$	$1217\ ^{+97}_{-79}$
W + jets	$298\ ^{+17}_{-41}$	$482\ ^{+77}_{-37}$
Z + jets	$113\ ^{+20}_{-13}$	$109\ ^{+31}_{-18}$
Diboson	$21\ ^{+2}_{-2}$	$16\ ^{+1}_{-1}$
QCD Multijet	$969\ ^{+292}_{-290}$	$1313\ ^{+393}_{-392}$
$t\bar{t}$	$45732\ ^{+2600}_{-2800}$	$26359\ ^{+1600}_{-1700}$
Total prediction	$49180\ ^{+2600}_{-2800}$	$29500\ ^{+1600}_{-1800}$
$t\bar{t}$ Significance	0.93	0.89
Data	48502	30345

The yields corresponding to the final set of selected events from simulation and data are listed in Table 8.1 including their statistical and systematic uncertainties added together. The table shows the total simulated MC yields split in their different

contributions: $t\bar{t}$ events plus the different background contributions. At the bottom of the table the signal significance (defined in Equation 7.3) of simulated $t\bar{t}$ over the total simulated shape is included for both channels, having a value of 0.93 and 0.89 for the μ + jets and e + jets channel respectively. So almost all the contribution to statistical and systematic uncertainties comes from the $t\bar{t}$ events.

8.1.1 Simulated Contributions to m_t Distribution

The distribution for the m_t variable with both channels was initially shown in the previous chapter in Figure 7.29. As this analysis performs a binned likelihood calculation for the measurement described in section 7.9 of the previous chapter the configuration of bins in that figure introduces a lot of fluctuations due to the reduced size of each of the bins. A customized configuration of bins was produced, shown in Figure 8.1 for both muon and electron channels. This configuration showed the optimal performance when calculating the statistical uncertainties from pseudo-experiments for both channels (section 7.9). The comparison included at the bottom in each plot is performed between the bin entries of the expected SM distribution with Γ_{top} = 1.33 GeV and the entries corresponding to templates with Γ_{top} values indicated in the legends.

Table 8.2 presents the fractional contributions of the different MC simulated processes shown in Table 8.1. From this table it is possible to see that the single top shape contributes in a similar way in both channels with a fraction equal to $\sim$ 4.1 %, W + jets processes have a fractional contribution of just $\sim$ 0.6 % for the muon channel and $\sim$ 1.6 % for the electron channel. Z + jets and Diboson processes contribute minimally for both channels having fractions $<$ 0.2 %. Finally the QCD multijet background events contribute with 1.9 % and 4.4 % fractions for the muon and the electron channels respectively.

From the figure it can be seen that the background shape with fractions $\sim$ 7 % and $\sim$ 11% for the muon and electron channels respectively as shown in the tables,

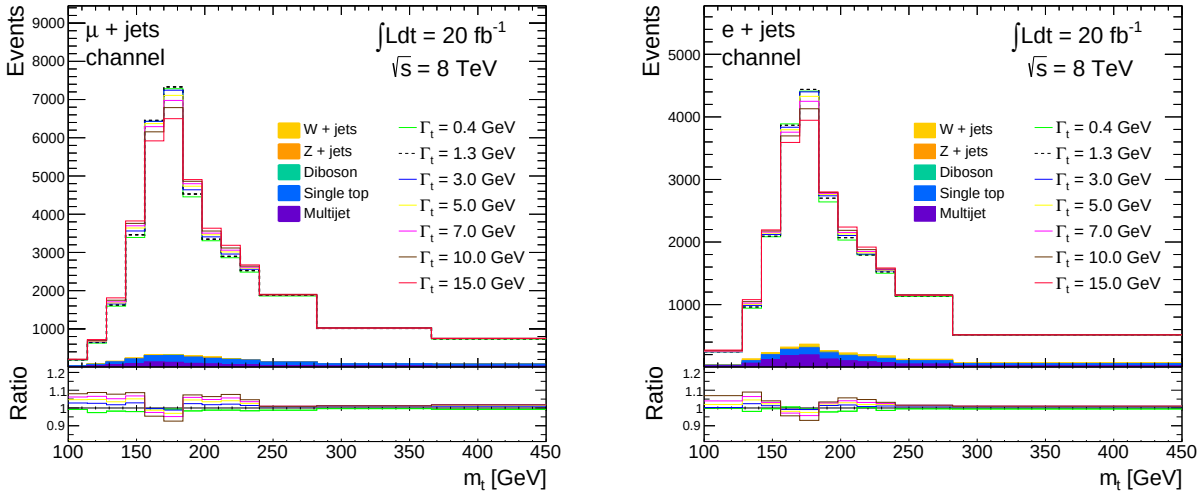

Figure 8.1: m_{top} distributions including the templates with different underlying Γ_{top}, they are normalized to the total integrated luminosity = 20.3 fb^{-1} at centre-of-mass collision energy $\sqrt{s} = 8$ TeV. The comparison in the pad below is performed with respect to the template with the $\Gamma_{top} = 1.33$ GeV, the SM expectation.

Table 8.2: Table showing the fractional contributions of the different processes included in the final simulated m_t distribution for both channels.

Process	μ + jets channel	e + jets channel
Single top	4.16 %	4.13 %
W + jets	0.61 %	1.64 %
Z + jets	0.23 %	0.37 %
Diboson	0.04 %	0.05 %
QCD Multijet	1.98 %	4.46 %
$t\bar{t}$	92.98 %	89.35 %

play a reduced role for contributions to total statistical and systematic uncertainties. The bin sizes for the m_t distributions were customized so they have bigger size for regions with reduced statistics which could be source of statistical fluctuations.

The bin configuration of distributions for both channels are slightly different as the electron channel has $\sim$ 20k events (40%) less than the muon channel and the fluctuation for the regions with low statistics are bigger for the electron channel.

8.1.2 Mass Distribution with Selected 8 TeV Data

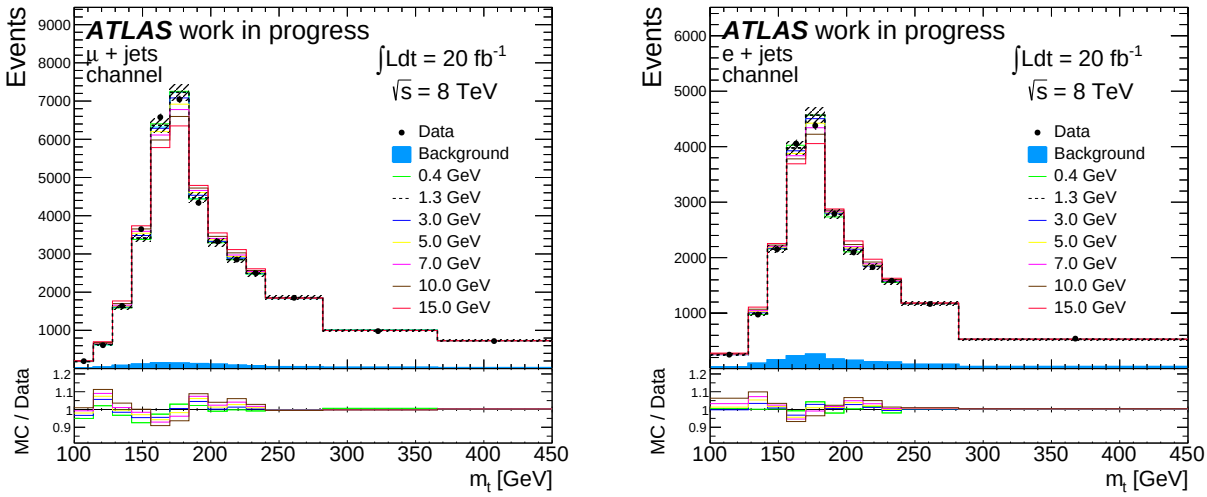

Figure 8.2: m_t distributions including the templates with different underlying Γ_{top} and the data samples corresponding to total integrated luminosity = 20.3 fb^{-1} and centre-of-mass collision energy $\sqrt{s}$ = 8 TeV.

The mass distributions shown in Figure 8.1 split into the different signal and background contributions are separated in two separated shapes shown in Figure 8.2. One shape regarded as the *signal shape*, adds the contributions from simulated $t\bar{t}$ events plus single top events. The reason for this is that both distributions contain information about the parameter of interest Γ_t and introduce sensitivity to it as each of the available templates used in the analysis have a different Γ_t value for this two distributions. This same approach has been adopted in previous top mass measurements [109]. The signal shapes are filled with white colour and have different line colours corresponding to different Γ_t values. The comparison included at the bottom in each plot is performed between the bin entries obtained from the observed data

and the corresponding entries to each of the templates with Γ_{top} values indicated in the legends.

The second shape filled with light blue colour in the plots corresponds to the rest of the background contributions added together. As described in section 7.9, events for these two shapes (signal and background) are generated separately in the pseudo-experiments varying their normalization and shape. The black dots account for the events observed in data for each of the bins, which for most of the cases are close to the expected SM template for both channels drawn with black colour.

8.2 Systematic Uncertainties on Γ_{top} Measurement

Systematic uncertainties affecting the jet objects such as the Jet Energy Scale (JES) and Jet Energy Resolution (JER), have the biggest contribution over the total systematic uncertainty for this analysis. In the following subsections the method of generating systematic variations, obtaining the resulting uncertainties and adding them together are outlined.

Near the completion of this thesis, internal collaboration prescriptions to obtain the systematic variations, especially for Jet Energy Resolution are being updated. The JER has been measured within the collaboration just recently, and an update of this prescription is expected to reduce this systematic uncertainty significantly for all the analyses at 8 TeV, but in particular this will be of great benefit to measurements of the top mass and top quark width. It is crucial to know very well the value of JER before applying a variation. Since the recent measurement of JER is more precise the prescription that will be available once the measurement is consolidated will reduce its uncertainty, which is over estimated in this thesis.

8.2.1 Methodology

The value of different parameters in the MC simulation, described in sections 8.2.2 to 8.2.12 are set to fixed values measured from data. These measurements carry 68 % and 95 % confidence level uncertainties. A systematic variation of the m_t distribution produced in the event reconstruction with the χ^2 method (section 7.8.1), is obtained by varying the value of a particular parameter in the MC simulation within their 68 % and 95 % uncertainties.

These variations are achieved in almost all cases by using collaboration tools that build the different systematic variations for a specific input distribution (in this case the m_t distribution). These varied 'systematic' m_t distributions are used to perform pseudo-experiments, comparing them with the nominal template mass distributions in Figure 8.2. A particular systematic uncertainty is obtained by evaluating by how much the new distribution from pseudo-experiments shifts from the distributions without systematic effects shown in Figure 7.38.

All of the outputs from each of the pseudo-experiments are stored in `ROOT Trees`, which store every single result in what is known as `Tree` object. For each distribution the result located exactly in the middle, once all the outputs are sorted by magnitude is extracted, which is the median of the distribution. Each systematic shift is obtained by comparing the median of each systematic distribution, with the nominal median value. The same results were obtained when using the mean of the distribution instead.

For this analysis the predominant systematic uncertainty is for the JER variation. The systematic uncertainties shown in Table 8.4 were calculated using an input width value $\Gamma_{top}^{input} = 5$ GeV. This value of Γ_{top}^{input} was initially selected to calculate the systematic uncertainties as it is located at the centre of the range under study (0, 10) GeV. However the total systematic uncertainty was found to have tiny variations for the different input widths keeping pretty much a constant value (section 8.3). The systematic uncertainties associated with Γ_t^{input} values < 4 GeV do not play an

important role when setting the final limits for Γ_t as their uncertainty intervals extend out of the physical range as can be seen in Figure 8.5. Being the uncertainties associated with $\Gamma_t^{input} > 4$ GeV values the ones that set the upper limits for the final measurements.

8.2.2 Luminosity

There is an uncertainty of 2.8 % on the recorded integrated luminosity measurement in ATLAS. This systematic uncertainty is applied to all physics MC samples. The impact of this uncertainty is negligible for this analysis as can be seen in Table 8.1. The reason for this is that the background contributions, as shown in Table 8.2, are very reduced with respect the signal $t\bar{t}$ events in the simulation, which have event yields over 45k and 26k for the μ + jets and e + jets channels respectively. So a 2.8 % variation over the background normalization does not affect the analysis results.

8.2.3 Parton Distribution Function

The selection of a specific parton distribution function for the different MC samples introduces a systematic uncertainty known as Parton Distributon Function (pdf), uncertainty. For this uncertainty the three different pdf sets indicated in Table 8.3, spread the uncertainty in three different ways as can be seen in Figure 8.3.

Table 8.3: Table for the Parton Distribution Function name sets used for the PDF uncertainty calculation. Each PDF set has a corresponding number of available variations that spread in a specic way indicated in the third column.

PDF set name	Number of pdf's variations	Combination Method
`cteq66` [123]	44	Symmetric Hessian
`MSTW2008nlo` [124]	40	Asymmetric Hessian
`NNPDF23_nlo` [125]	100	RMS

To estimate this uncertainty the LHAPDF package is required [134] as it provides all the pdf sets listed in the table. All the variations are generated by varying a set of uncorrelated parameters corresponding to each of the pdf names which have a specific number of parameters. This is the reason why each of them have different number of variations as shown in the table.

All the MC samples signal and background are weighted separately to the different pdf variations and then added together following the recommendations of the PDF4LHC group [126] and the LHAPDF group [134]. The energy fractions x_1 and x_2 of each of the partons that participate in the collision, are required for the calculation of the weights. Also it is necessary to know the value of the energy scale Q, which in this case is usually about 172.5 GeV, the input top mass value used in the MC samples. The PDG id numbers [37] of the incoming partons that generate the hard scattering interaction are also needed. The weight w, is calculated with the LHAPDF using the Equation 8.1, where pdf_0 accounts for the value of the pdf function as it is originally in the MC samples for both of the incoming participating partons. *pdf* stands for the value of the new pdf that is calculated by the LHAPDF program.

$$w = \frac{pdf(x_1, id_1, Q) \times pdf(x_2, id_2, Q)}{pdf_0(x_1, id_1, Q) \times pdf_0(x_2, id_2, Q)} \tag{8.1}$$

The weighted m_t distributions are compared with the nominal templates via pseudo-experiments to calculate the uncertainties. Each pdf name generates a distribution of uncertainties with its different variations as shown in the Figure 8.3, where the three distributions for both channels are shown. As each pdf name distributes the uncertainties in a different way, three different mechanisms are used to obtain three different regions known as envelopes that determine the contribution to the uncertainty for each pdf name.

The different uncertainties from the cteq66 pdf set are combined using the Sym-

metric Hessian method summarized in Equation 8.2. Where the sum is taken in steps of 2 so neighbouring uncertainties x_i^+ and x_{i+1}^- corresponding respectively to up and down variations of the same parameter, are compared with each other. The resulting envelope is shown with the hatched red area in the figure.

$$\Delta x = \frac{1}{2}\sqrt{\sum (x_i^+ - x_{i+1}^-)^2} \tag{8.2}$$

The `MSTW2008nlo` uncertainties are combined using the Hessian Asymmetric method which is summarized by equations 8.3 and 8.4, where a particlar uncertainty for this pdf set is compared with the nominal result with no variation, x_o. For this envelope a plus and down contribution is obtained that in general is expected to give a set of asymmetric values. The resulting envelope is shown in the figure with the hatched blue area.

$$\Delta x^+ = \sqrt{\sum (x_i - x_o)^2} \quad \text{if} \quad x_i - x_o > 0 \tag{8.3}$$

$$\Delta x^- = \sqrt{\sum (x_i - x_o)^2} \quad \text{if} \quad x_i - x_o > 0 \tag{8.4}$$

Finally for the `NNPDF23_nlo` set the RMS value is taken as plus and minus the total contribution because each of the variations are not specified as up and down variation of the same parameter as for the previous sets.

The size of the full evelope is the total uncertainty i.e the total up uncertainty corresponds to the highest plus limit of each of the envelopes and similarly for the down total uncertainty. The total uncertainties are $+0.303/-0.200$ GeV for the μ + jets channel and $+0.293/-0.229$ GeV for the e + jets channel respectively as listed in

Table 8.4.

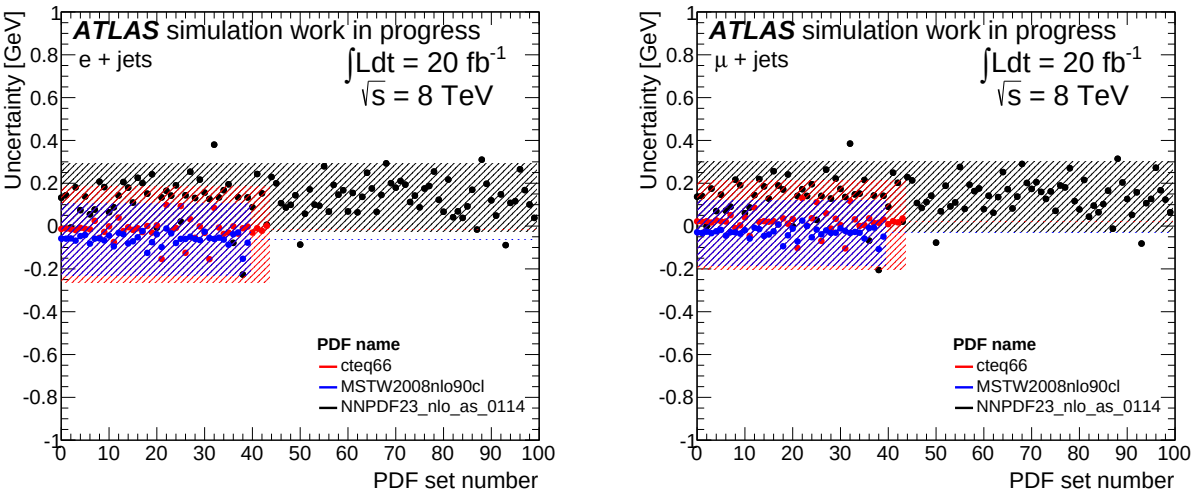

Figure 8.3: LHAPDF program is used to generate 185 variations corresponding to 3 different PDF names: cteq66 (symmetric hessian), MSTW2008nlo (asymmetric hessian) and NNPDF23_nlo (RMS).

8.2.4 Jet Uncertainties

For this analysis the event selection and event reconstruction described in the previous chapter, need information from the event jets, so variations of the jet properties affect the analysis results substantially, giving the biggest systematic uncertainties due to jet effects such as variations involving Jet Energy Scale (JES) or energy resolution (JER).

8.2.4.1 Jet and b-Jet Energy Scale

The Jet Energy Scale sets calibrations on the jets used in the analysis. These calibrations are determined from noise studies and by evaluating the calorimeter sub-detector response. The reason for this is that there are differences between the ATLAS detector simulation response and the actual detector response. The total

required information to calculate this systematic is obtained from combining information from test-beam data, LHC collision data and simulation [119], [120], [121], [122]. The calibration introduces several sources of systematic uncertainty on the jet energy calculation [120].

The JES uncertainty is split into 34 un-correlated sources addresing parameters included in the above mentioned calibration which have different p_T and η dependencies. The flavour response of the detector and its performance once pile-up effects and overlapping between jets located very close to each other are also considered. All the resulting individidual uncertainties are added together in quadrature following a common internal prescription within the collaboration, which is available through the use of the ATLAS `JetUncertainties` tool.

A similar procedure is followed for the b-JES uncertainty by considering only jets that have originated from truth b-quarks. This systematic error affects the performance of the b-tagging algorithms. The systematic effects over the jet energies are propagated into the Missing Energy uncertainty.

8.2.4.2 Jet Energy Resolution

This uncertainty is obtained by implementing the ATLAS `JERUncertaintyProvider` tool. A measurement of the JER has been performed with data and simulation using three in-situ measurements, [117], [118], [119], [120]. From the above tool it is possible to extract the expected fractional resolution of the jets' p_T as a function of their p_T and pseudorapidity values and the associated energy resolution. This uncertainty is generated by smearing the energies of jets within their resolutions. The resulting m_t distribution is compared with the nominal templates to extract the uncertainty for both channels. For this new variation to not overestimate the contribution of this uncertainty it is crucial to have a reasonable default value for the degree of smearing over the jet energies. Also it is necessary to have a precise knowledge of the uncertainty of the jets' p_T values as a function of their magnitude

and their associated energy resolution. This uncertainty by definition is one-sided since the jets in the MC simulation cannot be under-smeared. So only one variation of the m_t distribution is produced for this uncertainty. The systematic uncertainty is symmetrized, which means that the absolute value of the uncertainty obtained is taken as a positive and negative contribution to the total systematic. The uncertainties for the JER parameter are $\pm$ 2.49 GeV and $\pm$ 3.16 GeV for the μ + jets and e + jets channels, respectively.

8.2.5 Colour Reconnection and Underlying Event

Colour reconnection, CR, is the mechanism in which the partons produced from the hard scattering are connected by a colour string. The effect of this connection is a boost or increase in density in the connected partons direction. This uncertainty takes into account the effect of varying the density of colour charges by re-assigning the value of the colour charge to the different partons so colour reconnection strengths are reduced.

For the underlying event uncertainty, the effect of increasing the number of Multiple Interactions MPI's i.e number of extra or secondary interactions apart for the main hard scattering interaction is taken into account. This is achieved by modifying the parameter that regulates the number of MPI's in the simulation usually known as the underlying event (UE).

Special samples have been prepared with reduced colour reconnection effects and increased underlying event. Using `POWHEG` interfaced with the `PYTHIA` generator. The resulting m_t distributions are compared with the nominal templates to extract the uncertainty for both channels. As just a single variation is produced for each of these two uncertainties, the obtained uncertainties are symmetrised, as with the JER uncertainty in section 8.2.4.2.

The uncertaintes for colour reconection effects are $\pm$ 0.367 GeV and $\pm$ 0.391 GeV for the μ + jets and e + jets channel respectively. The uncertainties accounting for

underying event similarly are ± 0.583 GeV and ± 0.602 GeV for the μ + jets and e + jets channel respectively as listed in Table 8.4.

8.2.6 Monte Carlo Simulation

To take into account the uncertainty introduced due to the choice of the $t\bar{t}$ MC generator, variations of the m_t distribution are constructed using different $t\bar{t}$ generators from the default one that is produced with `POWHEG` interfaced with `PYTHIA`. The additional $t\bar{t}$ samples are produced as follows:

- `POWHEG` interfaced with `PYTHIA` but using fast simulation instead of full simulation.
- `HERWIG` interfaced with `JIMMY`. This is known as the `MC@NLO` sample.
- `ALPGEN` interfaced with `HERWIG`.

These $t\bar{t}$ samples are added separately to the common background distribution in the light blue colour in Figure 8.2 and three different variations for m_t distribution are produced. These three variations are compared with the nominal templates via pseudo-experiments. The largest systematic uncertainty is symmetrised as the JER uncertainty in section 8.2.4.2 and taken as the MC Generator systematic uncertainty. This uncertainty has values ± 0.629 GeV and ± 0.643 GeV for the μ + jets and e + jets channel respectively.

8.2.7 ISR / FSR Radiation

An uncertainty acounting for the the amount of radiation that is emitted before (Initial State Radiation, ISR) and after (Final State Radiation, FSR) the hard

scattering is also considered. Following the recommendation from the ATLAS experiment internal data and rapidity gap analysis teams, a set of samples taking into account modification of the α_s scale parameter are used to calculate this uncertainty. The α_s parameter regulates the amount of ISR and FSR radiation. Two systematic variations of the m_t distribution corresponding to up and down variations of the α_s parameter are produced.
The considered uncertainty is half of the difference between the two systematic uncertainties obtained with the samples with α_s scale up and down variations. This result is then symmetrised as the JER uncertainty in section 8.2.4.2 and taken as the uncertainty. The uncertainty obtained is $\pm$ 0.573 GeV and $\pm$ 0.514 GeV the μ + jets and e + jets channel respectively.

8.2.8 Lepton Momentum Resolution and Scale

Each of the selected events for this analysis contains a muon or an electron. These objects have been calibrated so the observed data are better described by the simulation. However this calibration has a set of associated uncertainties that are propagated in the analysis as systematic errors.

The muon momentum resolution is measured by complementing the measurements of the different sub-detectors in the inner detector and muon spectrometer. The muon momentum resolution for these different sub-detectors is varied within its uncertainties [112], producing up and down variations for the m_t distribution. These variations are used to obtain corresponding uncertainties over the Γ_{top} parameter by comparing them with the nominal templates via pseudo-experiments. The biggest uncertainty is symmetrised and taken as the systematic uncertainty.

The uncertainty in electron momentum resolution is obtained by performing studies with data and simulation, identifying differences between them in specific resonances [113]. In a similar way as with the muon momentum, variations of the m_t distribution are produced accounting for the increase and decrease in the resolution. The

uncertainties are obtained by comparing the m_t variations with the nominal templates via pseudo-experiments. The biggest uncertainty is symmetrised and taken as the systematic uncertainty.

Additionally, lepton scale factors are calculated via tag-and-probe studies. They are used to improve the modelling of the data by taking into account that the trigger efficiencies of the detector are different for data and MC. These scale factors are applied to all the simulated events and have associated uncertainties, which again produce two variations that are compared with the nominal templates to extract the systematic uncertainties in the same way as with the momentum resolution.

8.2.9 Transverse Missing Energy

Different scale factors are applied over the simulated events taking into account pile-up, lepton scale factors and additional calibrations which need to be propagated into the per-event Transverse Missing Energy, $E_{\mathrm{T}}^{\mathrm{miss}}$ calculation. As the variables of the objects in each of the events are varied after the corrections, the $E_{\mathrm{T}}^{\mathrm{miss}}$ has a different value. This introduces an additional calibration to correct the calculation of $E_{\mathrm{T}}^{\mathrm{miss}}$ in each event, which has an associated uncertainty. The calibration is varied within its uncertainty to produce four systematic variations for the m_t distributions accounting for momentum resolution and additional trigger corrections associated with $E_{\mathrm{T}}^{\mathrm{miss}}$. These variations are compared with the nominal templates via pseudo-experiments obtaining up and down uncertainties for Missing Energy momentum resolution and the same for additional scale factors.

8.2.10 Pileup

An ATLAS `pile-up re-weighting tool` is used to get variations for this uncertainty. A calibration is used to correct the simulated events due to pile-up effects. This calibration has an uncertainty that can be propagated to the analysis. The degree of pile-up or number of primary vertices per bunch crossing is shown in Figure

7.15 for both channels, showing how the simulated mean is made to coincide with the mean observed in data for the muon and electron channels respectively. The calibration is varied within its uncertainties to produce variations to the m_t distribution, which are compared with the nominal templates via pseudo-experiments. After adding all the contributions in quadrature the obtained systematic uncertainties are $+0.04/-0.03$ for the μ + jets and $+0.03/-0.02$ for the e + jets channel respectively.

8.2.11 QCD Multijet

As mentioned in the previous chapter (section 7.3.3) the QCD multijet background is obtained by weighting observed events in data. The weighting method has an associated systematic uncertainty. For this uncertainty five different variations are produced, accounting for variation of the normalization by ± 30 % of the QCD multijet background distribution, and three variations are obtained by using three different methods to weight the observed data. These methods have different efficiencies to obtain an accurate QCD multijet shape [114]. So five different variations of the QCD multijet background distribution are obtained. These variations are added separately to the $t\bar{t}$ distribution, producing five different variations of the m_t distribution.

The m_t variations are compared with the nominal templates via pseudo-experiments. The total uncertainty is obtained by adding in quadrature the normalization up uncertainty with the last three uncertainties and doing the same with the normalization down uncertainty, obtaining at the end for the μ + jets channel an uncertainty of $+0.109/-0.094$ GeV and $+0.119/-0.123$ GeV for the e + jets channel.

8.2.12 Additional Uncertainties

8.2.12.1 Jet Punchthrough

Jets with very high energy > 100 GeV may sometimes pass through the calorimeters without depositing all their energy. This effect causes an additional uncertainty

over the $E_{\mathrm{T}}^{\mathrm{miss}}$ calculation in each event. The variations on this uncertainty are produced by varying the degree of punch through in the detector simulation from what has been calibrated from data. The variations are compared with the nominal templates via pseudo-experiments producing up and down uncertainties for both channels. These uncertainties have a really small effect on this analysis having values < 0.01 GeV for the muon channel and < 0.02 GeV for the electron channel.

8.2.12.2 Re-weighting

The mechanism to obtain the different Γ_t templates for the signal shape ($t\bar{t}$ events plus single top events) is described in section 7.7. For the case of the simulated $t\bar{t}$ events, there are two top quarks present in each event, a top quark and an anti-top quark (whose average mass difference is zero). One of them is taken as reference to calculate the weights for different top width values. Both the top and the anti-top quarks have almost identical mass distributions at truth level but still a systematic is taken into account addressing any minimal difference. This systematic considers a difference in the result of the pseudo-experiments after using each of them as a reference to obtain the weights to different widths. This systematic has a negligible value of $\pm$ 0.002 GeV and $\pm$ 0.003 for the μ + jets and e + jets channels respectively.

Additionally each of the templates was varied within its uncertainties introduced in each bin by the re-weighting procedure weights described in section 7.7. This causes a very small effect on the Γ_{top} parameter: < 0.150 GeV for the μ + jets channel and < 0.170 GeV for the e + jets channel. Which sets, after adding in quadrature, a total systematic uncertainty for the re-weighting method of $\pm$ 0.150 GeV and $\pm$ 0.170 GeV for both channels respectively.

8.2.12.3 Central Top Mass Difference

As described in section 7.3.2 the nominal m_t distribution with the SM expected width $\Gamma_{top} = 1.33$ GeV has input top mass equal to $m_{top} = 172.5$ GeV. However,

as can be seen in Figure 6.5 the world's average for top mass measurements has a value of $\sim$ 173.3 GeV. From the plot on the left in Figure 6.6 this can be translated into a small shift in the top width of < 0.04 GeV. This is added to the systematic uncertainties for both channels.

8.2.12.4 Template Statistics

The statistical studies described in section 7.9 were repeated using signal samples with an initial set of events of 15M to 45M with full simulation and 75M and 100M events for fast simulated samples. All the samples were normalized in all cases to the observed integrated luminosity of 20.3 fb^{-1}. For all the samples, the confidence intervals shown in Figure 7.41, were found to be almost identical with differences not larger than 0.094 GeV for the μ + jets channel and 0.106 GeV for the e + jets channel, which is taken as a small additional contribution to systematic uncertainties. The measurement is performed with a full simulated $t\bar{t}$ sample with an initial number of events equal to 45M, described in section 7.3.2.

8.2.12.5 Additional Background Uncertainties

Apart from the QCD multijet background, which is completely generated from a data-driven method (section 7.3.3), all the systematic effects accounting for jet effects and calibrations, pile-up, lepton resolution and scales, missing energy, parton distribution functions, jet reconstruction efficiencies and luminosity, have also been propagated to the background distributions. The systematic variations of the background distribution are added to the corresponding varied signal distributions with the different systematic effects, so the calculation of each systematic uncertainty is completed.

Additional effects in the background distribution are taken into account, to address particular uncertainties associated with each of them. These additional uncertainties turned out to have a very small effect over this analysis given that the contribution

of the background is very reduced, as can be seen in Table 8.4.

The cross section for the W + jets background has been calculated using a data-driven method [115]. An ATLAS re-weighting tool is used to weight the W + jets simulated events with the SHERPA generator. So variations of this shape are produced accounting for normalization effects based on the uncertainty over the obtained cross section from data. Additional uncertainties are obtained by varying the generator theoretical scales, which affects the W + jets distribution shape slightly. All the obtained variations are added separately to the rest of the simulated shapes and then compared with the nominal templates via pseudo-experiments. The obtained uncertainties are added in quadrature. The total systematic uncertainty accounting for these additional effects are $+0.012/-\ 0.009$ for the μ + jets channel and $+0.015/-\ 0.011$ for the e + jets channel. These uncertainties are very small as the W + jets shape accounts for just 0.6 % and 1.6 % for the μ + jets and e + jets channels respectively, of the total simulated distribution.

The cross section for the single top background has been made equal to the NNLO degree of precision prediction for its three sub-channels: t-channel, s-channel and Wt-channel [116]. These individual distributions are weighted up and down accounting for the variation of the three channels cross-sections within their calculated uncertainties. These produce 6 additional variations (up and down variations for each channel) that are added separately to the rest of the simulated distribution. The uncertainties are obtained via pseudo-experiments comparing with the nominal templates. The obtained systematic uncertainties are added in quadrature, obtaining total systematic uncertainties values $+0.019/-\ 0.014$ for the μ + jets channel and $+0.018/-\ 0.016$ for the e + jets channel, respectively. A very small uncertainty as for the case with the W + jets uncertainty, the single top background has a contribution of only $\sim 4\%$ of the total simulated distribution for both channels.

Similar cross-section and shape uncertainties associated with Z + jets and diboson backgrounds were considered. However, as these backgrounds have an even smaller

contribution to the simulated distribution of only 0.2 % and 0.04 % for the μ + jets channel and 0.03 % and 0.05 % for the e + jets channel, which are very close to zero, each of the variations produced uncertainties smaller than 0.0001 GeV and so they are negligible systematic uncertainties for this analysis.

8.2.13 Total Systematic Uncertainty

The distributions obtained from pseudo-experiments using as input the m_t distribution with $\Gamma_{top} = 5$ GeV with different systematic effects are shown in Figure 8.4, which are spread around the value 5 GeV. In the left hand figure are shown the distributions corresponding to B-JES up and down variations compared with the nominal distribution with no systematic effects. The distribution corresponding to the JER variation is included as well to show its the large shift (> 2 GeV) with respect to the nominal distribution.

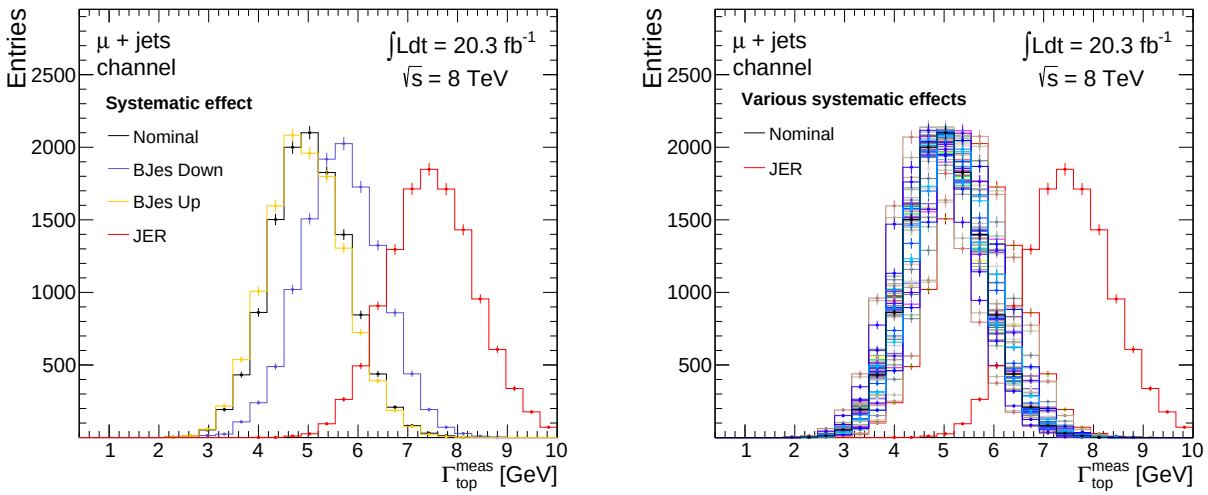

Figure 8.4: Distributions with gaussian-like shape and corresponding systematic shift, obtained after each of the m_t systematic variations are compared with the nominal templates via pseudo-experiments showing the effect of BJES and JER systematic effects (left), and all the effects put together (right), for the μ + jets channel. The uncertainty is extracted by comparing the nominal distribution with the obtained systematic distribution.

The plot in the right of the Figure 8.4 illustrates how large the JER uncertainty is, compared with the rest of the uncertainties which mostly have variations < 0.6 GeV. Here the JES uncertainty has been split in its 34 components, which are added in quadrature. Similarly, the distributions from pseudo-experiments with different systematic effects for the e + jets channel are shown in Figure 8.5. For this channel the systematic uncertainties distribute in a similar way as with the muon channel but most contributions are larger for the electron channel.

All the systematic uncertainties for this analysis are shown in Table 8.4, where all the uncertainties are listed with their respective up and down contributions for both channels. The total systematic uncertainty in the bottom of the table is obtained by adding all the separated positive and negative contributions in quadrature for both channels. Some uncertainties such as the ones accounting for JES and pile-up effects are made up by several components which are calculated separately.

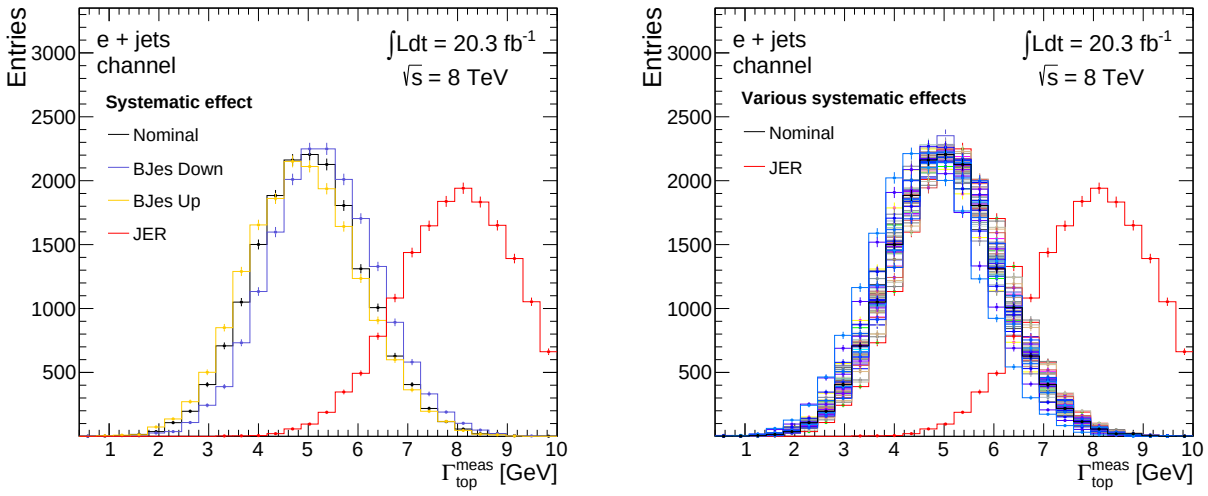

Figure 8.5: Distributions with gaussian-like shape and corresponding systematic shift, obtained after each of the m_t systematic variations are compared with the nominal templates via pseudo-experiments showing the effect of BJES and JER systematic effects (left), and all the effects put together (right), for the e + jets channel. The uncertainty is extracted by comparing the nominal distribution with the obtained systematic distribution.

Notably the JER systematic effect has the biggest contribution for both channels and the total uncertainties get their large value mostly due to this uncertainty. As described in section (8.2.4) the jets' energies deposited in the calorimeters are increased, and then the number of selected events changes substantially, as the object definitions (section 7.2) and selection requirements (section 7.6.1) are implemented again. This uncertainty affects the electron channel more than the muon channel. The reason for this is that for the electron channel, the electron isolation criteria in section 7.2.2 affect the selection of events significantly once the JER effect is introduced.

Additional p_{T} cuts were applied over all the event jets to analyze the possibility of reducing the JER uncertainty. For example it could be required that all jets satisfy $p_{\mathrm{T}} > 40$ GeV. These additional constraints reduce the JER uncertainty slightly, however the corresponding increase of the statistical uncertainty is larger, making the over-all uncertainty larger.

8.3 Uncertainty Dependence with Γ_t^{input}

The dependence of the total systematic uncertainty with the input Γ_t value used to generate the systematic variations, was explored. This dependence was found to be small but still was considered when building the final confidence intervals for different top width values shown in Figure 8.7. The dependence of the total systematic with Γ_t^{input} is shown in Table 8.5, where the total systematic is shown for different input Γ_t values. For both channels the total uncertainty slightly decreases as the Γ_t^{input} increases as shown in the table. However the uncertainties do not differ in more than 0.1 GeV for both channels.

Table 8.4: Sources of systematic uncertainties listed together. Each uncertainty has a up and down contribution. All the variations that produce a positive shift in the measured Γ_t parameter are added in quadrature together to the positive uncertainty and similarly for the negative contribution.

Systematic effect	**μ + jets**	**e + jets**
Colour Reconnection	± 0.37	± 0.39
Underlying Event	± 0.58	± 0.60
MC Generator	± 0.63	± 0.64
ISR/FSR	± 0.57	± 0.51
Jet Punch Through	+0.009/	+0.004 /−0.015
B-Jet Energy Scale	+0.65/−0.36	+0.30 /−0.10
Jet Energy Scale (JES)	+0.97/−0.52	+0.47 /−0.22
Jet Pseudorapidity Calibration	+0.33/−0.18	+0.22 /− 0.22
Pile-up	+0.04/−0.03	+0.03 /−0.02
Lepton Momentum Resolution	±0.09	±0.19
Lepton Energy Scale	+0.006/−0.019	+0.09/−0.04
Flavour Composition	+0.28/−0.27	+0.25 /−0.34
Flavour Response	+0.26/−0.14	+0.11 /−0.15
Jet Energy Resolution (JER)	±2.47	±3.16
Jet Reco Efficiency (Jeff)	±0.016	±0.006
Jet Vertex Fraction (JVF)	+0.09/	+0.14 /−0.09
PDF	+0.30/−0.20	+0.29/−0.23
MET Resolution	+0.15/−0.07	+0.05/−0.05
MET Scale	+0.06/−0.08	+0.05/−0.04
Luminosity	± 0.006	± 0.008
QCD Multijet	+0.11/− 0.09	+0.12/− 0.12
W + jets	+0.012/− 0.009	+0.02/− 0.01
Single Top	+0.02/− 0.01	+0.02/− 0.02
Template Statistics	± 0.09	± 0.11
Central Top Mass Value	± 0.04	± 0.04
Re-weighting Method	± 0.15	± 0.17
Total Systematic Uncertainty	+3.01/− 2.82	+3.44/−3.40

Table 8.5: Table presenting the dependence of the total uncertainty with Γ_t^{input}. In general the systematic uncertainty does not present a large variation with different input widths, however, it decreases slighly as the value of Γ_t^{input} increases.

Γ_t^{input} [GeV] / Channel	Total Syst. Unc. (μ + jets) [GeV]	Total Syst. Unc. (e + jets) [GeV]
1.0	+3.09 / -2.86	+3.49 / −3.45
2.0	+3.08 / -2.85	+3.48 / −3.44
3.0	+3.05 / -2.84	+3.47 / −3.43
4.0	+3.04 / -2.83	+3.45 / −3.42
5.0	+3.01 / -2.82	+3.44 / −3.40
6.0	+2.98 / -2.81	+3.42 / −3.40
7.0	+2.97 / -2.78	+3.41 / −3.38

8.4 Likelihood Scan with Data for Measurement of Γ_t

A distribution for the m_t variable with the observed data events listed in Table 8.1 is shown in Figure 8.2. A single likelihood scan as described in section 7.9 is performed using this distribution from data as input and comparing it with the nominal templates with different Γ_{top} values.

The resulting likelihood scans that give the measurement for Γ_t are shown in Figure 8.6 for both channels. The minimun of each of the likelihood scans give a value around the expected SM $\Gamma_t = 1.33$ GeV. The measured values of the top quark width are $\Gamma_t^{meas} = 1.65$ GeV for the μ + jets channel and $\Gamma_t^{meas} = 0.81$ GeV for the e + jets channel.

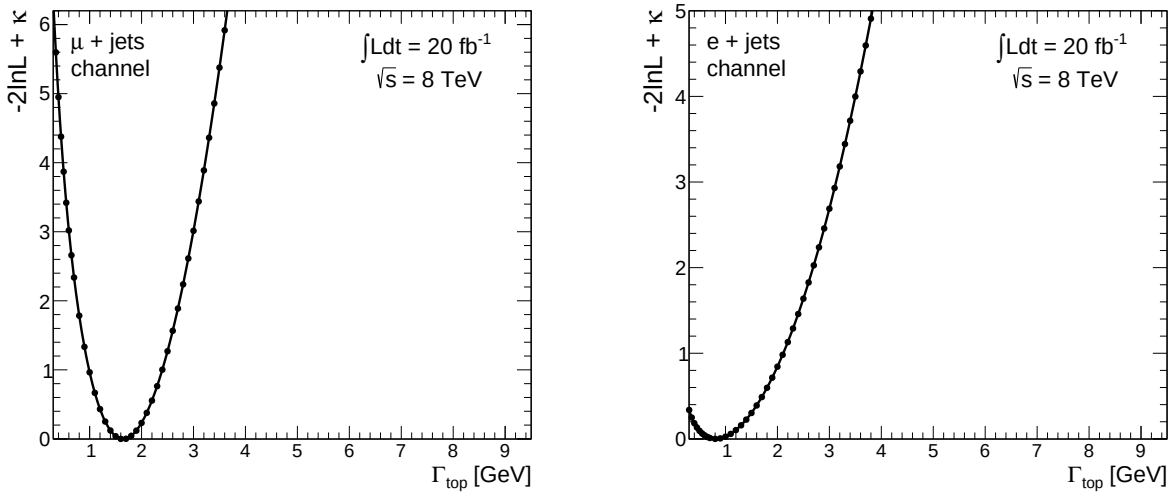

Figure 8.6: Likelihood scan for the measurement of the Γ_{top} parameter with the selected events from 20.3 fb^{-1} of data recorded with 8 TeV proton-proton collisions by the ATLAS experiment in the μ + jets (left) and e + jets (right) channels respectively.

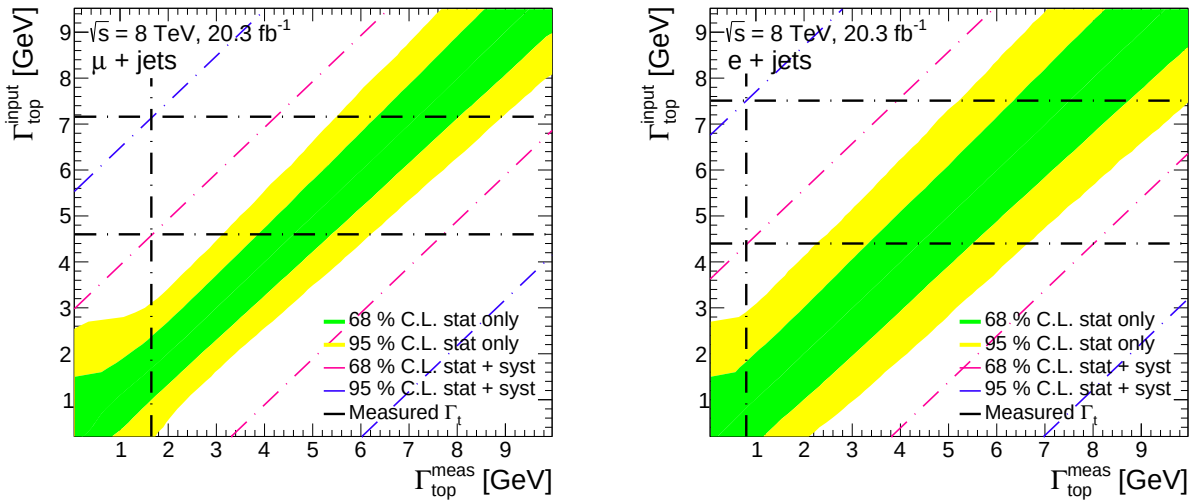

Figure 8.7: Confidence belts for both channels showing the relative sizes of statistical and systematic uncertainties for different Γ_{top}^{input}, μ + jets (left) and e + jets (right). Note that the 95 % C.L limits (blue dashline) of the confidence intervals for templates with Γ_{top} < 6 GeV, are shifted to the left out of the range into negative values of Γ_{top}^{meas}.

8.5 Confidence Belt

A summary of the statistical and systematic uncertainties obtained from pseudo-experiments for the different Γ_t^{input} values is displayed in Figure 8.7 through a confi-

dence interval belt obtained by applying the Feldman Cousins procedure described in section 7.9.2 for the statistical uncertainty. The systematic uncertainties shown in Table 8.4 correspond to 1-sigma systematic variations or variations at 68 % C.L., the calculation is repeated with 2-sigma systematic variations at 95 % C.L. to obtain the systematics uncertainties at 95 % C.L. Total systematic uncertainties at 68 % and 95 % C.L. are added in quadrature to the corresponding statistical uncertainties at 68 % and 95 % C.L. to obtain total uncertainties for the Γ_t^{input} values.

The different input width values, Γ_t^{input} are in the vertical axis in Figure 8.7, while the measured width values Γ_t^{meas} are read in the horizontal axis. The green coloured region determines the statistical part of the confidence interval for each of the width values at 68 % confidence level C.L., while the yellow colour corresponds to statistical uncertainty at 95 % C.L. The obtained limits after adding in quadrature the systematic uncertainties are indicated with the red and blue dash lines for 68 % and 95 % C.L. uncertainties respectively. The black vertical dash line indicates the measured Γ_t values for both channels while the two horizontal lines indicates the upper limtis at 68 % and 95 % C.L respectively that are set from the measurements in both channels.

8.6 Upper Limits for Γ_{top}

Table 8.6 Shows the numerical upper limits for the Γ_{top} parameter for both channels obtained from the measurements and the analysis uncertainties. The measured values in column 2 straddle the SM expected value $\Gamma_{top} = 1.33$ GeV. The measured Γ_{top} values are 1.65 GeV for the μ + jets channel and 0.81 GeV for the e + jets channel. Upper limits are $\Gamma_{top} < 4.60$ GeV at 68 % C.L. and $\Gamma_{top} < 7.16$ GeV at 95 % C.L. for the μ + jets channel, and $\Gamma_{top} < 4.40$ GeV at 68 % C.L. and $\Gamma_{top} < 7.51$ GeV at 95 % C.L. for the e + jets channel.

These limits are comparable for both channels, with the electron channel having

Table 8.6: Table presenting the measured values of Γ_t with the recorded data by ATLAS experiment from 8 TeV proton-proton collisions obtaining values around the SM expectation $\Gamma_t^{exp} = 1.33$ GeV. Columns number 3 and 4 show the obtained upper limits with 68 % and 95 % confidence level.

Channel	Measured Γ_t [GeV]	Upper Limit at 68 % C.L.	Upper Limit at 95 % C.L.
μ + jets	1.65	4.60	7.16
e + jets	0.81	4.40	7.51

slightly lower value for the limit at 68 % C.L. and a slightly higher limit at 95 % C.L. The electron channel in general has larger uncertainties as shown in Figure 8.7 for the different input widths than the muon channel, however for this measurement a lower width was measured for the electron channel than in the muon channel, which made the obtained upper limits comparable with each other as can be seen from the obtained confidence intervals for both channels.

8.7 Lower Limits for Top Quark Lifetime

Considering the relationship between the top quark lifetime τ_{top} and its width in equation 6.8, an indirect measurement of the top quark lifetime can be extracted from the results listed in table 8.6. The indirect measurement and limits for the top quark lifetime derived from the Γ_t measurement are shown in table 8.7. For this calculation a value for $\hbar = 6.582{\times}10^{-25}$ GeV s is considered [37].

The obtained values for τ_{top} are 3.99×10^{-25} s for the μ + jets channel and 8.13×10^{-25} s for the e + jets channel. Lower limits are $\tau_{top} > 1.43 \times 10^{-25}$ s at 68 % C.L. and $\tau_{top} > 0.92 \times 10^{-25}$ s at 95 % C.L. for the μ + jets channel, and $\tau_{top} > 1.50 \times 10^{-25}$ s at 68 % C.L. and $\tau_{top} > 0.87 \times 10^{-25}$ s at 95 % C.L. for the e + jets channel. These results are consistent with a expected SM lifetime $\sim 5 \times 10^{-25}$ s. for both channels.

Table 8.7: Table presenting the indirectly measured values of τ_t top quark lifetime with the recorded data by ATLAS experiment from 8 TeV proton-proton collisions obtaining values around the SM expectation. Columns number 3 and 4 show the obtained upper limits with 68 % and 95 % confidence level.

Channel	Measured τ_t $[10^{-25}s]$	Lower Limit at 68 % C.L. $[10^{-25}s]$	Lower Limit at 95 % C.L. $[10^{-25}s]$
μ + jets	3.99	1.43	0.92
e + jets	8.13	1.50	0.87

8.8 Summary and Conclusions

The obtained results for measured Γ_{top} and τ_{top} and its corresponding upper and lower limits, respectively are totally consistent with the SM expectation and with earlier CDF measurement described in section 6.4.2. These measurements represent the first attempt from the ATLAS collaboration to set limits over Γ_{top} and τ_{top} top quark properties, and from the LHC experiments using a direct approach.

A comprehensive set of systematic uncertainties has been obtained and summarized in Tables 8.4 and 8.5. Confidence intervals including systematic uncertainties were obtained implementing the techniques described in the previous chapter for both channels and are shown in Figure 8.7, indicating measured values for the Γ_{top} parameter for both channels and corresponding limits at 68 % and 95 % C.L. The numerical measured values for the Γ_{top} parameter and corresponding upper limits are shown in Table 8.6 for both channels, while the indirect measurement for the top quark lifetime τ_{top} and the corresponding limits are shown in Table 8.7.

Chapter 9

Summary and Conclusions

The measurement of top quark mass, m_{top} and top quark width, Γ_{top} have been investigated during the first run of the LHC by the ATLAS experiment, as their measurement allows the confirmation of the SM predicted relationship between these two variables. Also if they are measured with reasonable precision it is possible to constrain the value of the Higgs boson mass. The LHC has provided proton-proton collisions at unprecedented centre of mass energies $\sqrt{s} > 7$ TeV, and high luminosities most effective for the production of $t\bar{t}$ pairs studied in this analysis.

However, most of the time during this first campaign, especially for collisions at 8 TeV was devoted to work on different calibrations and corrections to model the data reasonably well for different kinematic control variables. The measurement of the resolution of different variables for the different physical objects, was performed in order to propagate the uncertainties of the measurements into the different analyses systematic uncertainties. However work on improved measurements of some of these resolutions such as the Jet Energy Resolution is in progress currently. This resolution in particular is crucial for the Γ_{top} measurement as it is the source of the biggest systematic uncertainty for this analysis. A precise measurement of the jet energy resolution is in progress within the collaboration, which will have an associated uncertainty that will be propagated to the different analyses. The current prescription to calculate the JER uncertainty for the analysis presented here, seems to over-estimate this systematic effect introducing contributions to the total systematic uncertainty equal to $\pm$ 2.4 GeV and $\pm$ 3.1 GeV for the μ + jets and e + jets channels respectively.

The results obtained from the measurement of the Γ_{top} parameter in this analysis are:

- $\Gamma_{top} = 1.65$ GeV, and $\Gamma_{top} < 4.60$ GeV at 68 % C.L., and $\Gamma_{top} < 7.16$ GeV at 95 % C.L. for the μ + jets channel

- $\Gamma_{top} = 0.81$ GeV, and $\Gamma_{top} < 4.40$ GeV at 68 % C.L., and $\Gamma_{top} < 7.51$ GeV at 95 % C.L. for the e + jets channel

These results are consistent with the expected SM value $\Gamma_{top} \sim 1.33$ GeV.

The corresponding obtained results for the top quark lifetime, τ_{top} measurement are:

- $\tau_{top} = 3.99 \times 10^{-25}$ s and $\tau_{top} > 1.43 \times 10^{-25}$ s at 68 % C.L. and $\tau_{top} > 0.92 \times 10^{-25}$ s at 95 % C.L. for the μ + jets channel

- $\tau_{top} = 8.13 \times 10^{-25}$ s and $\tau_{top} > 1.50 \times 10^{-25}$ s at 68 % C.L. and $\tau_{top} > 0.87 \times 10^{-25}$ s at 95 % C.L. for the e + jets channel

These results are consistent with the expected SM value $\tau_{top} \sim 5 \times 10^{-25}$ s.

These measurements represent the first attempt from the ATLAS collaboration to set limits over Γ_{top} and τ_{top} top quark properties, and from the LHC experiments using a direct approach. A new calculation of the Jet Energy Resolution and its uncertainty will be provided by the collaboration in the next few months, which can be propagated to the analysis and potentially decrease substantially the current overestimated systematic uncertainty. This would allow to set even tighter limits over these two properties. After the results are optimized with an updated calculation of the JER uncertainty, the measurements from both channels can be combined. A combination might improve the results, however as the size of the total systematic uncertainty is comparable for both channels, the improvement might be small.

The presented results are consistent with those obtained by the CDF collaboration at the Tevatron using a similar technique [81]. Measurements for m_{top} and Γ_{top}

during the LHC run-II are expected to be more precise, as an unpresented quantity of signal events will be recorded and the sources of systematic uncertainties will be understood better. However the effort should be focused on the latter, as for the analysis presented here, the size of the statistical uncertainties are not a limitation in setting lower limits than CDF for Γ_{top}. The result is limited by the large size of the systematic uncertainty.

Additionally the infrastructure used to complete this analysis was given to a subgroup within the ATLAS collaboration and is currently being used to expand the presented analysis to a 2-dimensional analysis that allows the measurement of the JER, such an analysis may give encouraging results before the end of this year.

Bibliography

[1] **David Griffiths**, Introduction to Elementary Particles, Wiley VCH; 2nd, Revised Edition edition (20 Aug. 2008).

[2] **Anderson, Carl D.**, The Positive Electron, The Physical Review, Volume 43, Number 6, pp. 491-49.

[3] **W. N. Cottingham and D. A. Greenwood**, An Introduction to the Standard Model of Particle Physics, Cambridge University Press; 2 edition (22 Feb. 2007).

[4] **O. Behnke, K. Kroninger, G. Schott, and T. Schorner-Sadenius** Data Analysis in High Energy Physics, Wiley VCH (19 Jun. 2013).

[5] **Francis Halzen and Alan D. Martin**, Quarks and Leptons: An Introductory Course in Modern Particle Physics, Wiley; 1st edition (January 20, 1984).

[6] **R. K. Ellis, W. J. Stirling and B. R. Webber**, QCD and Collider Physics, Cambridge University Press (4 Dec. 2003).

[7] **Frederick Reines and Clyde L. Cowan, Jr.**, The neutrino, Nature, number: 178, 446 (Year: 1956).

[8] **Aharon Levy**, Recent HERA results on proton structure, Talk given at Moriond QCD 2014, arXiv:1405.3753 [hep-ex].

[9] **CDF and D0 collaborations**, Precise measurements of the W mass at the Tevatron and indirect constraints on the Higgs mass, Moriond QCD 2012, FERMILAB-CONF-12-103-E, arXiv:1204.3260 [hep-ex].

[10] **James J. Beatty and Stefan Westerhoff**, Annual Review of Nuclear and Particle Science, Vol. 59 (2009): 319 -345.

[11] **John Campbell, Keith Ellis, Ciaran Williams**, MCFM - Monte Carlo for FeMtobarn processes, URL: http://mcfm.fnal.gov/

[12] **Andreas S. Kronfeld, Chris Quigg**, Resource Letter: Quantum Chromodynamics, FERMILAB-PUB-10/040-T, Am.J.Phys.78:1081-1116, 2010, arXiv:1002.5032 [hep-ph].

[13] **A.D. Martin, W.J. Stirling, R.S. Thorne, G. Watt**, Parton distributions for the LHC, Eur. Phys. J. C63:189-285, 2009, arXiv:0901.0002 [hep-ph].

[14] **A.DeRoeck, R.S.Thorne**, Structure functions, Progress in Particle and Nuclear Physics 66, 727 2011, 10.1016/j.ppnp.2011.06.001, arXiv:1103.0555 [hep-ph].

[15] **S. Dawson**, Introduction to Electroweak Symmetry Breaking, Lectures given at the 1998 Summer School in High Energy Physics and Cosmology, Trieste, Italy, June 29-uly 17, 1998, arXiv:hep-ph/9901280.

[16] **CDF Collaboration**, Observation of Top Quark Production in $P\bar{P}$ Collisions, Phys.Rev.Lett.74:2626-2631, 1995, arXiv:hep-ex/9503002.

[17] **DØ Collaboration**, Observation of the Top Quark, Phys.Rev.Lett.74:2632-2637, 1995, arXiv:hep-ex/9503003.

[18] ATLAS Experiment International Masterclasses Website,
URL: atlas.physicsmasterclasses.org
Accessed: 03/07/2015

[19] **I.F. Ginzburg**, Multi-Higgs models. Perspectives for identification of wide set of models in future experiments at colliders in the SM-like situation, arXiv:1502.07197 [hep-ph].

[20] **Nathaniel Craig**, The State of Supersymmetry after Run I of the LHC, Lectures delivered at the training week of the GGI workshop "Beyond the Standard Model after the first run of the LHC." 72 pages, 28 figures. v2: Minor typos corrected, searches updated, arXiv:1309.0528 [hep-ph].

[21] **L. Evans and P. Bryant**, LHC technical report, LHC Machine. 2008, JINST 3, S08001.

[22] **Pettersson, Thomas Sven**, The Large Hadron Collider: conceptual design, LefÃÍvre, P (ed.), CERN-AC-95-05 LHC.

[23] **W. Erdt, G. Riddone, R. Trant**, The cryogenic distribution line for the LHC: Funtional specification and conceptual design, DOI: 10.1007/978-1-4615-4215-5_55, LHC Division, CERN, CH-1211, Geneva.

[24] **LHC safety assessment group**, Review of safety of LHC collisions, Theory Division, Physics Department, CERN, CH 1211, Geneva, Switzerland. 2008 J. Phys. G: Nucl. Part. Phys. 35, 115004, doi:10.1088/0954-3899/35/11/115004

[25] **Report of the LHC safety study group**, Study of potentially dangerous events during heavy-Ion collisions at the LHC, CERN-2003-001

[26] Aerial View of The Large Hadron Collider,
URL: http://imgarcade.com/1/lhc-map/
Accessed: 03/07/2015

[27] CERN Document Server, URL: https://cds.cern.ch/collection/Photos?ln=en

[28] **Vaia Papadimitriou**, Luminosity Determination at Tevatron, LHC Lumi Days: LHC Workshop on LHC Luminosity Calibration CERN-Proceedings-2011-001, pp. 90-95, arXiv:1106.5182 [physics.ins-det].

[29] **ATLAS Collaboration**, The ATLAS Liquid Argon calorimeter: An overview, 2009 J. Phys. Conf. Ser. 160, 012043.

[30] **ATLAS Collaboration**, ATLAS calorimetry, Nuclear Instruments and Methods in Physics Research A 494 (2002) 340âĂŞ345, Published by Elsevier Science B.V.

[31] **TOTEM Collaboration**, Luminosity-Independent Measurement of the *pp* Total Cross Section at $\sqrt{s} = 8$âĂĽTeV, Phys. Rev. Lett. 111, 012001, Published 3 July 2013.

[32] **TOTEM Collaboration**, The TOTEM experiment at the CERN Large Hadron Collider, JINST 3 (2008) S08007.

[33] **LHCf Collaboration**, The LHCf detector at the CERN Large Hadron Collider, 2008 JINST 3 S08006.

[34] **LHCb Collaboration**, The LHCb Detector at the LHC, 2008 JINST 3 S08005.

[35] **ALICE Collaboration**, The ALICE experiment at the CERN LHC, 2008 JINST 3 S08002.

[36] **CMS Collaboration**, The CMS experiment at the CERN LHC, 2008 JINST 3 S08004.

[37] **J. Beringer et al. Particle Data Group**, PR D86, 010001 (2012) and 2013 partial update for the 2014 edition (URL: http://pdg.lbl.gov/).

[38] **J. Beringer et al. Particle Data Group**, Statistics Review, PR D86, 010001 (2012) and 2013 partial update for the 2014 edition, URL: http://pdg.lbl.gov/2012/reviews/rpp2012-rev-statistics.pdf.

[39] **LHC Higgs Cross Section Working Group**, Handbook of LHC Higgs Cross Sections: 3. Higgs Properties, 10.5170/CERN-2013-004, arXiv:1307.1347 [hep-ph].

[40] **ATLAS Collaboration**, Observation of a new particle in the search for the Standard Model Higgs boson with the ATLAS detector at the LHC, Phys.Lett. B716 (2012) 1-29, arXiv:1207.7214 [hep-ex].

[41] **Peter W. Higgs**, Broken Symmetries and the Masses of Gauge Bosons, Phys. Rev. Lett. 13, 508 âĂŞ Published 19 October 1964.

[42] **G. S. Guralnik, C. R. Hagen, and T. W. B. Kibble** Global Conservation Laws and Massless Particles, Phys. Rev. Lett. 13, 585, Published 16 November 1964.

[43] **F. Englert and R. Brout** Broken Symmetry and the Mass of Gauge Vector Mesons, Phys. Rev. Lett. 13, 321 Published 31 August 1964.

[44] **CERN press office**, http://press.web.cern.ch/press-releases/2012/07/cern-experiments-observe-particle-consistent-long-sought-higgs-boson
Accessed: 03/07/2015

[45] **A. Denner, S. Heinemeyer, I. Puljak, D. Rebuzzi, M. Spira**, Standard Model Higgs-Boson Branching Ratios with Uncertainties, arXiv:1107.5909 [hep-ph].

[46] ATLAS Experiment Website, Multimedia,
http://www.atlas.ch/photos/lhc.html.
Accessed: 03/07/2015

[47] ATLAS Public Plots at Inspire Website Data Base,
URL: http://inspirehep.net/record/878496/plots.
Accessed: 03/07/2015

[48] ATLAS Magnetic Field Website,
URL: http://atlas.web.cern.ch/Atlas/GROUPS/MUON/magfield/
Accessed: 03/07/2015

[49] **ATLAS Collaboration**, ATLAS detector and physics performance : Technical Design Report, ATLAS-TDR 14, CERN/LHCC 99-14,
URL: http://cds.cern.ch/record/391176?ln=en. Accessed: 03/07/2015

[50] **ATLAS Collaboration**, The ATLAS Inner Detector Commissioning and Calibration, Eur.Phys.J., C70, 787-821, 2010, arXiv:1004.5293 [physics.ins-det].

[51] **Peter Cwetanski**, Straw performance and quality assurance for the ATLAS transition radiation tracker, Report Series in Physics, HU-P-D133, University of Helsinki.

[52] **Jonathan Stahlman**, Commisioning and Performance of the ATLAS Transition Radiation Tracker with First High Energy proton-proton and Pb-Pb collisions at the LHC, University of Pennsylvania, Talk at the TIPP, Chicago, Illinois, June 2011.

[53] **Peter Krieger**, ATLAS Calorimetry at the Large Hadron Collider, Talk at the Western Regional Nuclear and Particle Physics Conference 2004.

[54] **Vincent Hedberg**, Website,
URL: http://hedberg.web.cern.ch/hedberg/home/atlas/atlas.html
Accessed: 03/07/2015

[55] **ATLAS Standard Model Physics Group**,
URL: https://atlas.web.cern.ch/Atlas/GROUPS/PHYSICS/
CombinedSummaryPlots/SM/ATLAS_b_SMSummary_FiducialXsect/
Accessed: 03/07/2015

[56] **ATLAS Experiment Luminosity Public Results**,
URL:https://twiki.cern.ch/twiki/bin/view/AtlasPublic/
LuminosityPublicResults

Accessed: 03/07/2015

[57] Pseudorapidity Diagram
URL: http://en.wikipedia.org/wiki/Pseudorapidity
Accessed: 03/07/2015

[58] ATLAS Full List of Publications,
URL: https://twiki.cern.ch/twiki/bin/view/AtlasPublic/Publications
Accessed: 03/07/2015

[59] **Capeans, M; Darbo, G; Einsweiller, K; Elsing, M; Flick, T; Garcia-Sciveres, M; Gemme, C; Pernegger, H; Rohne, O; Vuillermet, R**, ATLAS Insertable B-Layer Technical Design Report, CERN-LHCC-2010-013, ATLAS-TDR-19, CERN. Geneva. The LHC experiments Committee; LHCC.

[60] **Maxim Perelstein, Michael E. Peskin, Aaron Pierce**, Top Quarks and Electroweak Symmetry Breaking in Little Higgs Models, Phys.Rev. D69 (2004) 075002, arXiv:hep-ph/0310039.

[61] **Arnulf Quadt**, Top Quark Physics at Hadron Colliders (Advances in the Physics ofParticles and Nuclei), Volume 28, Springer-Verlag Berlin Heidelberg 2007.

[62] **D0 Collaboration**, A precision measurement of the mass of the top quark, Nature 429, 638-642 (10 June 2004), doi:10.1038/nature, 02589.

[63] **M.Beneke et. al.**, Top Quark Physics, CERN-TH/2000-100, arXiv:hep-ph/0003033.

[64] **CKMfitter Group - J. Charles et al.**, Eur. Phys. J. C41, 1-131 (2005) [hep-ph/0406184], URL: http://ckmfitter.in2p3.fr

[65] **J. Alwall, R. Frederix, J.-M. Gerard, A. Giammanco, M. Herquet, S. Kalinin, E. Kou, V. Lemaitre, F. Maltoni)**, Is Vtb=1 ?, Eur.Phys.J.C49:791-801, 2007, arXiv:hep-ph/0607115.

[66] **ATLAS collaboration**, Search for charged Higgs bosons through the violation of lepton universality in $t\bar{t}$ events using pp collisions data at $\sqrt{s} = 7$ TeV with the ATLAS experiment, Eur. Phys. J. C, 73 6 (2013) 2465, arXiv:1302.3694 [hep-ex].

[67] **CMS collaboration**, Combined search for the quarks of a sequential fourth generation, Phys. Rev. D 86 (2012) 112003, arXiv:1209.1062 [hep-ex].

[68] **ATLAS collaboration**, Measurement of spin correlation and search for stop quark pair production at 8 TeV (20.3/fb) with the ATLAS detector, Phys. Rev. Lett. 114, 142001 (2015), arXiv:1412.4742 [hep-ex].

[69] **Fedor Bezrukov, Mikhail Shaposhnikov**, Why should we care about the top quark Yukawa coupling?, J.Exp.Theor.Phys. 120 (2015) 3, 335-343; ZhETF 147 (2015) 3, 389, arXiv:1411.1923 [hep-ph].

[70] **M.Jezabek and J.H.Kuhn**, QCD corrections to decays of heavy quarks, Nucl.Phys.B 314,1 (1989).

[71] **ATLAS collaboration**, The impact of the simulation of the top-quark and W-boson widths on measurements of the top-quark mass, ATL-COM-PHYS-2013-417, URL: https://cds.cern.ch/record/1541469/files/ATL-COM-PHYS-2013-417.pdf

[72] **CMS Collaboration**, Measurement of the ratio B(t to Wb)/B(t to Wq) in pp collisions at $\sqrt{s} = 8$ TeV, Phys. Lett. B 736 (2014) 33, arXiv:1404.2292 [hep-ex].

[73] **Thorsten Wengler**, Top quark angular distributions at LHC, Talk at Top 2012 5th International Workshop on Top Physics URL: https:indico.cern.ch/event/180665/session/10/#20120920

[74] **ATLAS Collaboration**, Measurement of Spin Correlation in Top-Antitop Quark Events and Search for Top Squark Pair Production in pp Collisions at $\sqrt{s}$=8 TeV Using the ATLAS Detector, Phys. Rev. Lett. 114, 142001 (2015), arXiv:1412.4742 [hep-ex].

[75] **ATLAS Collaboration**, Measurement of the W boson polarization in top quark decays with the ATLAS detector, JHEP 1206 (2012) 088, arXiv:1205.2484 [hep-ex].

[76] **ATLAS Collaboration**, Summary plots from the ATLAS Top physics group, URL: https://atlas.web.cern.ch/Atlas/GROUPS/PHYSICS/CombinedSummaryPlots/TOP/

[77] **ATLAS Collaboration**, Measurement of the top quark mass with the template method in the top antitop → lepton + jets channel using ATLAS data, Eur.Phys.J. C72 (2012) 2046, arXiv:1203.5755 [hep-ex].

[78] **ATLAS Collaboration**, Measurement of the top-quark mass in the fully hadronic decay channel from ATLAS data at $\sqrt{s}$=7 TeV, Eur. Phys. J. C (2015) 75:158, arXiv:1409.0832 [hep-ex].

[79] **ATLAS Collaboration**, Measurement of the charge asymmetry in dileptonic decays of top quark pairs in pp collisions at $\sqrt{s}$=7 TeV using the ATLAS detector, JHEP 05 (2015) 061, arXiv:1501.07383 [hep-ex].

[80] **ATLAS Collaboration**, Measurement of the mass difference between top and anti-top quarks in pp collisions at sqrt(s) = 7 TeV using the ATLAS detector, 10.1016/j.physletb.2013.12.010, arXiv:1310.6527 [hep-ex].

[81] **CDF Collaboration**, A Direct Measurement of the Total Decay Width of the Top Quark, Phys. Rev. Lett. 111, 202001 (2013), arXiv:1308.4050 [hep-ex].

[82] **D0 Collaboration**, An improved determination of the width of the top quark, FERMILAB-PUB-12-014-E, 10.1103/PhysRevD.85.091104, arXiv:1201.4156 [hep-ex].

[83] **Nikolaos Kidonakis**, Next-to-next-to-leading-order collinear and soft gluon corrections for t-channel single top quark production, Phys. Rev. D83:091503, 2011, arXiv:1103.2792 [hep-ph].

[84] **Jun Gao, Chong Sheng Li, Hua Xing Zhu**, Top-Quark Decay at Next-to-Next-to-Leading Order in QCD, 10.1103/PhysRevLett.110.042001, arXiv:1210.2808 [hep-ph].

[85] **CMS collaboration**, Measurement of the single-top-quark t-channel cross section in pp collisions at $\sqrt{s} = 7$ TeV, JHEP 12 (2012) 035, CMS-TOP-11-021, CERN-PH-EP-2012-274, arXiv:1209.4533 [hep-ex].

[86] **ATLAS Collaboration**, Flavor changing neutral currents in top quark production and decay,To appear in the proceedings of the 6th International Workshop on Top Quark Physics (TOP 2013), Durbach, Germany, 14-19 September 2013, arXiv:1312.5435 [hep-ex].

[87] **Antonio Salvucci**, Measurement of muon momentum resolution of the ATLAS detector, Presented at the 2011 Hadron Collider Physics symposium (HCP-2011), Paris, France, November 14-18 2011, 3 pages, 7 figures, arXiv:1201.4704 [physics.ins-det].

[88] **ALICE Collaboration**, ALICE: Physics Performance Report, Volume I, J. Phys. G: Nucl. Part. Phys. 30 1517, doi:10.1088/0954-3899/30/11/001

[89] **ATLAS Collaboration**, The ATLAS Collaboration technical report, The ATLAS Experiment at the CERN Large Hadron Collider. 2008 JINST 3 S08003, doi:10.1088/1748-0221/3/08/S08003.

[90] **Science and Technology Facilities Council**, Research / Particle Physics www.stfc.ac.uk/646.aspx

[91] **ATLAS Collaboration**, Observation of a new particle in the search for the Standard Model Higgs boson with the ATLAS detector at the LHC, Phys.Lett. B716 (2012), 1-29, arXiv:1207.7214 [hep-ex].

[92] **ATLAS Collaboration**, Evidence for the Higgs-boson Yukawa coupling to tau leptons with the ATLAS detector, JHEP 04 (2015) 117, arXiv:1501.04943 [hep-ex].

[93] **ATLAS Collaboration**, ATLAS detector and physics performance : Technical Design Report, 1 ATLAS TDR 14, CERN LHCC 99-14 25/May/1999

[94] **CMS Collaboration**, The CMS Collaboration technical report, The CMS Experiment at the CERN LHC. 2008 JINST 3 S08004

[95] **LHCb Collaboration**, The LHCb Collaboration technical report, The LHCb Experiment at the LHC. 2008 JINST 3 S08005

[96] **ALICE Collaboration**, The ALICE Collaboration technical report, The ALICE Experiment, at the CERN LHC. 2008 JINST 3 S08002

[97] CERN timelines: The history of CERN,
URL http://timeline.web.cern.ch/timelines/The-history-of-CERN

[98] **Powell, CF, Fowler P. H. and Perkins, D. H.**, The study of elementary particles by the photographic method, Pergamon Press, New York, 1959.

[99] Root Analysis Framework Website, URL: https://root.cern.ch/drupal/

[100] **M. Cacciari, G. P. Salam, and G. Soyez**, The anti-kT jet clustering algorithm. JHEP 04 (2008) 063, arXiv:0802.1189 [hep-ph].

[101] **ATLAS Collaboration**, Calibration of the b-tagging efficiency for c jets with the ATLAS detector using events with a W boson produced in association with a single c quark, ATLAS Conference Note ATLAS-CONF-2013-109, CERN, Geneva, Switzerland.

[102] **ATLAS Collaboration**, Commissioning of the ATLAS high-performance b-tagging algorithms in the 7 TeV collision data, 2011 Europhysics Conference on High Energy Physics, Grenoble, France, 21 - 27 Jul 2011, ATLAS-CONF-2011-102, CERN, Generva, Switzerland.

[103] **Paolo Nason, Bryan Webber**, Next-to-Leading-Order Event Generators, Cavendish-HEP-2012-02; CERN-PH-TH-2012-028, arXiv:1202.1251 [hep-ph].

[104] **ATLAS Collaboration**, Improved luminosity determination in pp collisions at $\sqrt{s} = 7$ TeV using the ATLAS detector at the LHC, Eur. Phys. J. C 73 (2013) 2518, arXiv:1302.4393 [hep-ex].

[105] **GEANT4 Collaboration, S. Agostinelli et al**, Nucl. Instrum. Methods Phys. Res. Sect A 506, 250 (2003)

[106] **ATLAS Collaboration**, The ATLAS Simulation Infrastructure, Eur. Phys. J. C 70 823 (2010), arXiv:1005.4568 [physics.ins-det].

[107] **CDF Collaboration**, A precise measurement of the W-boson mass with the Collider Detector at Fermilab, Phys. Rev. D 89, 072003 (2014), arXiv:1311.0894 [hep-ex].

[108] **Frank W., Lozier, Daniel M., Boisvert, Ronald F., Clark, Charles W.**, Temme, N. M. (2010), Voigt function, in Olver,Cambridge University Press, NIST Handbook of Mathematical Functions, MR 2723248, ISBN 978-0521192255.

[109] **ATLAS Collaboration**, Measurement of the top quark mass with the template method in the top antitop -> lepton + jets channel using ATLAS data, Eur.Phys.J. C72 (2012) 2046, arXiv:1203.5755 [hep-ex].

[110] **Johannes Erdmann, Stefan Guindon, Kevin Kroeninger, Boris Lemmer, Olaf Nackenhorst, Arnulf Quadt, Philipp Stolte**, A likelihood-based reconstruction algorithm for top-quark pairs and the KLFitter framework, 10.1016j.nima.2014.02.029, arXiv:1312.5595 [hep-ex].

[111] **Gary J. Feldman, Robert D. Cousins**, A Unified Approach to the Classical Statistical Analysis of Small Signals, Phys.Rev.D57:3873-3889, 1998, arXiv:physics/9711021 [physics.data-an].

[112] **ATLAS Collaboration**, Measurement of muon momentum resolution of the ATLAS detector, Presented at the 2011 Hadron Collider Physics symposium (HCP-2011), Paris, France, November 14-18 2011, 3 pages, 7 figures, arXiv:1201.4704 [physics.ins-det].

[113] **ATLAS Collaboration**, Electron performance measurements with the ATLAS detector using the 2010 LHC proton-proton collision data, Eur. Phys. J. C72 (2012) 1909, arXiv:1110.3174 [hep-ex].

[114] **ATLAS Collaboration**, Estimation of non-prompt and fake lepton backgrounds in final states with top quarks produced in proton-proton collisions at $\sqrt{s}$=8 TeV, ATLAS-CONF-2014-058, CERN, Geneva, 01 October 2014.

[115] **ATLAS Collaboration**, Measurement of the W+W- production cross section in proton-proton collisions at $\sqrt{s}$=8 TeV with the ATLAS detector, ATLAS-CONF-2014-033, Geneva, 01 June 2014.

[116] **ATLAS Collaboration**, Measurement of t-Channel Single Top-Quark Production in pp Collisions at $\sqrt{s}$=8 TeV with the ATLAS detector, Geneva, March 2014.

[117] **ATLAS Collaboration**, Determination of the jet energy scale and resolution at ATLAS using Z γ-jet events in data at $\sqrt{s} = 8$ TeV. CONF-JETM-2014-03. CERN, Geneva Switzerland, May 2015.

[118] **ATLAS Collaboration**, Data-driven determination of the energy scale and resolution of jets reconstructed in the ATLAS calorimeters using dijet and multijet events at $\sqrt{(s)} = 8$ TeV, ATLAS-CONF-2015-017, CERN, Geneva, Mar, 2015.

[119] **ATLAS Collaboration**, Monte Carlo Calibration and Combination of In-situ Measurements of Jet Energy Scale, Jet Energy Resolution and Jet Mass in ATLAS. ATLAS-CONF-2014-04, May 28, 2015.

[120] **ATLAS Collaboration**, Jet energy measurement with the ATLAS detector in proton-proton collisions at $\sqrt{(s)} = 7$ TeV, Eur. Phys. J. C73 (2013) 2304, arXiv:1112.6426 [hep-ex].

[121] **ATLAS Collaboration**, In-situ jet energy scale and jet shape corrections for multiple interactions in the first ATLAS data at the LHC, Tech. Rep. ATLAS-CONF-2011-030, CERN, Geneva, Mar, 2011.

[122] **ATLAS Collaboration**, In-situ pseudorapidity intercalibration for evaluation of jet energy scale uncertainty using dijet events in proton-proton collisions at $\sqrt{s} = 7$ TeV, Tech. Rep. ATLAS-CONF-2011-014, CERN, Geneva, Mar, 2011.

[123] **P. M. Nadolsky, H.-L. Lai, Q.-H. Cao, J. Huston, J. Pumplin**, Implications of CTEQ global analysis for collider observables, Phys.Rev. D78 (2008) 013004, arXiv:0802.0007 [hep-ph].

[124] **A. Martin, W. Stirling, R. Thorne, and G. Watt**, Parton distributions for the LHC, Eur. Phys. J. C63 (2009), 189285, arXiv:0901.0002 [hep-ph].

[125] **S. Forte, L. Garrido, J. I. Latorre, and A. Piccione**, Neural network parametrization of deep inelastic structure functions, JHEP 0205 (2002) 062, arXiv:hep-ph/0204232 [hep-ph].

[126] **PDF4LHC group, M. Botje, J. Butterworth, A. Cooper-Sarkar, A. de Roeck, J. Feltesse**, The PDF4LHC Working Group Interim Recommendations, arXiv:1101.0538 [hep-ph].

[127] **Wouter Verkerke, David Kirkby**, The RooFit toolkit for data modeling, arXiv:physics/0306116 [physics.data-an].

[128] MINUIT's User Guide,
URL: http://seal.web.cern.ch/seal/documents/minuit/mnusersguide.pdf
Accessed: 03/07/2015

[129] RooFit Analysis Tools Website,
URL: https://root.cern.ch/drupal/content/roofit
Accessed: 03/07/2015

[130] AcerMC Monte-Carlo Generator Website,
URL: http://borut.web.cern.ch/borut/
Accessed: 03/07/2015

[131] SHERPA Generator Website,
URL:https://sherpa.hepforge.org/trac/wiki
Accessed: 03/07/2015

[132] RooHistPdf, RooFit Analysis Tools Website,
URL: https://root.cern.ch/root/html/RooHistPdf.html
Accessed: 03/07/2015

[133] SFrame - A ROOT data analysis framework Website,
URL: http://sourceforge.net/projects/sframe/
Accessed: 03/07/2015

[134] LHAPDF Documentation Website,
URL: https://lhapdf.hepforge.org/
Accessed: 03/07/2015

[135] LXPLUS Service, CERN Information and Technology Deparment Website,
URL: http://information-technology.web.cern.ch/services/lxplus-service
Accessed: 03/07/2015

[136] DO Collaboration, Diagrams for Conferences,
URL: http://www-d0.fnal.gov/Run2Physics/top/top_public_web_pages/
top_feynman_diagrams.html
Accessed: 03/07/2015

[137] Feynman Diagram,
URL:http://en.wikipedia.org/wiki/Feynman_diagram
Accessed: 03/07/2015

[138] Electromagnetic Shower,
URL: http://www-zeus.physik.uni-bonn.de/ brock/feynman/vtp_ws0506/

Accessed: 03/07/2015

[139] ATLAS Detector Simulation with GEANT4 Website,
URL:http://atlas-computing.web.cern.ch/atlas-computing/packages/
simulation/geant4/geant4.html
Accessed: 03/07/2015

[140] Open Science Grid Website,
URL:http://www.opensciencegrid.org/using-the-osg-to-test-theories-of-nature-
at-the-lhc/
Accessed: 03/07/2015

[141] ROOT data analysis framework - Kernel Density Estimation Website,
URL: https://root.cern.ch/root/html/TKDE.html
Accessed: 03/07/2015

[142] **Atlantis Group**, Event Display for ATLAS,
URL: http://cern.ch/atlantis/
Accessed: 03/07/2015

[143] **Atlantis Live Group Website**,
URL: http://atlas-live.cern.ch/
Accessed: 03/07/2015

[144] JiveXML Software in the ATLAS twiki Resources for Event Display,
URL: https://twiki.cern.ch/
twiki/bin/viewauth/Atlas/JiveXML
Accessed: 03/07/2015

[145] Official Java Documentation,
URL: http://java.com/en/download/faq/whatis_java.xml
Accessed: 03/07/2015

[146] Java Latest Releases Java Downloads Website,
URL: http://www.oracle.com/technetwork/java/
javase/ downloads/index.html
Accessed: 03/07/2015

[147] Athena Core Software,
URL: http://atlas-computing.web.cern.ch/atlas-computing/packages/athenaCore/athenaCore.php
Accessed: 03/07/2015

[148] ATLAS b-tagging efficiencies and results,
URL: https://twiki.cern.ch/twiki/bin/view/ AtlasPublic/FlavourTaggingPublicResultsCollisionData
Accessed: 03/07/2015